
# Two-Dimensional Zirconium-Based Metal-Organic Nanosheets for Separation Applications

**Jiangtian Tan**

**200203724**

**A thesis submitted in partial fulfilment of the requirements for the degree of**

**Doctor of Philosophy**

**The University of Sheffield**

**Faculty of Science**

**Department of Chemistry**

**January 2024**

# Abstract

The ability to separate mixtures of chemical species is key to technologies as diverse as drug delivery, water purification and carbon capture. Two-dimensional zirconium-based metal-organic nanosheets (MONs) have well-defined pore size, tunable functionalities, good water, thermal and chemical stability, making them ideal materials for use in separation applications. However, the separation capability of MONs when processed into membranes is not well-studied. In this thesis, Zr-BTB (BTB = 1,3,5-benzenetribenzoate) MONs were synthesised and processed into gels and membranes for use in a variety of solution and gas phase separations.

In **Chapter 2**, Zr-BTB MON suspensions were shown to form self-healing gels with a house of cards structure through a facile centrifugation method. Molecular cargoes could be loaded into the gels through centrifugation of mixtures composed the Zr-BTB MON suspensions and the cargo solutions. A significantly higher loading was observed for the charged cargoes such as methylene blue (MnB), methyl orange (MO), and brilliant blue G (BBG), compared to the neutral ones such as trans-anethole (T-Ane) and carbamazepine (CBZ). Neutral T-Ane cargoes smaller than the pore size of Zr-BTB were found to diffuse more rapidly out of the gels than the larger CBZ cargoes whilst charged cargoes (MnB, MO and BBG) were found to release much more slowly than the neutral ones. This was attributed to the different diffusion pathways open to different species with the porous nanosheets acting like "fishing nets" which smaller species could pass through whilst larger species had to travel around and charged species stuck to them.

In **Chapter 3**, Zr-BTB MON suspensions were spin-coated onto polyethersulfone (PES) supports to fabricate composite membranes. The fabricated membranes showed a high permeability toward small negatively charged dyes such as MO and a high rejection rate of up to ~90% toward larger dyes such as BBG. Deposition of the MONs onto the PES supports also increased the adsorption of positively charged dyes such as MnB on the membranes and finally improved their rejection rates toward MnB. In **Chapter 4**, Zr-BTB MONs were incorporated into Matrimid and PEBAX polymers to fabricate mixed matrix membranes (MMMs) for use in the separation of $CO_2$ and $N_2$. It was found that the incorporation of 5 wt% of MONs into the polymers decreased the $CO_2/N_2$ separation selectivity of the membranes. The MON suspensions were also processed into composite membranes by depositing them onto polyacrylonitrile supports. However, due to the relatively large pore size of the MONs (5.4 Å) compared to the kinetic diameters of the small gas molecules ($CO_2$: 3.3 Å, $N_2$: 3.68 Å) as well as the defects in the fabricated membranes, they showed high gas permeability, but almost no $CO_2/N_2$ separation selectivity. In both **Chapters 3 and 4**, MONs composed of $Zr_6$ clusters and 2'-amino-5'-(4-carboxyphenyl)-[1,1':3',1''-terphenyl]-4,4''-dicarboxylate (BTB-$NH_2$) or 4,4',4''-s-triazine-2,4,6-triyl-tribenzoate (TATB) ligands were also used to fabricate membranes. However, in comparison with Zr-BTB, the use of Zr-BTB-$NH_2$ and Zr-TATB did not significantly improve the separation performance of the membranes toward organic dyes and gases, which could be attributed to the isoreticular structure of the three MONs, giving them the same pore size.

Overall, this thesis demonstrates that two-dimensional zirconium-based MONs can be used to prepare gels for use in the selective loading and differential release of small molecules, and the MONs can also be processed into different types of membranes for use in the separation of dyes and gases. Through functionalisation of the MONs to tune their pore size and surface properties, we anticipate progress in the separation of small dyes, gas molecules and salts.

# Acknowledgements

First of all, I would like to thank my supervisor **Dr Jonathan Foster**. Without your help, it is impossible to finish this project. Thank you for your patience and encouragement, and for all the help you gave me during my one-year MSc and three-year PhD. Thank you for giving me opportunities to attend conferences to present my work and to meet people from different universities. I would also like to thank my second supervisor **Dr Robert Dawson** for helping me with the preparation of PIM-1.

Thanks to Foster Group members past and present, **Dr David Ashworth, Dr Joshua Nicks, Dr Kezia Sasitharan, Dr Ram Prasad, Dr Charlotte Kiker, Dr Michael Harris, Dr Freya Cleasby, Dr Amelia Wood, Dr Prioti Purba, Benedict Smith, Sanyou Xu (Victor) and Alana Barlow**. I really enjoyed the time working with you in the lab. Also thank you to the MChem students that I have supervised **Thomas Collett and Bethany Lingard**, I enjoyed the time working with you on water purifications.

I would like to thank **The Grantham Centre for Sustainable Futures** for accepting me as a Grantham Scholar. Thank you to **Jana Green** and **Deborah Beck** for organising the trainings. Thank you to **Tete' Mausse, Zongting Cai, Veysel Yildiz and Amal**, we organised an excellent Festival of Debate online event together. Thank you to **The Grantham Centre for Sustainable Futures** for funding my research project: "Porous two-dimensional materials for carbon capture". Thank you to **Qian Jia, Prof. Paul Wright, Dr Elsa Lasseuguette and Prof. Maria-Chiara Ferrari** for your help in this research project.

Thank you to the Department of Chemistry at the University of Sheffield and to all technical staff and administration staff within our department for the training and support. I would also like to thank **Christopher Hill** within the Department of Molecular Biology and Biotechnology for the SEM training.

Finally, I would like to thank my **parents** for encouraging me and funding me to complete this PhD project.

# Author's Declaration

This research has been performed between the months of October 2020 and January 2024, within the Department of Chemistry at the University of Sheffield, under the supervision of Dr Jonathan Foster.

1st referee, Prof. Anthony Ryan, The University of Sheffield

2nd referee (external), Prof. Andrew Burrows, University of Bath

I, the author, confirm that this Thesis is my own work. I am aware of the University's Guidance on the Use of Unfair Means (www.sheffield.ac.uk/ssid/unfair-means). This work has not previously been presented for an award at this, or any other, university.

# List of Publications

## Manuscripts in preparation or submission

1. Metal-organic nanosheet gels-hierarchically porous materials for selective loading and differential release, **Jiangtian Tan** and Jonathan A. Foster, manuscript in preparation.

2. An isoreticular series of Zr-tricarboxylate based metal-organic nanosheets for water purification applications, **Jiangtian Tan**, Bethany J. Lingard, Ram R. R. Prasad, and Jonathan A. Foster, manuscript in preparation.

3. Zirconium-based metal-organic nanosheets for gas separation applications, **Jiangtian Tan**, Elsa Lasseuguette, Qian Jia, Ram R. R. Prasad, Maria-Chiara Ferrari, Paul A. Wright, and Jonathan A. Foster, manuscript in preparation.

## Other manuscript contributions

1. Modulated self-assembly of catalytically active metal-organic nanosheets containing $Zr_6$ clusters and dicarboxylate ligands, Ram R. R. Prasad, Sophia S. Boyadjieva, Guojun Zhou, **Jiangtian Tan**, Francesca C. N. Firth, Sanliang Ling, Zhehao Huang, Matthew J. Cliffe, Jonathan A. Foster, and Ross S. Forgan, manuscript submitted for review.

2. ZIF nanosheets incorporated asymmetric mixed matrix membranes for gas separation, Qian Jia, **Jiangtian Tan**, Elsa Lasseuguette, Elliott L. Bruce, Jonathan A. Foster, Maria-Chiara Ferrari, and Paul A. Wright, manuscript in preparation.

# List of Conference Presentations

## Oral presentations

1. **Jiangtian Tan** and Jonathan A. Foster, "Metal-organic nanosheet gel for differential cargo release", 6th Annual UKPorMat Conference, Sheffield, June 2023.

2. **Jiangtian Tan** and Jonathan A. Foster, "Metal-organic nanosheet gels for differential cargo release", 2023 Early Career Researcher Macrocyclic and Supramolecular Chemistry (MASC) Meeting, London, July 2023.

3. **Jiangtian Tan** and Jonathan A. Foster, "Metal-organic nanosheet gel for differential cargo release", Grantham Centre for Sustainable Futures: Internal Seminar and Cake (ISAC), Sheffield, October 2023.

4. **Jiangtian Tan** and Jonathan A. Foster, "Metal-organic nanosheet gel for differential cargo release", RSC Dalton Division Northern Regional Meeting 2023, Sheffield, December 2023.

## Poster presentations

1. **Jiangtian Tan**, Robert Dawson and Jonathan A. Foster, "2D metal-organic nanosheets for membrane-based water purifications", Grantham Centre for Sustainable Futures: Annual Symposium 2021, Sheffield, November 2021.

2. **Jiangtian Tan**, Robert Dawson and Jonathan A. Foster, "Metal-organic nanosheets for water purification applications", Faculty of Science-Graduate School Research Showcase 2023, Sheffield, March 2023.

3. **Jiangtian Tan** and Jonathan A. Foster, "Metal-organic nanosheet gels for differential cargo release", DYME Dalton Young Members Event, Birmingham, August 2023.

# Table of Contents

# List of Abbreviations

| | |
|---|---|
| 1D | One-dimensional |
| 2D | Two-dimensional |
| 3D | Three-dimensional |
| 6FDA | 4,4′-(hexafluoroisopropylidene)diphthalic anhydride |
| AFM | Atomic force microscopy |
| Al-MOF | Aluminum tetra-(4-carboxyphenyl) porphyrin framework |
| BA | Benzoic acid |
| BB or BBG | Brilliant blue G |
| BDC | 1,4-benzenedicarboxylate |
| BDC-$NH_2$ | 2-aminoterephthalate |
| Bim | Benzimidazolate |
| BPDC | Biphenyl-4,4′-dicarboxylate |
| BPY | 4′,6′-bis(4-benzoic acid)-(2,2′-bipyridine)-5-carboxylate |
| BPYDC | 2,2′-bipyridine-5,5′-dicarboxylate |
| Bpy | 2-(5′-methyl(2,2′-bipyridin)-5-yl)acetic acid |
| BTB | 1,3,5-benzenetribenzoate |
| BTB-COOH | 2′,4′,6′-tris(4-carboxypheny)benzoate |
| BTB-$NH_2$ | 2′-amino-5′-(4-carboxyphenyl)-[1,1′:3′,1′′-terphenyl]-4,4′′-dicarboxylate |
| BUT | Beijing University of Technology |
| CBZ | Carbamazepine |
| CP | Copper phthalocyanine |
| DAM | Diaminomesitylene |
| DLS | Dynamic light scattering |
| DMF | *N,N*-dimethylformamide |
| DMNP | Dimethyl 4-nitrophenyl phosphate |
| EtOH | Ethanol |
| EuBTB | $[Eu(BTB)(H_2O)_2 \cdot solvent]_n$ |
| GO | Graphene oxide |
| $H_2O$ | Water |
| $H_2BDC$ | 1,4-benzenedicarboxylic acid |

| | |
|---|---|
| $H_2BPDC$ | Biphenyl-4,4’-dicarboxylic acid |
| $H_2BPYDC$ | 2,2’-bipyridine-5,5’-dicarboxylic acid |
| $H_3BPY$ | 4’,6’-bis(4-benzoic acid)-(2,2’-bipyridine)-5-carboxylic acid |
| $H_3BTB$ | 1,3,5-benzenetribenzoic acid |
| $H_3BTB$-COOH | 2’,4’,6’-tris(4-carboxypheny)benzoic acid |
| $H_3BTB$-$NH_2$ | 2’-amino-5’-(4-carboxyphenyl)-[1,1’:3’,1’’-terphenyl]-4,4’’-dicarboxylic acid |
| $H_3TATB$ | 4,4’,4’’-s-triazine-2,4,6-triyl-tribenzoic acid |
| TATB | 4,4’,4’’-s-triazine-2,4,6-triyl-tribenzoate |
| TTAC | Terphenyl tetracarboxylate |
| HCOOH | Formic acid |
| HPAN | Hydrolysed polyacrylonitrile |
| MAMS | Mesh adjustable molecular sieve |
| MF | Microfiltration |
| MIL | Materials Institute Lavoisier |
| MMM | Mixed matrix membrane |
| MnB | Methylene blue |
| MO | Methyl orange |
| MOF | Metal-organic framework |
| MOG | Metal-organic gel |
| MON | Metal-organic nanosheet |
| NF | Nanofiltration |
| NiTCPP | Nickel-tetrakis(4-carboxyphenyl)-porphyrin |
| PAN | Polyacrylonitrile |
| PCN | Porous coordination network |
| PDDA | Poly(diallyldimethylammonium chloride) |
| PEI | Polyethylenimine or Polyethyleneimine |
| PES | Polyethersulfone |
| PG | Phthalocyanine green |
| PI | Polyimide |
| PIM | Polymer of intrinsic microporosity |
| PXRD | Powder X-ray diffraction |
| RO | Reverse osmosis |

| | |
|---|---|
| SA | Sodium alginate |
| SEM | Scanning electron microscopy |
| T-Ane | Trans-anethole |
| TCPc | 2,9,16,23-tetracarboxyphthalocyanine |
| TCP(Fe) | Fe(III) meso-tetra(4-carboxyphenyl)porphine chloride |
| TEM | Transmission electron microscopy |
| THF | Tetrahydrofuran |
| UF | Ultrafiltration |
| UiO | Universitetet i Oslo |
| UV-Vis | Ultraviolet visible |
| WOR | Water oxidation reaction |
| VF | Vacuum filtration |
| ZIF | Zeolitic imidazolate framework |
| $ZrCl_4$ | Zirconium(IV) chloride |

# Chapter 1

# Introduction and Project Aims

## 1.1 Introduction

Graphene is the archetypal two-dimensional (2D) material, which is composed of $sp^2$-hybridised carbon atoms (**Figure 1a**).[1] Graphene was first developed by Novoselov and co-workers in 2004 by exfoliation of a highly-oriented pyrolytic graphite using a 'Scotch Tape' method.[2] The unique single-atom thickness and fascinating physical and chemical properties of graphene makes it a promising candidate for a wide range of applications.[3-5]

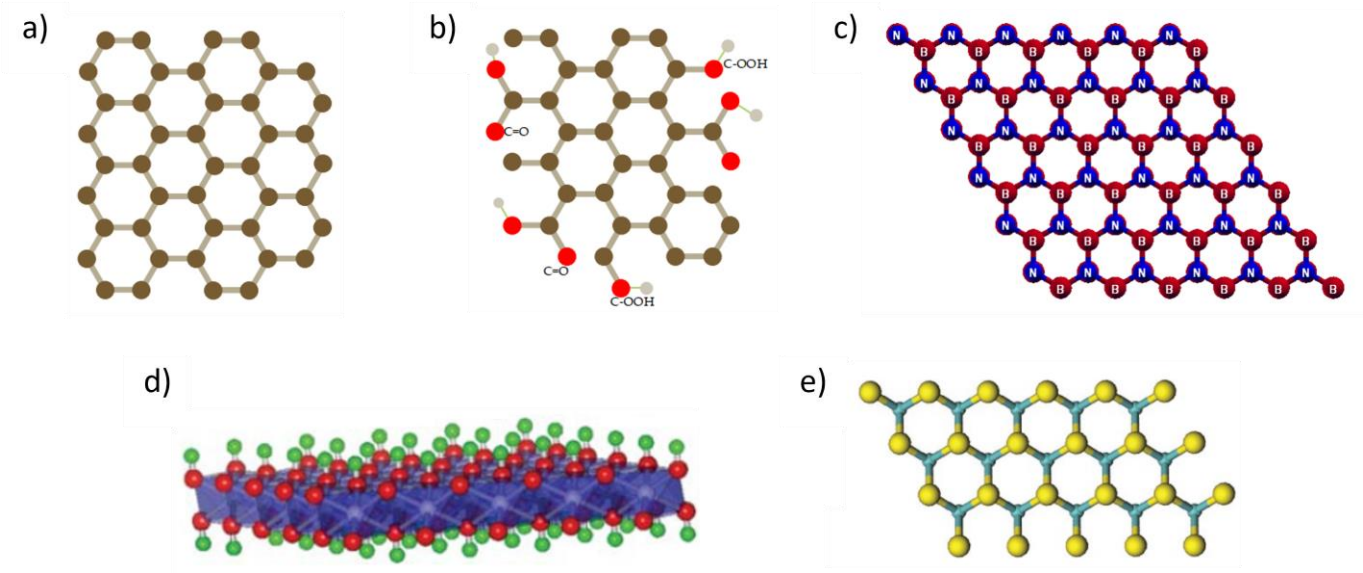


***Figure 1.*** *Structures of classic 2D materials (a) graphene,[6] (b) graphene oxide,[6] (c) hexagonal boron nitride,[7] (d) layered double hydroxides,[8] and (e) molybdenum disulphide.[9]*

Since the revolutionary discovery of graphene, a wide range of other 2D materials have been developed, including graphene oxide (GO),[6] hexagonal boron nitride,[7] layered double hydroxides,[8] and molybdenum disulphide[9] (**Figure 1b-1e**). As with graphene, the atomic-level thickness of these 2D materials endows them with good mechanical flexibility as well as good optical transparency, making them promising candidates for the preparation of flexible and transparent electronic/optoelectronic devices.[10-12] Their high surface-to-volume atom ratios and large specific surface areas make them ideal materials as catalysts,[13] because the reactant molecules can easily access their active sites.[14] The ultrathin nature of these 2D materials together with their large lateral dimension also make them ideal materials for constructing high-performance gas separation[15,16] and water purification membranes.[17,18] However, a common problem with these 2D materials is their relatively simple compositions, which limits the options available for further modification and optimisation of their structures and properties for particular applications.[19]

Metal-organic frameworks (MOFs) are highly crystalline and porous materials composed of metal ions or metal clusters linked by organic ligands.[20] These materials benefit from the wide range of metal sources (e.g., $Zn(NO_3)_2 \cdot 6H_2O$,[21] $Cu(NO_3)_2 \cdot 3H_2O$[22] and $ZrCl_4$[23]) and organic ligands (e.g., benzimidazolate,[24] 1,4-benzenedicarboxylate[25] and 1,3,5-benzenetricarboxylate[26]) available for constructing MOFs, more than 90,000 MOF materials have been successfully prepared and reported in the Cambridge Structural Database (CSD).[27] MOFs have many attractive properties, such as large surface area, high porosity, well-defined pore size, good thermal and water stability, good biocompatibility and biodegradability.[28,29] In addition, the modular nature of MOFs allows their structures and surface properties to be tuned with relative ease.[30] These features make MOFs ideal materials for a wide range of applications, including sensing,[31] catalysis,[32] drug delivery,[33] and they have also been widely used for separation applications due to their porous nature.[34,35] MOFs with different dimensions and morphologies have been developed, including one-dimensional (1D) MOF nanorods and nanowires,[36] three-dimensional (3D) bulk MOF crystals,[37] and two-dimensional (2D) metal-organic nanosheets (MONs).[19,38]

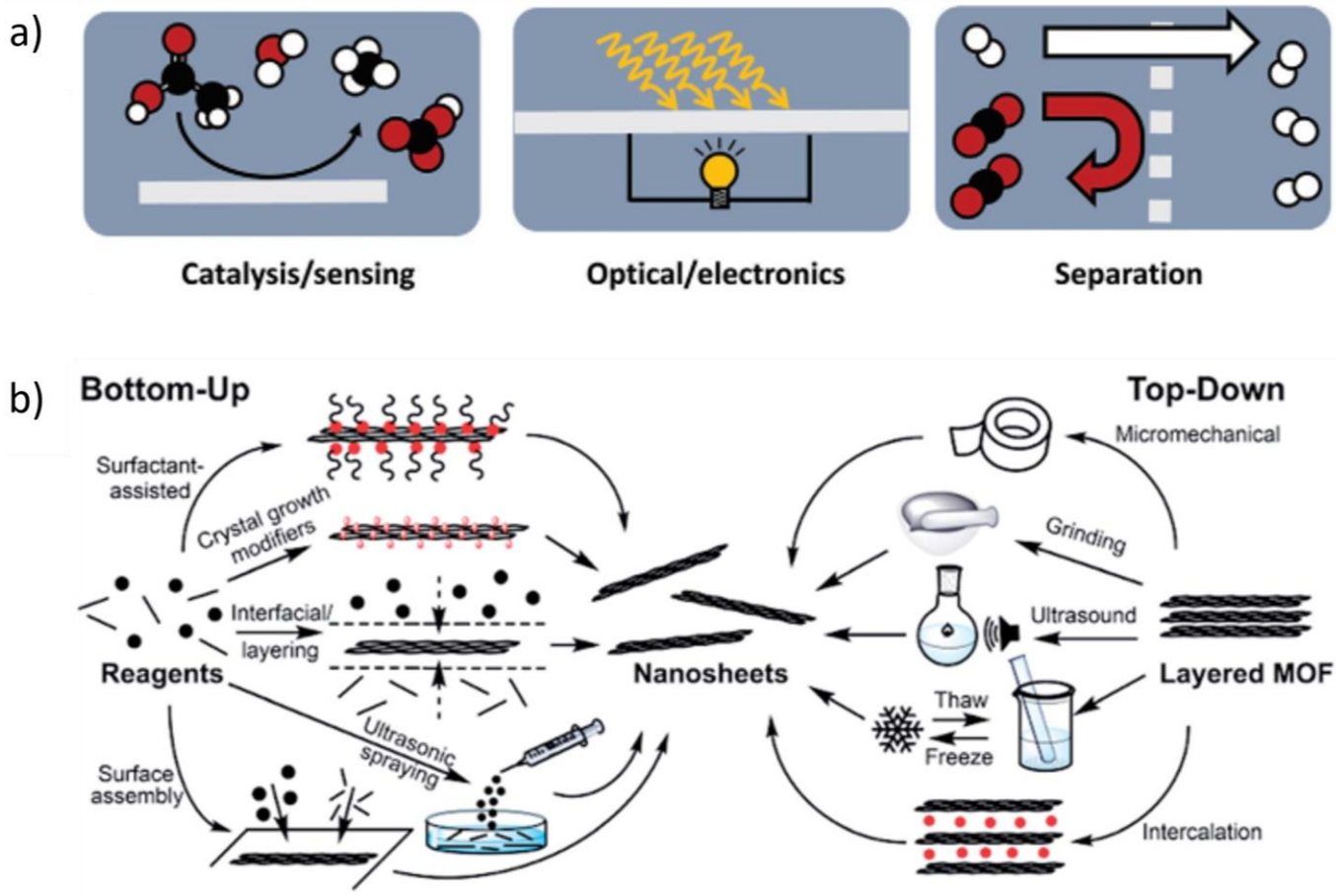


***Figure 2.*** *(a) Schematic illustrations of different applications of MONs.[38] (b) Schematic illustrations of different preparation methods of MONs.[19]*

MONs are anisotropic materials, which have a sheet-like morphology similar to other 2D materials.[38] Their metal centres and organic ligands are continuously connected within the 2D plane, but not in the 3rd dimension, which endows MONs with ideally monolayer thickness and high aspect ratios.[19] As with MOFs, MONs have diverse structures and tunable surface properties,[39,40] and they are porous materials with well-defined pore size and high external surface area.[38] These unique properties and advantages of MONs make them promising candidates for a wide range of applications, including catalysis,[41,42] sensing,[43,44] electronics,[45,46]and separation applications (**Figure 2a**).[38,47,48]

A wide variety of methods have been developed to prepare MONs, which can be roughly divided into two categories: bottom-up methods and top-down methods (**Figure 2b**).[19] Bottom-up method refers to direct synthesis of MONs from metal source and organic ligands.[47] The key step for bottom-up synthesis of MONs is to avoid the formation of 3D isotropic crystals, which requires selectively preventing the crystal growth along the 3rd dimension without affecting the crystal growth within the 2D plane of MONs.[14] So far, various bottom-up methods have been developed to prepare MONs, such as surfactant-assisted synthesis,[49-51] crystal growth modulation,[52] and interfacial synthesis.[53-55] Top-down method refers to exfoliation of layered MOFs into MONs.[14] In many layered MOFs, the 2D MON layers are stacked along one direction through weak interlayer interactions, such as van der Waals forces, π-π interactions and hydrogen bonding.[56] In comparison with the strong coordination bonds within the 2D plane of MONs, these weak interactions between the layers can be removed by top-down methods with relative ease.[14] So far, various top-down methods have been developed to prepare MONs, including micromechanical exfoliation,[57] grinding,[58] ultrasonication,[59-61] intercalation,[62] and freeze-thaw.[63]

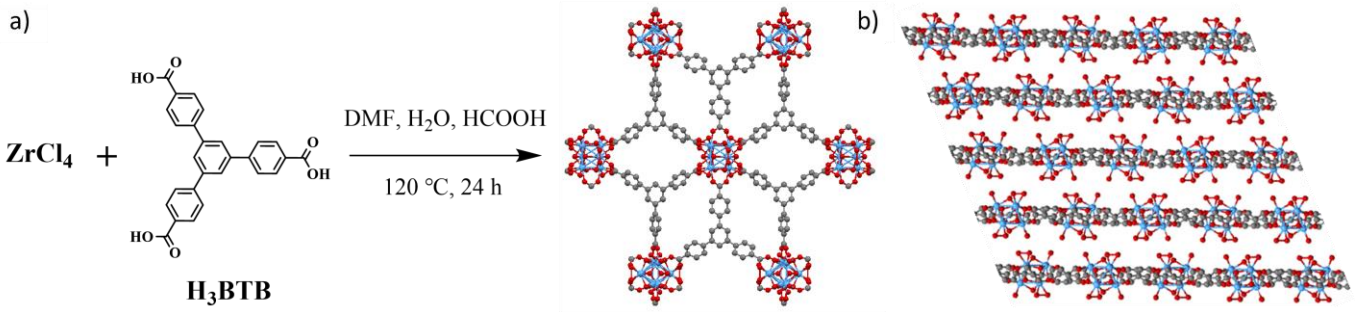


***Figure 3.*** *(a) Synthesis of Zr-BTB. DMF = N,N-dimethylformamide, $H_2O$ = water, HCOOH = formic acid. (b) Layered structure of Zr-BTB. The crystal structures of Zr-BTB are downloaded from CCDC (deposition number: 1567188).*[64]

In this thesis, 2D Zr-BTB MONs (**Figure 3**, BTB = 1,3,5-benzenetribenzoate) and their derivatives have been investigated for use in separation applications. In the rest of this chapter, an introduction to

Zr-BTB and other zirconium-based MONs including their different structures, functionalities and applications are outlined, followed by an introduction to the use of different MONs in separation applications. Examples of using Zr-BTB and other zirconium-based MONs in different separation applications are presented. Finally, the overall aims of this thesis are outlined.

## 1.2 Zirconium-based MONs

A large number of 3D zirconium-based MOFs (e.g., UiO-66,[65] UiO-67,[66] and MOF-808[67]) have been reported in the literature, and they have shown great promise in many applications, including drug delivery and biomedicine,[68] sensing,[69] and removal of water pollutants.[70] 2D Zr-BTB MON is formed by the coordination between $Zr_6$ clusters and tritopic 1,3,5-benzenetribenzoic acid ($H_3BTB$) ligands (**Figure 3**), and it has many advantages similar to the 3D zirconium-based MOFs, such as well-defined pore size, good stability in water and acidic conditions, as well as good thermal and chemical stability.[64,71]

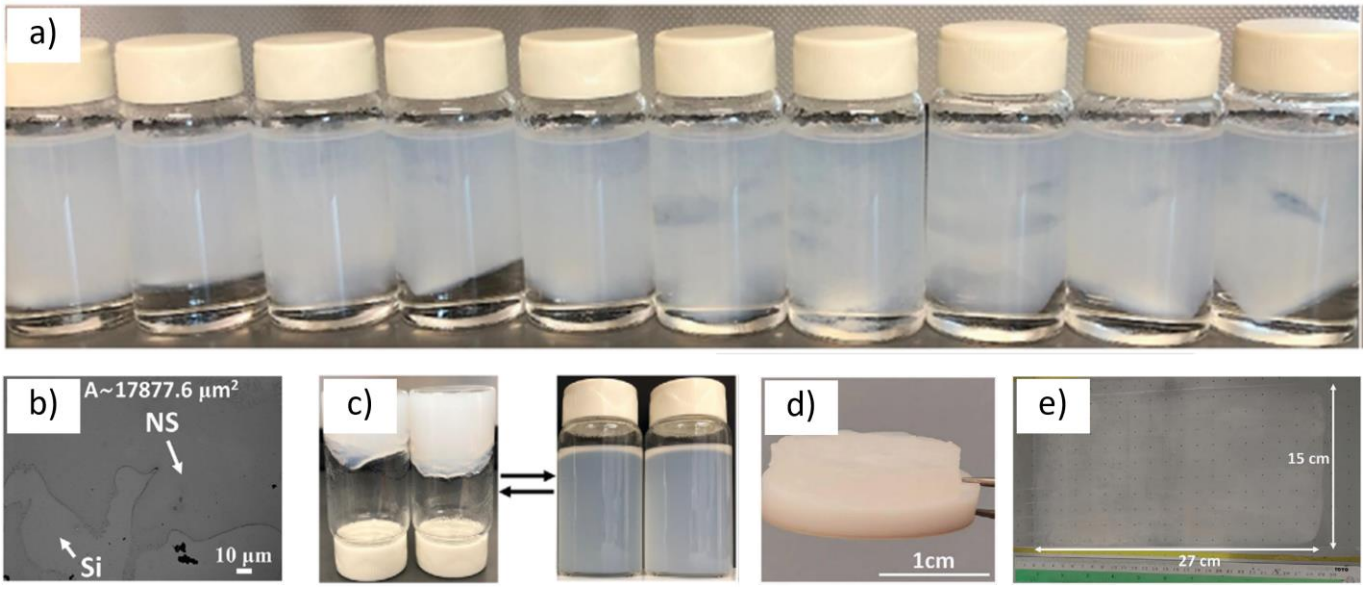


***Figure 4.*** *(a) Photograph of Zr-BTB MON suspensions (sols). (b) SEM image of one-piece Zr-BTB MON deposited on Si surface. (c) Reversible Zr-BTB sol-gel transformation. (d) Photograph of Zr-BTB monolith. (d) Photograph of Zr-BTB film on polystyrene substrate.*[72]

A wide variety of methods have been developed to prepare Zr-BTB MONs and the prepared nanosheets have been used in different applications. For example, Zhao and co-workers developed a facile and scalable bottom-up method for the preparation of Zr-BTB MONs.[72] In their work, *N,N*-dimethylformamide (DMF), formic acid (HCOOH) and water ($H_2O$) solutions containing zirconium(IV) chloride ($ZrCl_4$) and $H_3BTB$ were incubated at 120 °C for 24 h to synthesis the Zr-BTB MONs. The HCOOH

was used as a capping agent to selectively occupy six coordination sites of the $Zr_6$ clusters out of the 2D plane, whilst leaving the other six sites within the 2D plane unoccupied and available for the ligands to coordinate. This resulted in the formation of Zr-BTB MONs with a thickness of approximately 13 nm and a large area of approximately 17877.6 $\mu m^2$ (**Figure 4a and 4b**). The Zr-BTB MONs they prepared also had excellent solution processability. As shown in **Figure 4c**, reversible Zr-BTB sol-gel transformations could be realised by removing or adding solvents such as DMF, tetrahydrofuran (THF) or $H_2O$, and the Zr-BTB MON suspensions could also be processed into monoliths (**Figure 4d**), aerogels, xerogels and films (**Figure 4e**).

In addition to formic acid, other monocarboxylic acids have also been used as capping agents to modulate the crystal growth of Zr-BTB to prepare MONs. For example, Liu and co-workers used benzoic acid (BA) to prepare Zr-BTB, and the MONs they obtained showed great potential as a sensor for the detection of 2,4-dinitrophenol in water.[73] Wu and co-workers used a hydrothermal method and acetic acid for preparing Zr-BTB MONs.[74] In their work, $ZrCl_4$ and $H_3BTB$ were dissolved in a mixed solvent of deionised water and acetic acid in a round bottomed flask and the MONs were prepared after reacting at 120 °C for 20 h under condensation reflux. The Zr-BTB MONs they obtained had a thickness of approximately 10 nm and a high aspect ratio and were used for DNA detection.

Apart from using monocarboxylic acid modulators, a microdroplet flow synthesis method has also been developed to control the crystal growth of Zr-BTB to prepare nanosheets.[75] As shown in **Figure 5a and 5b**, DMF and formic acid solutions containing $ZrCl_4$ and $H_3BTB$ were continuously pumped into a stirred micromixer to form a homogeneous solution of reactants. This solution was then dispersed into microdroplets by shear forces between co-current silicone oil and reactant solution, which were immiscible with each other. The microdroplets then flowed through a cylindrical microchannel into the reaction coil which was heated at 130 °C. The resulting products were cooled to room temperature and washed to remove the silicone oil. The Zr-BTB MONs prepared by this method (**Figure 5c and 5e**) were significantly thinner than the ones prepared by conventional solvothermal synthesis method (**Figure 5d and 5f**) because the stacked growth of Zr-BTB along the vertical direction was restricted under the microdroplet flow reaction conditions. These ultrathin Zr-BTB MONs also exhibited higher external surface area and superior $CO_2$ and $CH_4$ adsorption performance compared to the ones prepared by conventional solvothermal synthesis method. In addition, the space-time yield of Zr-BTB MONs prepared by the microdroplet flow synthesis method was estimated to be 385 kg $m^{-3}$ $day^{-1}$, which was high enough for mass production.

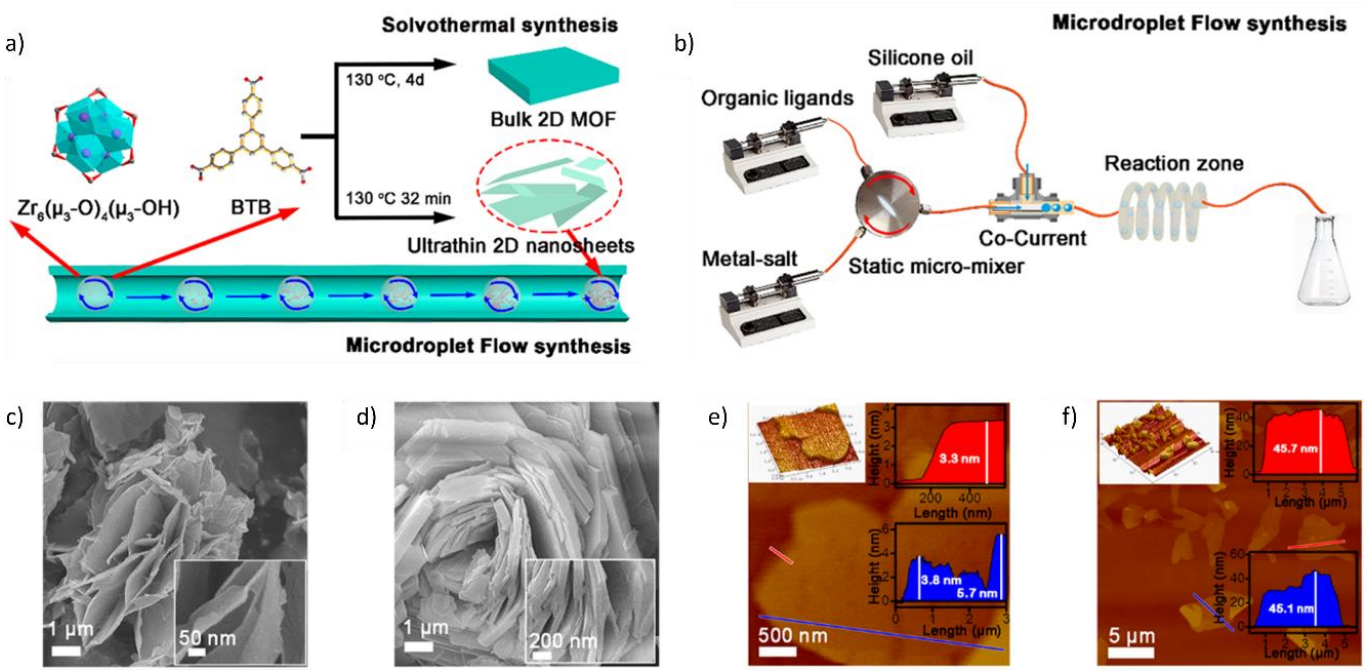


***Figure 5.*** *(a) Schematic illustration of Zr-BTB MONs prepared by microdroplet flow synthesis method and bulk Zr-BTB MOF prepared by solvothermal synthesis method. (b) The experimental setup for microdroplet flow synthesis of Zr-BTB MONs. SEM images of Zr-BTB prepared by (c) microdroplet flow synthesis method and (d) solvothermal synthesis method. Atomic force microscopy (AFM) images and corresponding height profiles of Zr-BTB prepared by (e) microdroplet flow synthesis method and (f) solvothermal synthesis method.*[75]

In addition to the microdroplet flow synthesis method, other methods have also been developed to prepare Zr-BTB MONs. For example, Wang and co-workers used a microwave-assisted synthesis method to prepare Zr-BTB and the MONs they obtained were used as catalysts to degrade dimethyl 4-nitrophenyl phosphate (DMNP) which was a chemical warfare agent simulant.[76] Liu and co-workers developed a top-down ball-milling method to exfoliate layered Zr-BTB MOFs into ultrathin nanosheets and the Zr-BTB MONs they obtained had a thickness of 1 nm and a high aspect ratio of approximately 1000, which was used with GO nanosheets to prepare membranes for use in gas separation applications.[77] In addition, the hafnium analogue of this MON, Hf-BTB, was also reported in the literature, in which the $Hf_6$ clusters were linked by BTB ligands forming nanosheets.[78,79]

Different methods have also been developed to post-synthetically functionalise the Zr-BTB MONs to tune their structures and properties. For example, Yu and co-workers functionalised Zr-BTB MONs using 31 types of different ditopic or tetratopic pillaring ligands and prepared a series of PCN-135 MOFs (PCN = porous coordination network, **Figure 6a and 6b**) and the one with Co-TCPc ligands (noted as L4-5, TCPc = 2,9,16,23-tetracarboxyphthalocyanine) exhibited excellent catalytic performance for selective oxidation

of anthracene.[80] Jiang and co-workers incubated DMF, water and benzoic acid (BA) solutions containing $ZrCl_4$ and $H_3BTB$ at 100 °C for 24 h and the material they prepared showed a nanoflower-like structure consisting of Zr-BTB MON petals.[81] As shown in **Figure 6c**, the authors functionalised the MONs by exchanging the BA on Zr-BTB with 2-(5'-methyl(2,2'-bipyridin)-5-yl)acetic acid (Bpy), and subsequent metalation of the prepared Zr-BTB-Bpy resulted in the formation of a Pd(II) catalyst Zr-BTB-Bpy-Pd which was used for cyclisation of isocyanides with *N*-acyl-*o*-alkynylanilines. In addition, Zhang and co-workers functionalised Zr-BTB MONs by introducing indium into the nanosheets by a metal-ion exchange method (**Figure 6d)**, and the In/Zr-BTB MONs they prepared were used in the preparation of high-performance lithium-sulfur batteries.[82]

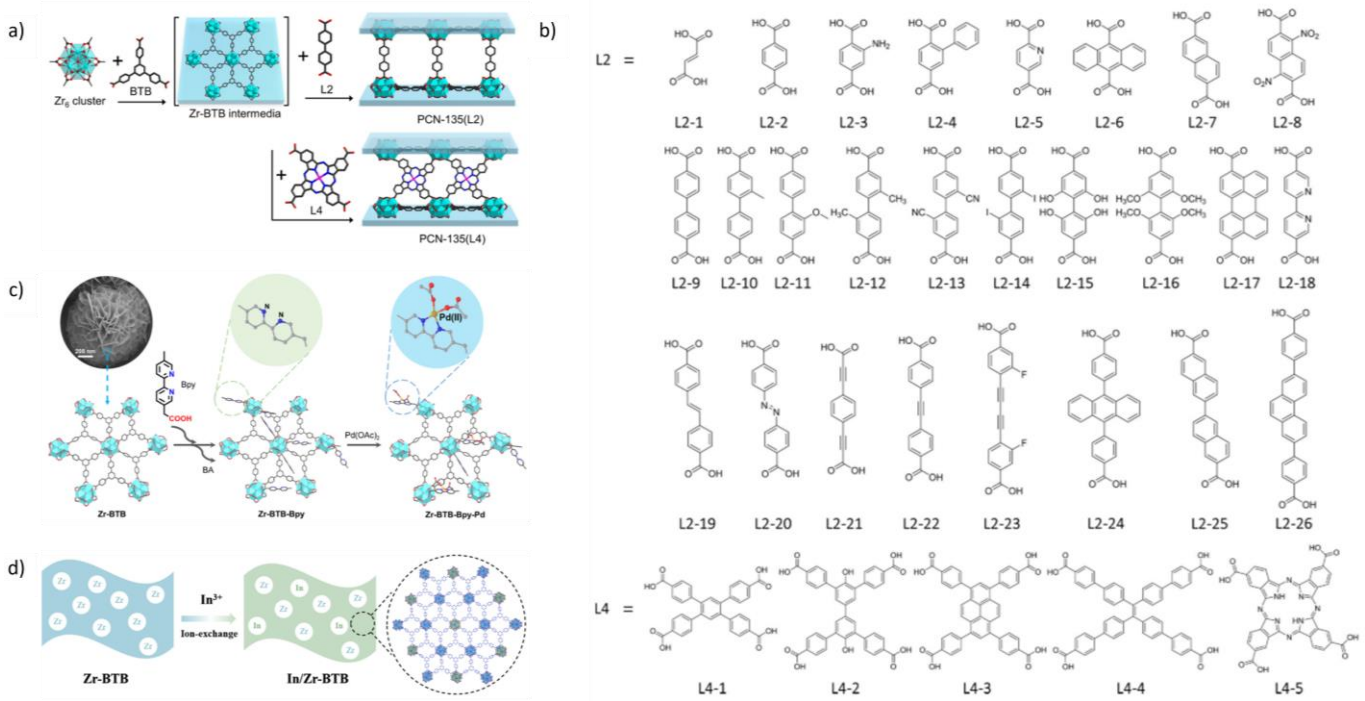


***Figure 6.*** *(a,b) The functionalisation of Zr-BTB MONs using different ditopic and tetratopic pillaring ligands to prepare a series of PCN-135 MOFs. Part b refers to the acids used to generate the ligands.[80] (c) The functionalisation of Zr-BTB with Bpy groups and the preparation of Zr-BTB-Bpy-Pd.[81] (d) The preparation of In/Zr-BTB MONs.[82]*

A wide variety of Zr-BTB derivatives composed of $Zr_6$ clusters and carboxylate ligands have also been developed for use in different applications. For example, Zhao and co-workers prepared Zr-BTB-COOH[83] and Zr-BTB-$NH_2$ MONs[84], in which the $Zr_6$ clusters were linked by tritopic 2',4',6'-tris(4-carboxypheny)benzoate (BTB-COOH) and 2'-amino-5'-(4-carboxyphenyl)-[1,1':3',1''-terphenyl]-4,4''-dicarboxylate (BTB-$NH_2$) ligands (**Figure 7a and 7b**), forming nanosheets with thicknesses of 4-8 nm and ~4 nm, respectively, and both Zr-BTB-COOH and Zr-BTB-$NH_2$ MONs were incorporated into PIM-1

polymers to prepare MMMs for use in gas separation applications. Lin and co-workers prepared Zr-BPY MONs, in which the $Zr_6$ clusters were linked by 4',6'-bis(4-benzoic acid)-(2,2'-bipyridine)-5-carboxylate (BPY) ligands (**Figure 7c**). The authors also introduced ruthenium-based units into the backbone of Zr-BPY MONs and prepared photocatalysts for use in intra/intermolecular [2+2] cycloaddition and Meerwein addition reactions. Klemm and co-workers prepared Zr-TATB MONs (**Figure 7d**), in which the $Zr_6$ clusters were linked by tritopic 4,4',4''-s-triazine-2,4,6-triyl-tribenzoate (TATB) ligands, forming nanosheets with an average thickness of 1.48 nm.[86] The authors also prepared a composite material by growing $Bi_2O_3$ nanowires on the Zr-TATB MONs, which showed excellent $CO_2$ electroreduction activity towards formate.

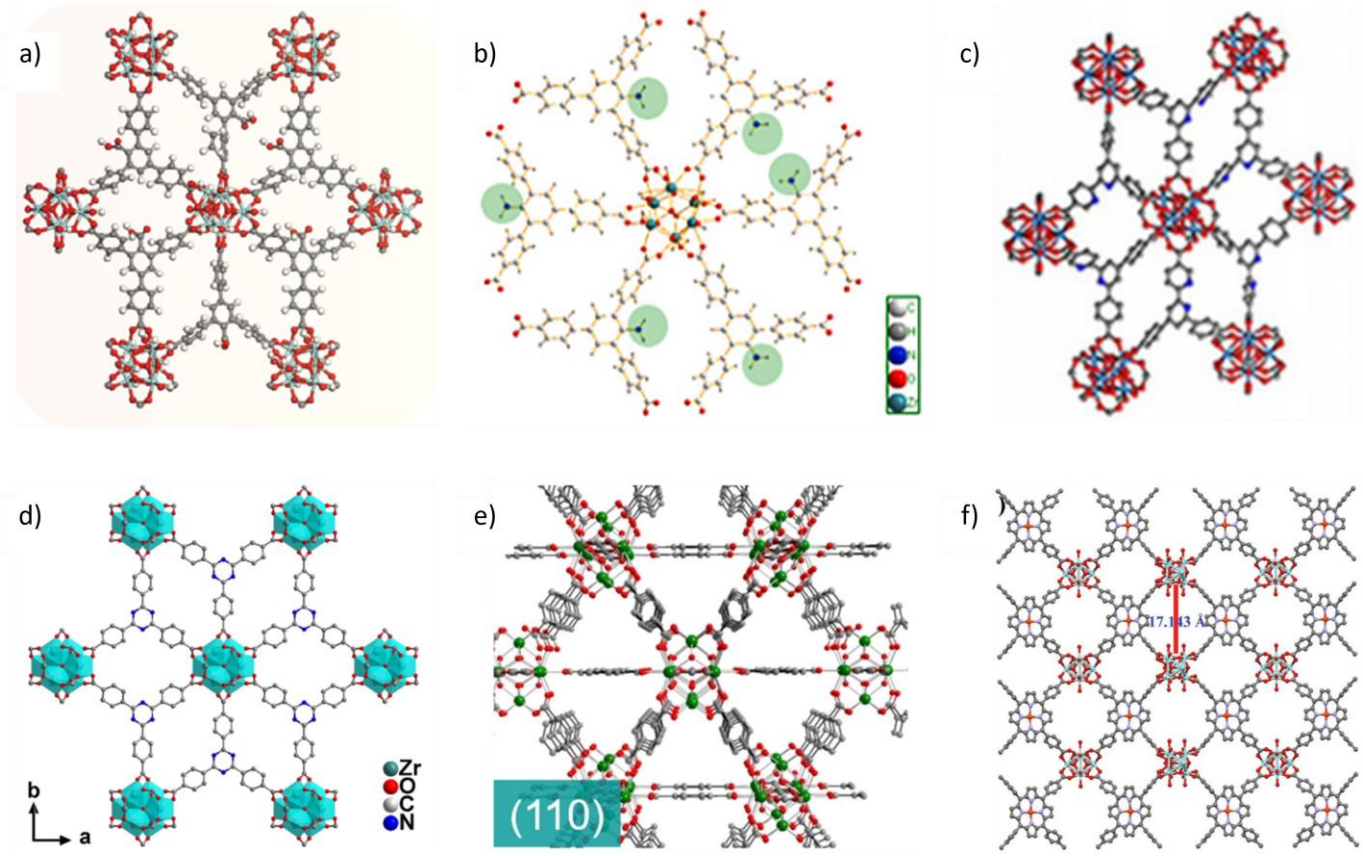


***Figure 7.*** *Structures of (a) Zr-BTB-COOH,[83] (b) Zr-BTB-$NH_2$,[84] (c) Zr-BPY,[85] (d) Zr-TATB,[86] (e) UiO-66,[87] and (f) Zr-NiTCPP.[88]*

In addition to tritopic carboxylate ligands, ditopic and tetratopic carboxylate ligands have also been used to construct $Zr_6$-based MONs. For example, Liu and co-workers reported UiO-66 (UiO = Universitetet i Oslo, **Figure 7e**) and UiO-66-$NH_2$ MONs, in which the $Zr_6$ clusters were linked by ditopic 1,4-benzenedicarboxylate (BDC) and 2-aminoterephthalate (BDC-$NH_2$) ligands, respectively, and the MONs they obtained were used in gas separation applications.[87] In addition, Wang and co-workers reported Zr-NiTCPP MONs, in which the $Zr_6$ clusters were linked by tetratopic nickel-tetrakis(4-carboxyphenyl)-

porphyrin (NiTCPP) ligands, and the MONs they obtained were used in photocatalysis applications (**Figure 7f**).[88]

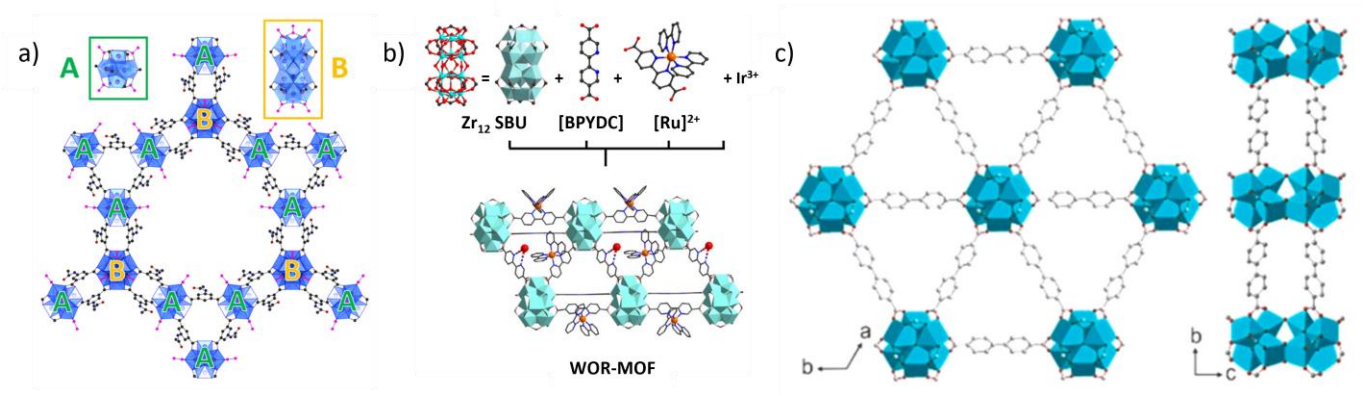


***Figure 8.*** *Structures of (a) CAU-45. A = $Zr_6$ cluster, B = $Zr_{12}$ cluster,[89] (b) WOR-MOF,[90] and (c) UiO-67(Zr).[91]*

In addition to the aforementioned examples, other zirconium-based MONs have also been reported in the literature. Stock and co-workers prepared a mesoporous MOF named CAU-45 which was composed of both $Zr_6$ and $Zr_{12}$ clusters and 5-acetamidoisophthalate ligands (**Figure 8a**), and the CAU-45 MOF they reported had a layered structure which could be exfoliated into MONs via liquid phase exfoliation.[89] MONs composed of carboxylate ligands and only $Zr_{12}$ clusters have also been developed. For example, Wang and co-workers prepared WOR-MOF nanosheets (WOR = water oxidation reaction, **Figure 8b**), in which the $Zr_{12}$ clusters were linked by Ru- or Ir-based 2,2'-bipyridine-5,5'-dicarboxylate (BPYDC) ligands and the MONs they obtained had thicknesses in the range of 1.2-11.5 nm.[90] Tang and co-workers used a microwave-assisted synthesis method to prepare UiO-67(Zr) MONs, in which the $Zr_{12}$ clusters were linked by biphenyl-4,4'-dicarboxylate (BPDC) ligands (**Figure 8c**).[91] The authors also prepared nanocomposites by encapsulation of gold nanoparticles into the UiO-67(Zr) MONs, which were used as catalysts for the reduction of 4-nitrophenol to 4-aminophenol. In addition, the hafnium analogue of this MONs, UiO-67(Hf), has also been reported in the literature, in which the $Hf_{12}$ clusters were linked by BPDC ligands forming nanosheets.[92]

In this section, zirconium-based MONs with different structures and functionalities are discussed. The next section will give an introduction to the use of different MONs in separation applications. Examples of using zirconium-based MONs in different separation applications will be discussed in **Section 1.4**.

### 1.3 MONs for separation applications

Separation process plays an important role in many fields, and compared to conventional separation technologies (e.g., distillation,[93] amine scrubbing,[94] and thermal desalination[95]), membrane-based separation technology has the advantages of low energy consumption, small capital cost, and small footprint.[47,96] Microfiltration (MF), ultrafiltration (UF), nanofiltration (NF), and reverse osmosis (RO) are four typical membrane technologies for water treatments, and as shown in **Figure 9**, the pore size of these four membranes decreases in order: MF > UF > NF > RO, thus they are capable of removing particles of different sizes from raw water, such as suspended particles, bacteria, cells, viruses, macromolecules, protein, and ions.[97] Apart from water treatments, membrane-based separation technologies have also been used in other applications, including fruit and vegetable juice processing,[98] organic vapor separation[99] and gas separation applications.[100]

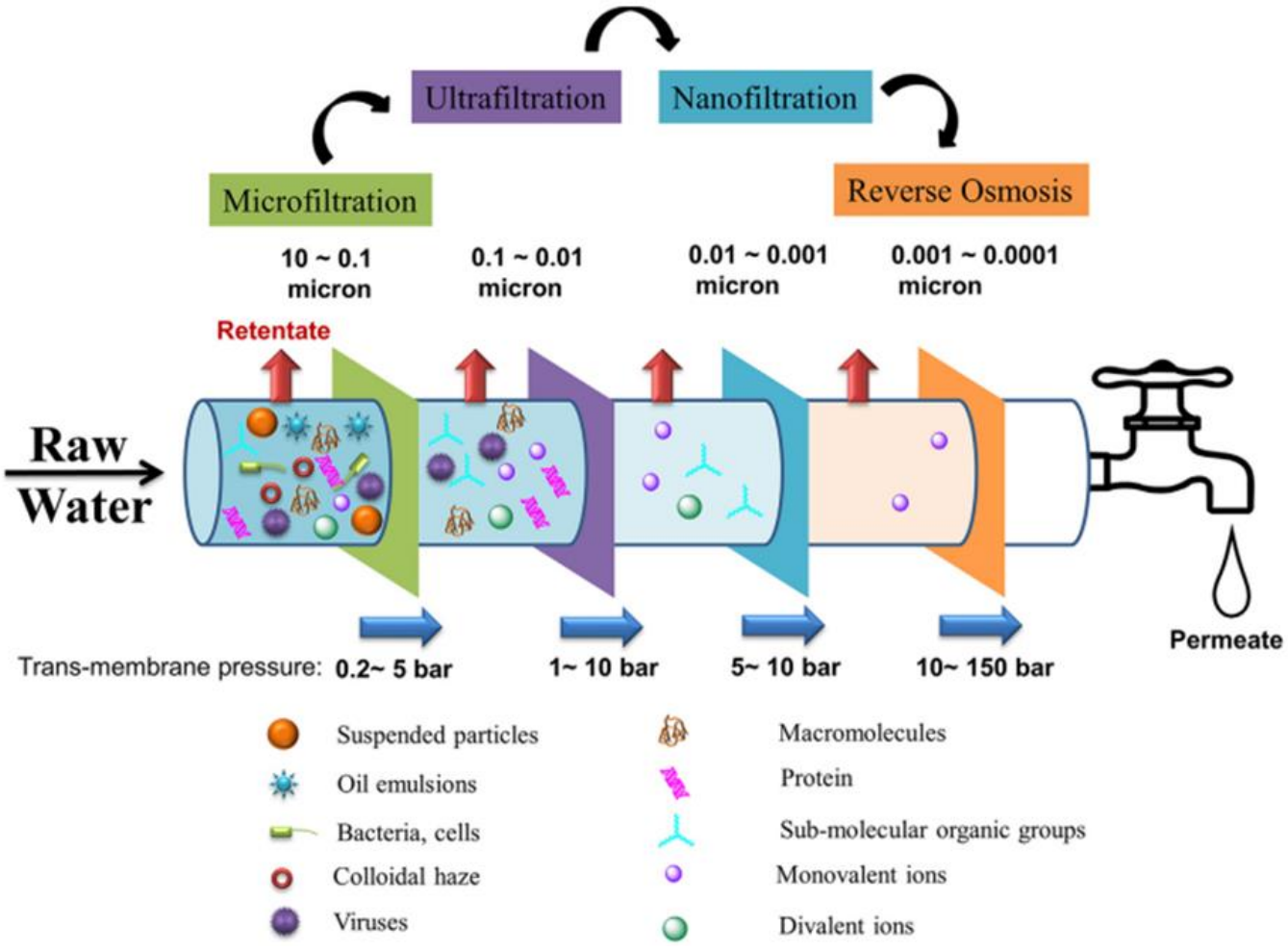


***Figure 9.*** *Schematic illustration of microfiltration, ultrafiltration, nanofiltration and reverse osmosis membranes for water treatments.*[97]

MONs are ultrathin materials with well-defined pore size, tunable structures and chemical properties, making them suitable for the preparation of high-performance separation membranes.[38,47] **Figure 10a** shows two typical MON-based membranes: (1) composite membrane, in which the MONs are deposited as a selective layer onto a porous support (e.g., nylon,[101] and α-$Al_2O_3$[102]) and (2) mixed matrix membrane (MMM), in which the MONs are incorporated as fillers into a polymeric matrix, such as PI,[103] and PIM-1[104] (PI = polyimide, PIM = polymer of intrinsic microporosity). As shown in **Figure 10b**, there are two distinct permeation pathways in MON-based membranes: (1) a direct pathway in which molecules pass through the pores of the MONs (shown in green) and (2) a tortuous pathway in which they go around the nanosheets via interlayer gaps between adjacent MONs (shown in red).[47] Molecules smaller than the pore size of MONs can rapidly pass through the membrane along the short pathway, whereas larger molecules have to take the long and tortuous pathways. This results in different permeation rates, allowing molecules of different sizes to be separated by the membrane.

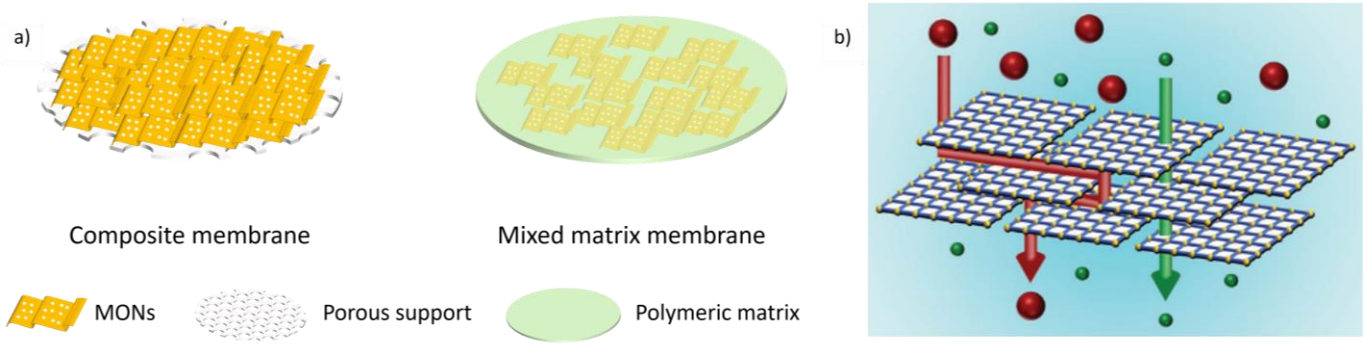


***Figure 10.*** *(a) Schematic illustrations of two typical MON-based membranes: composite membrane and MMM. (b) Schematic illustration of the short (green) and long (red) permeation pathways in MON-based membranes. The green balls and red balls represent molecules of different sizes.*[47]

A wide variety of MON-based membranes have been developed based on the separation mechanism depicted in **Figure 10b**, and these membranes have been used in different separation applications. For example, Ang and Hong used M-TCP(Fe) membranes for separation of dyes and salts in aqueous solutions (M = Zn, Co and Cu, TCP(Fe) = Fe(III) meso-tetra(4-carboxyphenyl)porphine chloride, **Figure 11a and 11b**).[101] In their work, the membranes were prepared by filtering the MON suspensions on nylon supports by a vacuum filtration method. The three M-TCP(Fe) membranes showed similar rejection rates toward organic dyes, and among them, the Zn-TCP(Fe) membrane showed the highest water permeance. To further improve the separation performance of the Zn-TCP(Fe) membrane, the authors used polycation cross-linkers polyethylenimine (PEI) and poly(diallyldimethylammonium chloride) (PDDA) during the membrane preparation process. The electrostatic attractive force between the cross-

linkers and the Zn-TCP(Fe) MONs as well as the compressive force derived from vacuum filtration resulted in the formation of crack-free Zn-TCP(Fe) membranes with a thickness of 48 nm (**Figure 11c-11e**). The PEI/Zn-TCP(Fe) and PDDA/Zn-TCP(Fe) membranes they prepared showed high rejection rates toward organic dyes with different sizes and charges, as well as higher water permeance and higher rejection rates toward salts compared to the Zn-TCP(Fe) membrane without cross-linkers (**Figure 11f and 11g**). In addition, compared to membranes prepared by other materials, the MON-based membranes prepared by Ang and Hong exhibited advantages of higher water permeance and lower energy consumption (**Figure 11h**).

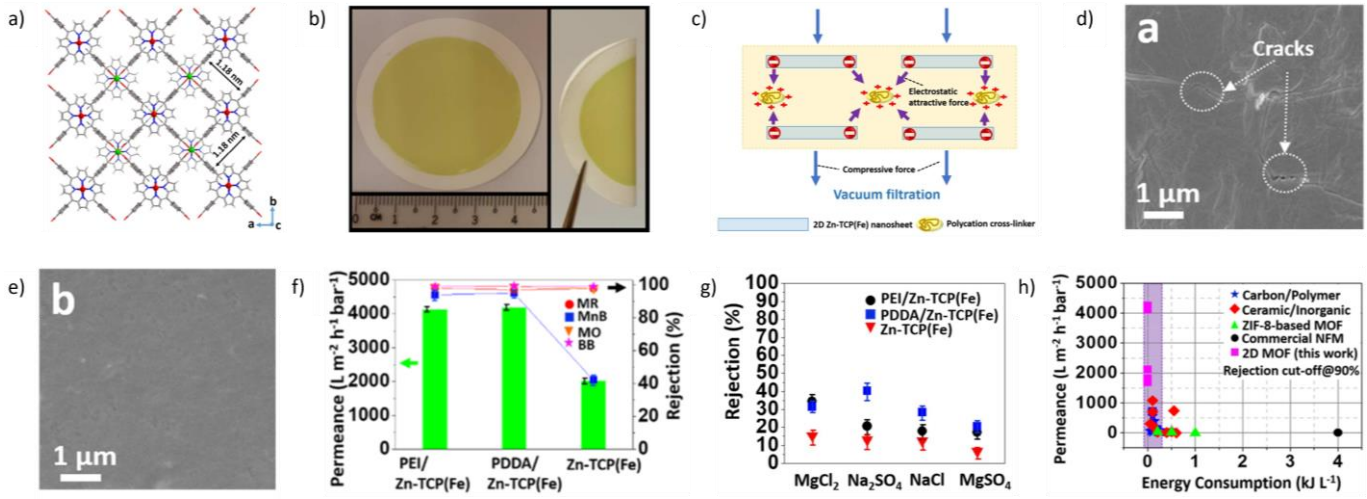


***Figure 11.*** *(a) Structure of Zn-TCP(Fe) MONs, (b) photographs of Zn-TCP(Fe) membrane. (c) Schematic illustration of the electrostatic attractive force between the cross-linkers and the MONs as well as the compressive force derived from vacuum filtration. (d) SEM image of Zn-TCP(Fe) membrane without cross-linkers. (e) SEM image of PEI/Zn-TCP(Fe) membrane. (f) Water permeance and rejection rate of Zn-TCP(Fe) membranes with and without cross-linkers toward different organic dyes. MR = methyl red, MnB = methylene blue, MO = methyl orange, BB = brilliant blue G. (g) Rejection rate of Zn-TCP(Fe) membranes with and without cross-linkers toward different salts. (h) Comparison of water permeance and energy consumption between M-TCP(Fe) MON-based membranes and other membranes.*[101]

In addition to the vacuum filtration method, other methods have also been used to prepare MON-based membranes to separate dyes. For example, Li and co-workers prepared MMMs with BUT-203 MONs and polyethyleneimine (PEI) polymers by a blending-spin coating method (BUT = Beijing University of Technology).[105] In their work, the MON suspension was blended with PEI solution and the resulting mixed solution was spin-coated onto hydrolysed polyacrylonitrile (HPAN) support (**Figure 12**). The membranes they prepared exhibited excellent dye separation performance, and the best-performing membrane was

prepared with 73% of BUT-203 loading which showed a high water permeance of up to 870 L/($m^2$·h·MPa) and high rejection rates (>97.9%) toward anionic dyes with molecular weight larger than 461. In addition, this membrane showed good antifouling and dye desalination ability and long-term running stability.

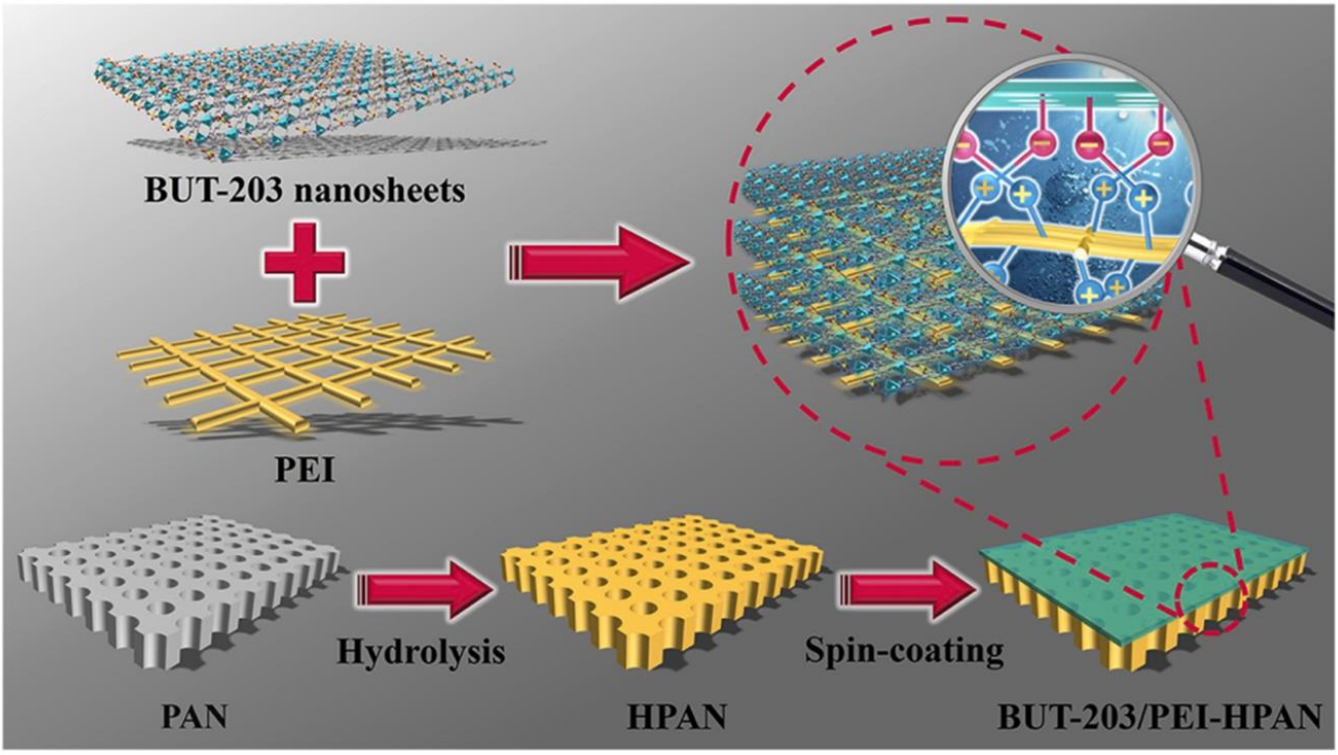


***Figure 12.*** *Schematic illustration of the preparation process for BUT-203/PEI-HPAN membrane.*[105]

In addition to flat sheet membranes, a MON-based portable separation device has also been developed for use in separation of dyes in ethanol solutions.[106] In the work of Xuan and co-workers, a $([Cu_2(TTAC)(DMF)_2]_n$ MON suspension (TTAC = terphenyl tetracarboxylate, **Figure 13a**) was transferred to a nylon syringe filter and passed through the filter mesh disc with a pore size of 0.1 μm, leaving the MONs on the filter mesh disc (**Figure 13b**). The syringe filter was then connected to a syringe for dye separation experiments (**Figure 13c**). The separation device exhibited high removal rates of >99.5% toward phthalocyanine green (PG) and copper phthalocyanine (CP), but almost no rejection (<0.5%) toward methyl orange (MO) and methylene blue (MnB). Interestingly, when a mixed solution containing equimolar mixture of PG and MO was driven through the separation device, 99.6% of the PG dyes in the solution were removed, whereas most of the MO dyes remained in the solution, resulting in a colour change of the mixed solution from green to yellow (**Figure 13d**).

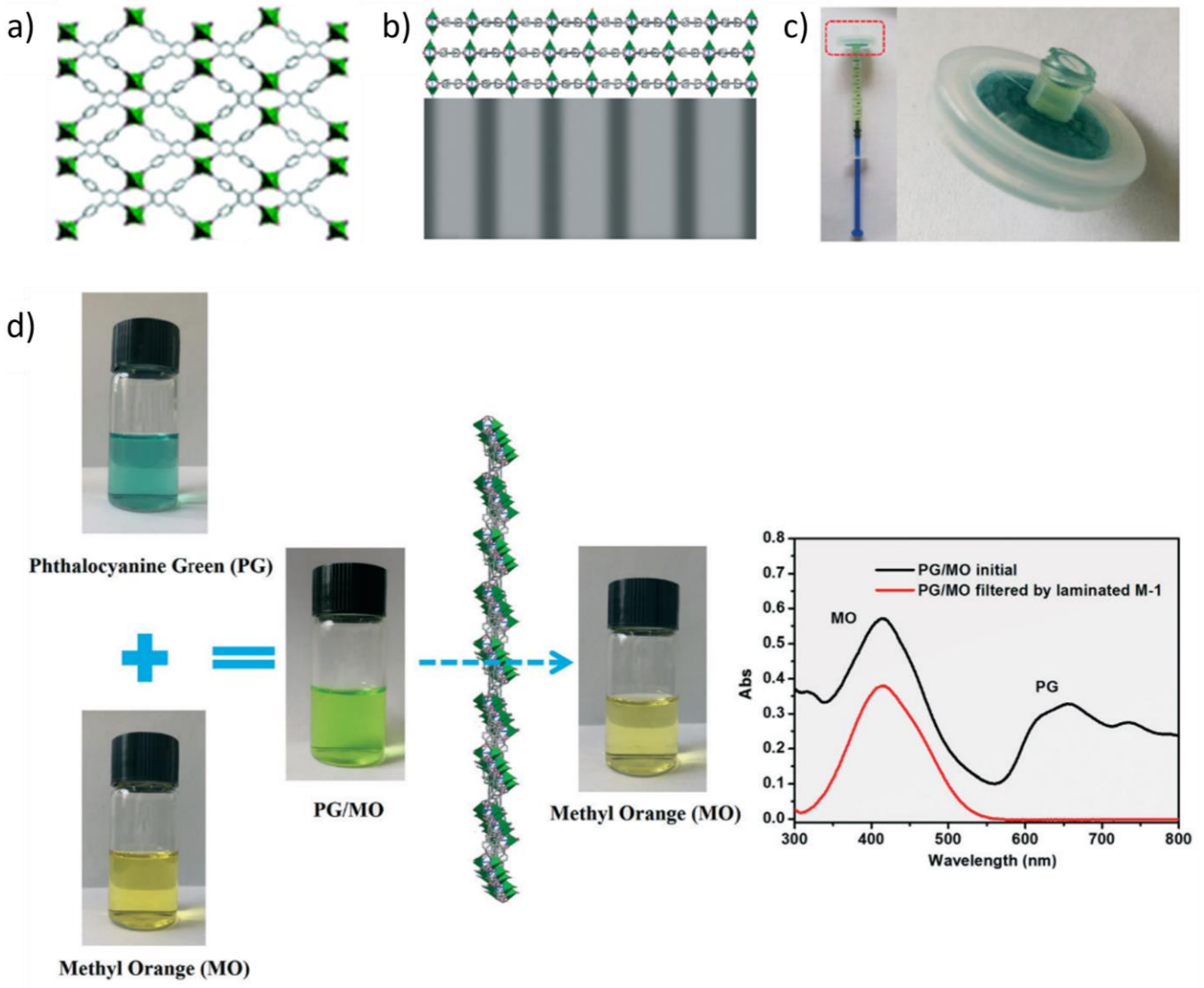


***Figure 13.*** *(a) Structure of ($[Cu_2(TTAC)(DMF)_2]_n$ MONs. (b) Schematic illustration of MONs deposited on the filter mesh disc. (c) Photographs of the separation device and the syringe filter. (d) Schematic illustration of the separation of PG/MO mixture and ultraviolet-visible (UV-Vis) spectra of the PG/MO solution before and after filtration.*[106]

Apart from separation of dyes and salts, MON-based membranes have also been used in organic solvent dehydration. For example, Bu and co-workers prepared MMMs with $[Eu(BTB)(H_2O)_2 \cdot solvent]_n$ MONs (abbreviated as EuBTB) for ethanol dehydration.[107] In their work, the EuBTB MON suspension was blended with sodium alginate (SA) solution and the resulting mixed solution was spin-coated onto a polyacrylonitrile (PAN) support (**Figure 14a and 14b**). The MMMs they prepared showed high mechanical strength and swelling resistance, because of the strong interfacial interaction between EuBTB MONs and SA. The ethanol dehydration experiments of the membranes were carried out using 90 wt% ethanol aqueous solution at 350 K. As shown in **Figure 14c**, the permeation flux and separation factor of membrane were dependent on the content of EuBTB MONs in the membrane, and the best-performing

membrane was achieved when the mass ratio of EuBTB to SA was 5 wt%. It exhibited a permeation flux of 1996 g/m$^2$h and a separation factor of 1160, enhanced by 58.5% and 91.4% compared to the membrane without EuBTB MONs, respectively. In addition, the membrane containing 5 wt% of EuBTB MONs exhibited good long-term operation stability (**Figure 14d**).

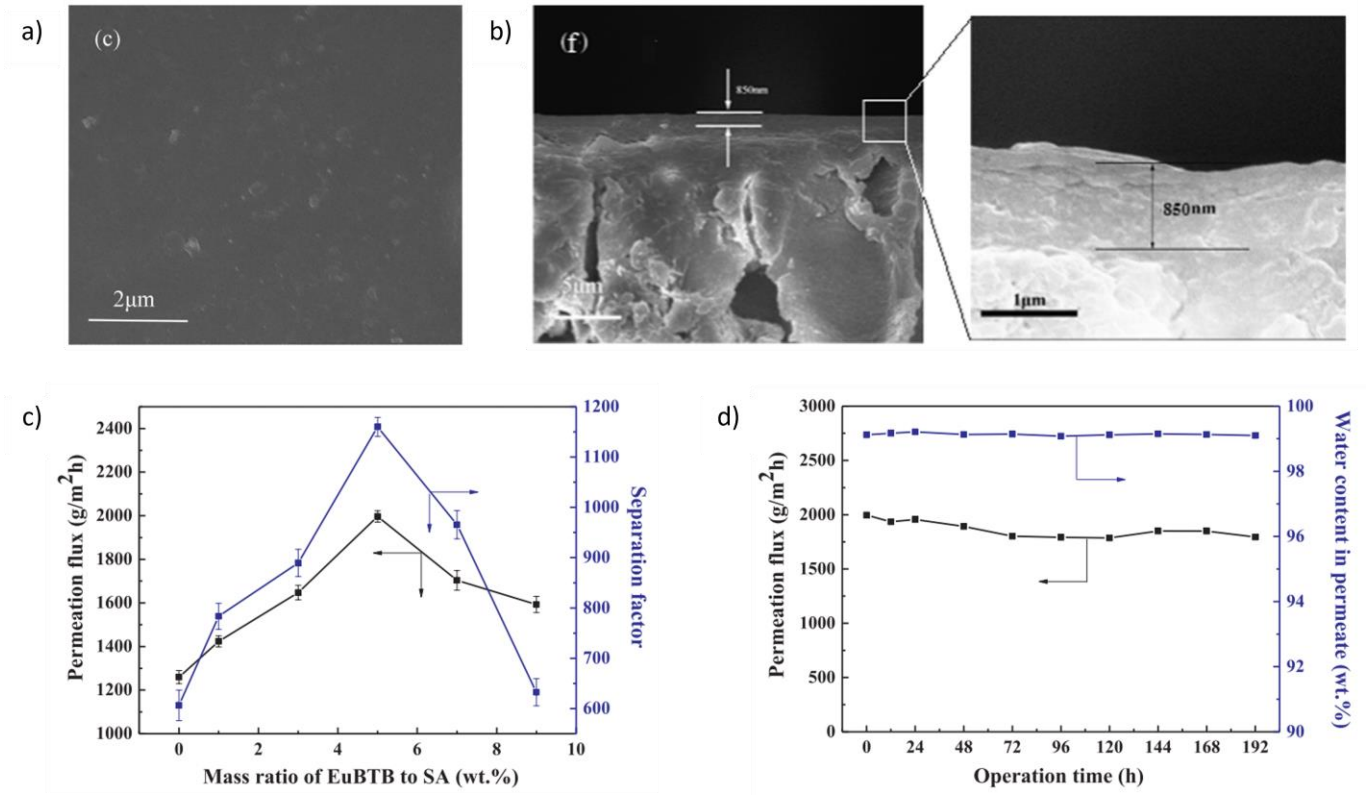


***Figure 14.*** *(a) Field emission scanning electron microscope (FESEM) surface image of MMM containing 5 wt% of EuBTB MONs. (b) FESEM image (cross-section view) of MMM containing 5 wt% of EuBTB MONs. (c) Ethanol dehydration performance of membranes with different EuBTB contents. (d) Long-term separation performance of MMM containing 5 wt% of EuBTB MONs.*[107]

MON-based membranes have also been used in gas separation applications. For example, Yang and co-workers prepared composite membranes with $Zn_2(Bim)_4$ MONs by a hot-drop coating method (Bim = benzimidazolate, **Figure 15a and 15b**).[102] In their work, the MON suspension was deposited dropwise onto the surface of an α-$Al_2O_3$ support, which was heated on a metallic heating plate. As shown in **Figure 15c-15e**, the texture of the underlying α-$Al_2O_3$ was still visible after coating the MONs, indicating that the layer of $Zn_2(Bim)_4$ MONs deposited on the support was very thin. The ultrathin nature of $Zn_2(Bim)_4$ membranes endowed them with ultrahigh $H_2$ permeance of up to a few thousand gas permeation units. As shown in **Figure 15f**, the $H_2/CO_2$ selectivity of $Zn_2(Bim)_4$ membranes was dependent on the support surface temperature during hot-drop coating and the best-performing membranes were prepared at 120 ℃, which exhibited $H_2/CO_2$ selectivity of 261 ± 39. Apart from $Zn_2(Bim)_4$, other MONs have also been

used to prepare composite membranes via hot-drop coating for use in gas separation applications, such as $Zn_2(Bim)_3$,[108] and MAMS-1 (MAMS = mesh adjustable molecular sieve, **Figure 15g-15i**).[63]

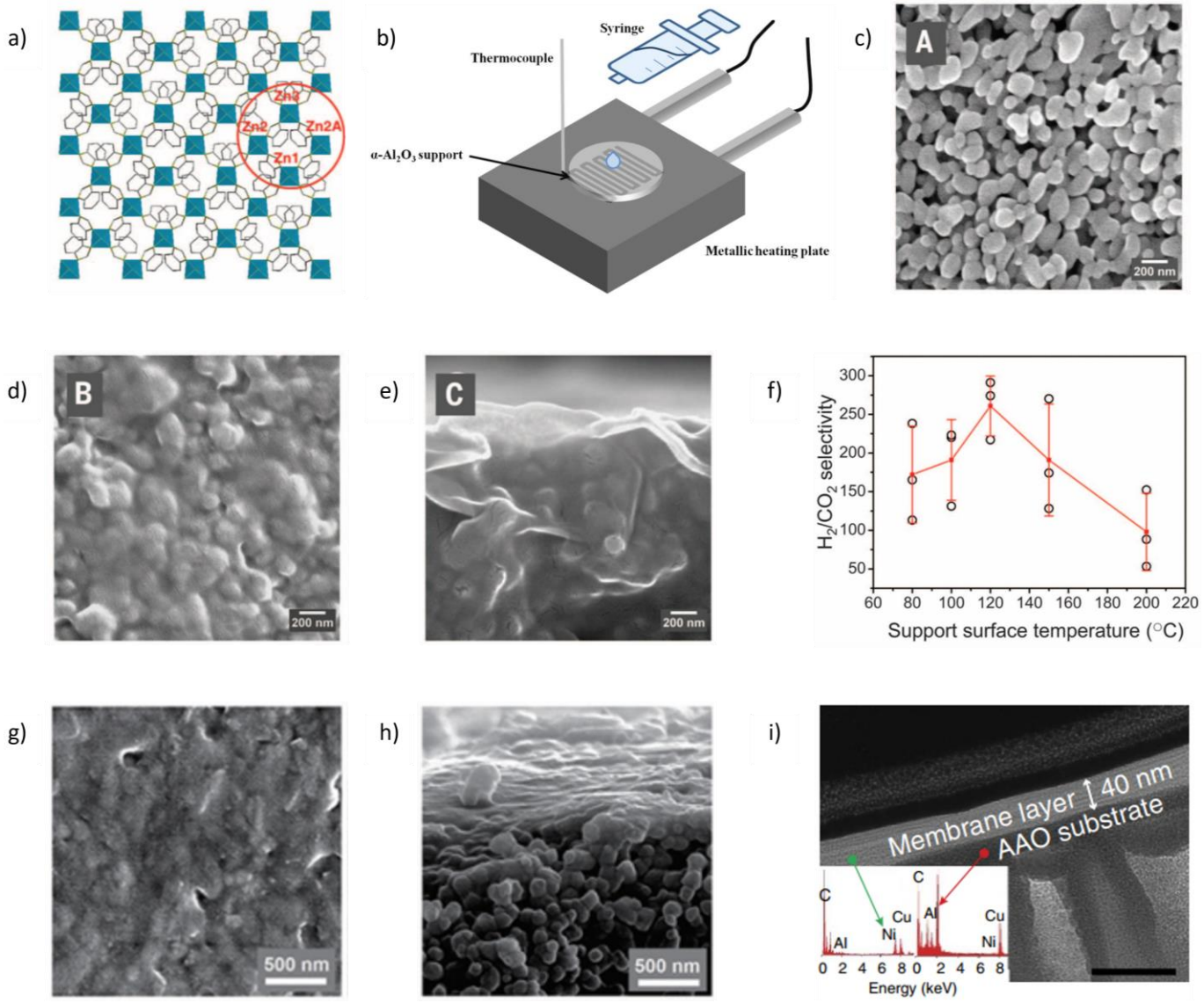


***Figure 15.*** *(a) Structure of $Zn_2(Bim)_4$ MONs. (b) Schematic illustration of hot-drop coating method. (c) SEM image of α-$Al_2O_3$ support. (d) SEM top view and (e) SEM cross-sectional view of $Zn_2(Bim)_4$ membrane. (f) $H_2/CO_2$ selectivity of $Zn_2(Bim)_4$ membranes prepared at different support surface temperatures.[102] (g) SEM image (top view) of $Zn_2(Bim)_3$ membrane on α-$Al_2O_3$ support. (h) SEM image (cross-section view) of $Zn_2(Bim)_3$ membrane on α-$Al_2O_3$ support.[108] (i) FIB-TEM image (cross-section view) and energy-dispersive X-ray spectra of MAMS-1 membrane on anodic aluminium oxide (AAO) support. FIB = Focused ion beam.[63]*

Apart from composite membranes, MONs have also been used to prepare MMMs for use in gas separation applications. Gascon and co-workers prepared MMMs with CuBDC by a doctor blade casting method (BDC = 1,4-benzenedicarboxylate, **Figure 16a**).[103] In their work, Matrimid 5218 polyimide (PI) polymer was added into CuBDC suspension and the resulting mixed solution was poured onto a glass plate

and processed into a membrane by a doctor blade knife (**Figure 16b and 16c**). CuBDC with different morphologies were used as fillers to prepare the MMMs and their $CO_2/CH_4$ separation performance was studied. As shown in **Figure 16d**, the incorporation of CuBDC MONs (nanosheets) into the PI matrix increased the $CO_2/CH_4$ separation selectivity of the membrane, and the separation selectivity of this membrane showed an increasing trend with the increase of pressure. Whereas, compared to the pure PI membrane, the use of bulk-type or submicrometre-sized isotropic CuBDC MOF fillers decreased the $CO_2/CH_4$ separation selectivity of the membrane. The authors attributed this to a superior occupation of the membrane cross-section by the CuBDC MON fillers compared to the isotropic CuBDC MOF fillers, which could improve the efficiency of molecular discrimination and eliminate unselective pathways for the permeating gases. Apart from PI, CuBDC MONs have also been incorporated into other polymers to prepare MMMs for use in gas separation applications, including 6FDA-DAM (6FDA = 4,4'-(hexafluoroisopropylidene)diphthalic anhydride, DAM = diaminomesitylene) and PIM-1 (**Figure 16e and 16f**).[109]

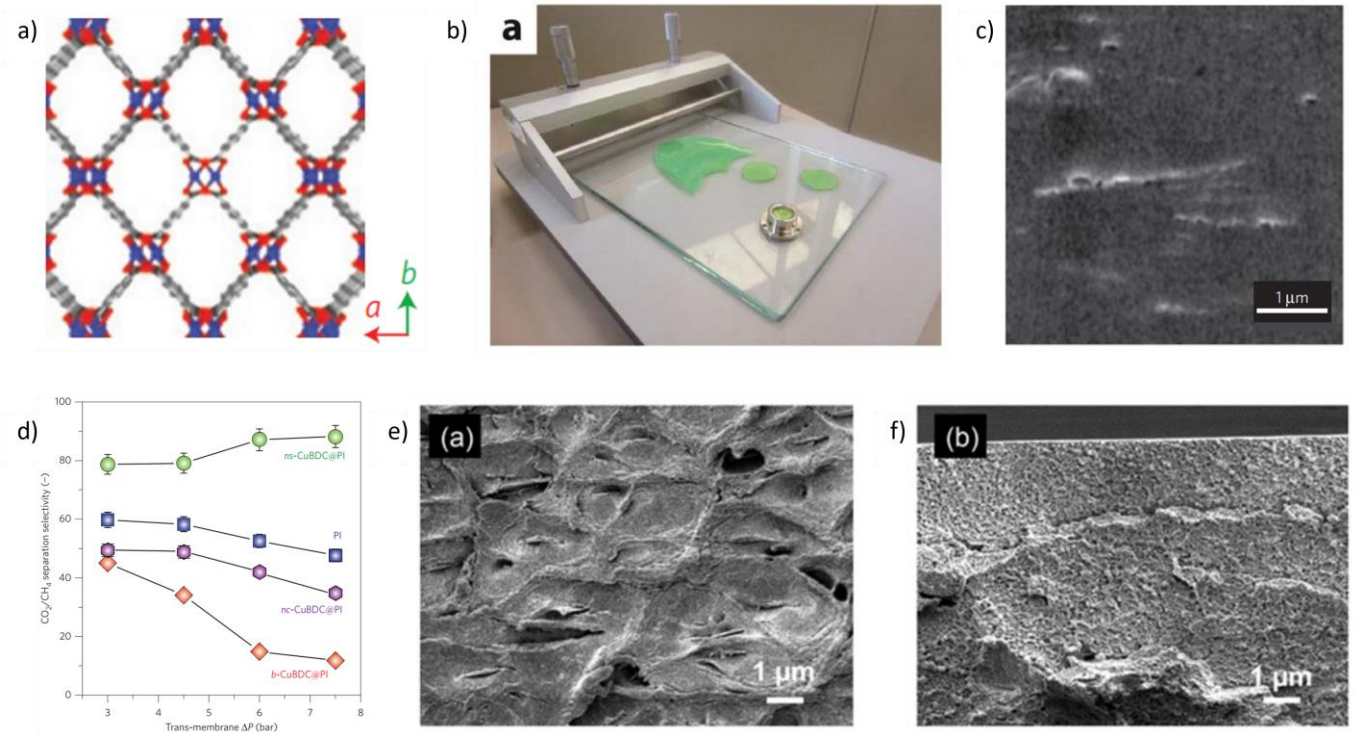


***Figure 16.*** *(a) Structure of CuBDC MONs. (b) Photograph of the doctor blade casting method used to prepare CuBDC MMMs. (c) SEM image of ns-CuBDC@PI MMM. (d) $CO_2/CH_4$ separation performance of pure PI membrane and CuBDC@PI MMMs. ns-CuBDC@PI, nc-CuBDC@PI and b-CuBDC@PI refer to MMMs with CuBDC MON fillers, submicrometre-sized CuBDC MOF fillers and bulk-type CuBDC MOF fillers, respectively. PI refers to pure Matrimid 5218 polyimide membrane.[103] SEM images of MMMs prepared by incorporation of CuBDC MONs as fillers into (e) 6FDA-DAM and (f) PIM-1.[109]*

In addition to the aforementioned examples, other MONs have also been used in separation applications, such as Al-MOF nanosheets,[110] $NH_2$-MIL-53(Al) MONs,[51] ZIF-67 MONs[111] (Al-MOF = aluminum tetra-(4-carboxyphenyl) porphyrin framework, MIL = Materials Institute Lavoisier), and particularly zirconium-based MONs.

### 1.4 Zirconium-based MONs for separation applications

Zirconium-based MONs have been processed into different types of membranes for use in separation applications. For example, Zhao and co-workers prepared composite membranes with Zr-BTB MONs for separation of dyes and salts in aqueous solutions.[112] In their work, the suspension of Zr-BTB MONs was dropped onto polyacrylonitrile (PAN)-400 supports and processed into membranes by a doctor blade casting method (**Figure 17a and 17b**). There were no noticeable morphological changes after mechanical bending and folding of the membranes, indicting their good adhesion properties and good flexibility (**Figure 17c and 17d**). The dye separation performance of the Zr-BTB/PAN-400 membranes was studied. As shown in **Figure 17e**, the water permeance of the 20 nm thick membrane was 3.2 $kg \cdot m^{-2} \cdot h^{-1} \cdot bar^{-1}$, and its rejection rate for acid fuchsin was 97.5%. When the thickness of Zr-BTB MON layer was increased to 1.3 μm, the rejection rate of the membrane increased to 99.3%, but the water permeance of the membrane decreased to 0.14 $kg \cdot m^{-2} \cdot h^{-1} \cdot bar^{-1}$. **Figure 17f** showed the separation performance of the 110 nm thick Zr-BTB/PAN-400 membrane toward dyes with different molecular weights. The membrane exhibited a near-complete (>98%) rejection for methyl blue (molecular wight = 799.8 g $mol^{-1}$) and a lower rejection rate (88%) for methyl orange (molecular weight = 327.3 g $mol^{-1}$). The authors also studied the desalination performance of the Zr-BTB/PAN-400 membranes towards different ions in aqueous solution. As shown in **Figure 17g**, the membrane exhibited a rejection rate of 72% for $Na^+$, and significantly higher rejection rates for $Ca^{2+}$, $Mg^{2+}$ and $Al^{3+}$, because of their larger hydrated ion diameters. In addition, the Zr-BTB/PAN-400 membranes prepared by Zhao and co-workers showed excellent separation performance toward dyes and salts in comparison with the state-of-the-art membranes (**Figure 17h**).

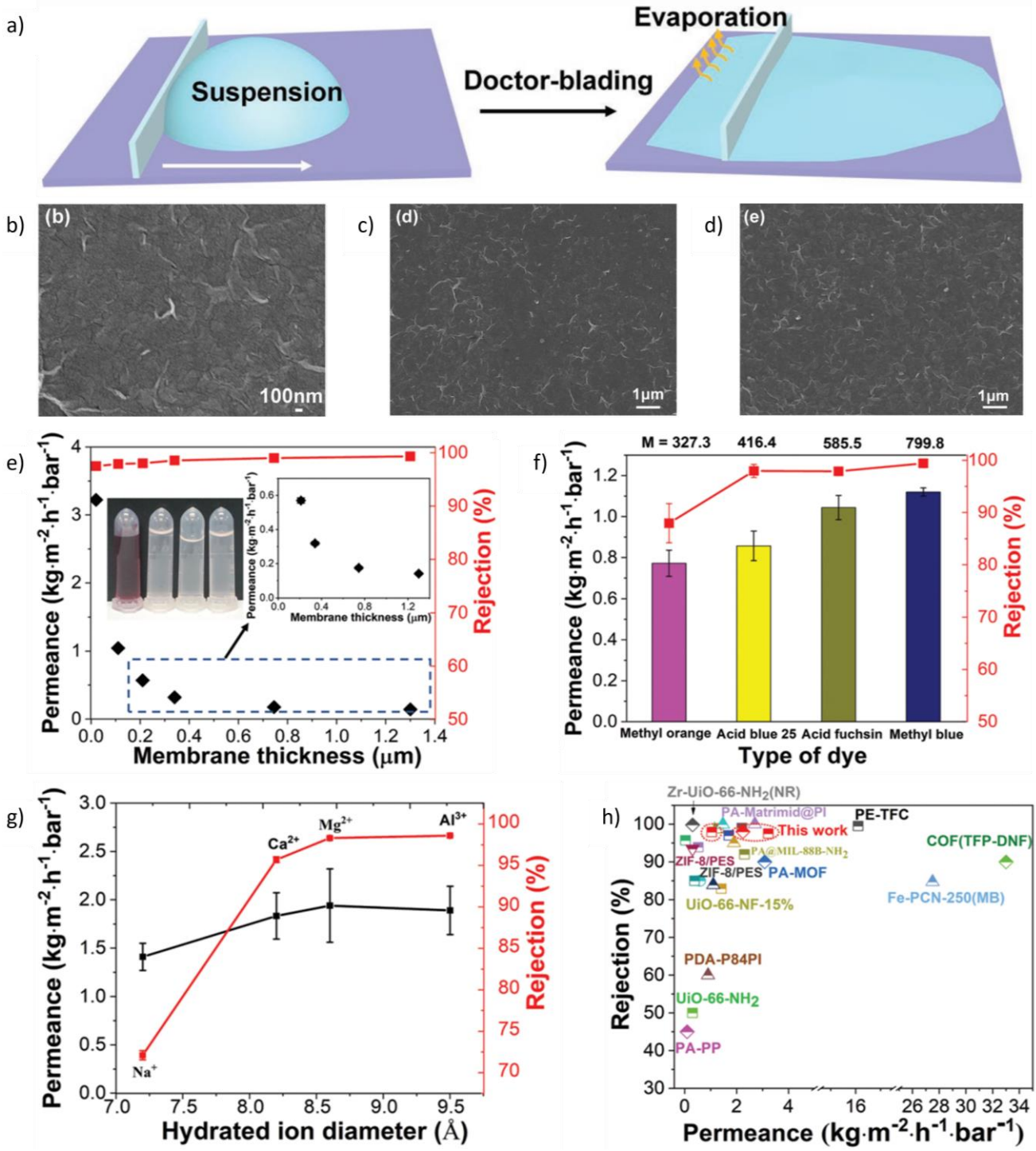


***Figure 17.*** *(a) Schematic illustration of the doctor blade casting method used to prepare the Zr-BTB/PAN-400 membranes. (b) SEM image of the Zr-BTB/PAN-400 membrane. (c) SEM image of the Zr-BTB/PAN-400 membrane after bending. (d) SEM image of the Zr-BTB/PAN-400 membrane after folding. (e) Dye separation performance of the Zr-BTB/PAN-400 membranes with different thicknesses, the photograph shows the original acid fuchsin solution and the filtrate solutions of three successive separations by the 110 nm thick Zr-BTB/PAN-400 membrane. (f) Water permeance and rejection rates of the 110 nm thick Zr-BTB/PAN-400 membrane toward different dyes. (g) Desalination performance of the 110 nm thick Zr-BTB/PAN-400 membrane toward different ions in aqueous solutions. (h) Comparison of the separation performance of the Zr-BTB/PAN-400 membranes with the state-of-the-art membranes.*[112]

Apart from separation of dyes and salts in aqueous solutions, Zr-BTB has also been used in gas separation applications. For example, Liu and co-workers fabricated Zr-BTB/GO membranes by filtering a mixed suspension containing Zr-BTB MONs and GO nanosheets onto cellulose acetate supports (pore size: 0.2 μm) by a heating vacuum filtration method. As shown in **Figure 18a**, when the amount of GO in the membranes was kept at 0.01 mg, the effect of the amount of Zr-BTB on the $H_2/CO_2$ separation performance of the membranes was studied. Increasing the amount of Zr-BTB from 0 to 0.3 mg decreased the $H_2$ permeance from $9.5 \times 10^{-7}$ to $1.5 \times 10^{-7}$ mol $m^{-2}$ $s^{-1}$ $pa^{-1}$ and increased the $H_2/CO_2$ ideal selectivity of the membrane from 4.8 to 16.8. However, when the amount of Zr-BTB was increased to 0.35 mg, the $H_2/CO_2$ ideal selectivity of the membrane started to decrease. When the amount of Zr-BTB in the membranes was kept at 0.3 mg, the effect of the amount of GO on the $H_2/CO_2$ separation performance of the membranes was studied (**Figure 18b**).[77] Increasing the amount of GO from 0.006 to 0.012 mg decreased the permeance of the membrane, which could be attributed to the blocking effect caused by the increase in nonporous GO nanosheets, and when the amount of GO was 0.01 mg, the membrane exhibited the highest $H_2/CO_2$ ideal selectivity of 16.8. In addition, the authors found that the $H_2/CO_2$ separation performance of the Zr-BTB/GO membrane was dependent on the membrane preparation temperature. As shown in **Figure 18c**, when the amount of Zr-BTB was kept at 0.1 mg and the amount of GO was kept at 0.01 mg, increasing the membrane preparation temperature from 298 K to 398 K increased the $H_2/CO_2$ ideal selectivity from 5.3 to 12.8 and did not significantly change the $H_2$ permeance of the membrane.

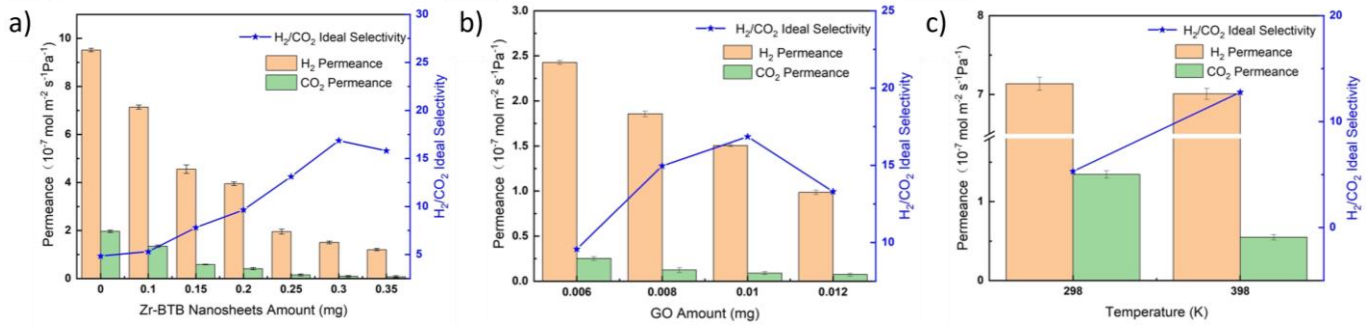


***Figure 18.*** *(a) The effect of the amount of Zr-BTB on the $H_2/CO_2$ separation performance of the Zr-BTB/GO membranes. The amount of GO was kept at 0.01 mg. (b) The effect of the amount of GO on the $H_2/CO_2$ separation performance of the Zr-BTB/GO membranes. The amount of Zr-BTB was kept at 0.3 mg. (c) The effect of the membrane preparation temperature on the $H_2/CO_2$ separation performance of the Zr-BTB/GO membranes. The amount of Zr-BTB was kept at 0.1 mg and the amount of GO was kept at 0.01 mg.*[77]

In addition to composite membranes, Zr-BTB has also been used to prepare MMMs for use in gas separation applications. For example, Zhao and co-workers prepared MMMs with Zr-BTB MONs and PIM-1 polymers by a solution casting method.[104] In their work, mixed solutions containing MONs and PIM-1 were poured into glass Petri dishes, and the membranes with different Zr-BTB loadings were collected after solvent evaporation (**Figure 19a**). Powder X-ray diffraction (PXRD) characterisations were performed on the membranes. As shown in **Figure 19b**, the pure PIM-1 membrane showed two broad peaks at 2θ = 21.8° and 28.5°, corresponding to the chain−chain distances of 4.1 Å and 3.1 Å within the membrane, respectively. The intensity of the characteristic peaks belonging to Zr-BTB MONs became stronger with the increase of filler loading (e.g., the peak at 2θ = 5.1°), indicating that the crystallinity of Zr-BTB MONs was maintained during the membrane preparation process. Interestingly, when the Zr-BTB loading reached 2 wt% or higher, the intensity of the characteristic peak belonging to PIM-1 (at 2θ = 28.5°) also became stronger. This indicated that the crystallinity of the PIM-1 matrix was enhanced after the addition of Zr-BTB MONs. Considering the π−π interactions and hydrogen bonding between the Zr-BTB fillers and the PIM-1 matrix. The authors attributed the enhanced PIM-1 crystallinity to the adsorption and alignment of the PIM-1 chains on the surface of Zr-BTB MONs, which generated a more ordered chain packing motif with a chain−chain distance of 3.1 Å within the MMMs (**Figure 19c**).

The gas separation performance of the membranes was studied.[104] As shown in **Figure 19d and 19e**, increasing the Zr-BTB loading from 0 to 2 wt% simultaneously increased the $CO_2$ permeability and $CO_2/CH_4$ and $CO_2/N_2$ selectivity of the membrane, and the MMM with 2 wt% of Zr-BTB loading exhibited a $CO_2$ permeability of approximately 6500 Barrer, which was approximately 65% higher than the pure PIM-1 membrane. This was because the Zr-BTB MONs possessed relatively large pores (pore size: 5.4 Å), which could provide fast gas permeation pathways within the MMMs, resulting in increased gas permeability. The MMM with 2 wt% of Zr-BTB loading also exhibited $CO_2/CH_4$ selectivity of 30.1 and $CO_2/N_2$ selectivity of 26.8, which were 117% and 72% higher than the pure PIM-1 membrane, respectively. The increase in selectivity could be attributed to the enhanced PIM-1 crystallinity. As discussed previously, the incorporation of Zr-BTB MONs into PIM-1 resulted in the generation of a more ordered chain packing motif within the MMMs with a chain−chain distance of 3.1 Å, which was very close to the size of $CO_2$ (kinetic diameter: 3.3 Å). Therefore, when larger $CH_4$ (kinetic diameter= 3.8 Å) and $N_2$ (kinetic diameter = 3.68 Å) passed through the orderly packed PIM-1 chains within the MMMs, they experienced more resistance compared to $CO_2$, resulting in the effective separation of these gas molecules based on their different sizes.

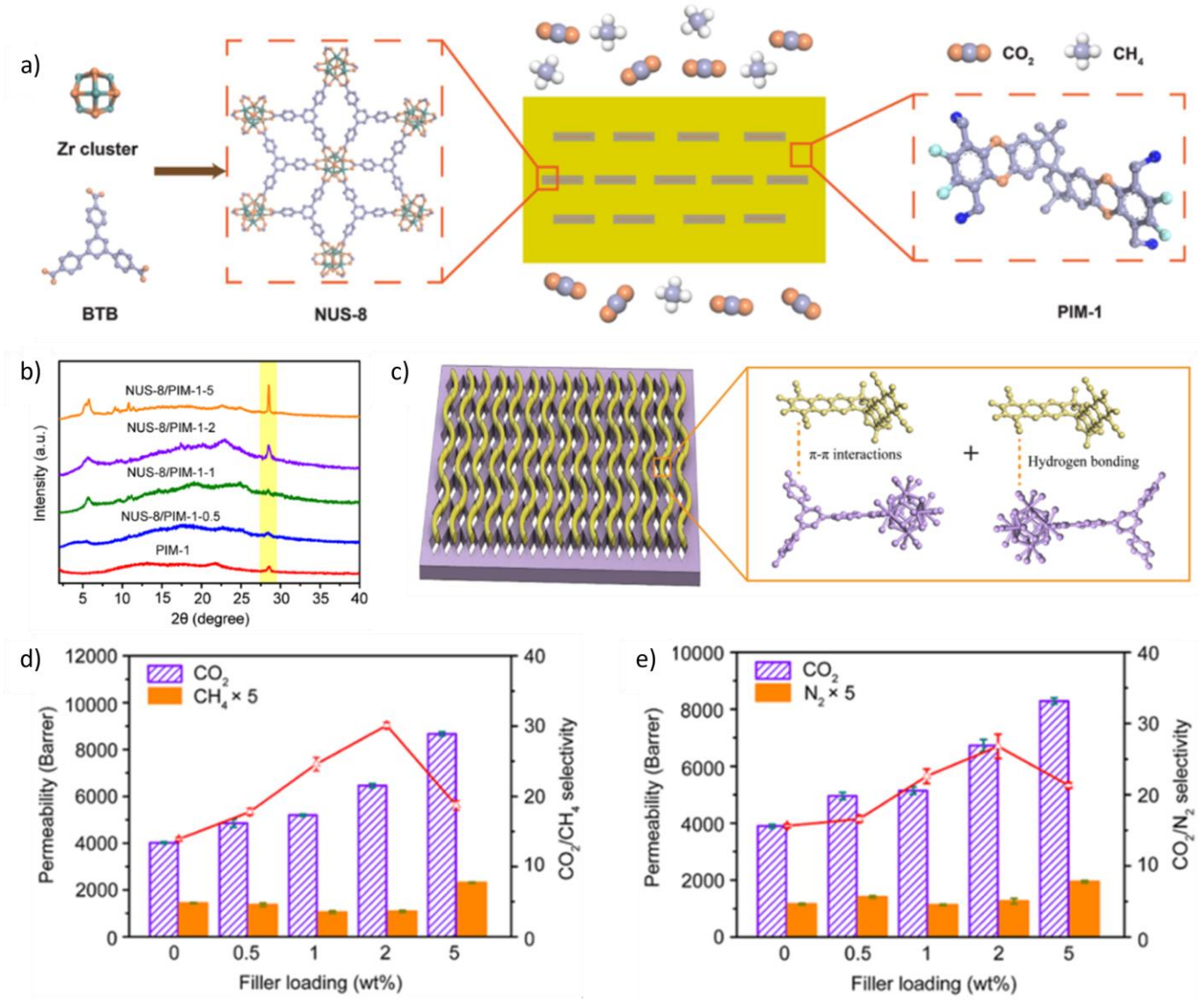


***Figure 19.*** *(a) Schematic illustration of the preparation of MMMs by incorporation of Zr-BTB (also known as NUS-8) into PIM-1 matrix for gas separation. NUS = National University of Singapore. (b) Powder X-ray diffraction (PXRD) patterns of the neat PIM-1 membrane and MMMs with different Zr-BTB loadings. (c) Schematic illustration of the adsorption and alignment of the PIM-1 chains on Zr-BTB MONs, due to the π–π interactions and hydrogen bonding between them. (d) $CO_2/CH_4$ separation performance of MMMs with different Zr-BTB loadings. (e) $CO_2/N_2$ separation performance of MMMs with different Zr-BTB loadings.*[104]

In addition to Zr-BTB, other zirconium-based MONs have also been used in separation applications.[83,84] For example, Zr-BTB-COOH MONs were incorporated as fillers into PIM-1 to prepare MMMs for use in gas separation applications.[83] As shown in **Figure 20a**, the hydrogen bonding interactions between the carboxyl groups in Zr-BTB-COOH MONs and the nitrile groups in PIM-1 enhanced the crystallinity of the PIM-1 matrix. This improved the $CO_2/CH_4$ and $CO_2/N_2$ separation performance of the membrane compared to the pure PIM-1 membrane. As shown in **Figure 20b and 20c**, the best-performing

MMMs exhibited $CO_2/CH_4$ and $CO_2/N_2$ selectivity of 17.03 and 30.95, respectively. Zr-BTB-$NH_2$ MONs were also incorporated into PIM-1 to prepare MMMs for use in gas separation applications.[84] As shown in **Figure 20d**, the hydrogen bonding interactions between Zr-BTB-$NH_2$ MONs and PIM-1 matrix improved their interfacial compatibility. Therefore, the MMMs exhibited excellent gas separation performance even at high filler loadings. As shown in **Figure 20e**, the membrane with 10.4 wt% of Zr-BTB-$NH_2$ loading showed a $CO_2$ permeability of 14638 Barrer and a $CO_2/N_2$ selectivity of 29.2, and when the Zr-BTB-$NH_2$ loading was increased to 15.0 wt%, the $CO_2/N_2$ selectivity of the membrane only slightly decreased to approximately 25. The Robeson upper bound plots are widely used to compare different gas separation membranes in terms of their selectivity and permeability.[113,114] As shown in **Figure 20e**, the $CO_2/N_2$ separation performance of the MMMs with Zr-BTB-$NH_2$ MONs surpassed the 2008 Robeson upper bound.[84,114]

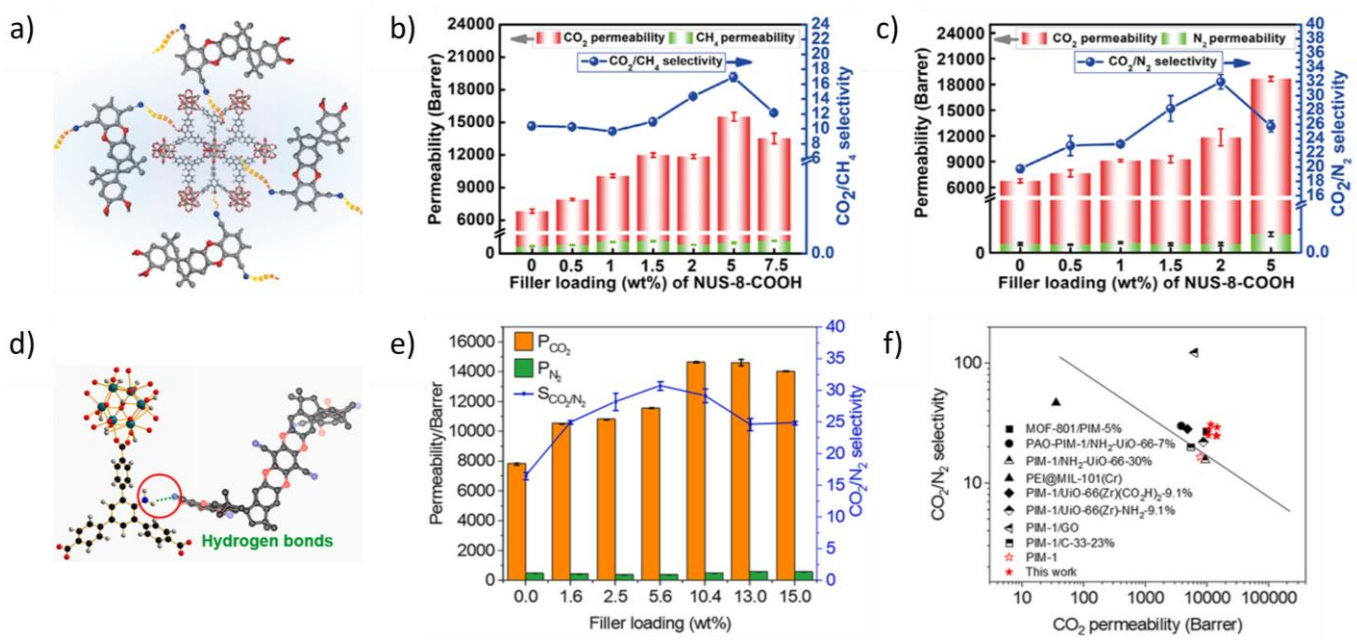


***Figure 20.*** *(a) Schematic illustration of the interactions between Zr-BTB-COOH and PIM-1. (b) $CO_2/CH_4$ separation performance of MMMs with different Zr-BTB-COOH loadings. (c) $CO_2/N_2$ separation performance of MMMs with different Zr-BTB-COOH loadings.[83] (d) Schematic illustration of the interactions between Zr-BTB-$NH_2$ and PIM-1. (e) $CO_2/N_2$ separation performance of MMMs with different Zr-BTB-$NH_2$ loadings. (f) Comparison of $CO_2/N_2$ separation performance of MMMs with different Zr-BTB-$NH_2$ loadings and other polymer-based MMMs based on the 2008 Robeson upper bound plot (the solid line).[84]*

Apart from MMMs, Zhao and co-workers also reported the use of stainless steel mesh membranes coated with Zr-BTB-$NH_2$ MONs in oil-water separation.[115] As shown in **Figure 21**, due to the hydrophobic nature of the Zr-BTB-$NH_2$-coated membrane, when 15 mL of water was added into the upper glassware, the water maintained above the membrane. However, when oil (chloroform dyed with oil red O) was

added into the upper glassware, the oil passed through the membrane with a high permeation flux of 1.0 × $10^5$ L $m^{-2}$ $h^{-1}$. The authors also conducted multiple separation cycles with chloroform/water mixture using the Zr-BTB-$NH_2$-coated membrane, and there was almost no change in the oil-water separation performance of the membrane after 50 continuous cycles, indicating its good separation stability.

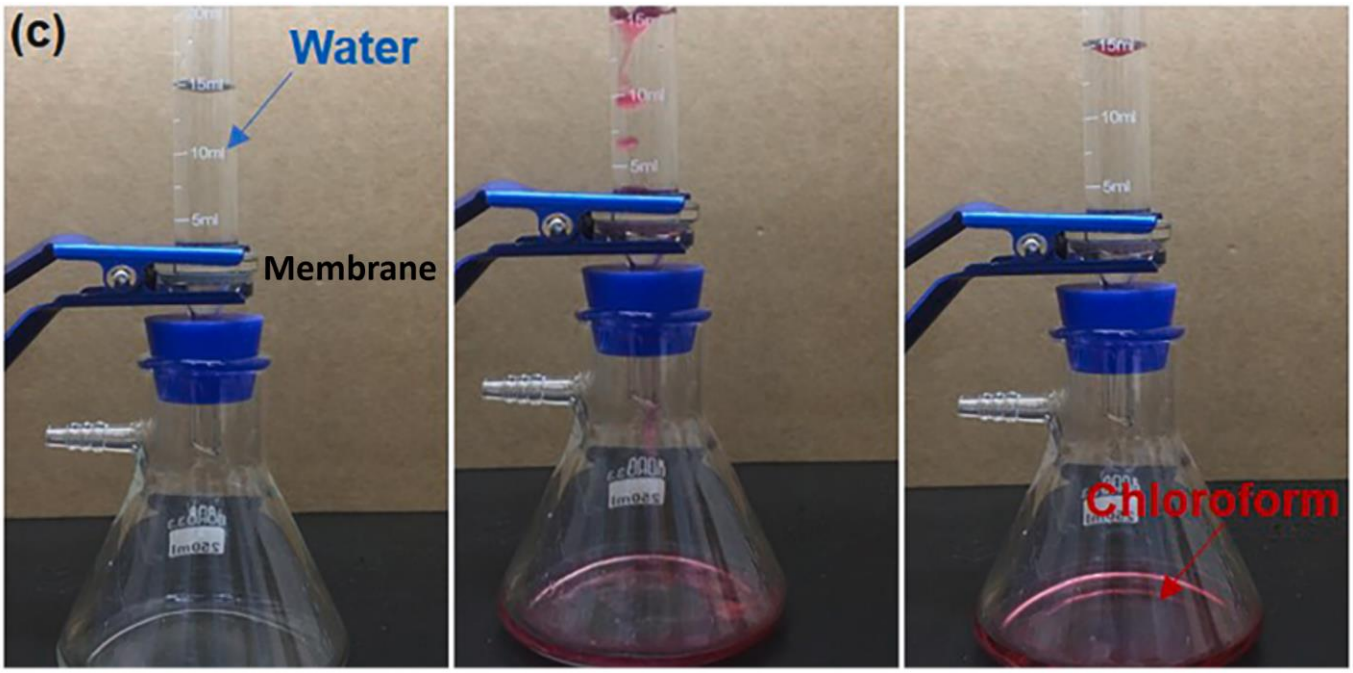


***Figure 21.*** *Oil-water separation using Zr-BTB-$NH_2$-coated membrane. The oil (chloroform) was dyed with oil red O.*[115]

In addition, Liu and co-workers reported the use of UiO-66 and UiO-66-$NH_2$ MONs in gas separation applications.[87] In their work, the UiO-66 MONs prepared by anisotropic etching of bulk UiO-66 crystals were used as seeds and deposited on a porous α-$Al_2O_3$ support by spin-coating method. Then, the remaining gaps in the UiO-66 seed layer were filled by a confined counter-diffusion-assisted epitaxial growth method (**Figure 22a**). Specifically, trace amounts of zirconium species ($ZrS_2$) were used as metal sources and were deposited on the back side of the α-$Al_2O_3$ support, followed by an epitaxial growth in a $H_2$BDC ligand-containing solution. The UiO-66 membrane they prepared had a thickness of 165 nm and exhibited an excellent $CO_2/N_2$ separation performance with a $CO_2/N_2$ separation selectivity of 35.4 and a $CO_2$ permeance of 2070 GPU, surpassing the upper bound of state-of-the-art 3D MOF membranes (**Figure 22b**). The UiO-66-$NH_2$ membrane with a thickness of 180 nm was also prepared using an identical method to the UiO-66 membrane, which exhibited excellent $H_2/CO_2$ separation performance with a $H_2/CO_2$ separation selectivity of 41.3 and a $H_2$ permeance of 1230 GPU, surpassing the upper bound of state-of-the-art 3D MOF membranes (**Figure 22c**). In addition, the authors also processed the UiO-66 MONs into

other types of membranes, including mixed matrix membrane (denoted as NS-MMM) prepared by blending the MON suspension with Pebax 2533 polymer solution followed by spin-coating the mixed solution onto an α-$Al_2O_3$ support, and thin film composite membrane (denoted as NS-TFC) prepared by spin-coating Pebax 2533 solution onto an α-$Al_2O_3$ supported UiO-66 MON layer. The membranes they prepared showed better gas separation performance compared to the pure Pebax 2533 membrane (denoted as Pure Pebax), and as shown in **Figure 22d**, the $CO_2/N_2$ separation performance of the NS-MMM surpassed the 2008 Robeson upper bound.[87,114]

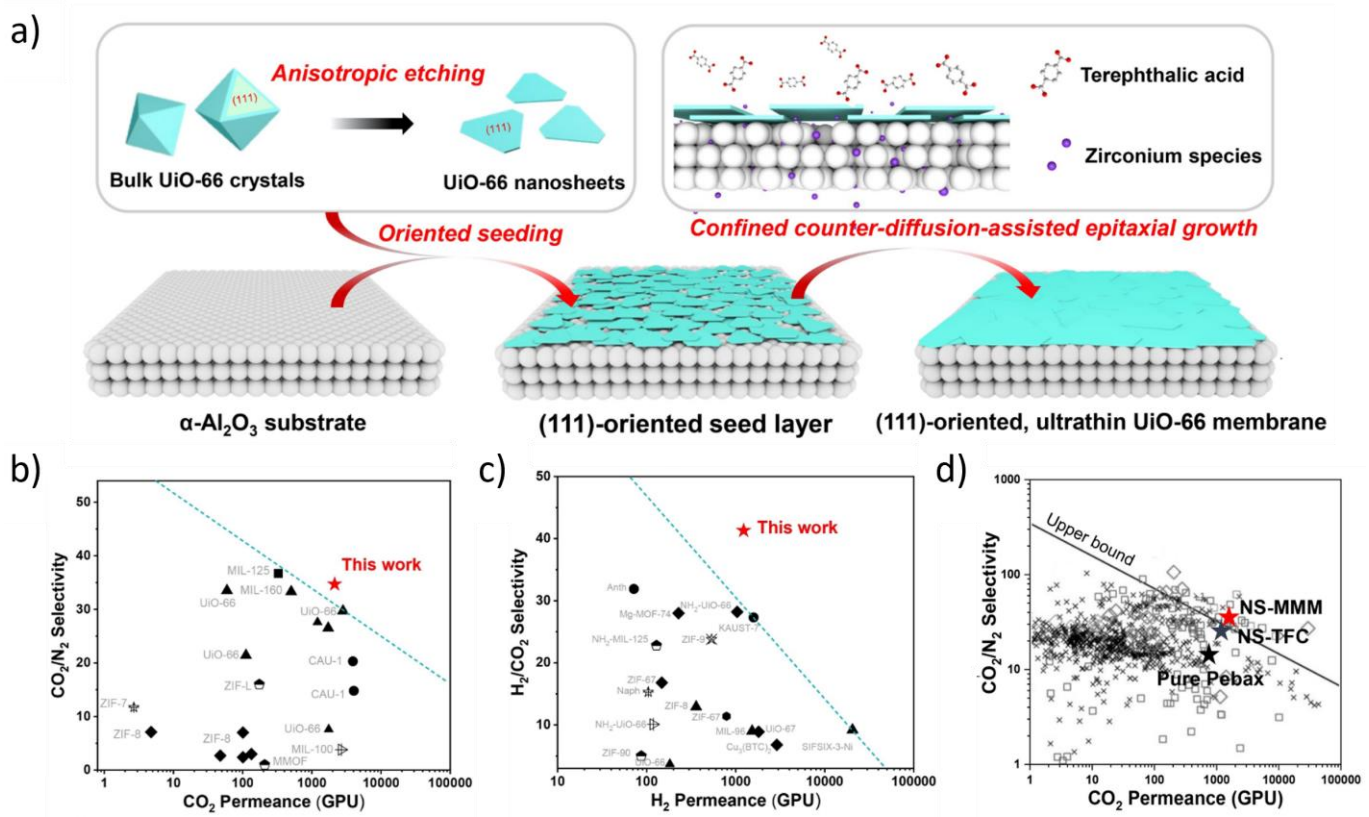


***Figure 22.*** *(a) Schematic illustration of the procedure for the preparation of UiO-66 MON membrane. (b) Comparison of $CO_2/N_2$ separation performance of UiO-66 MON membrane with state-of-the-art 3D MOF membranes. (c) Comparison of the $H_2/CO_2$ separation performance of UiO-66-$NH_2$ MON membrane with state-of-the-art 3D MOF membranes. (d) Comparison of $CO_2/N_2$ separation performance of NS-MMM, NS-TFC membrane with Pure Pebax and the 2008 Robeson upper bound.[87]*

## 1.5 Project aims

As an emerging class of tunable porous two-dimensional materials, MONs are promising candidates for use in separation applications.[38,47] The Foster group previously used a wide range of MONs to prepare membranes for use in water purification and gas separation applications, and the membranes prepared using Zr-dicarboxylates-based MONs showed promising results. Subsequent literature reports indicate that Zr-BTB and its derivatives are particularly promising due to their ease of synthesis and functionalisation, well-defined pore size, high aspect ratio and high stability.[64,71] However, there is much left to be investigated about Zr-BTB and its derivatives. Therefore, at the start of my PhD, I set out to better understand these systems, to follow up on recent literature reports of gel formation[72] and of their use in different water purification[112] and gas separation applications.[83,84,104,112]

As discussed in **Section 1.2**, Zhao and co-workers reported that Zr-BTB MONs could be used to prepare non-flowing gels by removing the excess solvents.[72] However, compared to the well-studied polymeric gels,[116,117] there is much left to be investigated about these novel Zr-BTB gels. Therefore, in **Chapter 2** the rheological behaviour of Zr-BTB gels is investigated along with studies into the mechanism of formation and structure of the gels. The gels have a unique hierarchically porous structure that combines the micropores of the Zr-BTB MONs with macropores of the gels opening up new opportunities for use in separation and release applications. This chapter therefore also investigates the use of Zr-BTB gels in the loading and release of molecules with different sizes and charges.

A wide variety of methods have been developed to process MONs into membranes that can be used to separate molecules, as depicted in **Figure 10**.[47] It was reported that the water-stable Zr-BTB MONs could be used to fabricate composite membranes that exhibited excellent water purification and desalination performance.[112] A lot of Zr-BTB derivatives composed of $Zr_6$ clusters and tritopic carboxylic acid ligands have also been developed, but have not been investigated in water purification applications.[83-86,115] Therefore, **Chapter 3** explores the use of Zr-BTB and its derivatives to fabricate water purification membranes to separate dyes with different sizes and charges in aqueous solutions to understand the effect of the different structures and surface properties of the MONs on the water purification performance of the membranes.

It has also been reported that Zr-BTB MON and its derivatives could be incorporated as fillers into PIM-1 polymer to fabricate MMMs that exhibited excellent gas separation performance.[83,84,104] However, the gas separation performance of MMMs prepared using other polymers (i.e., the generality of this method) is not well-studied. Therefore, **Chapter 4** investigates MMMs composed of Zr-BTB and Zr-BTB-

$NH_2$ MONs and other polymers apart from PIM-1 to understand the effect of different filler-polymer interactions on the gas separation performance of the membranes. This chapter also explores composite membranes of Zr-BTB and Zr-BTB-$NH_2$ to compare the gas separation performance of membranes prepared by different methods.

This thesis therefore aims to improve our understanding of this promising class of zirconium-based MONs and explore their use in a wide range of different separation applications.

## 1.6 References


1. D. A. C. Brownson, D. K. Kampouris and C. E. Banks, *J. Power Sources*, 2011, **196**, 4873-4885.
2. K. S. Novoselov, A. K. Geim, S. V. Morozov, D. Jiang, Y. Zhang, S. V. Dubonos, I. V. Grigorieva and A. A. Firsov, *Science*, 2004, **306**, 666-669.
3. P. Avouris and C. Dimitrakopoulos, *Mater. Today*, 2012, **15**, 86-97.
4. E. P. Randviir, D. A. C. Brownson and C. E. Banks, *Mater. Today*, 2014, **17**, 426-432.
5. Y. Zhang, T. R. Nayak, H. Hong and W. Cai, *Nanoscale*, 2012, **4**, 3833-3842.
6. D. Li, T. Wang, Z. Li, X. Xu, C. Wang and Y. Duan, *Sensors*, 2020, **20**, 54.
7. A. Shuaibu, O. J. Adeyemi, U. R. Ushiekpan, O. G. Olowomofe, B. J. Akinade and O. A. Kafayat, *Am. J. Condens. Matter Phys.*, 2019, **9**, 1-5.
8. R. Ma, Z. Liu, L. Li, N. Iyi and T. Sasaki, *J. Mater. Chem.*, 2006, **16**, 3809–3813.
9. H. Zeng, J. Dai, W. Yao, D. Xiao and X. Cui, *Nat. Nanotechnol.*, 2012, **7**, 490-493.
10. A. K. Katiyar, A. T. Hoang, D. Xu, J. Hong, B. J. Kim, S. Ji and J.-H. Ahn, *Chem. Rev.*, 2023.
11. S. J. Kim, K. Choi, B. Lee, Y. Kim and B. H. Hong, *Annu. Rev. Mater. Res.*, 2015, **45**, 63-84.
12. H. Zhang, *ACS Nano*, 2015, **9**, 9451–9469
13. L. Zhao, B. Wang and R. Wang, *Adv. Mater. Interfaces*, 2022, **9**, 2200771.
14. M. Zhao, Y. Huang, Y. Peng, Z. Huang, Q. Ma and H. Zhang, *Chem. Soc. Rev.*, 2018, **47**, 6267-6295.
15. M.-C. Ferrari, *Curr. Opin. Chem. Eng.*, 2023, **40**, 100905.
16. F. Moghadam and H. B. Park, *Curr. Opin. Chem. Eng.*, 2018, **20**, 28-38.
17. M. Fathizadeh, W. L. Xu, F. Zhou, Y. Yoon and M. Yu, *Adv. Mater. Interfaces*, 2017, **4**, 1600918.
18. J. Yang, Z. Li, Z. Wang, S. Yuan, Y. Li, W. Zhao and X. Zhang, *Adv. Mater. Technol.*, 2021, **6**, 2000862.
19. D. J. Ashworth and J. A. Foster, *J. Mater. Chem. A*, 2018, **6**, 16292-16307.
20. H. C. Zhou and S. Kitagawa, *Chem. Soc. Rev.*, 2014, **43**, 5415-5418.
21. K. Kida, M. Okita, K. Fujita, S. Tanaka and Y. Miyake, *CrystEngComm*, 2013, **15**, 1794–1801.
22. J. Chen, Z. Zhu, G. Monge and W.-N. Wang, *Chem. Eng. J.*, 2022, **447**, 137544.
23. M. R. Khdhayyer, E. Esposito, A. Fuoco, M. Monteleone, L. Giorno, J. C. Jansen, M. P. Attfield and P. M. Budd, *Sep. Purif. Technol.*, 2017, **173**, 304-313.
24. X. Wu, M. Niknam Shahrak, B. Yuan and S. Deng, *Microporous Mesoporous Mater.*, 2014, **190**, 189-196.
25. P. Mishra, H. P. Uppara, B. Mandal and S. Gumma, *Ind. Eng. Chem. Res.*, 2014, **53**, 19747-19753.
26. Y. Wang, G. Yang, H. Guo, X. Meng, G. Kong, Z. Kang, R. Guillet-Nicolas and S. Mintova, *J. Membr. Sci.*, 2022, **643**, 120070.
27. P. Z. Moghadam, A. Li, X. W. Liu, R. Bueno-Perez, S. D. Wang, S. B. Wiggin, P. A. Wood and D. Fairen-Jimenez, *Chem. Sci.*, 2020, **11**, 8373-8387.
28. T. Rasheed, K. Rizwan, M. Bilal and H. M. N. Iqbal, *Molecules*, 2020, **25**, 1598.

29. G. A. Udourioh, M. M. Solomon, C. O. Matthews-Amune, E. I. Epelle, J. A. Okolie, V. E. Agbazue and U. Onyenze, *React. Chem. Eng.*, 2023, **8**, 278-310.
30. W. Lu, Z. Wei, Z. Y. Gu, T. F. Liu, J. Park, J. Park, J. Tian, M. Zhang, Q. Zhang, T. Gentle, 3rd, M. Bosch and H. C. Zhou, *Chem. Soc. Rev.*, 2014, **43**, 5561-5593.
31. P. Kumar, A. Deep and K.-H. Kim, *Trends Anal. Chem.*, 2015, **73**, 39-53.
32. D. Li, H.-Q. Xu, L. Jiao and H.-L. Jiang, *EnergyChem*, 2019, **1**, 100005.
33. H. D. Lawson, S. P. Walton and C. Chan, *ACS Appl. Mater. Interfaces*, 2021, **13**, 7004-7020.
34. X. Zhao, Y. Wang, D.-S. Li, X. Bu and P. Feng, *Adv. Mater.*, 2018, **30**, e1705189.
35. J.-R. Li, J. Sculley and H.-C. Zhou, *Chem. Rev.*, 2012, **112**, 869-932.
36. R. C. Arbulu, Y. B. Jiang, E. J. Peterson and Y. Qin, *Angew. Chem. Int. Ed.*, 2018, **57**, 5813-5817.
37. Q. Zhao, W. Yuan, J. Liang and J. Li, *Int. J. Hydrog. Energy*, 2013, **38**, 13104-13109.
38. J. Nicks, K. Sasitharan, R. R. R. Prasad, D. J. Ashworth and J. A. Foster, *Adv. Funct. Mater.*, 2021, **31**, 2103723.
39. D. J. Ashworth, A. Cooper, M. Trueman, R. W. M. Al-Saedi, L. D. Smith, A. Meijer and J. A. Foster, *Chem. Eur. J.*, 2018, **24**, 17986-17996.
40. Y.-z. Li, Z.-h. Fu and G. Xu, *Coord. Chem. Rev.*, 2019, **388**, 79-106.
41. Y. L. Liu, X. Y. Liu, L. Feng, L. X. Shao, S. J. Li, J. Tang, H. Cheng, Z. Chen, R. Huang, H. C. Xu and J. L. Zhuang, *ChemSusChem*, 2022, **15**, e202102603.
42. J. Nicks, J. Zhang and J. A. Foster, *Chem. Commun.*, 2019, **55**, 8788-8791.
43. V. K. Maka, A. Mukhopadhyay, G. Savitha and J. N. Moorthy, *Nanoscale*, 2018, **10**, 22389-22399.
44. F. Moghzi, J. Soleimannejad, E. C. Sanudo and J. Janczak, *ACS Appl. Mater. Interfaces*, 2020, **12**, 44499-44507.
45. Q. Liu, Z. Guo, C. Wang, S. Guo, Z. Xu, C. Hu, Y. Liu, Y. Wang, J. He and W. Y. Wong, *Adv. Sci.*, 2023, **10**, e2207545.
46. W. Zhao, J. Peng, W. Wang, S. Liu, Q. Zhao and W. Huang, *Coord. Chem. Rev.*, 2018, **377**, 44-63.
47. Y. Peng and W. Yang, *Adv. Mater. Interfaces*, 2019, **7**, 1901514.
48. Y. Peng, R. Yao and W. Yang, *Chem. Commun.*, 2019, **55**, 3935-3938.
49. M. Zhao, Y. Wang, Q. Ma, Y. Huang, X. Zhang, J. Ping, Z. Zhang, Q. Lu, Y. Yu, H. Xu, Y. Zhao and H. Zhang, *Adv. Mater.*, 2015, **27**, 7372–7378.
50. X. Gao, R. Cui, M. Zhang and Z. Liu, *Mater. Lett.*, 2017, **197**, 217-220.
51. A. Pustovarenko, M. G. Goesten, S. Sachdeva, M. Shan, Z. Amghouz, Y. Belmabkhout, A. Dikhtiarenko, T. Rodenas, D. Keskin, I. K. Voets, B. M. Weckhuysen, M. Eddaoudi, L. de Smet, E. J. R. Sudholter, F. Kapteijn, B. Seoane and J. Gascon, *Adv. Mater.*, 2018, **30**, e1707234.
52. M.-H. Pham, G.-T. Vuong, F.-G. Fontaine and T.-O. Do, *Cryst. Growth Des.*, 2012, **12**, 3091-3095.
53. R. Makiura, K. Tsuchiyama and O. Sakata, *CrystEngComm*, 2011, **13**, 5538–5541.
54. K. Takada, R. Sakamoto, S. T. Yi, S. Katagiri, T. Kambe and H. Nishihara, *J. Am. Chem. Soc.*, 2015, **137**, 4681-4689.
55. R. Makiura, R. Usui, Y. Sakai, A. Nomoto, A. Ogawa, O. Sakata and A. Fujiwara, *ChemPlusChem*, 2014, **79**, 1352-1360.
56. Q. Jiang, C. Zhou, H. Meng, Y. Han, X. Shi, C. Zhan and R. Zhang, *J. Mater. Chem. A*, 2020, **8**, 15271-15301.
57. A. Abherve, S. Manas-Valero, M. Clemente-Leon and E. Coronado, *Chem. Sci.*, 2015, **6**, 4665-4673.
58. P. Tamuly, F. Sama and J. N. Moorthy, *Adv. Mater. Interfaces*, 2022, **9**, 2200337.
59. P. Amo-Ochoa, L. Welte, R. Gonzalez-Prieto, P. J. Sanz Miguel, C. J. Gomez-Garcia, E. Mateo-Marti, S. Delgado, J. Gomez-Herrero and F. Zamora, *Chem. Commun.*, 2010, **46**, 3262-3264.
60. J. A. Foster, S. Henke, A. Schneemann, R. A. Fischer and A. K. Cheetham, *Chem. Commun.*, 2016, **52**, 10474-10477.

61. D. J. Ashworth, T. M. Roseveare, A. Schneemann, M. Flint, I. Dominguez Bernaldes, P. Vervoorts, R. A. Fischer, L. Brammer and J. A. Foster, *Inorg. Chem.*, 2019, **58**, 10837-10845.
62. H.-S. Wang, J. Li, J.-Y. Li, K. Wang, Y. Ding and X.-H. Xia, *NPG Asia Mater.*, 2017, **9**, e354.
63. X. Wang, C. Chi, K. Zhang, Y. Qian, K. M. Gupta, Z. Kang, J. Jiang and D. Zhao, *Nat. Commun.*, 2017, **8**, 14460.
64. Z. Hu, E. M. Mahdi, Y. Peng, Y. Qian, B. Zhang, N. Yan, D. Yuan, J.-C. Tan and D. Zhao, *J. Mater. Chem. A*, 2017, **5**, 8954-8963.
65. M. Nasrabadi, M. A. Ghasemzadeh and M. R. Z. Monfared, *New J. Chem.*, 2019, **43**, 16033-16040.
66. Q. Yang, Y. Wang, J. Wang, F. Liu, N. Hu, H. Pei, W. Yang, Z. Li, Y. Suo and J. Wang, *Food Chem.*, 2018, **254**, 241-248.
67. Z.-Q. Li, J.-C. Yang, K.-W. Sui and N. Yin, *Mater. Lett.*, 2015, **160**, 412-414.
68. I. Abánades Lázaro and R. S. Forgan, *Coord. Chem. Rev.*, 2019, **380**, 230-259.
69. C. Jia, T. He and G.-M. Wang, *Coord. Chem. Rev.*, 2023, **476**, 214930.
70. N. Yuan, X. Gong, W. Sun and C. Yu, *Chemosphere*, 2021, **267**, 128863.
71. G.-Y. Qiao, S. Yuan, J. Pang, H. Rao, C. T. Lollar, D. Dang, J.-S. Qin, H.-C. Zhou and J. Yu, *Angew. Chem. Int. Ed.*, 2020, **59**, 18224–18228.
72. H. Yuan, G. Liu, Z. Qiao, N. Li, P. J. S. Buenconsejo, S. Xi, A. Karmakar, M. Li, H. Cai, S. J. Pennycook and D. Zhao, *Adv. Mater.*, 2021, **33**, e2101257.
73. D. Zhan, Z. Yu, A. Saeed, Q. Hu, N. Zhao, W. Xu, J. Wang, L. Kong and J. Liu, *J. Mater. Chem. C*, 2023, **11**, 10738-10747.
74. H. Zhang, B. Luo, P. An, X. Zhan, F. Lan and Y. Wu, *ACS Appl. Bio Mater.*, 2022, **5**, 3500-3508.
75. Y. Wang, L. Li, L. Yan, X. Gu, P. Dai, D. Liu, J. G. Bell, G. Zhao, X. Zhao and K. M. Thomas, *Chem. Mater.*, 2018, **30**, 3048-3059.
76. J. Zhao, R. Chen, J. Huang, F. Wang, C. A. Tao and J. Wang, *ACS Appl. Mater. Interfaces*, 2021, **13**, 40863-40871.
77. Y. Li, T. Wang and D. Liu, *Chem Asian J.*, 2021, **16**, 3413-3418.
78. S. S. Yang, C. Wang, J. Xiao, X. Yu, W. Shang, D. D. Y. Chen and Z. Y. Gu, *Analyst*, 2020, **145**, 4432-4435.
79. J. Zhao, R. Chen, J. Huang, F. Wang, C.-A. Tao and J. Wang, *Ind. Eng. Chem. Res.* , 2021, **61**, 413-420.
80. G.-Y. Qiao, S. Yuan, J. Pang, H. Rao, C. T. Lollar, D. Dang, J.-S. Qin, H.-C. Zhou and J. Yu, *Angew Chem Int Ed Engl*, 2020, **59**, 18224-18228.
81. X. Feng, Y. Ren, H. Wang, W. Wu and H. Jiang, *Catal. Sci. Technol.*, 2023, **13**, 7036-7045.
82. Z. Cheng, J. Lian, Y. Chen, Y. Tang, Y. Huang, J. Zhang, S. Xiang and Z. Zhang, *CCS Chem.*, 2023, DOI: 10.31635/ccschem.023.202303074.
83. D. Wang, Y. Ying, Y. Zheng, Y. Pu, Z. Yang and D. Zhao, *J. Membr. Sci. Lett.*, 2022, **2**, 100017.
84. Y. Pu, Z. Yang, V. Wee, Z. Wu, Z. Jiang and D. Zhao, *J. Membr. Sci.*, 2022, **641**, 119912.
85. R. Xu, T. Drake, G. Lan and W. Lin, *Chem. Eur. J.* , 2018, **24**, 15772-15776.
86. H. Liu, H. Wang, Q. Song, K. Kuster, U. Starke, P. A. van Aken and E. Klemm, *Angew. Chem. Int. Ed.*, 2022, **61**, e202117058.
87. Y. Sun, J. Yan, Y. Gao, T. Ji, S. Chen, C. Wang, P. Lu, Y. Li and Y. Liu, *Angew. Chem. Int. Ed.*, 2023, **62**, e202216697.
88. T. He, B. Ni, S. Zhang, Y. Gong, H. Wang, L. Gu, J. Zhuang, W. Hu and X. Wang, *Small*, 2018, **14**, e1703929.
89. S. Leubner, V. E. G. Bengtsson, K. Synnatschke, J. Gosch, A. Koch, H. Reinsch, H. Xu, C. Backes, X. Zou and N. Stock, *J. Am. Chem. Soc.*, 2020, **142**, 15995-16000.
90. H. Hu, Z. Wang, L. Cao, L. Zeng, C. Zhang, W. Lin and C. Wang, *Nat. Chem.*, 2021, **13**, 358-366.
91. X. Liu, Y. Li, Y. Liu, S. Li, L. Feng, J. Zhuang and J. Tang, *J. Alloys Compd.*, 2022, **922**, 165939.

92. M. J. Cliffe, E. Castillo-Martinez, Y. Wu, J. Lee, A. C. Forse, F. C. N. Firth, P. Z. Moghadam, D. Fairen-Jimenez, M. W. Gaultois, J. A. Hill, O. V. Magdysyuk, B. Slater, A. L. Goodwin and C. P. Grey, *J. Am. Chem. Soc.*, 2017, **139**, 5397-5404.
93. S. Widagdo and W. D. Seider, *AIChE J.*, 2004, **42**, 96-130.
94. G. T. Rochelle, *Science*, 2009, **325**, 1652-1654.
95. W. A. P. Menachem Elimelech, *Science*, 2011, **333**, 712-717.
96. Y. Cheng, Y. Pu and D. Zhao, *Chem Asian J.*, 2020, **15**, 2241-2270.
97. Y. Liao, C.-H. Loh, M. Tian, R. Wang and A. G. Fane, *Prog. Polym. Sci.*, 2018, **77**, 69-94.
98. S. A. Ilame and V. S. Satyavir, *Crit. Rev. Food Sci. Nutr.*, 2015, **55**, 964-987.
99. Z. Lai, G. Bonilla, I. Diaz, J. G. Nery, K. Sujaoti, M. A. Amat, E. Kokkoli, O. Terasaki, R. W. Thompson, M. Tsapatsis and D. G. Vlachos, *Science*, **300**, 456-460.
100. L. M. Robeson, *Curr. Opin. Solid State Mater. Sci.*, 1999, **4**, 549–552.
101. H. Ang and L. Hong, *ACS Appl. Mater. Interfaces*, 2017, **9**, 28079-28088.
102. Y. Peng, Y. Li, Y. Ban, H. Jin, W. Jiao, X. Liu and W. Yang, *Science*, 2014, **346**, 1356-1359.
103. T. Rodenas, I. Luz, G. Prieto, B. Seoane, H. Miro, A. Corma, F. Kapteijn, I. X. F. X. Llabres and J. Gascon, *Nat. Mater.*, 2015, **14**, 48-55.
104. Y. Cheng, S. R. Tavares, C. M. Doherty, Y. Ying, E. Sarnello, G. Maurin, M. R. Hill, T. Li and D. Zhao, *ACS Appl. Mater. Interfaces*, 2018, **10**, 43095-43103.
105. L. Shu, L.-H. Xie, Y. Meng, T. Liu, C. Zhao and J.-R. Li, *J. Membr. Sci.*, 2020, **603**, 118049.
106. A. Li, X. Ma, J. Ma, Q. Yuan, J. Zhang and X. Xuan, *CrystEngComm*, 2021, **23**, 3989-3994.
107. B. Gao, Z. Jiang, M. Zhao, H. Wu, F. Pan, J. Q. Mayta, Z. Chang and X. Bu, *J. Membr. Sci.*, 2018, **546**, 31-40.
108. Y. Peng, Y. Li, Y. Ban and W. Yang, *Angew. Chem. Int. Ed.*, 2017, **56**, 9757-9761.
109. Y. Yang, K. Goh, R. Wang and T. H. Bae, *Chem. Commun.*, 2017, **53**, 4254-4257.
110. M. Jian, R. Qiu, Y. Xia, J. Lu, Y. Chen, Q. Gu, R. Liu, C. Hu, J. Qu, H. Wang and X. Zhang, *Sci. Adv.*, 2020, **6**, eaay3998.
111. S. Feng, M. Bu, J. Pang, W. Fan, L. Fan, H. Zhao, G. Yang, H. Guo, G. Kong, H. Sun, Z. Kang and D. Sun, *J. Membr. Sci.*, 2020, **593**, 117404.
112. H. Yuan, K. Li, D. Shi, H. Yang, X. Yu, W. Fan, P. J. S. Buenconsejo and D. Zhao, *Adv. Mater.*, 2023, **35**, e2211859.
113. L. M. Robeson, *J. Membr. Sci.*, 1991, **62**, 165-185.
114. L. M. Robeson, *J. Membr. Sci.*, 2008, **320**, 390-400.
115. G. Liu, Y. Cai, H. Yuan, J. Zhang, Z. Zhang and D. Zhao, *J. Membr. Sci.*, 2023, **668**, 121077.
116. J. Jagur-Grodzinski, *Polym. Adv. Technol.*, 2010, **21**, 27–47.
117. S. Chaterji, I. K. Kwon and K. Park, *Prog. Polym. Sci.*, 2007, **32**, 1083-1122.

# Chapter 2

# Metal-Organic Nanosheet Gels-Hierarchically Porous Materials for Selective Loading and Differential Release

## Chapter 2

Metal-organic nanosheet gels-hierarchically porous materials for selective loading and differential release

Unpublished paper (full article)

**Jiangtian Tan** and Jonathan A. Foster

**Author Contributions**

| | |
|---|---|
| **Jiangtian Tan** | Performed all experiments and characterisations. Drafted manuscript and SI and created all figures. |
| Jonathan A. Foster | Supervised Jiangtian Tan. Assisted in editing of manuscript. |

ARTICLE

# Metal-organic nanosheet gels-hierarchically porous materials for selective loading and differential release

Received 00th January 20xx,
Accepted 00th January 20xx

DOI: 10.1039/x0xx00000x

Jiangtian Tan[a] and Jonathan A. Foster*[a]

Metal-organic nanosheets (MONs) are intrinsically porous two-dimensional (2D) materials with a high surface area and tunable chemistry which have been widely used in suspension or on surfaces for a variety of applications. Here, we show how MONs can be used to form gels through a simple centrifugation process and their hierarchically porous structures used to enable the selective loading and differential release of small molecules based on their size and charge. Centrifugation of a suspension of monolayer Zr-BTB MONs (BTB = 1,3,5-benzenetribenzoate) formed organogels and hydrogels with a concentration of 1.5 wt% depending on the solvent (ethanol and water) used. The gels showed self-healing behaviour which was attributed to electrostatic interactions between the nanosheets forming a "house of cards" structure. Rapid and selective loading of the gels with a range of small molecules could be achieved by centrifugation of suspensions of nanosheets containing different cargo solutions. Small neutral molecules were found to diffuse out of the gel significantly more rapidly than larger molecules, which was attributed to smaller molecules being able to pass more easily through the pores of the MONs. Charged molecules were released slower than the neutral ones, which was attributed to electrostatic interactions with the nanosheets. We anticipate that hierarchically porous MON-based gels will open up a variety of interesting new applications, including sensing, separation, controlled release, drug loading and drug delivery.

## Introduction

The gel state offers solid-like rheology for a material which is largely liquid in composition making it ideal for the loading and release of small molecules into and out of solution.[1] The ability to do this selectively and in a controlled way is key to a wide range of applications including water purification,[2] delivery of drugs[3] and fertilisers.[4] The majority of gels are formed through physical entanglement or chemical crosslinking of polymers,[5] or aggregation of growing particles through a sol-gel process.[6] Whereas, clays and other sheet-like materials can form gels with a "house of cards" structure, caused by favourable electrostatic interactions between the edges and faces of the nanosheets.[7, 8]

Metal-organic gels (MOGs), formed from three-dimensional metal-organic frameworks (MOFs), have attracted considerable attention thanks to their highly tunable structures and intrinsic porosity.[9, 10] Most MOGs are formed through a sol-gel process in which growing 3D MOF crystals fuse with each other to form a sample spanning network.[11] Other examples combine MOFs with gel forming polymers,[12] or use crosslinkers to chemically or physically cross-link MOFs followed by removing metal ions.[13, 14] A variety of MOG derived materials have also been developed in which the MOGs act as sacrificial templates to create porous gel-derived materials.[15, 16] Due to the inherent microporosity of MOFs and the additional porosity formed during gelation, MOGs usually have a unique hierarchical porosity,[9] which have been used to remove dyes from water,[17] or separate enantiomers.[18] Solution processability is another key advantage of MOGs over traditional microcrystalline MOF powders. For example, Somjit and co-workers studied UiO-66 MOG, and showed that it can be processed into a thin film with sub-100 nm thickness via spin-coating, which enhanced the electrical conductivity of their devices.[19] A variety of other MOGs, such as HKUST-1, UiO-66-$NH_2$, have been processed into monolithic materials and have shown great promise for gas uptake applications.[20-22]

Metal-organic nanosheets (MONs) are two-dimensional (2D) MOFs with a sheet-like morphology.[23] Their ultrathin nature, high aspect ratios and high surface areas make them ideal materials for a wide range of applications, including sensing, catalysis and electronics.[24] Their intrinsically porous nature and well-defined pore sizes also make them ideal materials for use in membrane-based water-purification and gas separation applications.[25, 26] Among the diverse range of MONs that have been reported in the literature, Zr-BTB MONs (BTB = 1,3,5-benzenetribenzoate) have attracted considerable attention due to their high water, chemical and thermal stability, ease of synthesis and functionalisation,[27-29] which have been used in a wide range of different applications.[30-33] In one recent publication, Zhao and co-workers mention gel-like behaviour by Zr-BTB MONs as part of a study where they processed the MONs into thin films and harnessed them as

[a] *Department of Chemistry, University of Sheffield, Sheffield, UK. E-mail: jona.foster@sheffield.ac.uk.*

† Footnotes relating to the title and/or authors should appear here.
Electronic Supplementary Information (ESI) available: [details of any supplementary information available should be included here]. See DOI: 10.1039/x0xx00000x

sensors for capacitive gas sensing,[29] however no further characterisation of the gel state is provided.

Intrigued by their observations, we set out to characterise this gel-like behaviour of Zr-BTB more fully in different solvents and undertake rheological and microscopic studies to understand the structures and properties of the gels. In this work, we discovered a new approach to the formation of gels through centrifugation of the nanosheets, which allows for rapid loading of the gels with different cargo molecules. We anticipated that the high surface area and porosity of the gels could make them interesting candidates for small molecule cargo loading and release applications. In particular, we envisaged the microporous, sheet-like MONs acting as "fishing nets" with small molecule "fish" being able to pass through the pores, whereas larger molecules are blocked by the pores, and charged molecules stick to the MONs. We anticipated that this could enable size- and charge-selective loading and differential release of cargo molecules from MON-based gels, opening up new levels of control for drug delivery applications.

## Results and Discussion

**Preparation and characterisation of Zr-BTB MONs.** Zr-BTB MONs were synthesised according to the solvothermal method reported by Zhao and co-workers.[29] As shown in **Figure 1a**, zirconium(IV) chloride ($ZrCl_4$, 0.129 mmol) and 1,3,5-benzenetribenzoic acid ($H_3BTB$, 0.068 mmol) were dissolved in a mixture of formic acid (HCOOH, 2 mL), water ($H_2O$, 2 mL) and *N,N*-dimethylformamide (DMF, 15 mL). The reaction mixture was heated in a reaction oven at 120 °C for 24 h. The resulting viscous suspension of Zr-BTB MONs was then centrifuged and washed three times with fresh DMF then ethanol. The washed MONs were stored in fresh ethanol as a homogeneous suspension with a concentration of 2.5 mg $mL^{-1}$ until needed.

Ethanol suspension of Zr-BTB MONs (1 mL) was dried using a hot plate at 80 °C to remove most of the solvent followed by a complete drying at 120 °C. The dried solids were characterised by powder X-ray diffraction (PXRD). The PXRD pattern of the as-synthesised Zr-BTB MONs was consistent with that reported by Zhao and co-workers,[29] suggesting that phase pure materials were synthesised. Whereas, compared to the simulated PXRD pattern of 3D Zr-BTB, the as-synthesised Zr-BTB MONs showed significantly reduced number of peaks. This could be attributed to the extreme aspect ratio of the nanosheets resulting in line broadening and preferred orientation effects (**Figure S1**). The hkls were assigned on the PXRD pattern of the as-synthesised Zr-BTB MONs which matched with a 2D hexagonal lattice. The Brunauer-Emmett-Teller (BET) surface area of Zr-BTB MONs was calculated to be 360 $m^2$ $g^{-1}$ (**Figure S2**), which was consistent with the surface area reported in the literature.[29]

Scanning electron microscopy (SEM) characterisation of the Zr-BTB MONs showed their 2D sheet-like morphology (**Figure S5**) and dynamic light scattering (DLS) characterisation showed that the particle size of the Zr-BTB MONs was in the range of 1.4 µm-6.5 µm (**Figure S3**). Atomic force microscopy (AFM) characterisations showed that the thickness of Zr-BTB MONs was approximately 1.5 nm, which was comparable to the van der Waals sizes of $Zr_6$ clusters in Zr-BTB (1.2 nm),[34] confirming the formation of monolayer nanosheets (**Figure 1b-1e**). It is worth noting that the Zr-BTB MONs prepared in this work were thinner than the 13 nm thick Zr-BTB nanosheets reported by Zhao and co-workers,[29] but comparable to the 1.2 nm thick Zr-BTB nanosheets reported by Lin and co-workers.[34]

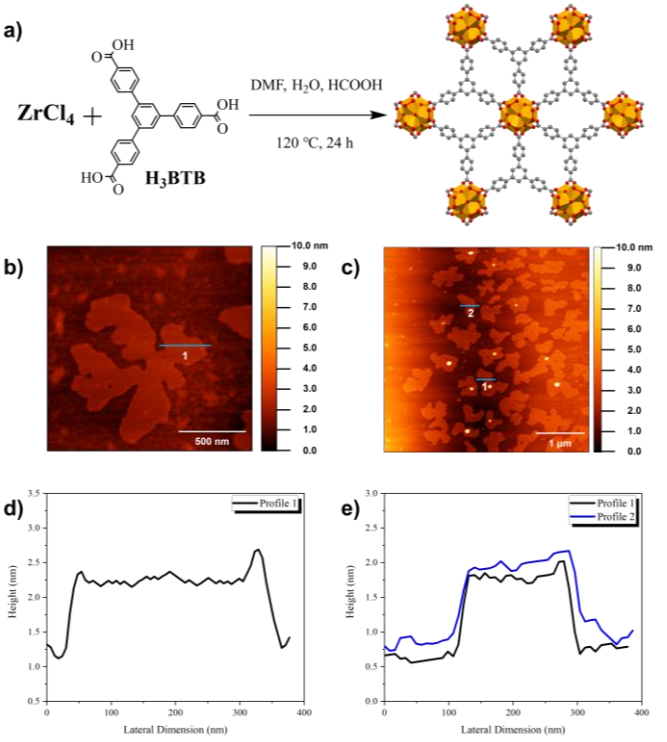


**Figure 1.** (a) Synthesis of Zr-BTB MONs. The crystal structure of Zr-BTB was downloaded from CCDC (deposition number: 1567188).[28] (b-e) AFM images and associated height profiles of Zr-BTB MONs.

**Preparation and characterisation of the gels.** An ethanol suspension of Zr-BTB MONs (2.5 mg $mL^{-1}$) was centrifuged at 4500 rpm for 1 hour. After centrifugation, the supernatant was removed and an organogel formed at the bottom of the centrifuge tube (**Figure 2a**). The content of MONs in the organogel was calculated to be 1.5 wt% (mass of MONs divided by mass of gel). Similar hydrogel formation was also observed after centrifugation when deionised water was used as the solvent.

In order to explore the range of concentrations in which the gels formed, ethanol suspension of Zr-BTB MONs (2.5 mg $mL^{-1}$) was heated at 80 °C using a hot plate, and the content of MONs in suspension was checked every 15 minutes (**Figure 2a and Figure S4**). After 1.5 h of solvent evaporation, the material in the vial changed from flowing liquid to a non-flowing organogel stable with respect to inversion of the vial. After further heating for 0.5 h, the content of MONs in the organogel increased from 1 wt% to 2 wt%, and a shrinkage in the volume of the organogel was observed. This could be attributed to the capillary forces exerted during solvent evaporation.[35] SEM characterisations of

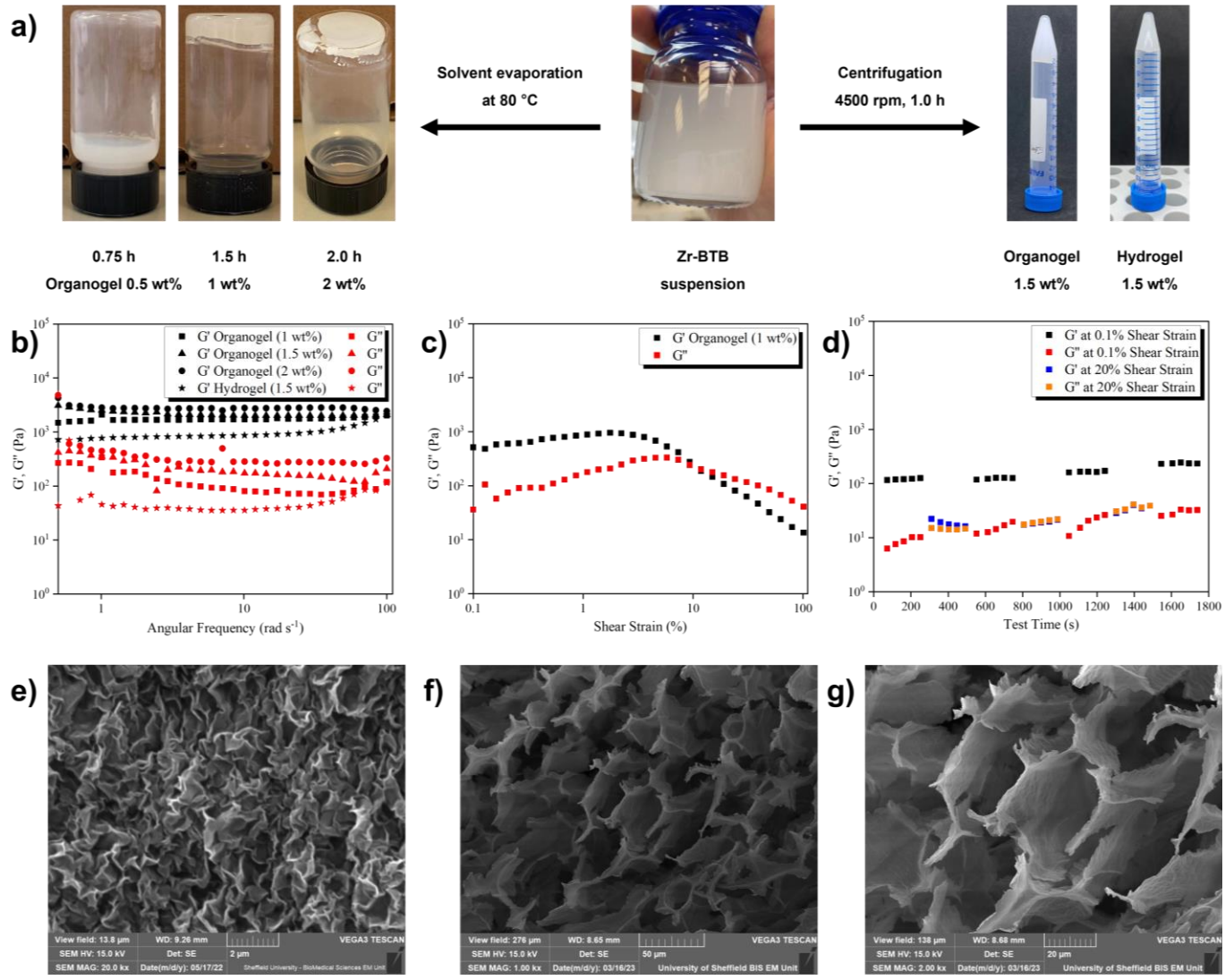


**Figure 2.** (a) Preparation of Zr-BTB organogels and hydrogels. (b) Frequency-sweep rheological measurements of organogels with fixed shear strain of 0.1 %. (c) Strain-sweep rheological measurements of 1 wt% organogel with fixed angular frequency of 1 rad $s^{-1}$. (d) Rheological measurements of 1 wt% organogel at different shear strains showing its self-healing behaviour. This rheological experiment was conducted with fixed angular frequency of 1 rad $s^{-1}$. (e) SEM image of 1 wt% organogel. The organogel sample was dried on the SEM sample disc at room temperature. (f,g) SEM images of Zr-BTB aerogel prepared by freeze-drying of the hydrogel sample, showing a "house of cards" structure. Additional SEM images of the aerogel can be found in the Supplementary Information, **Figure S9b-S9f.**

the completely dried organogels showed wrinkled architectures composed of sheet-like materials (**Figure 2e and Figure S6-S8**), indicating that the morphology of Zr-BTB MONs did not change during centrifugation and solvent evaporation processes.

Rheological measurements were then conducted to study the viscoelastic properties of the gels. The storage modulus (G') and loss modulus (G'') were measured as a function of angular frequency and shear strain for organogels and hydrogels with different Zr-BTB contents (1-2 wt%). At low strain (0.1 %), G' remained approximately one order of magnitude higher than G'' throughout the frequency range (0.5 to 100 rad $s^{-1}$), confirming the formation of a gel state across all samples (**Figure 2b**).[19] When the 1 wt% organogel was subjected to high shear strain (>10%), G' became lower than G'', indicating the gel broke down to display predominantly liquid-like behaviour (**Figure 2c**). At higher concentrations of Zr-BTB only partial breakdown of the gel was observed up to 100% shear strain with both G' and G'' having similar values for the 1.5 wt% organogel (**Figure S10**) and G' remaining higher than G'' for the 2 wt% organogel (**Figure S11**). Interestingly, rapid self-healing of the organogel was observed when the shear strain was alternated between 0.1 and 20% (**Figure S13**), and this self-healing behaviour persisted after three low strain-high strain cycles (**Figure 2d**).

To further investigate the structure of Zr-BTB gels and to minimise the structure change caused by thermal drying, the hydrogel sample was first frozen into a solid and then freeze-dried to form an aerogel (Figure S9a), which was characterised by SEM. As shown in Figure 2f and 2g, the aerogel had a hierarchically porous structure composed of the macropores of the gel and the intrinsic micropores of the Zr-BTB MONs. Interestingly, due to the different orientations of nanosheets in

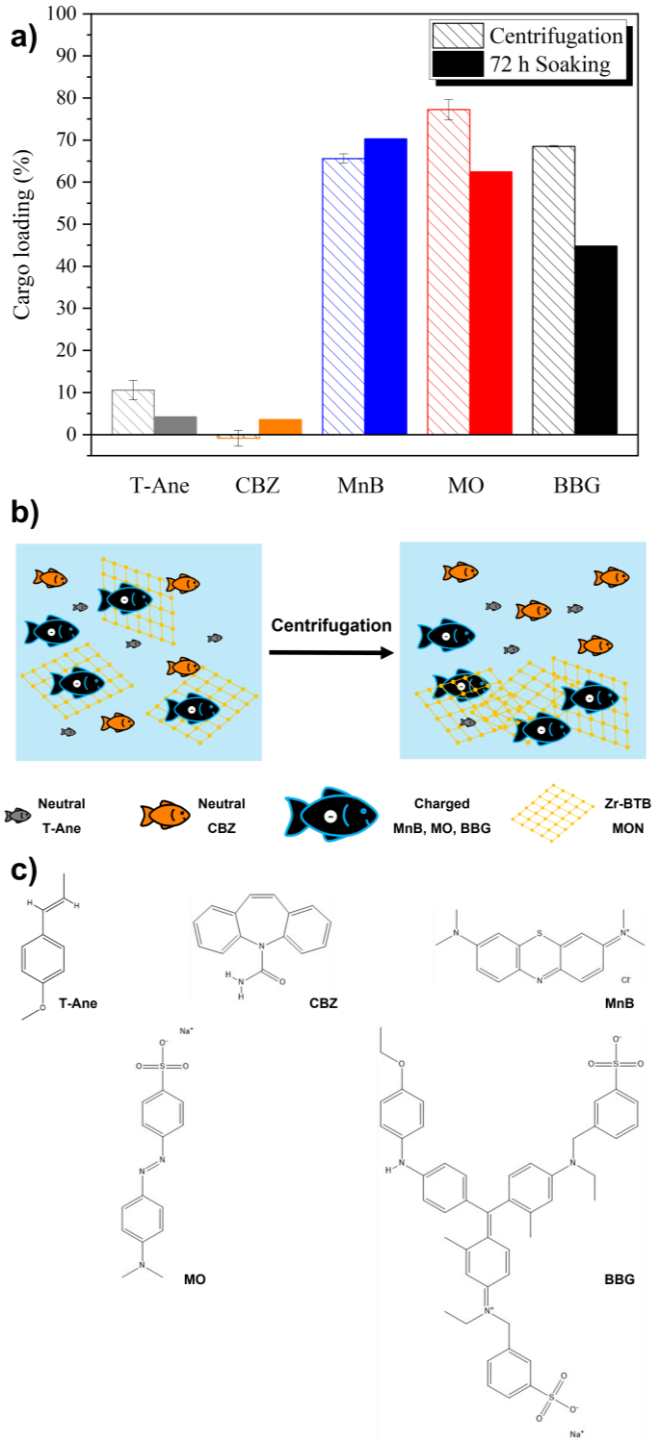


**Figure 3.** (a) UV-Vis results of the cargo loading experiments, comparing the centrifugation method and the soaking method. For the centrifugation method, n = 3 for error bars. The models of T-Ane, CBZ, MnB, MO and BBG can be found in the Supplementary Information, **Figure S36-S40**. (b) Schematic illustration of the selective loading of cargo molecules into Zr-BTB gels using the centrifugation method. Charged cargo molecules showed significantly higher loadings compared to the neutral ones. (c) Chemical structures of cargo molecules.

the aerogel, a structure similar to a "house of cards" was also observed (**Figure 2f,2g and Figure S9b-S9f**) and this structure is commonly observed for nonporous clay nanosheet-based gels.[36, 37]

**Cargo loading experiments.** MOFs[38] and gels[39] have been widely used in drug loading and release applications due to their porous nature and tunable chemistry, but a key limitation of both is the rate at which cargo molecules can be absorbed from solutions. Here, we sought to take advantage of the facile centrifugation method to rapidly load a range of model cargoes into the Zr-BTB gels. Five model cargoes were investigated to understand the effect of charge on cargo loading, including neutral trans-anethole (T-Ane) and carbamazepine (CBZ), charged methylene blue (MnB), methyl orange (MO) and brilliant blue G (BBG, **Figure 3c**).

The cargo loading experiments were conducted by centrifugation of ethanol suspensions containing Zr-BTB MONs and the corresponding cargo molecules. After centrifugation at 4500 rpm for 1 h, the cargo-loaded organogel formed at the bottom of the cuvette (**Figure S14a and S14b**). The concentrations of the cargo solutions before and after the experiment were measured by UV-Vis spectroscopy to calculate the percentage loading, and the results were summarised

in **Figure 3a and Table S3**. The concentrations of the two neutral molecules (T-Ane and CBZ) in solutions were almost unchanged before and after the experiments (**Figure S15 and S16**), indicating low cargo loadings into the gels. Whereas, significantly higher loadings were observed for charged cargo molecules MnB (66%), MO (77%) and BBG (69%, **Figure 3a and Table S3**). This could be attributed to electrostatic interactions between the charged cargo molecules and the nanosheets. As shown in **Table S1**, zeta potential analysis of Zr-BTB MONs showed that they are not neutral, indicating that the MONs have defect-rich structures with both positively and negatively charged sites which could bind to the charged cargo molecules (MnB, MO and BBG, **Figure 3b**), increasing their loadings.

For comparison, a more conventional soaking method was also used, in which the cargo solutions were layered on top of pre-formed Zr-BTB organogels (**Figure S20**). As shown in **Figure 3a and Table S4**, the soaking method took nearly 72 h to achieve comparable loadings to the centrifugation method. Gel formation by centrifugation therefore provides a faster and facile route to load strongly interacting cargo molecules into the Zr-BTB gels by taking advantage of the high surface area of MONs in suspension.

**Cargo release experiments.** MONs have shown great promise for use in separation applications, including gas separation,[40] dye separation[25] and desalination[32]. Their open structure provides well defined channels through which can exclude molecules above a certain size.[41] Their two-dimensional shape also creates a tortuous pathway around which larger molecules must pass interacting with the surface of the nanosheets as they go allowing for differentiation.[41] The nanosheets can be imagined as "fishing nets", which allow some small molecule "fish" to pass through, large molecules to go around, and charged molecules to get temporarily trapped (**Figure 4a**). We hypothesised that these mechanisms might also be harnessed within the "house of cards" gel structure to enable differential release of molecules depending on their size and charge.

In order to test this hypothesis, fresh ethanol was layered on top of Zr-BTB organogels loaded with different cargo molecules (**Figure S26a and S26b**), and the cargo concentrations in ethanol above the

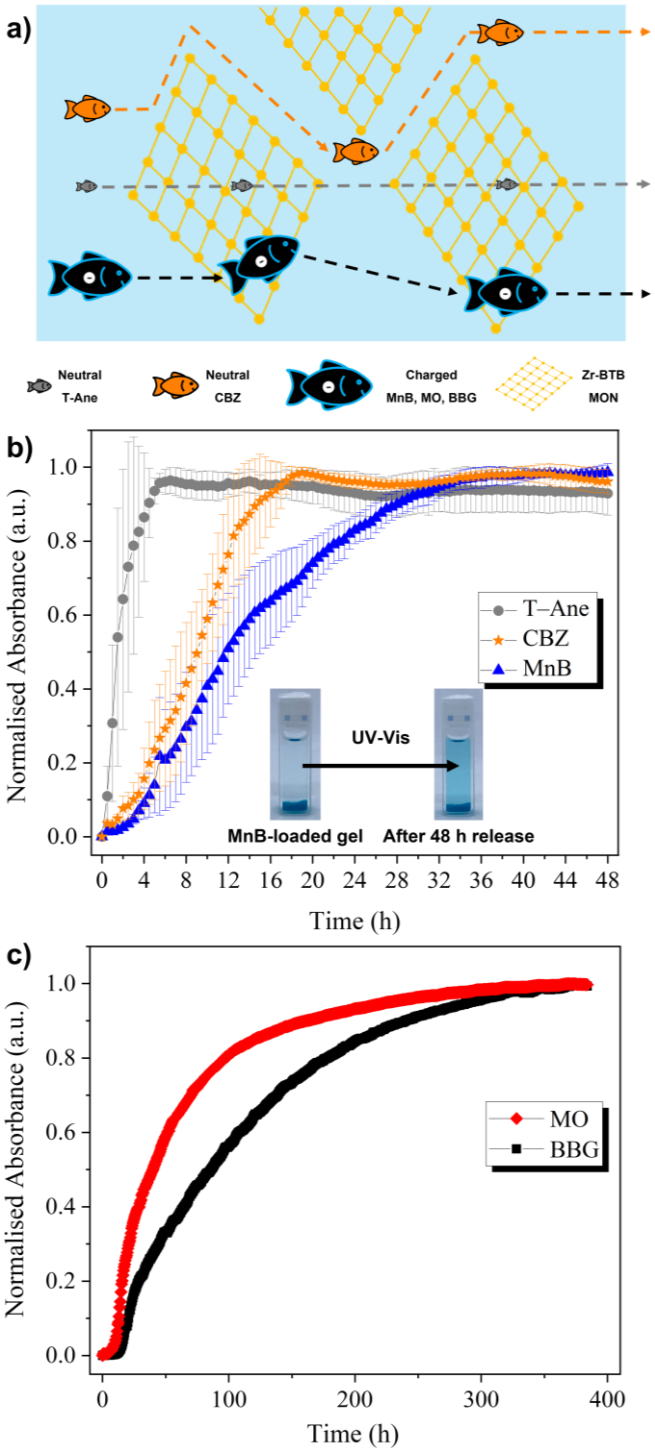


**Figure 4.** (a) Schematic illustration of the "fish and fishing net" hypothesis. Small neutral "fish" are able to pass more easily through the pores of Zr-BTB MONs, larger molecules have to take a more tortuous pathway around nanosheets slowing down their release rates. Charged molecules stick to the nanosheets through electrostatic interactions resulting in even slower release rates. (b) UV-Vis results of T-Ane, CBZ and MnB release experiments, n= 3 for error bars. The inset photos show the MnB-loaded gel before and after the release experiment, the full experiment can be found in the Supplementary Information, **Figure S26a and S26b**. (c) UV-Vis results of MO and BBG release experiments.

gel were monitored by UV-Vis spectroscopy over time (**Figure S28-S32**). As shown in **Figure 4b**, the T-Ane showed the fastest release rate among the five cargo molecules, its concentration reached equilibrium after 6 h, whereas the concentration of CBZ in ethanol took around 18 h to reach equilibrium.

No significant absorption was observed for T-Ane and CBZ in the cargo loading experiments, indicating that there were only weak interactions between the two neutral cargo molecules and the Zr-BTB MONs. The reported pore size of Zr-BTB in the literature is approximately 0.54 nm,[42] larger than the calculated width of T-Ane at 0.43 nm (**Figure S36**), but smaller than the width of CBZ at 0.67 nm (**Figure S37**). Based on the release profiles and taken into account differences in molecular weights (**Table S5**), the distance of diffusion for CBZ was calculated to be approximately 1.1 cm, longer than the 0.73 cm distance calculated for T-Ane. These results therefore broadly support our "fish and fishing net" hypothesis with T-Ane molecules small enough to be able to pass through the pores of Zr-BTB MONs allowing them to take more direct and shorter diffusion pathways, whereas larger CBZ molecules have to pass around the nanosheets, so took more tortuous and longer diffusion pathways when they were released from the gels (**Figure 4a**).

The release rates of charged cargo molecules were significantly slower than the neutral ones. As shown in **Figure 4b**, the concentration of positively charged MnB levels off after around 34 h, almost double the release time of CBZ. Moreover, the two negatively charged cargo molecules (MO and BBG) required approximately two weeks to reach their concentration equilibria (**Figure 4c**). This could be attributed to electrostatic interactions between the charged cargo molecules and the Zr-BTB MONs. The defect-rich nanosheets have both positively charged and negatively charged sites which could bind to the charged cargo molecules, increasing their absorptions and loadings, but resulting in their slower release rates compared to the neutral ones. Therefore, in the "fish and fishing net" hypothesis (**Figure 4a**), the much longer release time of charged cargo molecules can be explained by the "charged fishes" sticking to the "fishing nets".

## Conclusions

In this work, we showed how suspensions of MONs can be centrifuged to form hierarchically porous gels able to differentially absorb and release molecules based on their size and charge. Monolayer Zr-BTB nanosheets were shown to form both organogels and hydrogels through a facile centrifugation process and their self-healing rheology and "house of cards" structure were characterised for the first time. The structure and properties of the Zr-BTB gels are similar to those seen for clay nanosheet-based gels, but with the addition of the intrinsic micropores of Zr-BTB MONs alongside the macropores of the gels. Rapid and uniform loading of cargo molecules into the gels was achieved by harnessing the high surface area of the nanosheets in suspension, then centrifuging to trigger gel formation. Molecular cargo was found to diffuse out of the gels at very different rates (from 6 h to about 2 weeks), which was attributed to the different diffusion pathways available to

different molecules depending on their size and charge. Neutral molecules small enough to pass through the pores of Zr-BTB MONs diffused more rapidly out of the gel, whereas larger molecules had to take a more tortuous diffusion pathway around the nanosheets. Both positively and negatively charged cargo molecules stuck to the surface of the defect-rich Zr-BTB MONs, resulting in their slow release rates compared to the neutral ones.

We anticipate that our rapid and facile centrifugation approach will enable the formation of gels from a wide range of other nanosheets. Moreover, the unique combination of intrinsic porosity and high surface area brought about by using MONs to form gels will open up new opportunities for a variety of applications, including sensing, separation, controlled release, drug loading and drug delivery.

## Experimental

**General considerations.** All chemicals and solvents were obtained from commercial suppliers and used without any purification. Details of all equipment used and material characterisations can be found in the Supplementary Information.

**Preparation of Zr-BTB MONs.** Zr-BTB MONs were prepared according to the solvothermal method reported by Zhao and co-workers.[29] $ZrCl_4$ (0.129 mmol) and $H_3BTB$ (0.068 mmol) were dissolved in a mixture of HCOOH (2 mL), deionised water (2 mL) and DMF (15 mL) in a reaction vial. The vial was placed in a reaction oven at 120 °C for 24 h, and the resulting suspension of Zr-BTB MONs was centrifuged and washed three times with fresh DMF then ethanol. The washed MONs were stored in fresh ethanol as a homogeneous suspension with a concentration of 2.5 mg $mL^{-1}$ until needed.

**Preparation of organogel and hydrogel by centrifugation.** The organogel was prepared by centrifuging the ethanol suspension of Zr-BTB MONs (10 mL, 2.5 mg $mL^{-1}$) at 4500 rpm for 1 h, and the organogel formed at the bottom of the centrifuge tube after centrifugation.

For the preparation of Zr-BTB hydrogel, the ethanol suspension of Zr-BTB MONs was centrifuged and then washed four times with deionised water. The washed MONs were dispersed in fresh deionised water with a concentration of 2.5 mg $mL^{-1}$. The aqueous suspension of Zr-BTB MONs (10 mL) was then centrifuged at 4500 rpm for 1 h, and the hydrogel formed at the bottom of the centrifuge tube after centrifugation.

**Preparation of aerogel.** To prepare the aerogel, the hydrogel sample was first frozen into a solid at -80 °C, and then freeze-dried using a 'Lablyo Mini' freeze dryer at -50 °C to form an aerogel.

**Preparation of organogel by solvent evaporation.** The ethanol suspension of Zr-BTB MONs (10 mL, 2.5 mg $mL^{-1}$) was added into a glass vial, which was then heated at 80 °C using a hot plate to slowly remove the solvent from the organogel. The content of Zr-BTB MONs in the organogel was carefully checked every 15 minutes (**Figure S4**).

**Cargo loading experiments.** 2.5 mL of MnB ethanol solution was added into a cuvette and its concentration was measured by UV-Vis spectroscopy. Then, the ethanol suspension of Zr-BTB MONs (0.5 mL, 2.5 mg $mL^{-1}$) was added into the cuvette and mixed with the MnB solution. The cuvette was then fixed in a centrifuge tube and centrifuged at 4500 rpm for 1 h. After centrifugation, the concentration of MnB in the supernatant was measured again by UV-Vis spectroscopy. The cargo loading experiments was conducted at room temperature and repeated three times. The T-Ane, CBZ, MO and BBG loading experiments were conducted using the same method as the MnB loading experiment. Details of the cargo loading experiments (centrifugation method) can be found in the Supplementary Information, **S3.2**.

Details of the cargo loading experiments (soaking method) can be found in the Supplementary Information, **S3.3**.

The concentrations of T-Ane, CBZ, MnB, MO and BBG solutions for the cargo loading experiments can be found in **Table S2**.

**Cargo release experiments.** 1.5 mL of MnB solution was mixed with the ethanol suspension of Zr-BTB MONs (0.5 mL, 2.5 mg $mL^{-1}$) in a cuvette. The cuvette was then fixed in a centrifuge tube and centrifuged at 4500 rpm for 1 h. After centrifugation, the MnB-loaded gel formed at the bottom of the cuvette and the supernatant was removed. 2.5 mL of fresh ethanol was then carefully layered on top of the gel, and the cuvette was centrifuged at 4500 rpm for 10 mins. After centrifugation, the cuvette was placed in a UV-Vis equipment for 48 h, and the UV-Vis spectrum was recorded every 30 minutes at room temperature and the MnB release experiment was repeated 3 times. The T-Ane and CBZ release experiments were conducted using the same method as the MnB release experiment.

The release rates of MO and BBG from the gels were slower than the release rates of T-Ane, CBZ and MnB. Therefore, the MO and BBG release experiments were conducted for a longer period of time (384 h) and were only conducted once.

Details of the cargo release experiments can be found in the Supplementary Information, **S3.4**. The concentrations of T-Ane, CBZ, MnB, MO and BBG solutions for the cargo release experiments can be found in **Table S2**.

## Conflicts of interest

There are no conflicts to declare.

## Acknowledgements

Thanks to Christopher J Hill for the SEM characterisations of the aerogel.

## References

1. J. A. Foster, R. M. Parker, A. M. Belenguer, N. Kishi, S. Sutton, C. Abell and J. R. Nitschke, *J. Am. Chem. Soc.*, 2015, **137**, 9722–9729.
2. Y. Yang, Q. Zhu, X. Peng, J. Sun, C. Li, X. Zhang, H. Zhang, J. Chen, X. Zhou, H. Zeng and Y. Zhang, *Environ. Chem. Lett.*, 2022, **20**, 2665-2685.
3. J. Li and D. J. Mooney, *Nat. Rev. Mater.*, 2016, **1**, 16071.

4. R. A. Ramli, *Polym. Chem.*, 2019, **10**, 6073-6090.
5. Z. Yuan, J. Ding, Y. Zhang, B. Huang, Z. Song, X. Meng, X. Ma, X. Gong, Z. Huang, S. Ma, S. Xiang and W. Xu, *Eur. Polym. J.*, 2022, **177**, 111473.
6. D. Bokov, A. Turki Jalil, S. Chupradit, W. Suksatan, M. Javed Ansari, I. H. Shewael, G. H. Valiev, E. Kianfar and Z. Wang, *Adv. Mater. Sci. Eng.*, 2021, **2021**, 5102014.
7. M. Ghadiri, W. Chrzanowski, W. H. Lee and R. Rohanizadeh, *RSC Adv.*, 2014, **4**, 35332-35343.
8. J. D. Mangadlao, K. J. Lim, C. Danda, M. L. Dalida and R. C. Advincula, *Macromol. Mater. Eng.*, 2018, **303**, 1700314.
9. J. K. Wychowaniec, H. Saini, B. Scheibe, D. P. Dubal, A. Schneemann and K. Jayaramulu, *Chem. Soc. Rev.*, 2022, **51**, 9068-9126.
10. J. Hou, A. F. Sapnik and T. D. Bennett, *Chem. Sci.*, 2020, **11**, 310-323.
11. K. Sumida, K. Liang, J. Reboul, I. A. Ibarra, S. Furukawa and P. Falcaro, *Chem. Mater.*, 2017, **29**, 2626-2645.
12. H. Zhu, X. Yang, E. D. Cranston and S. Zhu, *Adv. Mater.*, 2016, **28**, 7652-7657.
13. T. Ishiwata, Y. Furukawa, K. Sugikawa, K. Kokado and K. Sada, *J. Am. Chem. Soc.*, 2013, **135**, 5427-5432.
14. Y. Furukawa, T. Ishiwata, K. Sugikawa, K. Kokado and K. Sada, *Angew. Chem. Int. Ed.*, 2012, **51**, 10566-10569.
15. E. C. Vermisoglou, P. Jakubec, O. Malina, V. Kupka, A. Schneemann, R. A. Fischer, R. Zboril, K. Jayaramulu and M. Otyepka, *Front. Chem.*, 2020, **8**, 544.
16. W. Xia, B. Qiu, D. Xia and R. Zou, *Sci. Rep.*, 2013, **3**, 1935.
17. A. Mahmood, W. Xia, N. Mahmood, Q. Wang and R. Zou, *Sci. Rep.*, 2015, **5**, 10556.
18. Y. Ma, A. Li, X. Gao, F. Huang, X. Kuang, P. Yang, J. Yue and B. Tang, *Macromol. Rapid Commun.*, 2019, **40**, 1800862.
19. V. Somjit, P. Thinsoongnoen, S. Waiprasoet, T. Pila, P. Pattanasattayavong, S. Horike and K. Kongpatpanich, *ACS Appl. Mater. Interfaces*, 2021, **13**, 30844-30852.
20. T. Tian, Z. Zeng, D. Vulpe, M. E. Casco, G. Divitini, P. A. Midgley, J. Silvestre-Albero, J. C. Tan, P. Z. Moghadam and D. Fairen-Jimenez, *Nat. Mater.*, 2018, **17**, 174-179.
21. G. J. H. Lim, Y. Wu, B. B. Shah, J. J. Koh, C. K. Liu, D. Zhao, A. K. Cheetham, J. Wang and J. Ding, *ACS Materials Lett.*, 2019, **1**, 147-153.
22. S. M. F. Vilela, P. Salcedo-Abraira, L. Micheron, E. L. Solla, P. G. Yot and P. Horcajada, *Chem. Commun.*, 2018, **54**, 13088-13091.
23. D. J. Ashworth and J. A. Foster, *J. Mater. Chem. A*, 2018, **6**, 16292-16307.
24. J. Nicks, K. Sasitharan, R. R. R. Prasad, D. J. Ashworth and J. A. Foster, *Adv. Funct. Mater.*, 2021, **31**, 2103723.
25. H. Ang and L. Hong, *ACS Appl. Mater. Interfaces*, 2017, **9**, 28079-28088.
26. Y. Peng, Y. Li, Y. Ban, H. Jin, W. Jiao, X. Liu and W. Yang, *Science*, 2014, **346**, 1356-1359.
27. G.-Y. Qiao, S. Yuan, J. Pang, H. Rao, C. T. Lollar, D. Dang, J.-S. Qin, H.-C. Zhou and J. Yu, *Angew. Chem. Int. Ed.*, 2020, **59**, 18224–18228.
28. Z. Hu, E. M. Mahdi, Y. Peng, Y. Qian, B. Zhang, N. Yan, D. Yuan, J.-C. Tan and D. Zhao, *J. Mater. Chem. A*, 2017, **5**, 8954-8963.
29. H. Yuan, G. Liu, Z. Qiao, N. Li, P. J. S. Buenconsejo, S. Xi, A. Karmakar, M. Li, H. Cai, S. J. Pennycook and D. Zhao, *Adv. Mater.*, 2021, **33**, 2101257.
30. X. Feng, Y. Ren, H. Wang, W. Wu and H. Jiang, *Catal. Sci. Technol.*, 2023, **13**, 7036-7045.
31. D. Zhan, Z. Yu, A. Saeed, Q. Hu, N. Zhao, W. Xu, J. Wang, L. Kong and J. Liu, *J. Mater. Chem. C*, 2023, **11**, 10738-10747.
32. H. Yuan, K. Li, D. Shi, H. Yang, X. Yu, W. Fan, P. J. S. Buenconsejo and D. Zhao, *Adv. Mater.*, 2023, **35**, e2211859.
33. Y. Cheng, S. R. Tavares, C. M. Doherty, Y. Ying, E. Sarnello, G. Maurin, M. R. Hill, T. Li and D. Zhao, *ACS Appl. Mater. Interfaces*, 2018, **10**, 43095-43103.
34. X. Feng, Y. Song and W. Lin, *J. Am. Chem. Soc.*, 2021, **143**, 8184-8192.
35. B. Bueken, N. Van Velthoven, T. Willhammar, T. Stassin, I. Stassen, D. A. Keen, G. V. Baron, J. F. M. Denayer, R. Ameloot, S. Bals, D. De Vos and T. D. Bennett, *Chem. Sci.*, 2017, **8**, 3939-3948.
36. S. Afewerki, L. Magalhaes, A. D. R. Silva, T. D. Stocco, E. C. Silva Filho, F. R. Marciano and A. O. Lobo, *Adv. Healthcare Mater.*, 2019, **8**, e1900158.
37. H. Z. Cummins, *J. Non-Cryst. Solids*, 2007, **353**, 3891-3905.
38. H. Molavi, H. Moghimi and R. A. Taheri, *Appl. Organometal. Chem.* , 2020, **34**, e5549.
39. Q. Wang, S. Li, Z. Wang, H. Liu and C. Li, *J. Appl. Polym. Sci.*, 2008, **111**, 1417-1425.
40. Y. Peng, Y. Li, Y. Ban and W. Yang, *Angew. Chem. Int. Ed.*, 2017, **56**, 9757-9761.
41. Y. Peng and W. Yang, *Adv. Mater. Interfaces*, 2019, **7**, 1901514.
42. Y. Pu, Z. Yang, V. Wee, Z. Wu, Z. Jiang and D. Zhao, *J. Membr. Sci.*, 2022, **641**, 119912.

## Supplementary Information

# Metal-organic nanosheet gels-hierarchically porous materials for selective loading and differential release

Jiangtian Tan[a] and Jonathan A. Foster*[a]

[a]*Department of Chemistry, University of Sheffield, Sheffield, UK.*

**Table of contents**

## S1. Equipment and Software

### S1.1. Atomic force microscopy

Atomic force microscopy (AFM) images were recorded using a Bruker Multimode 5 Atomic Force Microscope, operating in soft-tapping mode in air under standard ambient temperature and pressure, fitted with Bruker OTESPA-R3 silicon cantilevers. Samples were prepared by drop-casting 10 µL of diluted ethanol suspension of Zr-BTB metal-organic nanosheets (MONs) onto the centre of freshly cleaved mica sheets heated to 120 °C on a hot plate. These mica sheets were stuck to stainless steel, magnetic Agar scanning probe microscopy specimen discs. All AFM images reported in this work were processed using Gwyddion software.

### S1.2. Gas sorption measurements

Gas sorption measurements to determine BET surface area were performed using a Micromeritics ASAP 2020 Plus analyser employing nitrogen gas under 77 K. 0.0646 g of sample was degassed under dynamic vacuum prior to gas sorption measurements.

### S1.3. Powder X-ray diffraction

Powder X-ray diffraction (PXRD) data of the Zr-BTB MONs were collected using a Bruker-AXS D8 diffractometer using Cu Kα (λ=1.5418 Å) radiation and a LynxEye position sensitive detector in Bragg Brentano parafocussing geometry using a flat silicon plate.

### S1.4. Rheological measurements

Rheological measurements of the Zr-BTB organogels and hydrogel were conducted using an Anton Paar MCR 502 rotational rheometer under 25 ℃. Measuring plate PP25/TG was used for all rheological measurements.

### S1.5. Scanning electron microscopy

Scanning electron microscopy (SEM) samples were prepared by loading dried Zr-BTB MONs or gels onto carbon sticky tabs placed on aluminium SEM sample stubs, coated with gold using an Edwards S150B gold sputter coater and loaded into a TESCAN VEGA3 LMU SEM. All SEM images reported in this work were collected using the secondary electron detector.

**S1.6. Ultraviolet-visible spectroscopy**

Ultraviolet-visible (UV-Vis) absorption spectra were collected on a Cary 60 UV-Vis instrument, using a 1 cm internal length quartz cuvette. Cary WinUV, Scanning Kinetics software was used for cargo release experiment, blank experiment, and cargo loading experiments (soaking method), and the UV-Vis spectrum was recorded every 30 minutes at room temperature. Cary WinUV, Scan software was used for cargo loading experiment (centrifugation method), and the UV-Vis spectra was recorded at room temperature.

**S1.7. Zeta potential and dynamic light scattering**

Zeta potential data of Zr-BTB MONs were collected using a Malvern ZETA SIZER Nano series instrument, operating in the zeta potential mode, using DTS1070, Disposable folded capillary cell and according to the Smoluchowski method, and the temperature for zeta potential experiment was set to 20 °C. Dynamic light scattering (DLS) data were collected with the same instrument, using a He-Ne laser at 633 nm, operating in backscatter mode (173 °). A polystyrene disposable cuvette was used for DLS experiment and the temperature for DLS experiment was set to 25 °C.

## S2. Zr-BTB MONs and Gels

**Table S1.** Zeta potential data of Zr-BTB MONs.

| Sample name | Temperature (°C) | Zeta potential (mV) | Zeta deviation (mV) | Mobility (μmcm $Vs^{-1}$) | Conductivity (mS $cm^{-1}$) |
|---|---|---|---|---|---|
| Zr-BTB | 20 | -52.6 | 140 | -0.079 | 0.007 |
| Zr-BTB | 20 | -64.7 | 141 | -0.098 | 0.022 |
| Zr-BTB | 20 | -65.2 | 143 | -0.099 | 0.007 |
| | **Average:** | -60.8 | 141 | -0.092 | 0.012 |
| | **Solvent:** | Ethanol | | | |

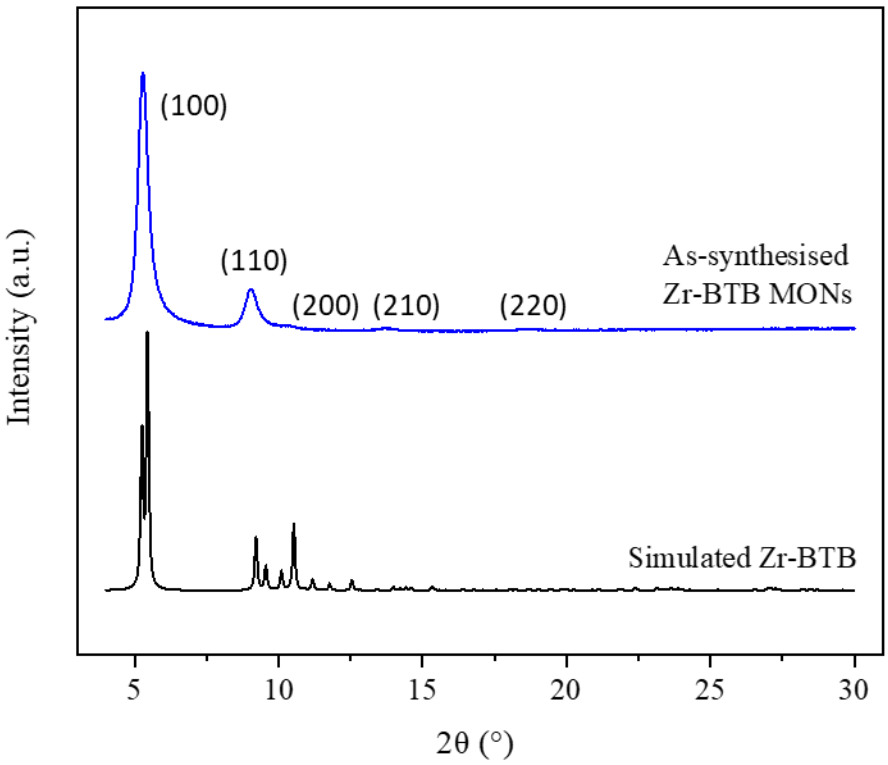


**Figure S1.** PXRD pattern of the as-synthesised Zr-BTB MONs, comparing with the simulated pattern of Zr-BTB.

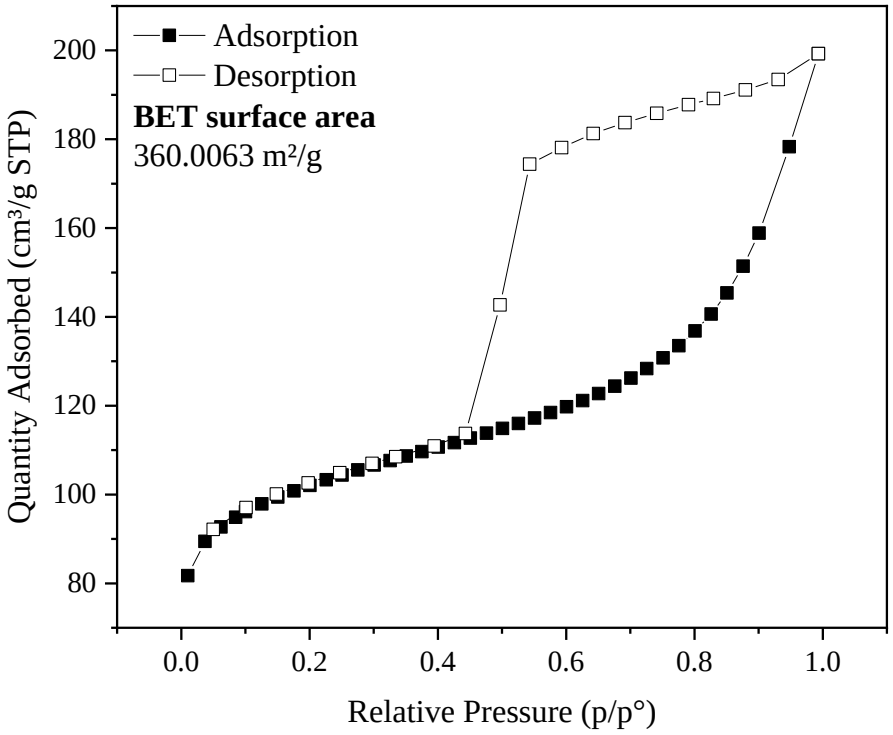


**Figure S2.** $N_2$ sorption isotherm of Zr-BTB MONs at 77 K.

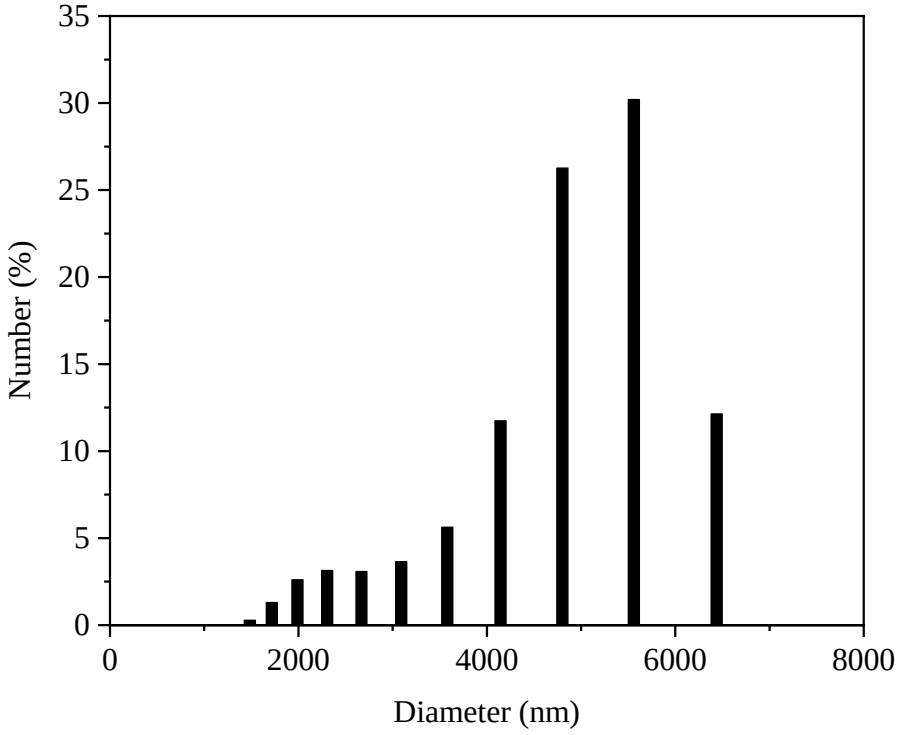


**Figure S3.** DLS graph showing particle size distribution of Zr-BTB MONs.

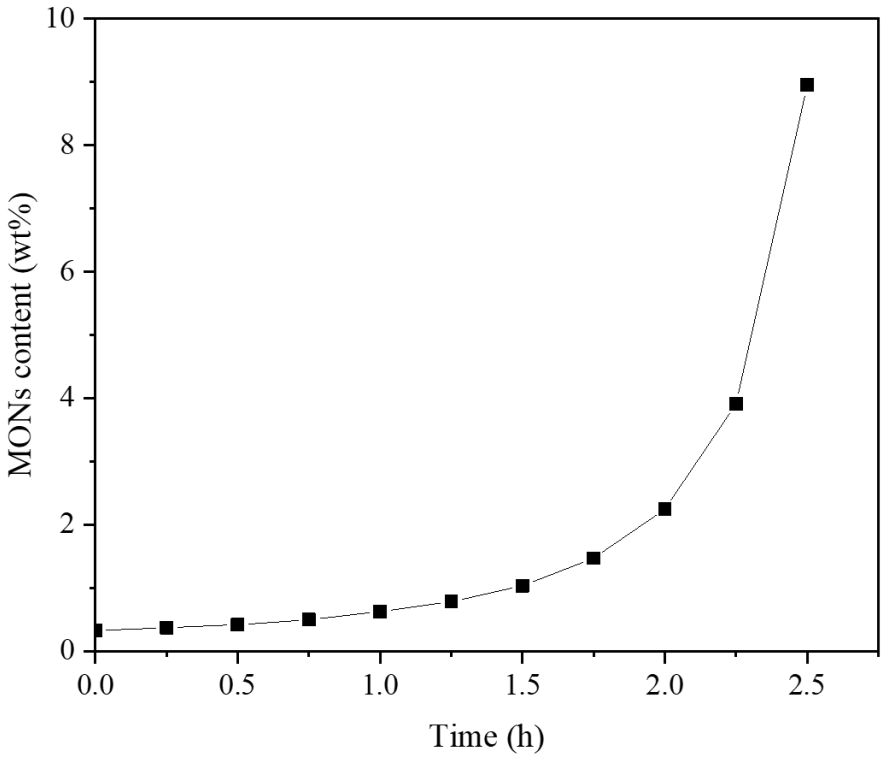


**Figure S4.** Preparation of organogel by solvent evaporation. The plot shows the increase of Zr-BTB MONs content in the organogel over time.

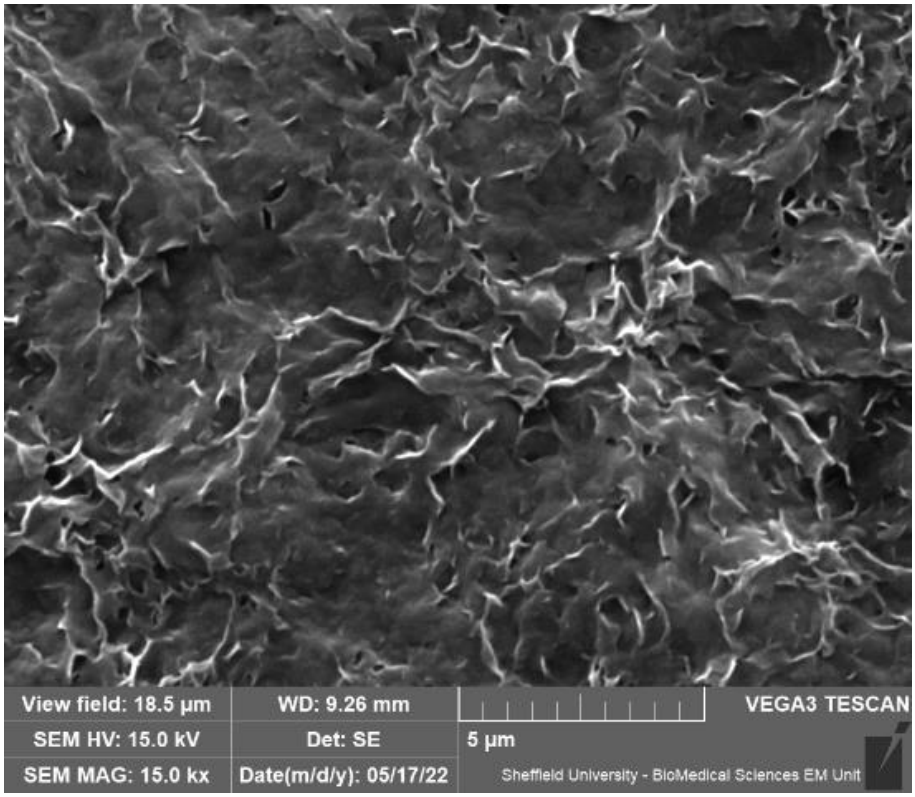


**Figure S5.** SEM image of the Zr-BTB MONs.

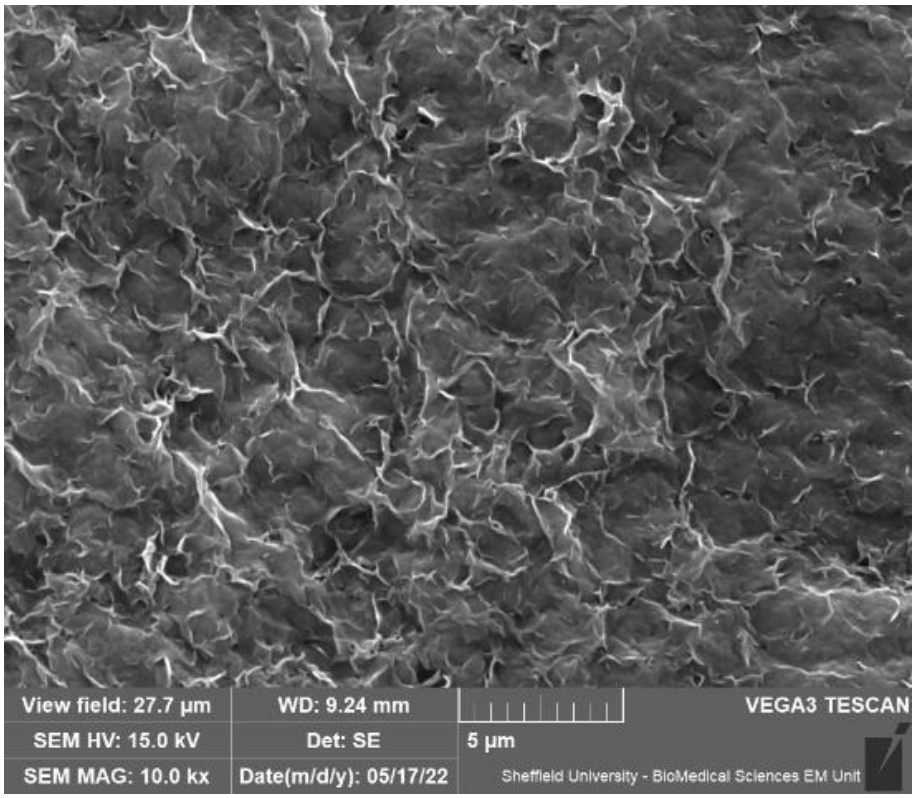


**Figure S6.** SEM image of the 2 wt% organogel. The gel was dried at room temperature to prepare the SEM sample.

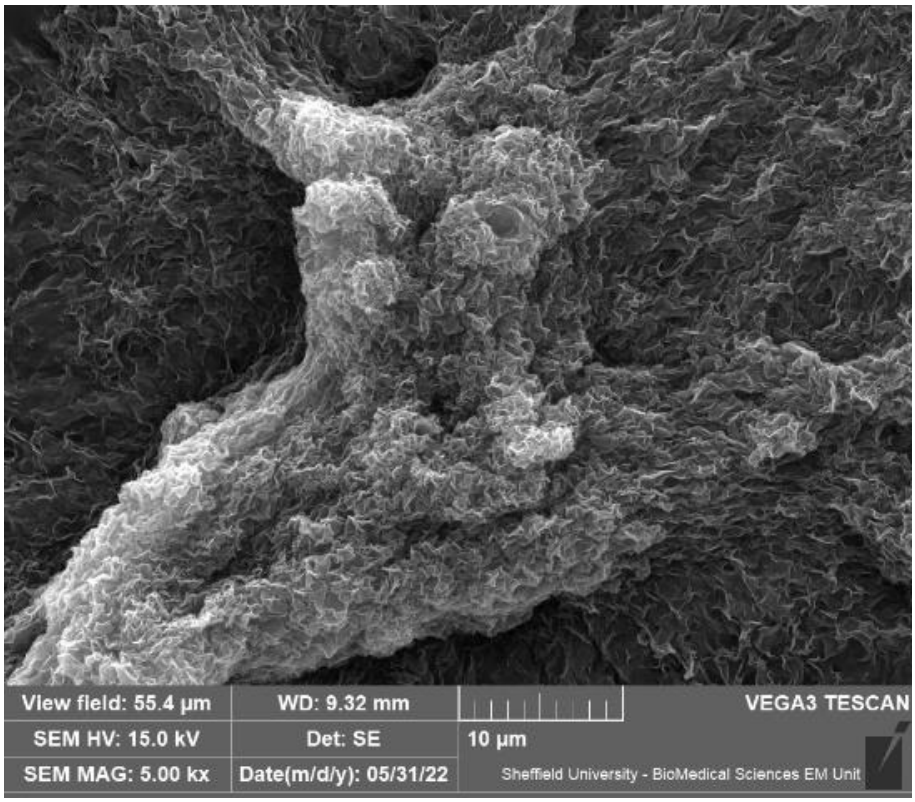


**Figure S7.** SEM image of the 1.5 wt% organogel. The gel was dried at room temperature to prepare the SEM sample.

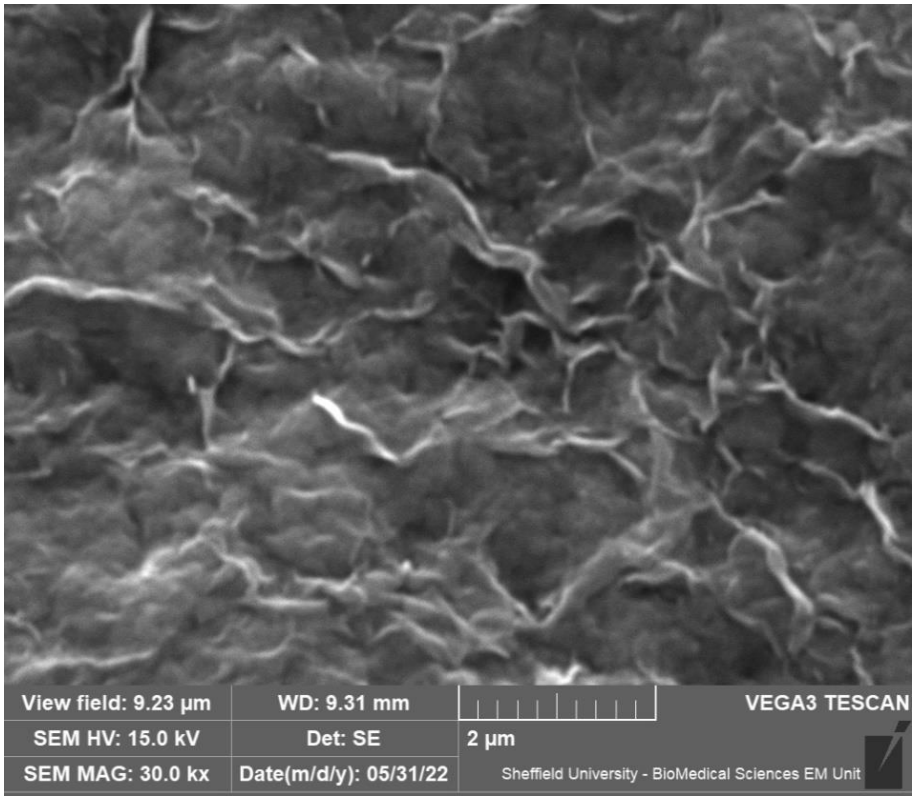


**Figure S8.** SEM image of the 1.5 wt% hydrogel. The gel was dried at room temperature to prepare the SEM sample.

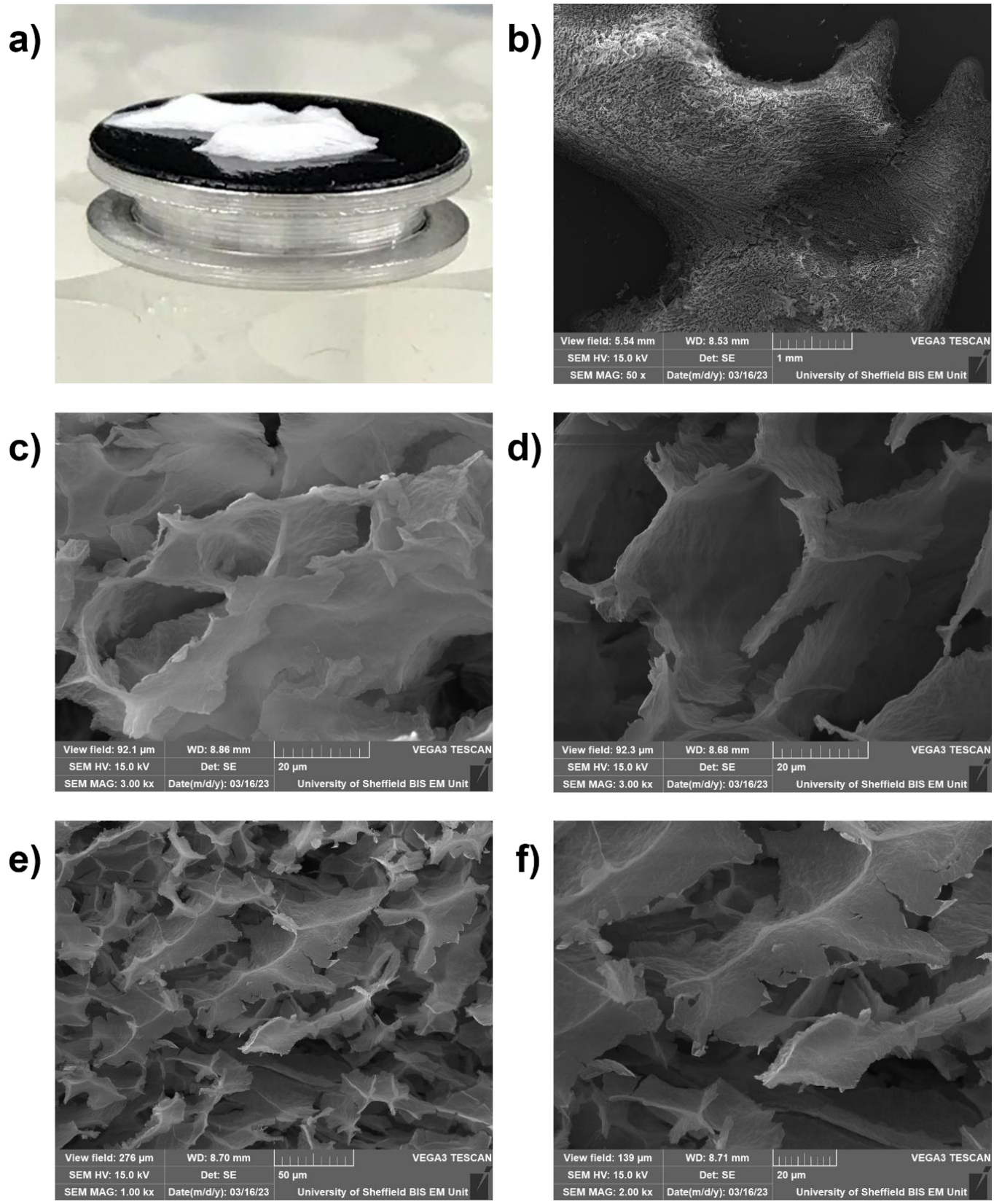


**Figure S9.** (a) Photograph of the Zr-BTB aerogel. (b-f) SEM images of the Zr-BTB aerogel.

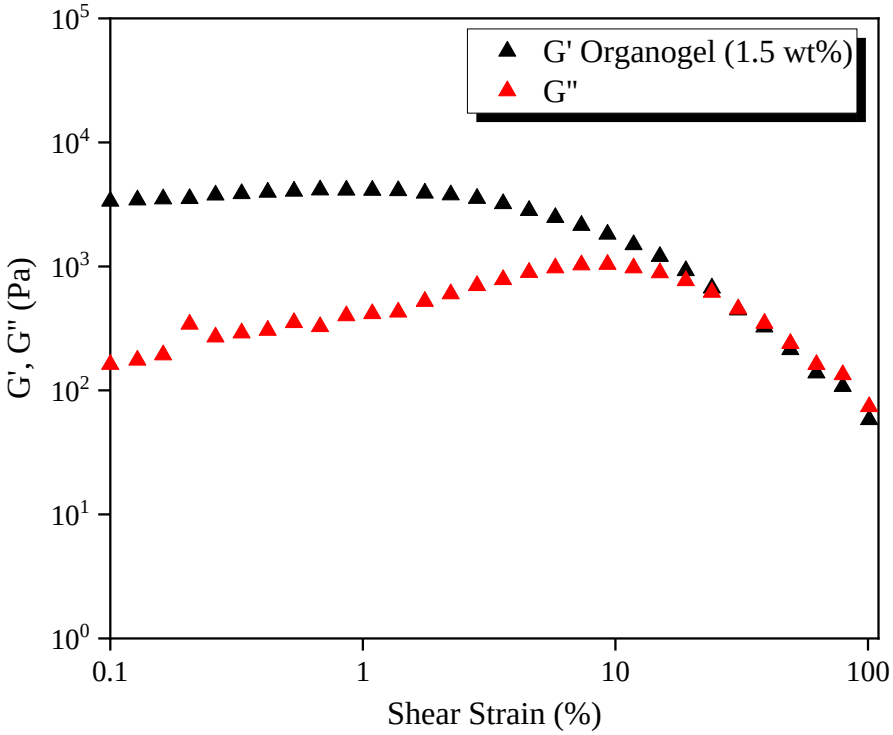


**Figure S10.** Strain-sweep rheological measurements of the 1.5 wt% organogel with fixed angular frequency of 1 rad $s^{-1}$.

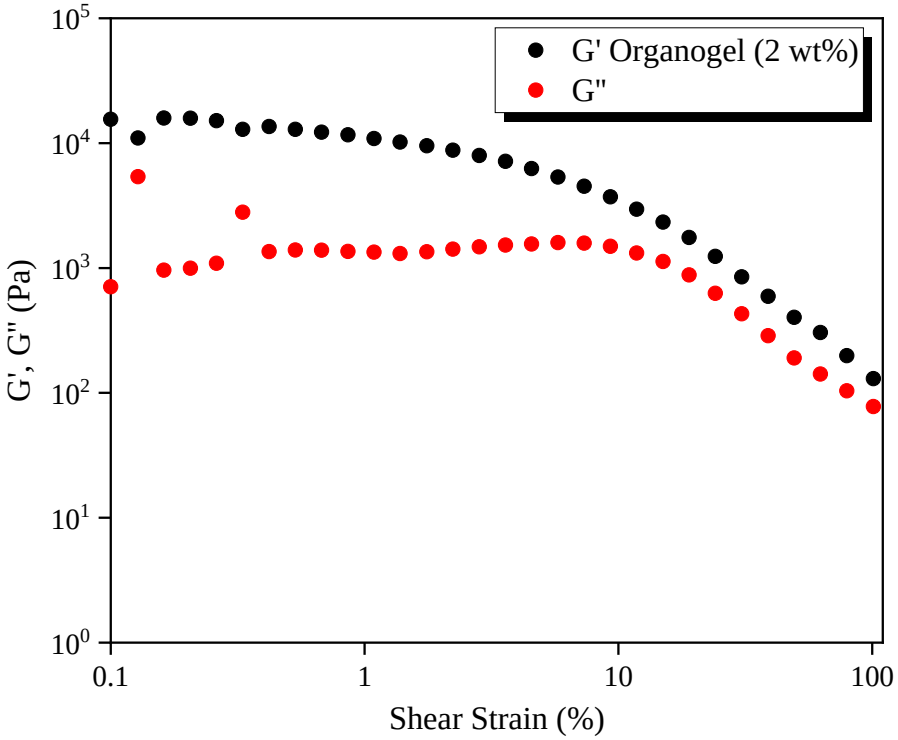


**Figure S11.** Strain-sweep rheological measurements of the 2 wt% organogel with fixed angular frequency of 1 rad $s^{-1}$.

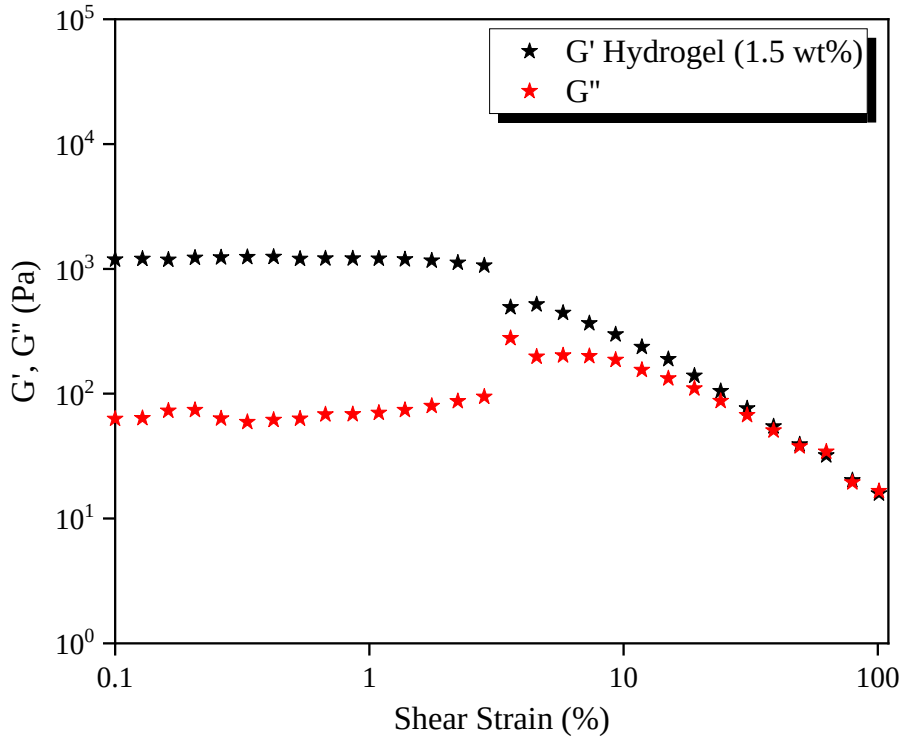


**Figure S12.** Strain-sweep rheological measurements of the 1.5 wt% hydrogel with fixed angular frequency of 1 rad $s^{-1}$.

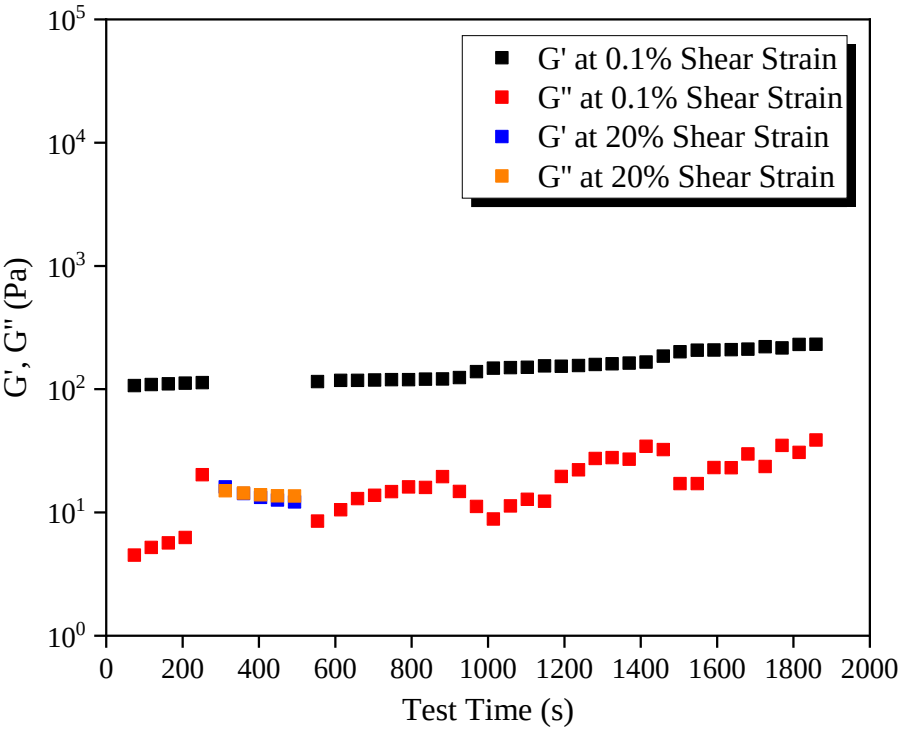


**Figure S13.** Rheological measurements of the 1 wt% organogel at different shear strains showing its self-healing behaviour. This rheological experiment was conducted with fixed angular frequency of 1 rad $s^{-1}$.

## S3. Cargo Loading and Release

### S3.1. Cargo solutions

**Table S2.** Concentrations of trans-anethole (T-Ane), carbamazepine (CBZ), methylene blue (MnB), methyl orange (MO) and brilliant blue G (BBG) solutions for the cargo loading and release experiments.

| Experiment | Concentration of T-Ane, CBZ and MnB* ($\mu mol\ mL^{-1}$) | Concentration of MO* ($\mu mol\ mL^{-1}$) | Concentration of BBG* ($\mu mol\ mL^{-1}$) |
|---|---|---|---|
| Cargo loading (centrifugation method) | 0.0097 | 0.0091 | 0.0095 |
| Cargo loading (soaking method) | 0.0073 | 0.0068 | 0.0071 |
| Cargo release | 0.0587 | 0.0545 | 0.0571 |

*Ethanol solutions of T-Ane, CBZ, MnB, MO and BBG were used for the cargo loading (centrifugation method), cargo loading (soaking method) and cargo release experiments.

### S3.2. Cargo loading experiment (centrifugation method)

As shown in **Figure S14a**, 2.5 mL of MnB solution was added into a cuvette and was measured by UV-Vis. The recorded absorbance was denoted as MnB-before (**Figure S17**). Then 0.5 mL of ethanol suspension of Zr-BTB MONs (2.5 mg $mL^{-1}$) was added into the cuvette and was mixed with the MnB solution. The cuvette was then fixed in a centrifuge tube and centrifuged at 4500 rpm for 1 hour. After centrifugation, the MnB-loaded gel formed at the bottom of the cuvette (**Figure S14b**), and the concentration of MnB in the supernatant was measured by UV-Vis, and the recorded absorbance was denoted as MnB-after (**Figure S17**). The MnB loading experiment was conducted at room temperature and was repeated three times. The T-Ane, CBZ, MO and BBG loading experiments were conducted using the same method as the MnB loading experiment. The concentrations of T-Ane, CBZ, MnB, MO and BBG solutions for the cargo loading experiments (centrifugation method) can be found in **Table S2**.

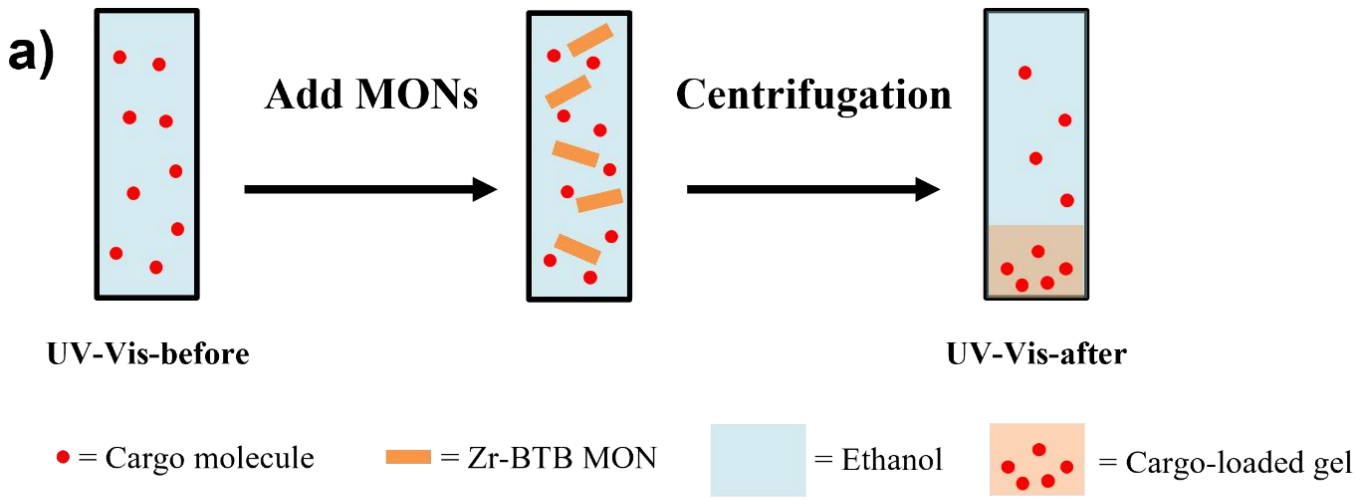


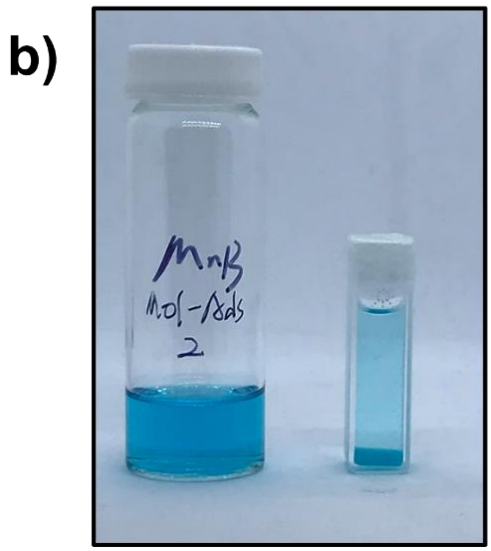


**Figure S14.** (a) Schematic illustration of the cargo loading experiment (centrifugation method). (b) Photograph of the MnB solution before (left) and after (right) the cargo loading experiment (centrifugation method). The MnB-loaded gel formed at the bottom of the cuvette after centrifugation.

**Table S3.** Summary of the results of the T-Ane, CBZ, MnB, MO and BBG loading experiments (centrifugation method).

| Experiment | Absorbance before centrifugation[a] (a.u.) | Absorbance after centrifugation[a] (a.u.) | Cargo loading centrifugation[b] (%) |
|---|---|---|---|
| T-Ane | 0.3304 | 0.2921 | 11.5986 |
| T-Ane | 0.3222 | 0.2966 | 7.9237 |
| T-Ane | 0.3426 | 0.3007 | 12.2274 |
| | | **Average loading (T-Ane)** | 10.5832 |
| CBZ | 0.1732 | 0.1760 | -1.6094 |
| CBZ | 0.1557 | 0.1593 | -2.2574 |
| CBZ | 0.1631 | 0.1610 | 1.2952 |
| | | **Average loading (CBZ)** | -0.8572 |
| MnB | 1.1886 | 0.3968 | 66.6194 |
| MnB | 1.1896 | 0.4067 | 65.8143 |
| MnB | 1.1888 | 0.4231 | 64.4099 |
| | | **Average loading (MnB)** | 65.6145 |
| MO | 0.2601 | 0.0665 | 74.4505 |
| MO | 0.2482 | 0.0543 | 78.1209 |
| MO | 0.2567 | 0.0537 | 79.0919 |
| | | **Average loading (MO)** | 77.2211 |
| BBG | 0.5849 | 0.1828 | 68.7405 |
| BBG | 0.5833 | 0.1847 | 68.3312 |
| BBG | 0.5829 | 0.1834 | 68.5392 |
| | | **Average loading (BBG)** | 68.5370 |

[a]The absorbance values are measured from the UV-Vis spectra at $\lambda_{max}$ (**Figure S15-S19**).

[b]The T-Ane, CBZ, MnB, MO and BBG loadings of the centrifugation method are calculated by **eq S1**.

$$\textbf{Cargo loading centrifugation} = \frac{\textbf{Absorbance before centrifugation} - \textbf{Absorbance after centrifugation}}{\textbf{Absorbance before centrifugation}} \times \mathbf{100}\% \qquad \text{(equation S1)}$$

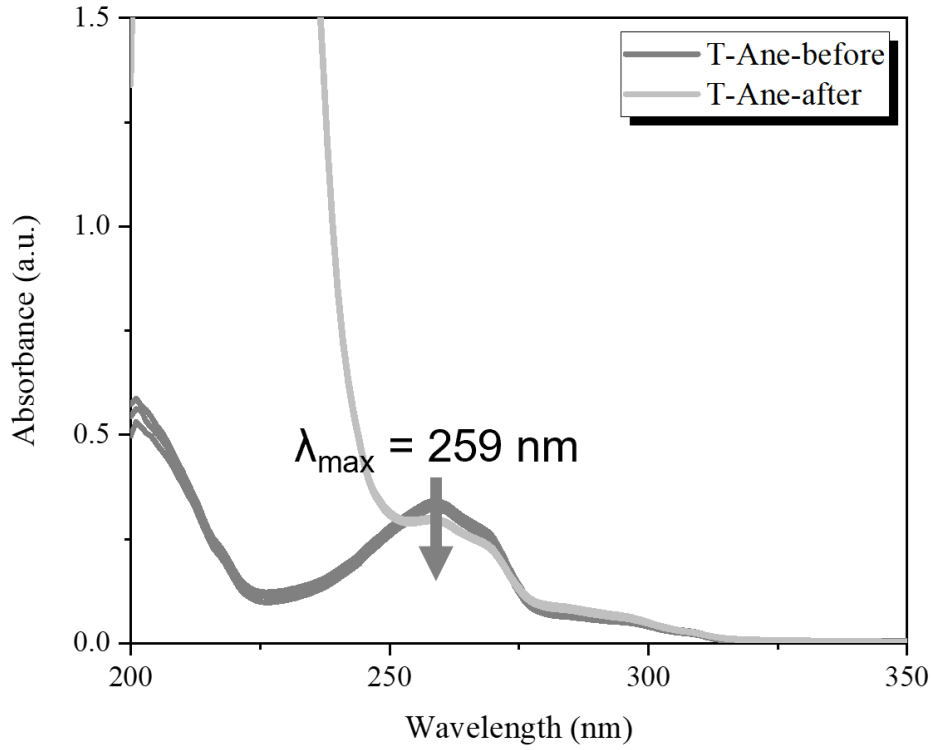


**Figure S15.** (a) UV-Vis spectra of the T-Ane loading experiments (centrifugation method).

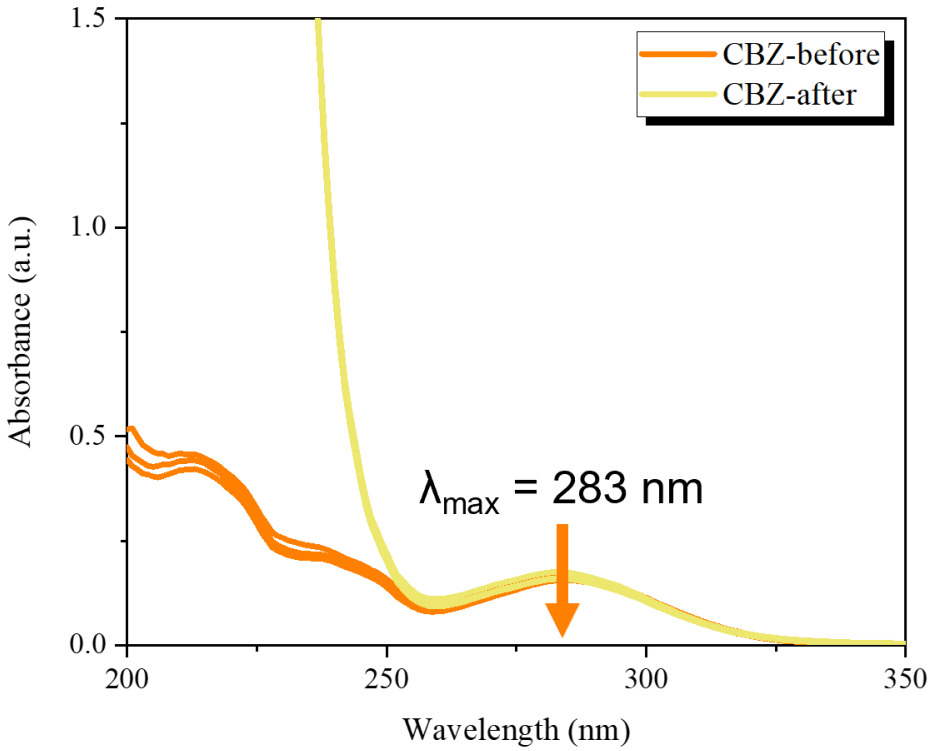


**Figure S16.** (a) UV-Vis spectra of the CBZ loading experiments (centrifugation method).

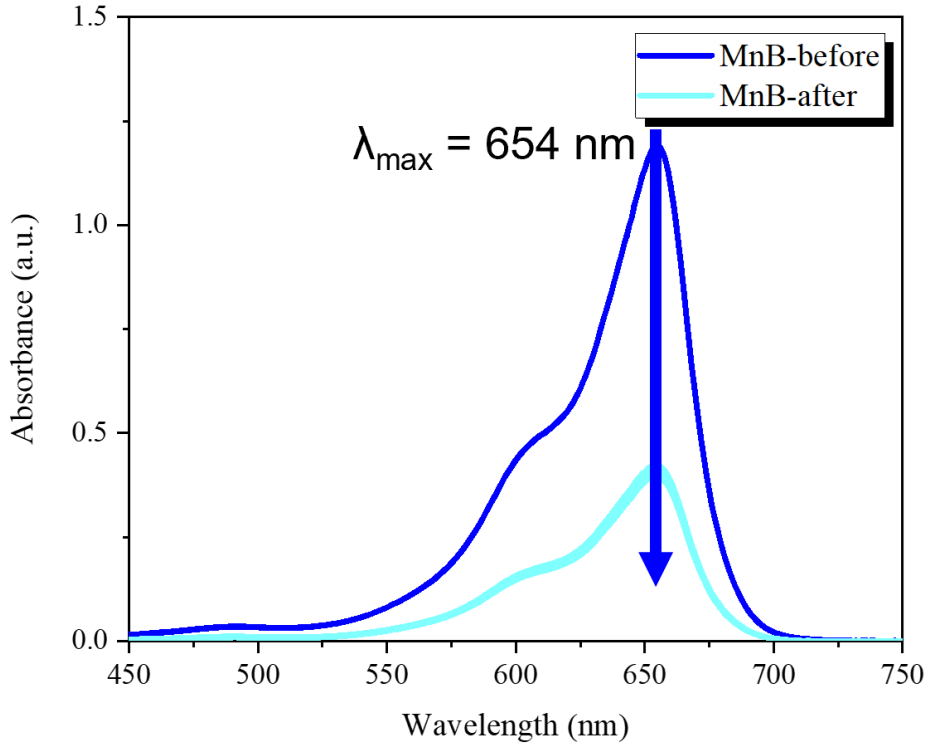


**Figure S17.** (a) UV-Vis spectra of the MnB loading experiments (centrifugation method).

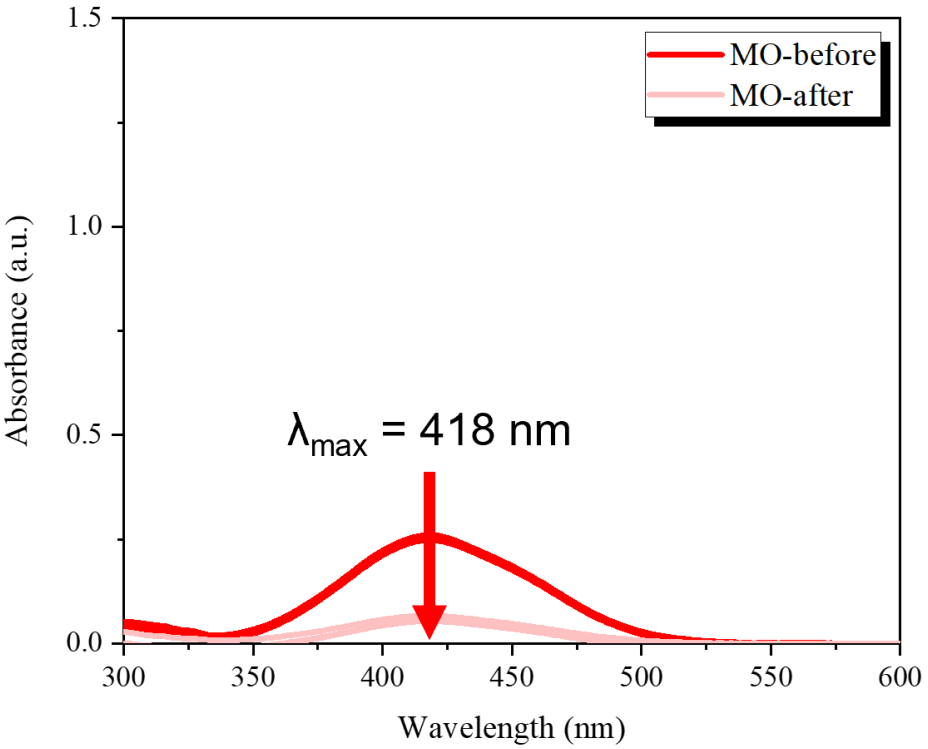


**Figure S18.** (a) UV-Vis spectra of the MO loading experiments (centrifugation method).

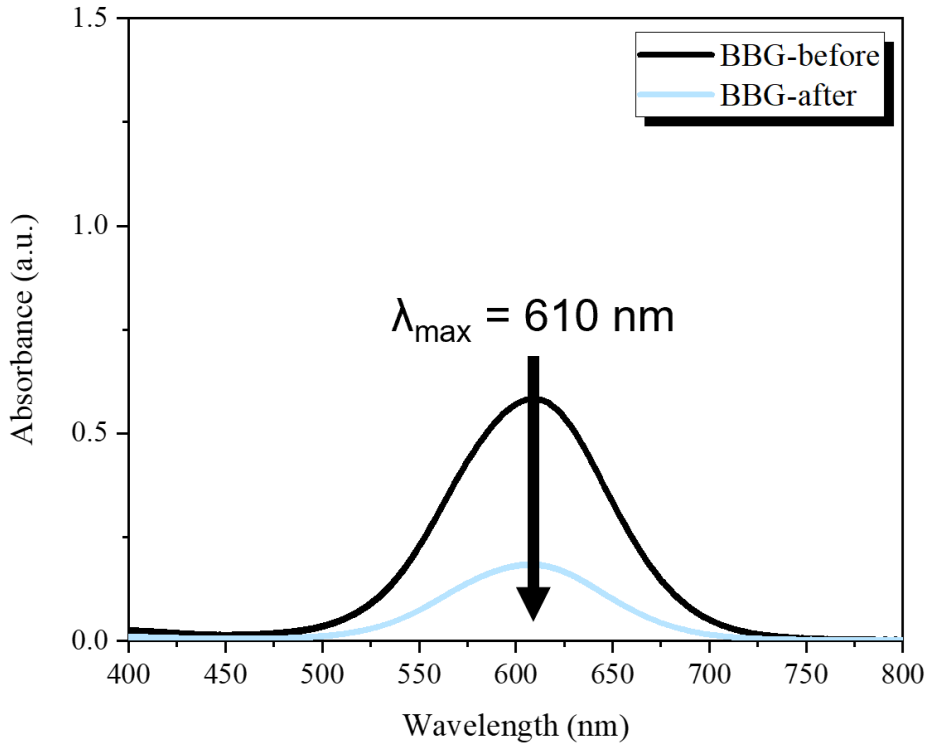


**Figure S19.** (a) UV-Vis spectra of the BBG loading experiments (centrifugation method).

### S3.3. Cargo loading experiment (soaking method)

As shown in **Figure S20**, 0.5 mL of ethanol suspension of Zr-BTB MONs (2.5 mg $mL^{-1}$) was added into a cuvette. The cuvette was then fixed in a centrifuge tube and centrifuged at 4500 rpm for 1 hour. After centrifugation, the organogel formed at the bottom of the cuvette, and the supernatant was removed. 2.5 mL of MnB solution was then carefully layered on top of the gel, and the cuvette was centrifuged at 4500 rpm for 10 mins. After centrifugation, the cuvette was placed in the UV-Vis equipment for 72 h, and the UV-Vis spectrum of the MnB loading experiment (soaking method) was recorded every 30 minutes at room temperature (**Figure S23**). The T-Ane, CBZ, MO and BBG loading experiments were conducted using the same method as the MnB loading experiment. The concentrations of T-Ane, CBZ, MnB, MO and BBG solutions for the cargo loading experiments (soaking method) can be found in **Table S2**.

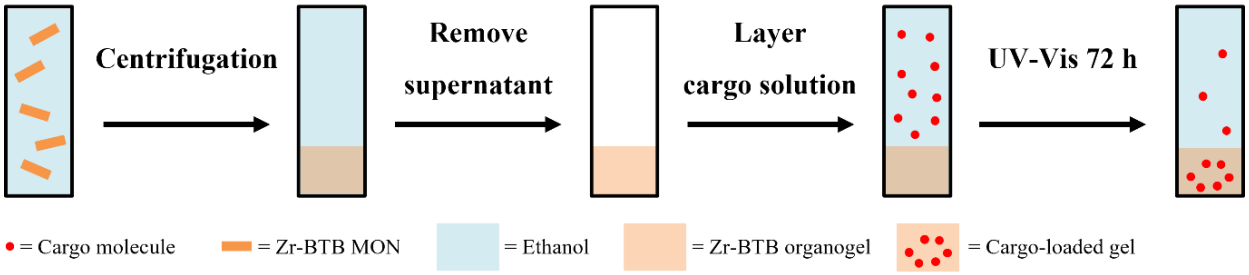


**Figure S20.** Schematic illustration of the cargo loading experiment (soaking method).

**Table S4.** Summary of the results of the T-Ane, CBZ, MnB, MO and BBG loading experiments (soaking method).

| Experiment | Absorbance at 0 min of experiment[a] (a.u.) | Absorbance after 72 h of experiment[a] (a.u.) | Cargo loading soaking[b] (%) |
|---|---|---|---|
| T-Ane | 0.2257 | 0.2162 | 4.2026 |
| CBZ | 0.1545 | 0.1489 | 3.6200 |
| MnB | 0.7566 | 0.2246 | 70.3118 |
| MO | 0.1843 | 0.0692 | 62.4715 |
| BBG | 0.4091 | 0.2259 | 44.7903 |

[a]The absorbance values are measured from the UV-Vis spectra at $\lambda_{max}$ (**Figure S21-S25**).

[b]The T-Ane, CBZ, MnB, MO and BBG loadings of the soaking method are calculated by **eq S2**.

$$\textbf{Cargo loading soaking} = \frac{\textbf{Absorbance at 0 min of experiment} - \textbf{Absorbance after 72 h of experiment}}{\textbf{Absorbance at 0 min of experiment}} \times \mathbf{100\%} \qquad \text{(equation S2)}$$

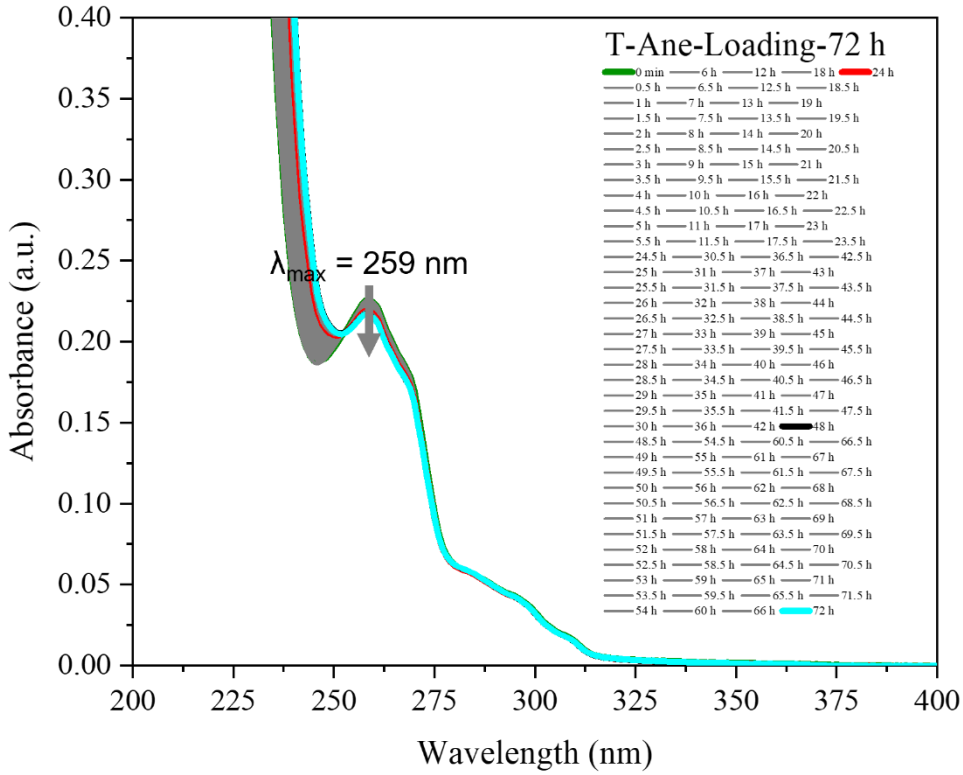


**Figure S21.** Time-resolved UV-Vis spectra of the T-Ane loading experiment (soaking method).

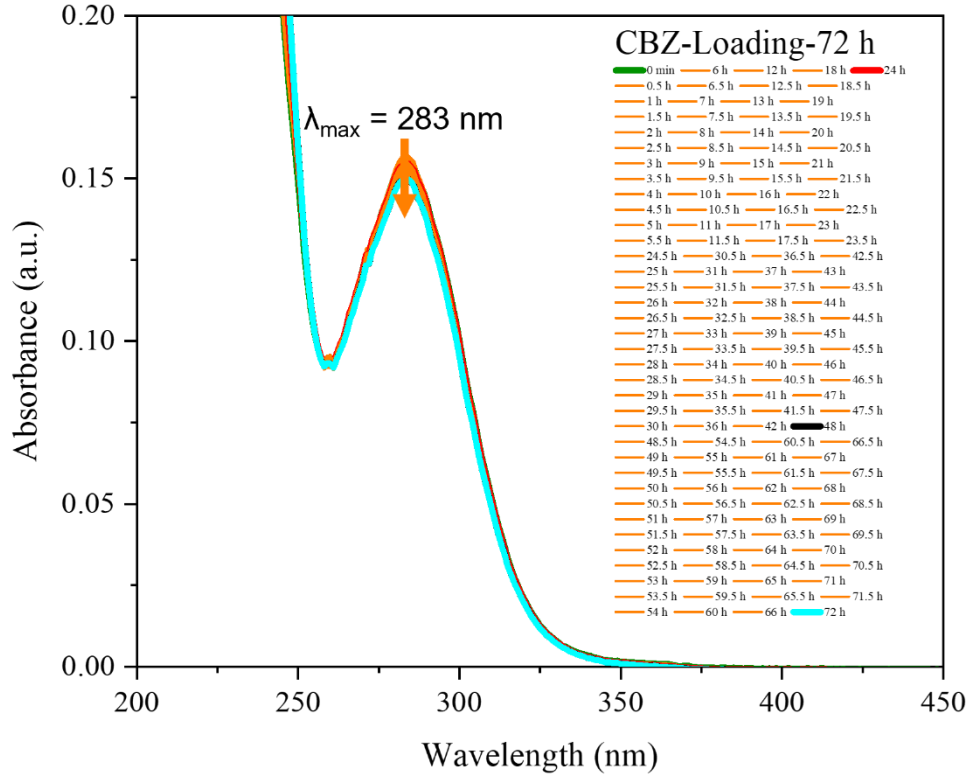


**Figure S22.** Time-resolved UV-Vis spectra of the CBZ loading experiment (soaking method).

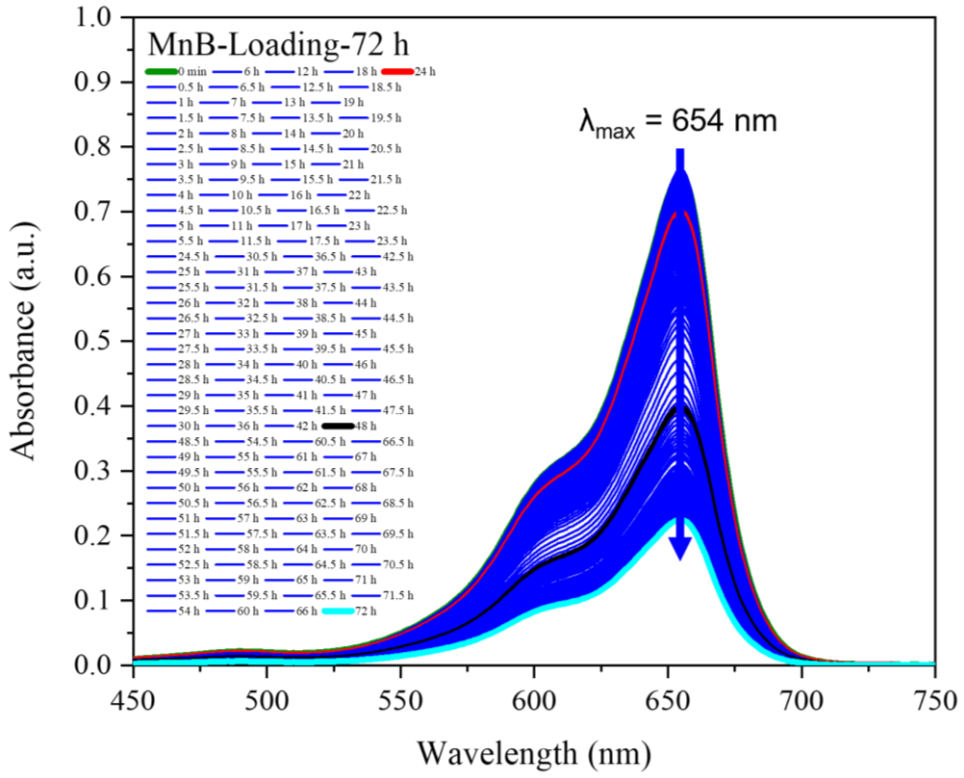


**Figure S23.** Time-resolved UV-Vis spectra of the MnB loading experiment (soaking method).

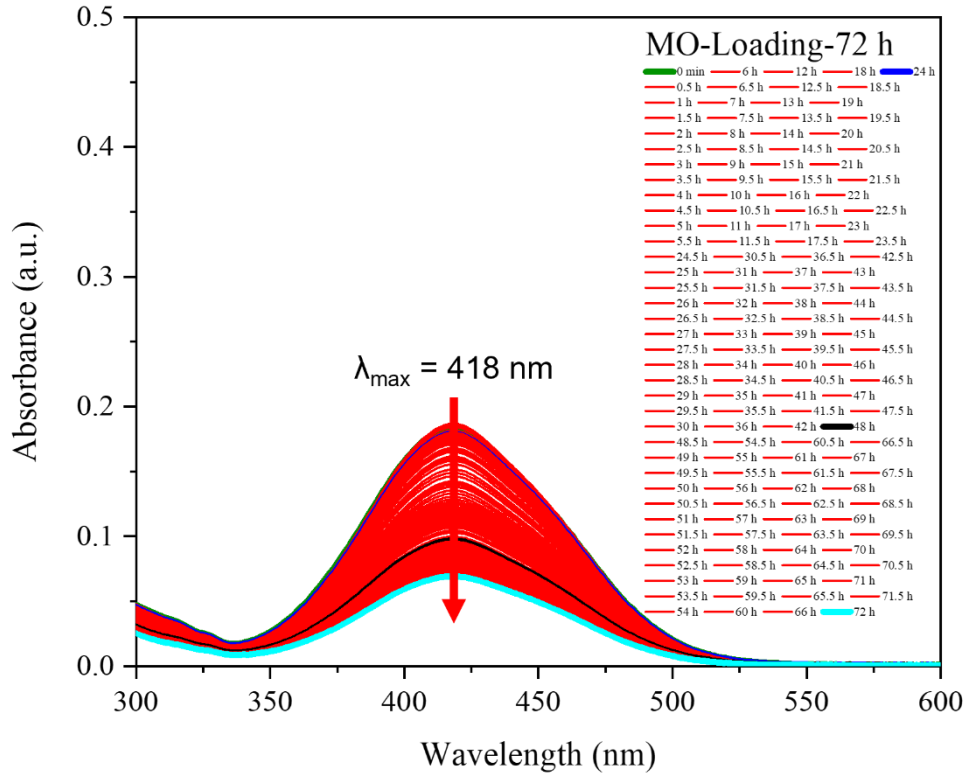


**Figure S24.** Time-resolved UV-Vis spectra of the MO loading experiment (soaking method).

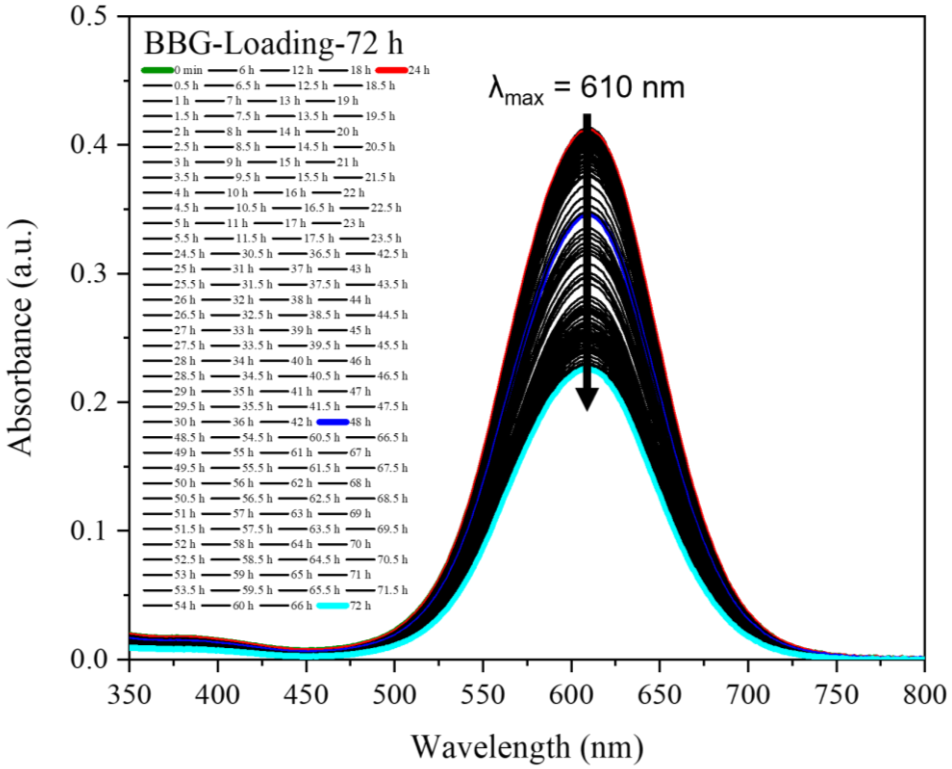


**Figure S25.** Time-resolved UV-Vis spectra of the BBG loading experiment (soaking method).

**S3.4. Cargo release experiment**

As shown in **Figure S26a and S26b**, 1.5 mL of MnB solution was mixed with 0.5 mL of ethanol suspension of Zr-BTB MONs (2.5 mg $mL^{-1}$) in a cuvette. The cuvette was then fixed in a centrifuge tube and centrifuged at 4500 rpm for 1 hour. After centrifugation, the MnB-loaded gel formed at the bottom of the cuvette, and the supernatant was removed. 2.5 mL of fresh ethanol was then carefully layered on top of the gel, and the cuvette was centrifuged at 4500 rpm for 10 mins. After centrifugation, the cuvette was placed in the UV-Vis equipment for 48 h, and the UV-Vis spectrum was recorded every 30 minutes at room temperature and the MnB release experiment was repeated 3 times (**Figure S30**). The T-Ane and CBZ release experiments were conducted using the same method as the MnB release experiment.

The release rates of MO and BBG from the gels were slower than the release rates of T-Ane, CBZ and MnB. Therefore, the MO and BBG release experiments were conducted for a longer period of time (384 h, **Figure S31 and S32**) and were only conducted once. The concentrations of T-Ane, CBZ, MnB, MO and BBG solutions for the cargo release experiments can be found in **Table S2**. The absorbance values of the released T-Ane, CBZ, MnB, MO and BBG are measured from the UV-Vis spectra at $\lambda_{max}$ (**Figure S28-S32**), and the changes of their absorbance values with release time are shown in **Figures 4b and 4c**.

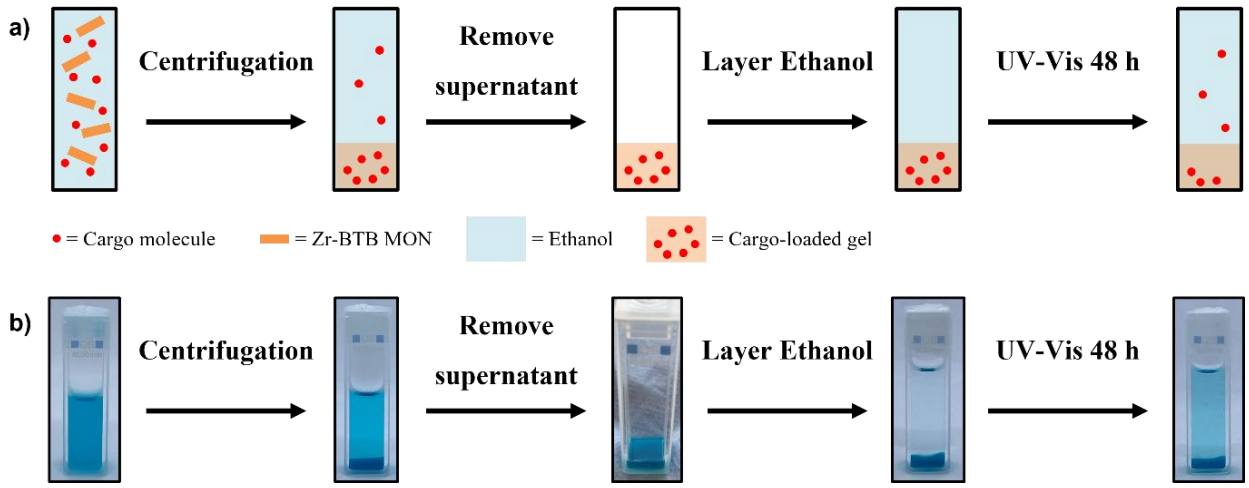


**Figure S26.** (a) Schematic illustration of the cargo release experiment. (b) Example of the MnB release experiment.

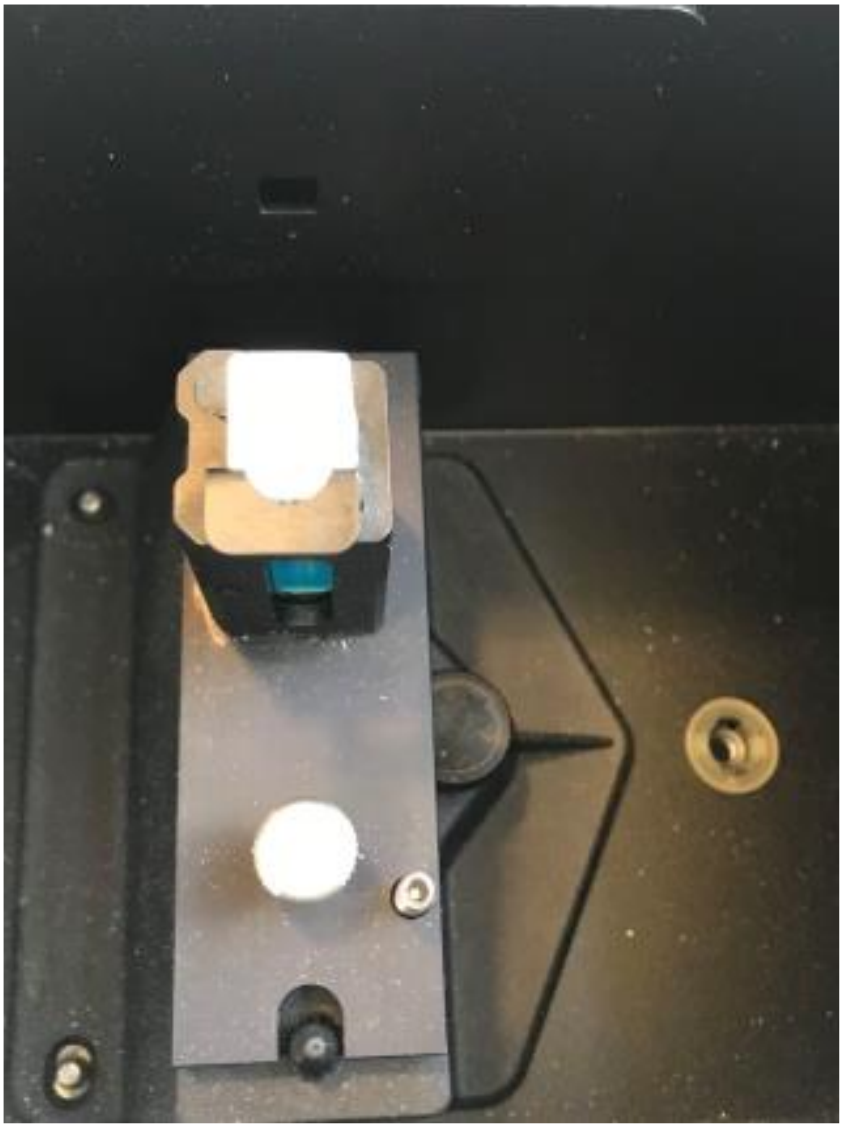

**Figure S27.** Photograph of the MnB release experiment in the UV-Vis equipment.

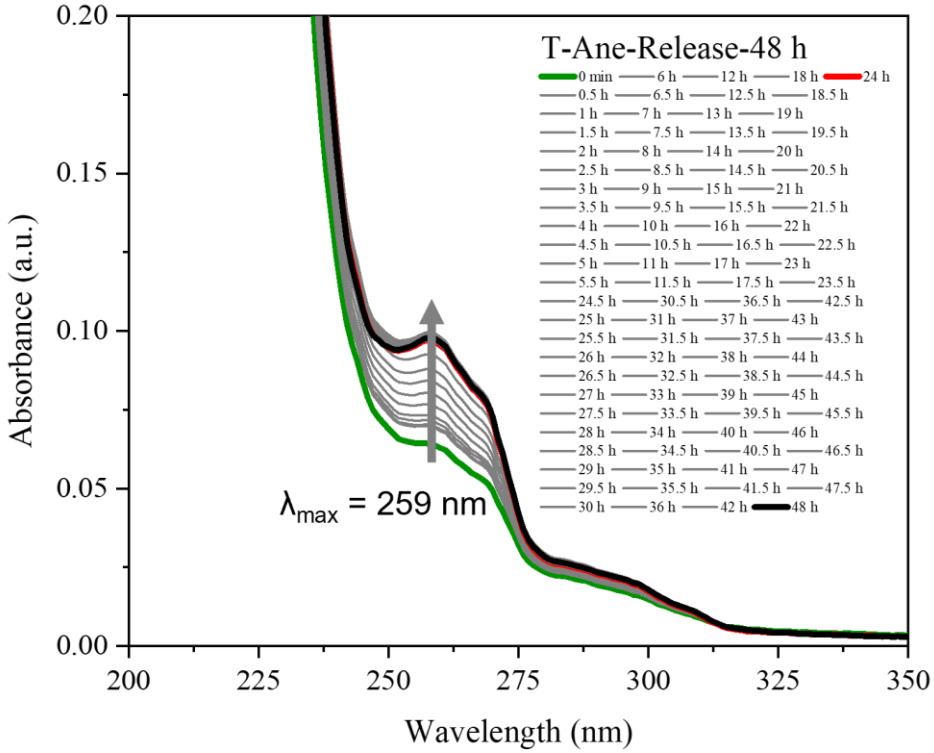


**Figure S28.** Time-resolved UV-Vis spectra of the T-Ane release experiment.

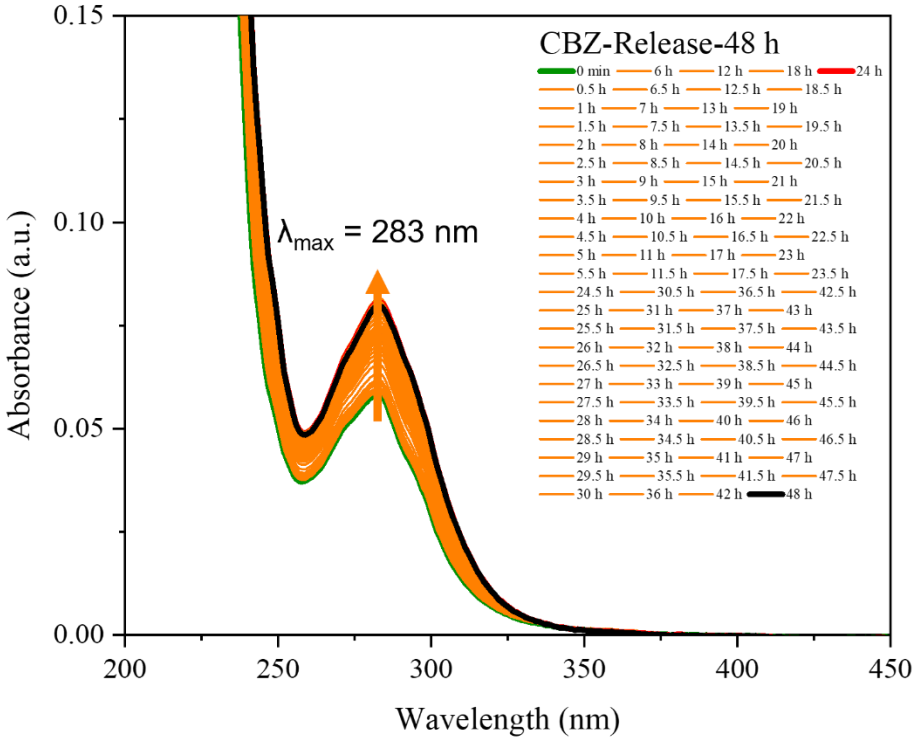


**Figure S29.** Time-resolved UV-Vis spectra of the CBZ release experiment.

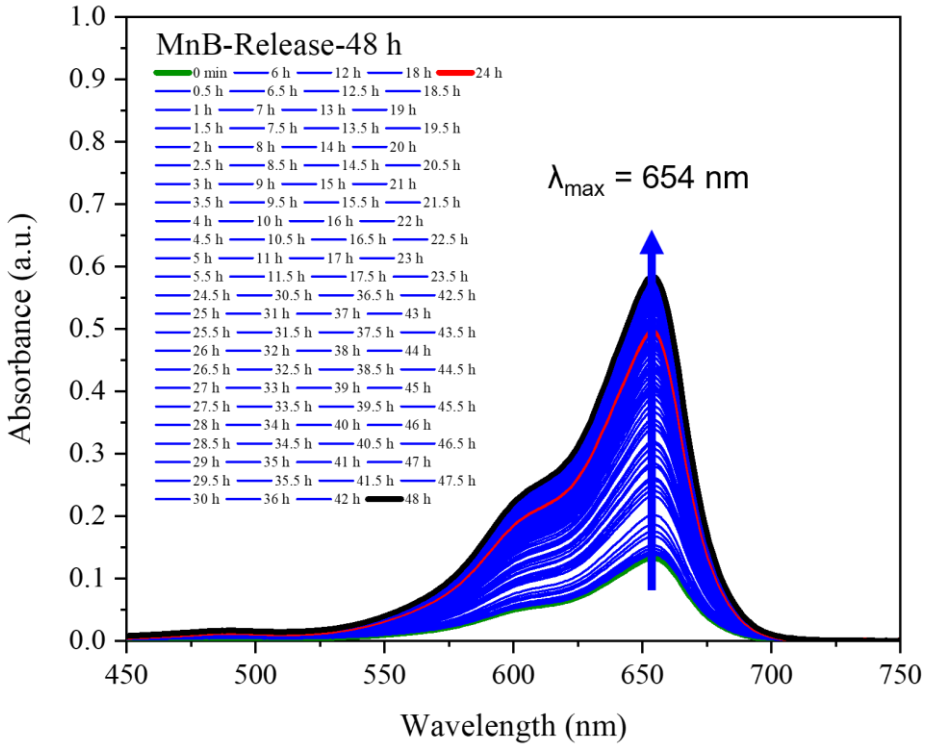


**Figure S30.** Time-resolved UV-Vis spectra of the MnB release experiment.

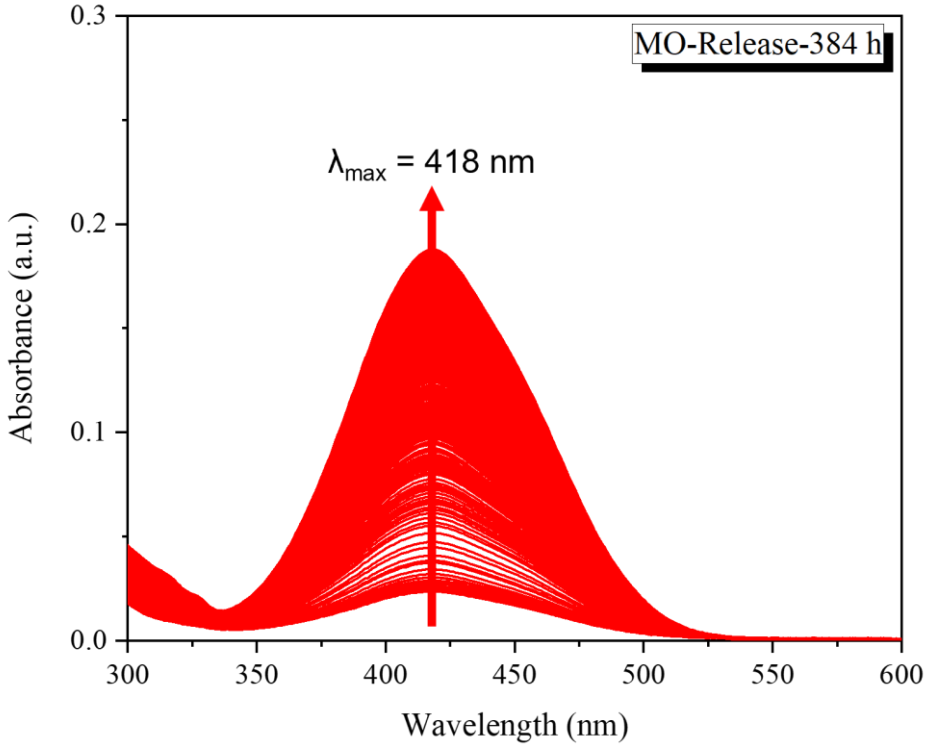


**Figure S31.** Time-resolved UV-Vis spectra of the MO release experiment.

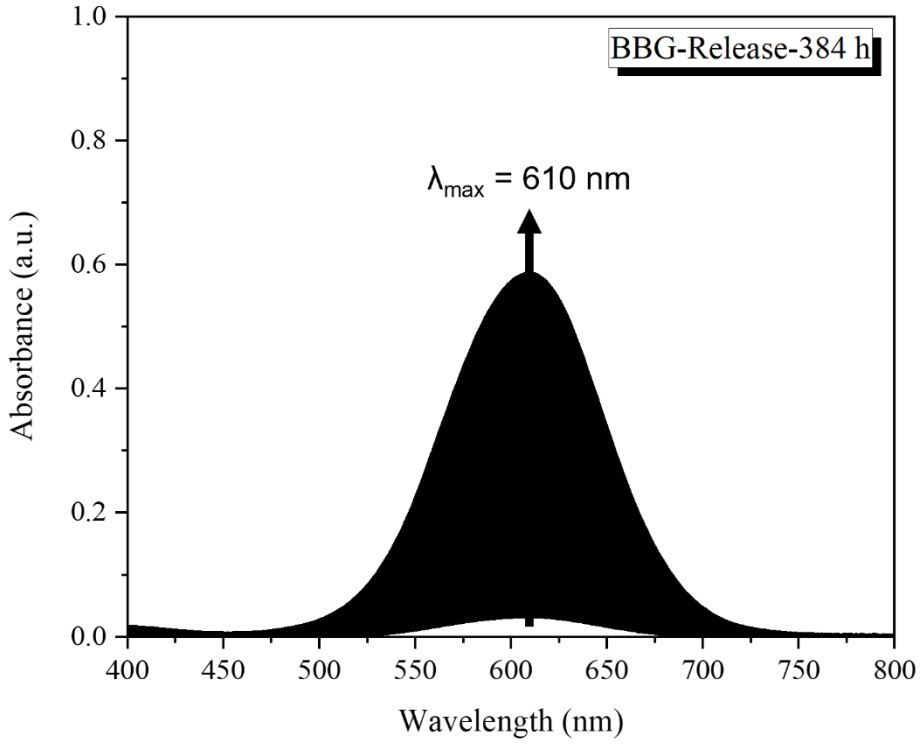


**Figure S32.** Time-resolved UV-Vis spectra of the BBG release experiment.

### S3.5. Blank experiment

As shown in **Figure S33**, 0.5 mL of ethanol suspension of Zr-BTB MONs (2.5 mg $mL^{-1}$) was added into a cuvette. The cuvette was then fixed in a centrifuge tube and centrifuged at 4500 rpm for 1 hour. After centrifugation, the organogel formed at the bottom of the cuvette, and the supernatant was removed. 2.5 mL of ethanol was then carefully layered on top of the gel, and the cuvette was centrifuged at 4500 rpm for 10 mins. After centrifugation, the cuvette was placed in the UV-Vis equipment for 48 h, and the UV-Vis spectrum was recorded every 30 minutes at room temperature (**Figure S34**). The UV-Vis results showed that there was no change in absorbance during the blank experiment (**Figure S35**), indicating that the Zr-BTB organogel was stable during the experiment.

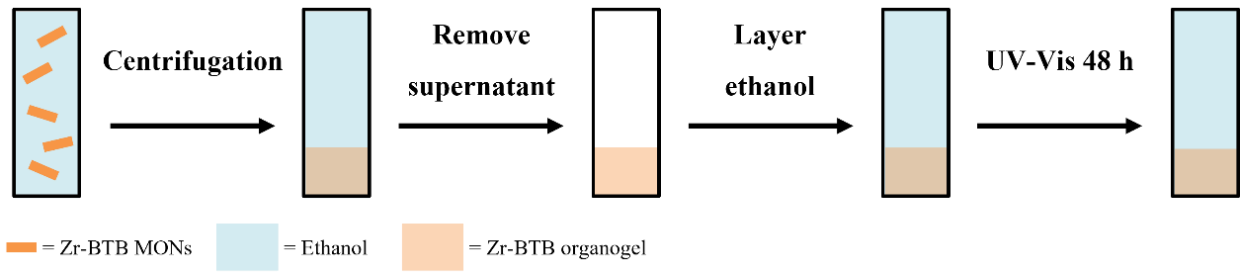


**Figure S33.** Schematic illustration of the blank experiment.

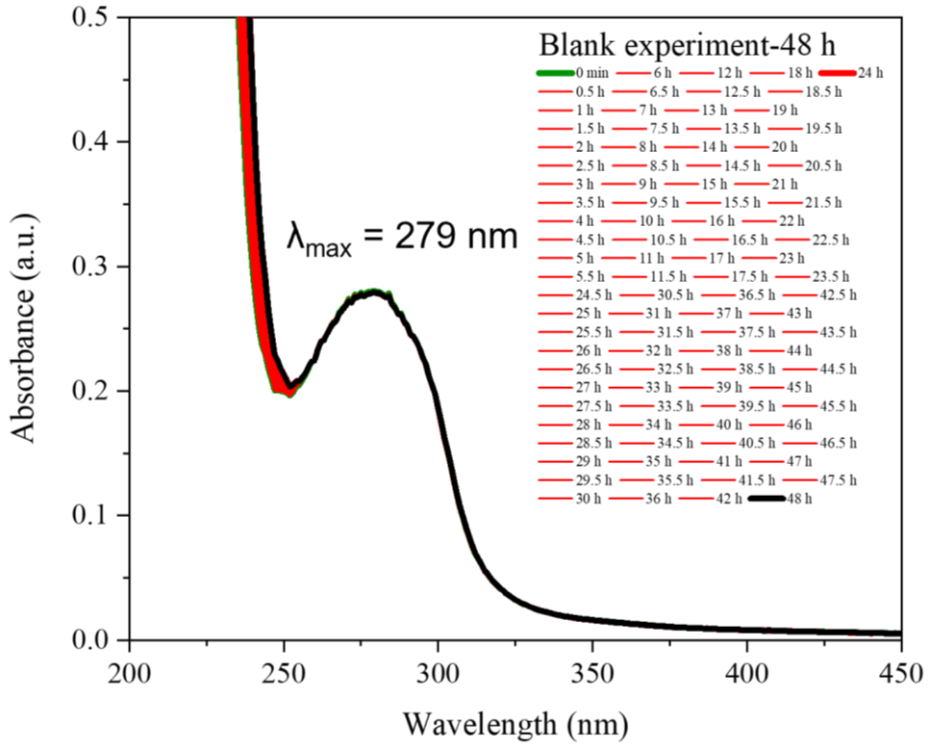


**Figure S34.** Time-resolved UV-Vis spectra of the blank experiment.

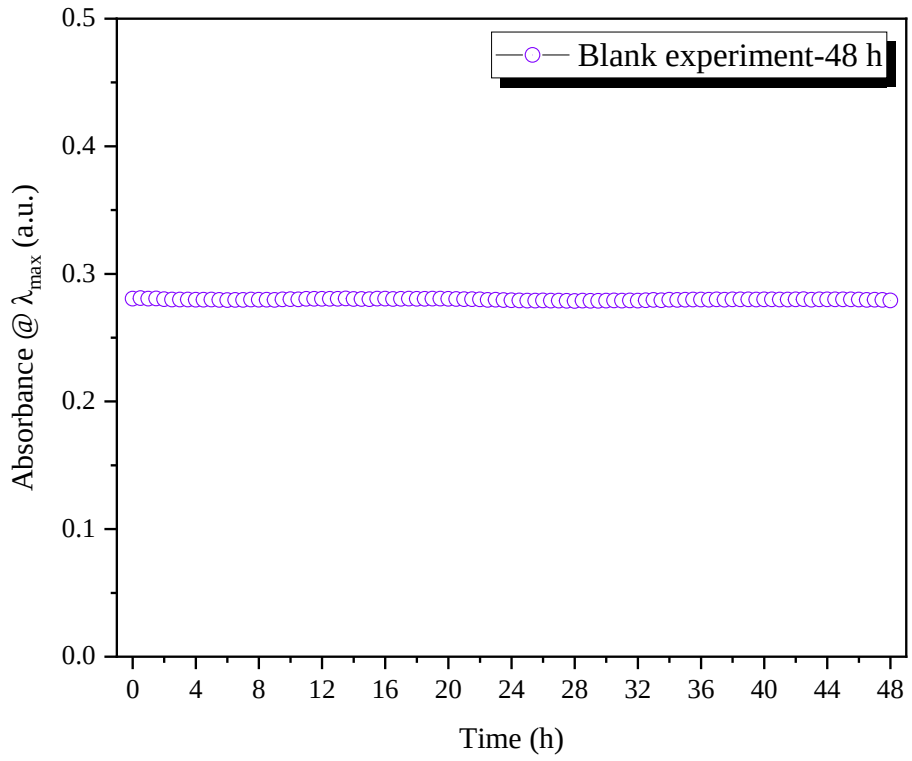


**Figure S35.** UV-Vis results of the blank experiment.

**S3.6. Distance of diffusion**

The distances of diffusion, $\boldsymbol{x}$, of the five cargo molecules (T-Ane, CBZ, MnB, MO and BBG) in the Zr-BTB organogels are calculated by **eq S3**.[1]

$$\boldsymbol{x} = \sqrt{\boldsymbol{2Dt}} \qquad \text{(equation S3)}$$

Where, $\boldsymbol{D}$ is the is the diffusion coefficient of the cargo molecules, $\boldsymbol{t}$ is the diffusion time of the cargo molecules (**Table S5**) which is estimated based on their release profiles **Figure 4b and 4c**.

The diffusion coefficients, $\boldsymbol{D}$, of the five cargo molecules (T-Ane, CBZ, MnB, MO and BBG) are calculated by the Stokes-Einstein Gierer-Wirtz Estimation (SEGWE) calculator published by Morris and co-workers.[2-4] The input solvent is methanol-d4, because it is close to the ethanol system used in our study and the input temperature is 298.15 K. The calculator was built based on **eq S4**.

$$\boldsymbol{D} = \frac{\boldsymbol{k_B T}\left(\frac{\boldsymbol{3a}}{\boldsymbol{2}} + \frac{\boldsymbol{1}}{\boldsymbol{1+a}}\right)}{\boldsymbol{6\pi\eta}\sqrt[3]{\frac{\boldsymbol{3MW}}{\boldsymbol{4\pi\rho_{eff}N_A}}}}, \text{where } \boldsymbol{a} = \sqrt[3]{\frac{\boldsymbol{MW_S}}{\boldsymbol{MW}}} \qquad \text{(equation S4)}$$

Where, $\boldsymbol{k_B}$ is the is the Boltzmann constant, $\boldsymbol{T}$ is the temperature of the cargo release experiments, $\boldsymbol{\eta}$ is the viscosity, $\boldsymbol{MW}$ is the molecular weights of the cargo molecules (**Table S5**), $\boldsymbol{\rho_{eff}}$ is the effective density of molecules, $\boldsymbol{N_A}$ is the Avogadro number, $\boldsymbol{MW_S}$ is the molecular weight of the solvent.

The calculated diffusion coefficients of the five cargo molecules (T-Ane, CBZ, MnB, MO and BBG) and their distances of diffusion in the Zr-BTB organogels are summarised in **Table S5**.

**Table S5.** Summary of the diffusion coefficients and distances of diffusion of the five cargo molecules.

| Cargo molecule | Molecular weight (g mol$^{-1}$) | Diffusion time (h) | Diffusion coefficient (cm$^2$ s$^{-1}$) | Distance of diffusion (cm) |
|---|---|---|---|---|
| T-Ane | 148.21 | 6 | 1.232E-05 | 0.72954 |
| CBZ | 236.27 | 18 | 9.873E-06 | 1.13117 |
| MnB (including $Cl^-$) | 319.85 | 34 | 8.590E-06 | 1.45011 |
| MO (including $Na^+$) | 327.33 | 369 | 8.501E-06 | 4.75242 |
| BBG (including $Na^+$) | 854.02 | 379.5 | 5.595E-06 | 3.90996 |

### S3.7. Models of cargo molecules

The models of the five cargo molecules (T-Ane, CBZ, MnB, MO and BBG) are built using JSmol software (**Figure S36-S40**).[5] The distances between atoms are also measured using this software to estimate the sizes of the cargo molecules. JSmol is the HTML5 modality of Jmol, able to be embedded into web pages. All the functionality of Jmol (as a standalone application) is also present in JSmol. The website of Jmol recommends us to cite the software in this way:

Jmol: an open-source Java viewer for chemical structures in 3D. http://www.jmol.org/

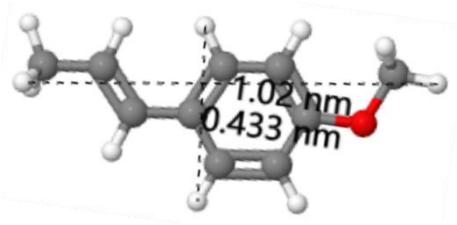


**Figure S36.** Model of T-Ane. Grey: carbon, red: oxygen, white: hydrogen.

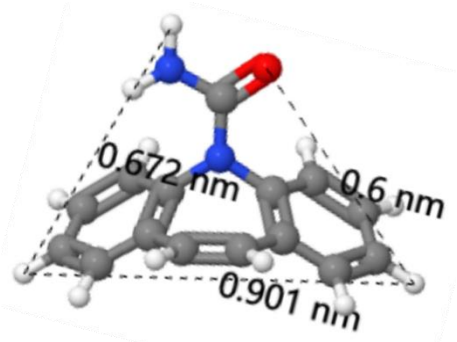


**Figure S37.** Model of CBZ. Grey: carbon, red: oxygen, white: hydrogen, blue: nitrogen.

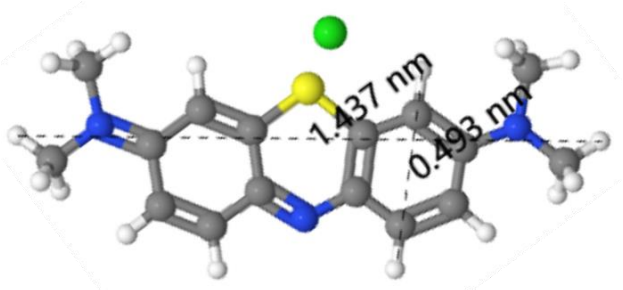


**Figure S38.** Model of MnB. Grey: carbon, red: oxygen, white: hydrogen, blue: nitrogen, yellow: sulfur, green: chlorine.

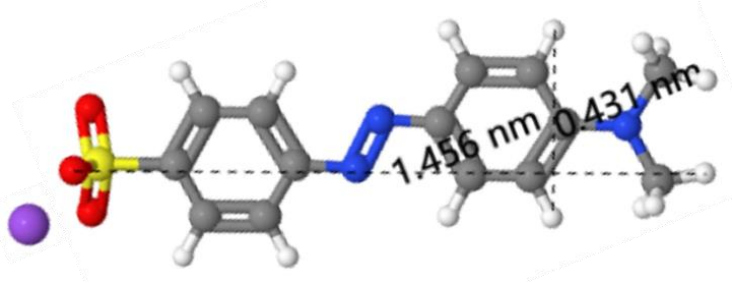


**Figure S39.** Model of MO. Grey: carbon, red: oxygen, white: hydrogen, blue: nitrogen, yellow: sulfur, purple: sodium.

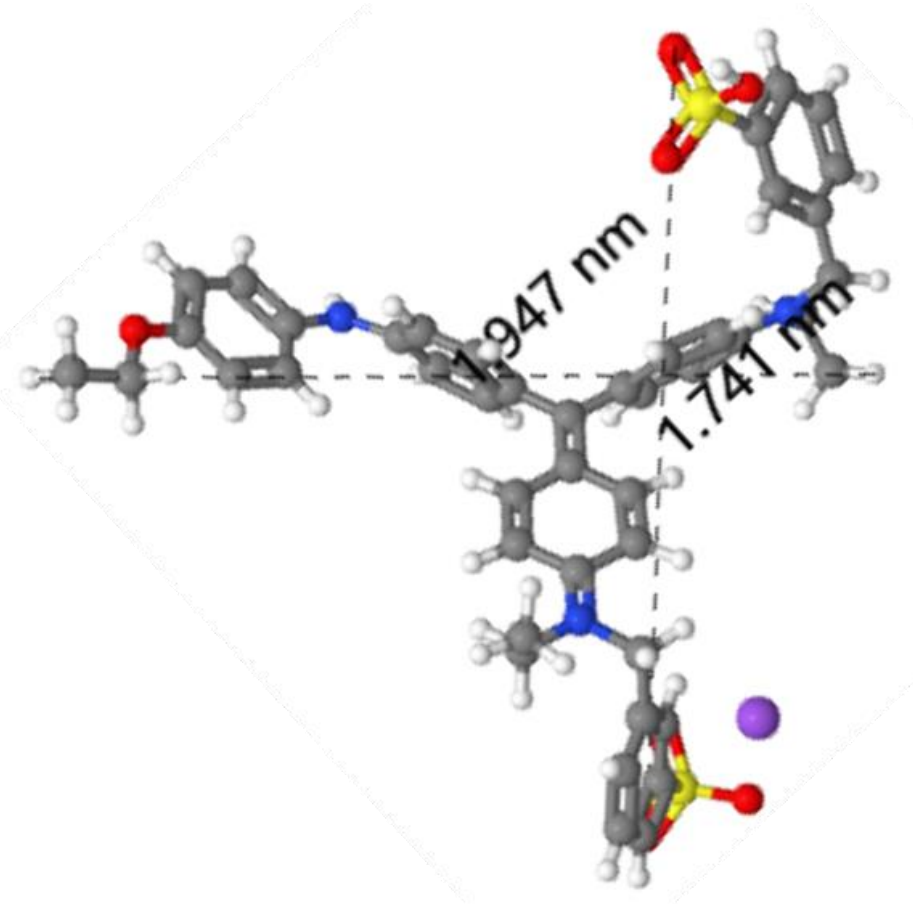


**Figure S40.** Model of BBG. Grey: carbon, red: oxygen, white: hydrogen, blue: nitrogen, yellow: sulfur, purple: sodium.

## S4. References


1. Diffusion Time Calculator, https://www.physiologyweb.com/calculators/diffusion_time_calculator.html, (accessed May 2023).

2. R. Evans, Z. Deng, A. K. Rogerson, A. S. McLachlan, J. J. Richards, M. Nilsson and G. A. Morris, *Angew. Chem. Int. Ed.*, 2013, **52**, 3199-3202.

3. R. Evans, G. D. Poggetto, M. Nilsson and G. A. Morris, *Anal. Chem.*, 2018, **90**, 3987-3994.

4. SEGWE calculator: Diffusion coefficient and molecular weight estimation, https://nmr.chemistry.manchester.ac.uk/?q=node/432, (accessed May 2023).

5. JSmol, https://jmol.sourceforge.net/, (accessed May 2023).

# Chapter 3

# An Isoreticular Series of Zr-Tricarboxylate Based Metal-Organic Nanosheets for Water Purification Applications

## Chapter 3

An isoreticular series of Zr-tricarboxylate based metal-organic nanosheets for water purification applications

Unpublished paper (full article)

**Jiangtian Tan,** Bethany J. Lingard, Ram R. R. Prasad and Jonathan A. Foster

**Author Contributions**

| | |
|---|---|
| **Jiangtian Tan** | Supervised Bethany J. Lingard. Performed all AFM and SEM characterisations. Performed water purification experiments. Drafted manuscript and SI and created all figures. |
| Bethany J. Lingard | Performed initial syntheses and characterisations of MONs and membranes. Performed preliminary water purification experiments. |
| Ram R. R. Prasad | Provided $H_3$BTB-$NH_2$ and $H_3$TATB ligands for the synthesis of MONs. |
| Jonathan A. Foster | Supervised Jiangtian Tan, Bethany J. Lingard, Ram R. R. Prasad. Assisted in editing of manuscript. |

ARTICLE

# An isoreticular series of Zr-tricarboxylate based metal-organic nanosheets for water purification applications

Received 00th January 20xx,
Accepted 00th January 20xx

DOI: 10.1039/x0xx00000x

Jiangtian Tan,[a] Bethany J. Lingard,[a] Ram R. R. Prasad,[a] and Jonathan A. Foster*[a]

As porous two-dimensional materials, metal-organic nanosheets (MONs) have shown enormous potential for use in a wide range of separation applications. We investigated an isoreticular series of Zr-tricarboxylate based MONs bearing different organic ligands for dye separation applications, including 1,3,5-benzenetribenzoate (BTB), 2'-amino-5'-(4-carboxyphenyl)-[1,1':3',1''-terphenyl]-4,4''-dicarboxylate (BTB-$NH_2$) and 4,4',4''-s-triazine-2,4,6-triyl-tribenzoate (TATB). Ethanol suspensions containing monolayer Zr-BTB, Zr-BTB-$NH_2$ and Zr-TATB MONs were spin-coated onto polyethersulfone (PES) supports to prepare composite membranes. All three membranes remained highly permeable toward small anionic dyes such as methyl orange (MO) but rejected (~90%) larger anionic dyes such as brilliant blue G (BBG) due to size exclusion effect of the MONs. Higher rejection rates toward similarly sized but positively charged methylene blue (MnB) dyes were observed compared to MO, which could be attributed to the higher adsorption rates of MnB on the membranes. This work demonstrates that two-dimensional Zr-tricarboxylate based MONs have great potential to be used in water purification applications.

## Introduction

Metal-organic nanosheets (MONs) are a class of porous two-dimensional (2D) materials formed by the coordination of metal ions or metal clusters to organic ligands.[1,2] MONs have diverse chemical properties and tunable structures, making them ideal materials for a wide range of applications, including sensing,[3] catalysis,[4] optoelectronics[5] and drug delivery.[6] In particular, MONs are ideally suited for use in membrane-based separation applications due to their ultrathin nature and well-defined pore sizes.[2,7]

Amongst the wide variety of MONs reported in the literature, Zr-BTB (BTB = 1,3,5-benzenetribenzoate) has attracted considerable attention due to its high water, chemical and thermal stability and ease of preparation and functionalisation.[8-10] For example, Zhao and co-workers reported the facile and scalable synthesis of Zr-BTB MONs by a crystal growth modulation method, and the nanosheets they obtained were used to prepare sensors for capacitive gas sensing.[8] The use of Zr-BTB in other applications has also been investigated, including DNA detection,[11] 2,4-dinitrophenol sensing[12] and catalysis[13] applications. Various methods have also been developed to post-synthetically functionalise Zr-BTB MONs to systematically tune their structures and properties, including functionalisation of Zr-BTB with pillaring ligands[10] and introduction of indium into Zr-BTB MONs by metal-ion exchange.[14] In addition, a series of Zr-tricarboxylate based MONs with an isoreticular structure to Zr-BTB have also been reported in the literature, including its amino, methyl and carboxyl derivatives (Zr-BTB-$NH_2$, Zr-BTB-$CH_3$ and Zr-BTB-COOH)[8,15] and Zr-TATB in which the $Zr_6$ clusters are linked by 4,4',4''-s-triazine-2,4,6-triyl-tribenzoate (TATB) ligands forming nanosheets with an average thickness of 1.48 nm.[16]

MONs have so far been used for a variety of separation applications. For example, Zhao and co-workers incorporated Zr-BTB MONs as fillers into PIM-1 membranes (PIM = polymer of intrinsic microporosity) and improved their $CO_2/CH_4$ and $CO_2/N_2$ separation performance.[17] Zr-BTB-$NH_2$[18] and Zr-BTB-COOH[15] MONs have also been used to prepare effective membranes for gas separation applications. MONs have also been investigated for use in water purification applications. For example, Ang and Hong reported polycation-crosslinked Zn-TCP(Fe) membranes (TCP(Fe) = Fe(III) mesotetra(4-carboxyphenyl)porphine chloride) that exhibited a high water permeance of up to 4243 L $m^{-2}$ $h^{-1}$ $bar^{-1}$ and excellent rejection rates toward organic dyes in aqueous solutions.[19] Other MONs, such as BUT-203[20] (BUT = Beijing University of Technology) and $Zn_2(Bim)_3(OH)(H_2O)$ (Bim = benzimidazolate)[21] have also been used to prepare membranes for use in water purification applications.

To our knowledge, only one previous example of Zr-tricarboxylate based MONs for water purification has been reported in the literature, in which Zr-BTB MONs were deposited onto polyacrylonitrile (PAN)-400 supports to prepare composite membranes by a doctor blade casting method.[22] The Zr-BTB/PAN-400 membranes exhibited high rejection rates toward organic dyes, such as acid fuchsin and methyl blue, as well as excellent desalination performance toward $Mg^{2+}$ and $Al^{3+}$ in aqueous solutions. However, compared to other MON-based water purification membranes,[19] the relatively low water permeances of the Zr-BTB/PAN-400 membranes (1 to 3.2 L $m^{-2}$ $h^{-1}$ $bar^{-1}$) could impede their industrial applications.

In this work, we investigated an isoreticular series of Zr-tricarboxylate based MONs bearing different organic ligands for

[a] Department of Chemistry, University of Sheffield, Sheffield, UK. E-mail: jona.foster@sheffield.ac.uk.

† Footnotes relating to the title and/or authors should appear here.
Electronic Supplementary Information (ESI) available: [details of any supplementary information available should be included here]. See DOI: 10.1039/x0xx00000x

water purification applications, including 1,3,5-benzenetribenzoate (BTB), 2'-amino-5'-(4-carboxyphenyl)-[1,1':3',1''-terphenyl]-4,4''-dicarboxylate (BTB-$NH_2$) and 4,4',4''-s-triazine-2,4,6-triyl-tribenzoate (TATB). Ethanol suspensions of the three MONs were spin-coated onto highly permeable polyethersulfone (PES) supports to prepare composite membranes. The water purification performance of all membranes were systematically studied for a series of dyes with different sizes and charges.

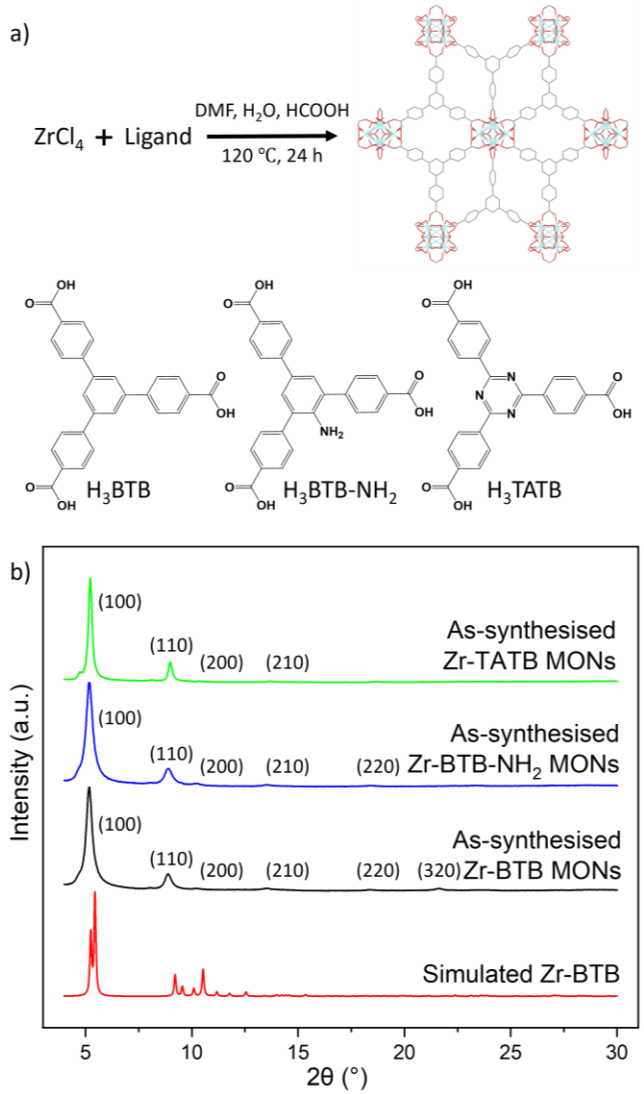


**Figure 1.** (a) Synthesis of an isoreticular series of Zr-tricarboxylate based MONs using different ligands, including $H_3BTB$, $H_3BTB$-$NH_2$ and $H_3TATB$. The crystal structure is downloaded from CCDC (deposition number: 1567188).[9] (b) PXRD patterns of the as-synthesised Zr-BTB, Zr-BTB-$NH_2$ and Zr-TATB MONs, comparing with the simulated pattern of Zr-BTB.

## Results and Discussion

**Preparation and characterisation of MONs.** The three Zr-tricarboxylate based MONs were synthesised by adapting the method reported by Zhao and co-workers.[8] As shown in **Figure 1a**, zirconium(IV) chloride ($ZrCl_4$, 0.129 mmol) and $H_3BTB$, $H_3BTB$-$NH_2$ or $H_3TATB$ (0.068 mmol) were dissolved in a mixture of formic acid (HCOOH, 2 mL), deionised water ($H_2O$, 2 mL) and *N,N*-dimethylformamide (DMF, 15 mL), which was then heated at 120 °C for 24 h in a reaction oven. The resulting viscous suspensions of the three MONs were then centrifuged and washed three times with fresh DMF then ethanol. The washed MONs were stored in ethanol as homogeneous suspensions with a concentration of 2.5 mg $mL^{-1}$ until needed.

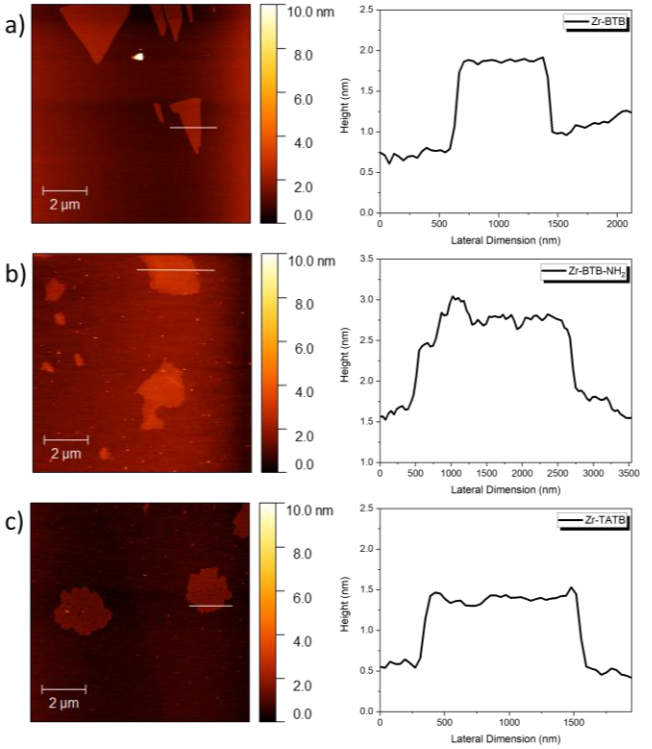


**Figure 2.** AFM images and corresponding height profiles of (a) Zr-BTB, (b) Zr-BTB-$NH_2$ and (c) Zr-TATB MONs.

Ethanol susupensions of the Zr-BTB, Zr-BTB-$NH_2$ and Zr-TATB MONs (1 mL) were dried using a hot plate at 80 °C to remove most of the solvent and then at 120 °C for complete drying. The resulting solids were characterised by powder X-ray diffraction (PXRD). The PXRD patterns of the three as-synthesised MONs matched well with those reported in the literature,[8,16,18] suggesting that phase pure MONs were synthesised (**Figure 1b**). Compared to the simulated PXRD pattern of 3D Zr-BTB, the PXRD patterns of the three as-synthesised MONs showed only two peaks at 2θ = 5.1° and 8.9°, and the other peaks were not observed. This could be attributed to the extreme aspect ratios of the nanosheets resulting in line broadening and preferred orientation effects.[16,17] Zr-BTB-$NH_2$ and Zr-TATB showed the same characteristic as Zr-BTB, indicating that the three MONs have an isoreticular structure. The hkls were assigned on the PXRD patterns of the as-synthesised MONs which matched with a 2D hexagonal lattice.

The as-synthesised MONs were also characterised using atomic force microscopy (AFM) and the results showed that the three nanosheets had a similar thickness between 1-1.5 nm (**Figure 2a-2c**). This is comparable to the van der Waals size of $Zr_6$ clusters (1.2 nm) in MONs reported in the literature,[23] indicating the formation of monolayer nanosheets. SEM characterisations of the three MONs confirmed their two-dimensional sheet-like morphologies

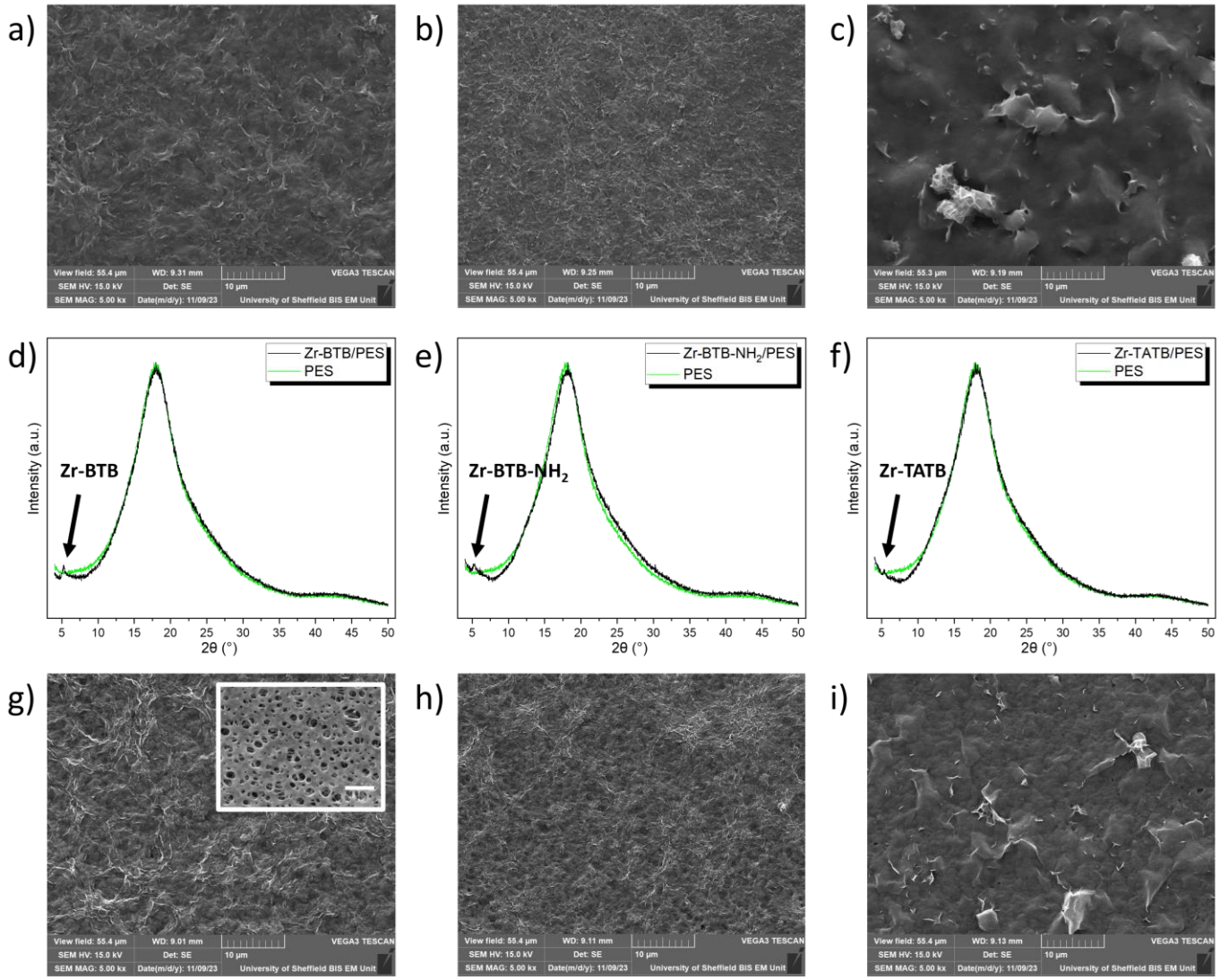


**Figure 3.** SEM images of (a) Zr-BTB, (b) Zr-BTB-$NH_2$ and (c) Zr-TATB MONs. (d-f) PXRD characterisations of the PES support, Zr-BTB/PES, Zr-BTB-$NH_2$/PES and Zr-TATB/PES membranes. SEM images of (g) Zr-BTB/PES, (h) Zr-BTB-$NH_2$/PES and (i) Zr-TATB/PES membranes. The inset SEM image in (g) shows the PES support, scale bar: 5 µm.

(**Figure 3a-3c and Figure S1-S3**) and dynamic light scattering (DLS) results showed that the three MONs have similar particle size distributions in the range of 2-6.5 µm (**Figure S4-S6**).

These results indicated that an isoreticular series of Zr-tricarboxylate based MONs with monolayer thickness and similar particle size distributions were successfully prepared by simply varying the organic ligands in the synthesis of Zr-BTB. The reported pore size of Zr-BTB and Zr-BTB-$NH_2$ MONs in the literature is 0.54 nm,[18] smaller than the sizes of organic dyes in aqueous solutions, such as brilliant blue G (BBG, 1.6 × 1.9 nm), methyl orange (MO, 1.0 × 1.2 nm) and methylene blue (MnB, 1.4 × 0.9 nm, **Table 1**).[19] Therefore, all three MONs were considered promising materials for the preparation of water purification membranes for use in dye separations.

**Water purification membranes.** Composite membranes of Zr-BTB, Zr-BTB-$NH_2$ and Zr-TATB MONs for water purification experiments were prepared by a facile spin-coating method. As mentioned earlier, the Zr-BTB/PAN-400 membranes reported by Zhao and co-workers showed relatively low water permeances in their dye separation and desalination experiments.[22] This could be attributed to the low water permeance of the PAN-400 supports (pore size: about 10 nm), which exhibited a rejection rate of 68.0% and a water permeance of only 49.9 L $m^{-2}$ $h^{-1}$ $bar^{-1}$ in their acid fuchsin separation experiment. Therefore, a highly permeable polyethersulfone (PES) support with a larger pore size of 200 nm was used in this work to increase the water permeance of the membranes. The PES support was fixed in a spin coater and spun at 2500 rpm. Two 500 µL portions of ethanol suspension of MONs (2.5 mg $mL^{-1}$) were deposited onto the PES support and spun for 640 s. The obtained composite membranes (denoted as Zr-BTB/PES, Zr-BTB-$NH_2$/PES and Zr-TATB/PES) were dried at room temperature and characterised by PXRD. The PES support is amorphous in nature and showed only one broad peak at 2θ = 18° which was found in the PXRD patterns of all three composite membranes (**Figure 3d-3f**). A small, but characteristic peak belonging

**Table 1.** Structures and properties of BBG, MO and MnB dyes and water purification performance of membranes.

| Dye | Structure | Properties | Membrane | Water permeance (L $m^{-2}$ $h^{-1}$ $bar^{-1}$) | Rejection rate (%) | Adsorption rate (%) |
|---|---|---|---|---|---|---|
| BBG | 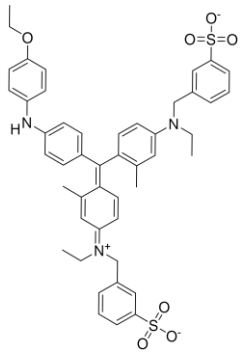 | **Molecular weight (g $mol^{-1}$)**<br>831.03<br>**Dimensions of hydrated BBG* (nm)**<br>1.6 × 1.9<br>**Formal charge**<br>-1 | PES<br>PES<br>PES<br>Zr-BTB/PES<br>Zr-BTB/PES<br>Zr-BTB/PES<br>Zr-BTB-$NH_2$/PES<br>Zr-BTB-$NH_2$/PES<br>Zr-BTB-$NH_2$/PES<br>Zr-TATB/PES<br>Zr-TATB/PES<br>Zr-TATB/PES | 7822±481<br>48±26<br>73±46<br>120±84 | 21±3<br>83±7<br>79±17<br>73±19 | 18±4<br>17±10<br>21±9<br>23±8 |
| MO | 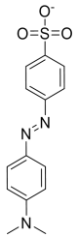 | **Molecular weight (g $mol^{-1}$)**<br>304.34<br>**Dimensions of hydrated MO* (nm)**<br>1.0 × 1.2<br>**Formal charge**<br>-1 | PES<br>PES<br>PES<br>Zr-BTB/PES<br>Zr-BTB/PES<br>Zr-BTB/PES<br>Zr-BTB-$NH_2$/PES<br>Zr-BTB-$NH_2$/PES<br>Zr-BTB-$NH_2$/PES<br>Zr-TATB/PES<br>Zr-TATB/PES<br>Zr-TATB/PES | 9276±516<br>4600±1254<br>3332±1516<br>3675±1854 | 0.9±0.2<br>2±0.4<br>1±0.3<br>2±0.6 | 0.8±0.2<br>2±0.4<br>1±0.2<br>1±0.4 |
| MnB | 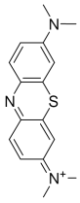 | **Molecular weight (g $mol^{-1}$)**<br>284.40<br>**Dimensions of hydrated MnB* (nm)**<br>1.4 × 0.9<br>**Formal charge**<br>+1 | PES<br>PES<br>PES<br>Zr-BTB/PES<br>Zr-BTB/PES<br>Zr-BTB/PES<br>Zr-BTB-$NH_2$/PES<br>Zr-BTB-$NH_2$/PES<br>Zr-BTB-$NH_2$/PES<br>Zr-TATB/PES<br>Zr-TATB/PES<br>Zr-TATB/PES | 9705±394<br>4769±1152<br>2194±1437<br>2907±2194 | 7±5<br>26±21<br>18±16<br>22±7 | 6±5<br>21±17<br>15±14<br>18±6 |

*Dimensions of hydrated BBG, MO and MnB dyes were reported by Ang and Hong.[19]

to the MONs (at 2θ = 5.1°) was observed in the PXRD patterns of the three composite membranes (**Figure 3d-3f**), indicating that the crystallinity of all three MONs was maintained during membrane preparation. SEM imaging of the PES support revealed an expected porous structure (**Figure 3g**). Energy-dispersive X-ray spectroscopy (EDS) elemental mapping characterisations showed homogeneous distributions of C, O and S elements in the PES support (**Figure S8**). SEM imaging of the Zr-BTB/PES membrane showed that the deposited MONs formed a continuous layer on the surface of PES, and confirmed a good adhesion between the MONs and the PES supports (**Figure 3g and S10**). The Zr-BTB-$NH_2$/PES membrane (**Figure 3h and S12**) showed a similar surface morphology to the Zr-BTB/PES membrane and EDS elemental mapping characterisations of the two membranes showed the presence of Zr element in them (Zr-BTB/PES: 6.6 wt%, Zr-BTB-$NH_2$/PES: 5.4 wt%, **Figure S11 and S13**). SEM imaging of the Zr-TATB/PES membrane (**Figure 3i and S14**) showed that it had a similar surface morphology to the other two composite membranes.

These results indicated that the Zr-BTB/PES, Zr-BTB-$NH_2$/PES and Zr-TATB/PES membranes with maintained MON crystallinity and similar surface morphologies were successfully prepared, and the use of these membranes in water purification were studied.

**Water purification experiments.** The water purification performance of the three composite membranes (Zr-BTB/PES, Zr-BTB-$NH_2$/PES and Zr-TATB/PES) and the PES supports were investigated for a series of dyes with different sizes and charges, such as BBG, MO and MnB (**Table 1**). The PES supports used in this work have a pore size of 200 nm that is significantly larger than the sizes of hydrated dyes Therefore, we anticipate that the PES support has little rejection to the dyes, but high water permeance. The three MONs deposited on the PES supports have an isoreticular structure and the same pore size of 0.54 nm that is smaller than the sizes of the dyes (**Table 1**).[18,19] Therefore, they can act as selective layers on the PES supports to separate the dyes in aqueous solutions. In addition, the adsorptions of BBG, MO and MnB dyes on the three

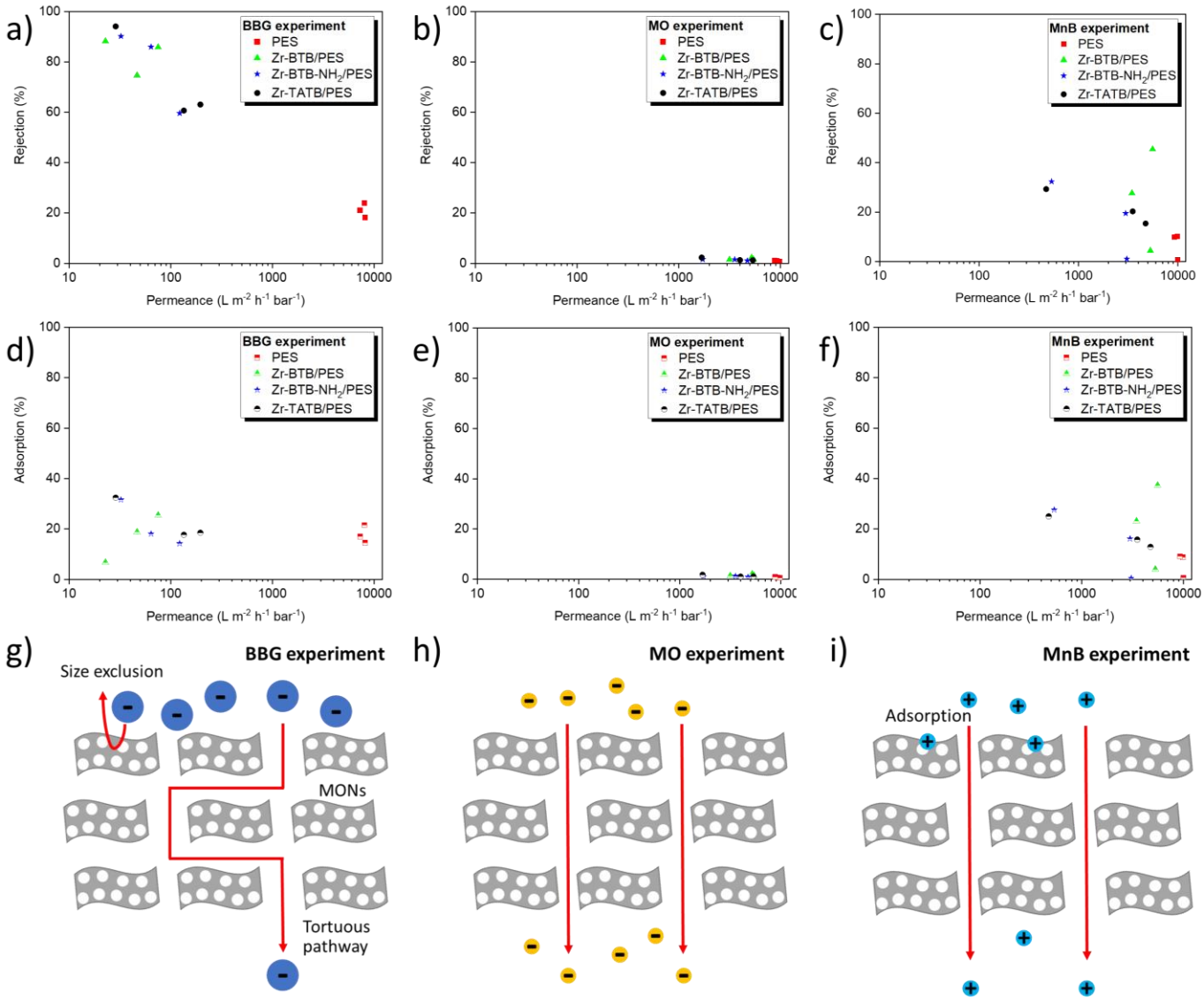


**Figure 4.** Rejection rate and water permeance of the PES support, Zr-BTB/PES, Zr-BTB-$NH_2$/PES and Zr-TATB/PES membranes in (a) BBG, (b) MO and (c) MnB experiments. Adsorption rate and water permeance of the PES support, Zr-BTB/PES, Zr-BTB-$NH_2$/PES and Zr-TATB/PES membranes in (d) BBG, (e) MO and (f) MnB experiments. Schematic illustrations showing how different dyes passed through the selective layers composed of MONs in (g) BBG, (h) MO and (i) MnB experiments.

composite membranes and the PES supports during water purification experiments were also investigated to understand the interactions between the membranes and the dyes with different charges and their effects on the water purification performance of the membranes.

The water purification experiments were conducted using a Sterlitech HP4750 stirred cell operated at 1 bar pressure (**Figure S16**) and all experiments were stirred at 500 rpm in order to minimise the concentration polarisation effect.[19] 0.25 L of aqueous dye solution feed (10 mg $L^{-1}$) was added and the experiment stopped when approximately 0.2 L of permeate was collected. The water purification experiment was repeated three times for each membrane. The water permeance, rejection rate and adsorption rate of the membranes toward aqueous BBG, MO and MnB solutions are calculated as detailed in the **Experimental** section and the results are summarised in **Table 1**.

The water purification performance of the membranes toward negatively charged BBG dyes was studied. As shown in **Figure 4a and Table 1**, the PES supports showed water permeances between 7270.3 L $m^{-2}$ $h^{-1}$ $bar^{-1}$ and 8152.9 L $m^{-2}$ $h^{-1}$ $bar^{-1}$ and rejection rates between 18.2% and 24.0% toward BBG. It is worth noting that this is significantly higher baseline water permeance and lower rejection rate than the PAN-400 supports used by Zhao and co-workers.[22] Spin-coating of Zr-BTB, Zr-BTB-$NH_2$ and Zr-TATB MONs onto the PES supports significantly increased their rejection rates toward BBG (**Figure 4a**). In three repeated experiments, the best-performing Zr-BTB/PES, Zr-BTB-$NH_2$/PES and Zr-TATB/PES membranes exhibited rejection rates of 88.2%, 90.2% and 94.1% towards BBG, respectively (**Table 1**). This was because the pore size of the MONs (0.54 nm) was smaller than the size of hydrated BBG dyes (1.6 × 1.9 nm),[18,19] thus the three MONs deposited on the PES supports effectively rejected BBG dyes based on size exclusion (**Figure 4g**), improving their BBG rejection rates. It was also found that the adsorption rates of BBG on

the composite membranes were significantly lower than their rejection rates toward BBG (**Figure 4a and 4d**). This indicated that the high rejection rate of the composite membranes toward BBG was predominantly due to the size exclusion effect of the MONs, rather than the adsorption of dyes by the membranes.

Deposition of the three MONs onto the PES supports also decreased their permeances toward aqueous BBG solutions. This was because the BBG dyes could not directly pass through the pores of MONs due to their large size, they had to follow tortuous pathways between the nanosheets when they were passing through the selective layers composed of MONs (**Figure 4g**), lowering their permeances. Zhao and co-workers observed a similar decrease in water permeance and increase in dye rejection rate after coating Zr-BTB MONs onto PAN-400 supports.[22] Whereas, compared to their Zr-BTB/PAN-400 membranes (1-3.2 L $m^{-2}$ $h^{-1}$ $bar^{-1}$), the composite membranes prepared in this work showed higher water permeances (**Table 1**). In addition, the morphologies of the Zr-BTB/PES, Zr-BTB-$NH_2$/PES and Zr-TATB/PES membranes almost did not change after the BBG experiments (**Figure S18-S20**), indicating the good stability of the membranes.

The water purification performance of the membranes towards negatively charged MO dyes was investigated. Compared to BBG, the PES supports exhibited higher water permeance between 8782.6 L $m^{-2}$ $h^{-1}$ $bar^{-1}$ and 9811.8 L $m^{-2}$ $h^{-1}$ $bar^{-1}$, but almost no rejection toward MO (0.7%-1.1%, **Table 1**). Spin-coating of the three MONs onto the PES supports did not significantly improve their rejection rates toward MO(**Figure 4b**), and the best-performing Zr-BTB/PES, Zr-BTB-$NH_2$/PES and Zr-TATB/PES membranes showed rejection rates of only 2.3%, 1.6% and 2.3% toward MO, respectively (**Table 1**). The size of hydrated MO is 1.0 × 1.2 nm,[19] which is larger than the pore size of the three MONs (0.54 nm).[18,19] Therefore, the MO dyes should theoretically follow the tortuous pathways when they pass through the selective layers composed of MONs. However, compared to BBG, the slightly smaller MO dyes are more likely to pass through the gaps between adjacent MONs (**Figure 4h**). Therefore, all composite membranes exhibited high water permeances but almost no rejection toward MO.

The water purification performance of the membranes toward positively charged MnB dyes was studied. The PES supports exhibited permeances between 9252.8 L $m^{-2}$ $h^{-1}$ $bar^{-1}$ and 9973.7 L $m^{-2}$ $h^{-1}$ $bar^{-1}$ toward aqueous MnB solutions (**Table 1**), which were close to their permeances toward aqueous MO solutions because the two dyes are similar in size.[19] The removal of MnB dyes in aqueous solutions by the PES supports was predominantly due to adsorption. The best-performing PES support exhibited a rejection rate of 10.1% towards MnB, while the adsorption rate of MnB on this membrane reached 8.8% (**Table 1**). This is because the surface of PES support is negatively charged in water,[24] whereas the MnB dyes are positively charged (**Table 1**). Therefore, the electrostatic interactions between them can facilitate the adsorption of MnB on the PES supports.

Spin-coating of the three MONs onto the PES supports decreased their water permeances, but increased the adsorption rates of MnB on the membranes and their rejection rates toward MnB (**Figure 4c and Figure 4f**). In three repeated experiments, the best-performing Zr-BTB/PES, Zr-BTB-$NH_2$/PES and Zr-TATB/PES membranes exhibited rejection rates of 45.4%, 32.4% and 29.3% toward MnB dyes, respectively, and the adsorption rates of MnB on the membranes were 37.3%, 27.6% and 25.0%, respectively (**Table 1**). This indicated that the removal of MnB dyes in aqueous solutions by the composite membranes predominantly came from adsorption (**Figure 4i**) and the MONs deposited on the PES supports did not significantly improve their size exclusion capability towards MnB.

These results indicated that both size exclusion and adsorption can affect the water purification performance of the membranes (**Figure 4g-4i**). The Zr-BTB, Zr-BTB-$NH_2$ and Zr-TATB MONs have the same pore size of 0.54 nm[18] which is smaller than the size of hydrated BBG dyes (1.6 × 1.9 nm, **Table 1**)[19] Therefore, the MONs deposited on the PES supports effectively blocked BBG dyes based on size exclusion (**Figure 4g**), improving the rejection rates of the membranes toward aqueous BBG solutions. However, the improvements in BBG rejection rates was accompanied by a reduction in their water permeances. This is because the BBG dyes had to follow tortuous pathways between the nanosheets when they passed through the selective layers composed of MONs, decreasing their water permeances (**Figure 4g**). MO and BBG are both negatively charged in aqueous solutions, but the size of MO (1.0 × 1.2 nm, **Table 1**) is smaller than the size of BBG.[19] Therefore, the MO dyes are more likely to pass through the gaps between adjacent MONs (**Figure 4h**). As a result, all composite membranes exhibited high permeances but almost no rejection towards MO dyes. The size of hydrated MnB (1.4 × 0.9 nm, **Table 1**) is similar to MO,[19] but these two dyes have different charges. Due to electrostatic interactions, the negatively charged PES supports[24] exhibited higher adsorption rates toward positively charged MnB than negatively charged MO. Spin-coating of the three MONs onto the PES supports further increased the adsorptions of MnB on the membranes (**Figure 4i**), improving their rejection rates toward MnB dyes.

## Conclusions

An isoreticular series of Zr-tricarboxylate based MONs were investigated for dye separation applications. Ethanol suspensions containing monolayer Zr-BTB, Zr-BTB-$NH_2$ and Zr-TATB MONs were spin-coated onto highly permeable PES supports to prepare composite membranes. All three membranes exhibited high water permeances toward small anionic dyes such as MO, but rejected approximately 90% of larger anionic dyes such as BBG, which could be attributed to the size exclusion effect of the MONs. Compared to MO, the membranes showed higher rejection rates toward similarly sized but positively charged MnB due to the higher adsorption rates of MnB on the membranes. This work demonstrates that Zr-tricarboxylate based MONs are promising materials for use in water purification applications.

## Experimental

**General considerations.** All chemicals and solvents were obtained from commercial suppliers and used without any purification, apart

from the $H_3BTB\text{-}NH_2$ and $H_3TATB$ ligands were provided by Ram R. R. Prasad. Details of all equipment used and material characterisations can be found in the Supplementary Information.

**Preparation of Zr-BTB, Zr-BTB-$NH_2$ and Zr-TATB MONs.** The three MONs were synthesised by adapting the method reported by Zhao and co-workers.[8] $ZrCl_4$ (0.129 mmol) and $H_3BTB$, $H_3BTB\text{-}NH_2$ or $H_3TATB$ (0.068 mmol) were dissolved in DMF (15 mL), $H_2O$ (2 mL), and HCOOH (2 mL) in a glass reaction vial, which was placed in a reaction oven and heated at 120 ℃ for 24 hours. The resulting suspensions of the three MONs were centrifuged and washed three times with fresh DMF then ethanol. The washed MONs were stored in fresh ethanol as homogeneous suspensions with a concentration of 2.5 mg $mL^{-1}$ until needed.

**Preparation of water purification membranes.** The membranes were prepared by depositing two 500 µL portions of ethanol suspension of Zr-BTB, $ZrBTB\text{-}NH_2$ or Zr-TATB MONs (2.5 mg $mL^{-1}$) onto PES supports using a spin-coating method. The spin-coating of all membranes was conducted at 2500 rpm for 640 s using an Ossila spin coater. The PES supports used in this work were purchased from Sterlitech Corporation (diameter: 47 mm, pore size: 200 nm). All membranes were dried at room temperature before characterisations and water purification experiments.

**Water purification experiments.** The membranes were fixed in a Sterlitech HP4750 stirred cell for the water purification experiments (**Figure S16**). The cell was pressurised using $N_2$ gas at 1 bar, and the feed solution was stirred at 500 rpm during the experiments. For each experiment, 0.25 L of aqueous BBG, MO or MnB solution (10 mg $L^{-1}$) was used as the feed which was filtered by the membrane and the experiment stopped when approximately 0.2 L of permeate was collected. The concentrations of the feed, permeate and retentate were measured by an UV-Vis spectrophotometer, and the water purification experiment was repeated three times for each membrane. The water permeance, rejection rate and adsorption rate of the membranes are calculated using equations reported in the literature[19] and the results are summarised in **Table 1**.

The water permeance, $\mathbf{F}$, of each membrane is calculated by **eq 1**.

$$\mathbf{F} = \frac{\mathbf{V_P}}{\mathbf{A} \times \mathbf{t} \times \mathbf{\Delta_P}} \qquad \text{(equation 1)}$$

Where, $\mathbf{V_P}$ is the volume of the permeate (unit: L), $\mathbf{A}$ is the effective area of the membrane (unit: $m^2$), $\mathbf{t}$ is the time of collecting approximately 0.2 L of permeate solution (unit: h), and $\mathbf{\Delta_P}$ is the operating pressure (unit: bar). Thus, the unit of $\mathbf{F}$ is L $m^{-2}$ $h^{-1}$ $bar^{-1}$. In this work, $\mathbf{A}$ and $\mathbf{\Delta_P}$ are 1.46E-03 $m^2$ and 1 bar, respectively.

The rejection rate, $\mathbf{R}$, of each membrane is calculated by **eq 2**.

$$\mathbf{R} = \frac{\mathbf{C_F} - \mathbf{C_P}}{\mathbf{C_F}} \times \mathbf{100}\% \qquad \text{(equation 2)}$$

Where, $\mathbf{C_F}$ and $\mathbf{C_P}$ are the concentrations of the feed and the permeate solutions, respectively.

The adsorption rate, $\mathbf{Ads}$, of each membrane is calculated by **eq 3**.

$$\mathbf{Ads} = \frac{\mathbf{V_F C_F} - (\mathbf{V_R C_R} + \mathbf{V_P C_P})}{\mathbf{V_F C_F}} \times \mathbf{100}\% \qquad \text{(equation 3)}$$

Where, $\mathbf{V_F}$, $\mathbf{V_p}$ **and** $\mathbf{V_R}$ are the volumes of the feed, permeate, and retentate solutions, respectively $\mathbf{C_F}$, $\mathbf{C_p}$ **and** $\mathbf{C_R}$ are the concentrations of the feed, permeate and retentate solutions, respectively. In this work, $\mathbf{V_F}$, $\mathbf{V_p}$ **and** $\mathbf{V_R}$ are approximately 0.25 L, 0.2 L and 0.05 L, respectively.

## Conflicts of interest

There are no conflicts to declare.

## Acknowledgements

Thanks to EPSRC for funding Ram R. R. Prasad.

## References


1. D. J. Ashworth and J. A. Foster, *J. Mater. Chem. A*, 2018, **6**, 16292-16307.
2. J. Nicks, K. Sasitharan, R. R. R. Prasad, D. J. Ashworth and J. A. Foster, *Adv. Funct. Mater.*, 2021, **31**, 2103723.
3. F. Moghzi, J. Soleimannejad, E. C. Sañudo and J. Janczak, *ACS Appl. Mater. Interfaces*, 2020, **12**, 44499-44507.
4. J. Nicks, J. Zhang and J. A. Foster, *Chem. Commun.*, 2019, **55**, 8788-8791.
5. K. Sasitharan, D. G. Bossanyi, N. Vaenas, A. J. Parnell, J. Clark, A. Iraqi, D. G. Lidzey and J. A. Foster, *J. Mater. Chem. A*, 2020, **8**, 6067-6075.
6. Y. Song, J. Yang, L. Wang and Z. Xie, *ChemMedChem*, 2020, **15**, 416-419.
7. Y. Peng and W. Yang, *Adv. Mater. Interfaces*, 2019, **7**, 1901514.
8. H. Yuan, G. Liu, Z. Qiao, N. Li, P. J. S. Buenconsejo, S. Xi, A. Karmakar, M. Li, H. Cai, S. J. Pennycook and D. Zhao, *Adv. Mater.*, 2021, **33**, e2101257.
9. Z. Hu, E. M. Mahdi, Y. Peng, Y. Qian, B. Zhang, N. Yan, D. Yuan, J.-C. Tan and D. Zhao, *J. Mater. Chem. A*, 2017, **5**, 8954-8963.
10. G.-Y. Qiao, S. Yuan, J. Pang, H. Rao, C. T. Lollar, D. Dang, J.-S. Qin, H.-C. Zhou and J. Yu, *Angew. Chem. Int. Ed.*, 2020, **59**, 18224–18228.
11. H. Zhang, B. Luo, P. An, X. Zhan, F. Lan and Y. Wu, *ACS Appl. Bio Mater.*, 2022, **5**, 3500-3508.
12. D. Zhan, Z. Yu, A. Saeed, Q. Hu, N. Zhao, W. Xu, J. Wang, L. Kong and J. Liu, *J. Mater. Chem. C*, 2023, **11**, 10738-10747.
13. X. Feng, Y. Ren, H. Wang, W. Wu and H. Jiang, *Catal. Sci. Technol.*, 2023, **13**, 7036-7045.
14. Z. Cheng, J. Lian, Y. Chen, Y. Tang, Y. Huang, J. Zhang, S. Xiang and Z. Zhang, *CCS Chem.*, 2023, DOI: 10.31635/ccschem.023.202303074.
15. D. Wang, Y. Ying, Y. Zheng, Y. Pu, Z. Yang and D. Zhao, *J. Membr. Sci. Lett.*, 2022, **2**, 100017.

16. H. Liu, H. Wang, Q. Song, K. Kuster, U. Starke, P. A. van Aken and E. Klemm, *Angew. Chem. Int. Ed.*, 2022, **61**, e202117058.
17. Y. Cheng, S. R. Tavares, C. M. Doherty, Y. Ying, E. Sarnello, G. Maurin, M. R. Hill, T. Li and D. Zhao, *ACS Appl. Mater. Interfaces*, 2018, **10**, 43095-43103.
18. Y. Pu, Z. Yang, V. Wee, Z. Wu, Z. Jiang and D. Zhao, *J. Membr. Sci.*, 2022, **641**, 119912.
19. H. Ang and L. Hong, *ACS Appl. Mater. Interfaces*, 2017, **9**, 28079-28088.
20. L. Shu, L.-H. Xie, Y. Meng, T. Liu, C. Zhao and J.-R. Li, *J. Membr. Sci.*, 2020, **603**, 118049.
21. Y. Peng, R. Yao and W. Yang, *Chem. Commun.*, 2019, **55**, 3935-3938.
22. H. Yuan, K. Li, D. Shi, H. Yang, X. Yu, W. Fan, P. J. S. Buenconsejo and D. Zhao, *Adv. Mater.*, 2023, **35**, e2211859.
23. X. Feng, Y. Song and W. Lin, *J. Am. Chem. Soc.*, 2021, **143**, 8184-8192.
24. D. Breite, M. Went, I. Thomas, A. Prager and A. Schulze, *RSC Adv.*, 2016, **6**, 65383-65391.

## Supplementary Information

# An isoreticular series of Zr-tricarboxylate based metal-organic nanosheets for water purification applications

Jiangtian Tan,[a] Bethany J. Lingard,[a] Ram R. R. Prasad[a] and Jonathan A. Foster*[a]

[a]*Department of Chemistry, University of Sheffield, Sheffield, UK.*

**Table of contents**

## S1. Equipment and Software

### S1.1. Atomic force microscopy

Atomic force microscopy (AFM) images were recorded using a Bruker Multimode 5 Atomic Force Microscope, operating in soft-tapping mode in air under standard ambient temperature and pressure, fitted with Bruker OTESPA-R3 silicon cantilevers. AFM samples were prepared by drop-casting 10 µL of diluted ethanol suspensions of metal-organic nanosheets (MONs) onto the centre of freshly cleaved mica sheets heated to 120 °C on a hot plate. These mica sheets were stuck to stainless steel, magnetic Agar scanning probe microscopy specimen discs. All AFM images reported in this work were processed using Gwyddion software.

### S1.2. Dynamic light scattering

Dynamic light scattering (DLS) data for the MONs were collected using a Malvern ZETA SIZER Nano series instrument, using a He-Ne laser at 633 nm, operating in backscatter mode (173°). Polystyrene disposable cuvettes were used for the DLS experiments, and the temperature for the DLS experiments was set to 25 °C.

### S1.3. Powder X-ray diffraction

Powder X-ray diffraction (PXRD) data of the MONs and the membranes were collected using a Bruker-AXS D8 diffractometer using Cu $K_\alpha$ ($\lambda$=1.5418 Å) radiation and a LynxEye position sensitive detector in Bragg Brentano parafocussing geometry using a flat silicon plate.

### S1.4. Scanning electron microscopy

Scanning electron microscopy (SEM) samples were prepared by loading the MONs and membranes onto carbon sticky tabs placed on aluminium SEM sample stubs, coated with gold using an Edwards S150B gold sputter coater and loaded into a TESCAN VEGA3 LMU SEM. All SEM images and EDS element layered images reported in this work were collected using the secondary electron detector.

### S1.5. Ultraviolet-visible spectroscopy

Ultraviolet-visible (UV-Vis) absorption spectra were collected using a Cary 60 or a Cary 50 Probe UV-Vis instrument, using a 1 cm internal length quartz cuvette and the Cary WinUV, Scan software.

## S2. MONs and Membranes

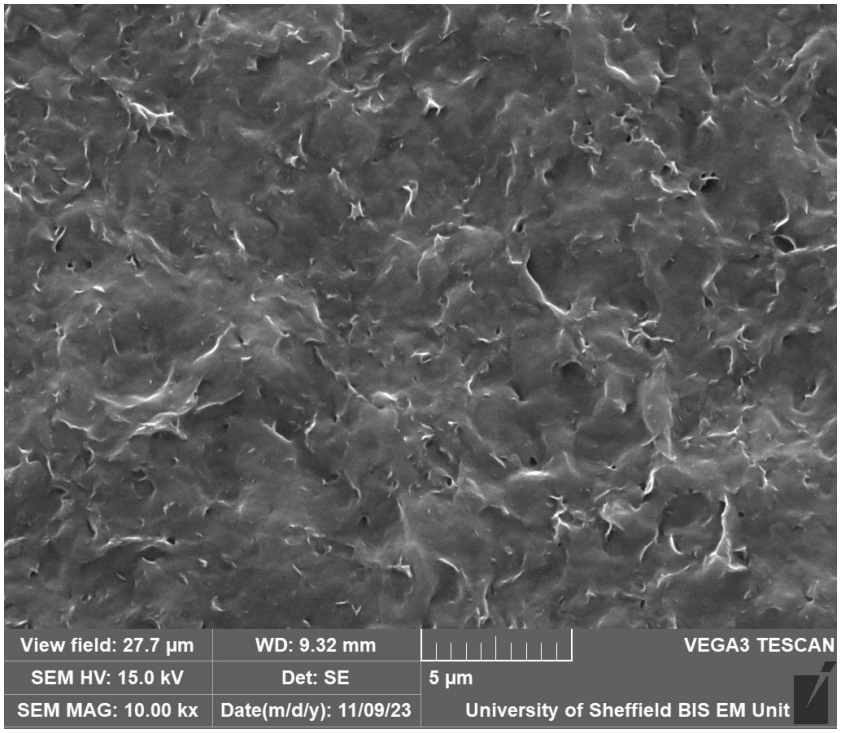


**Figure S1.** SEM image of Zr-BTB MONs.

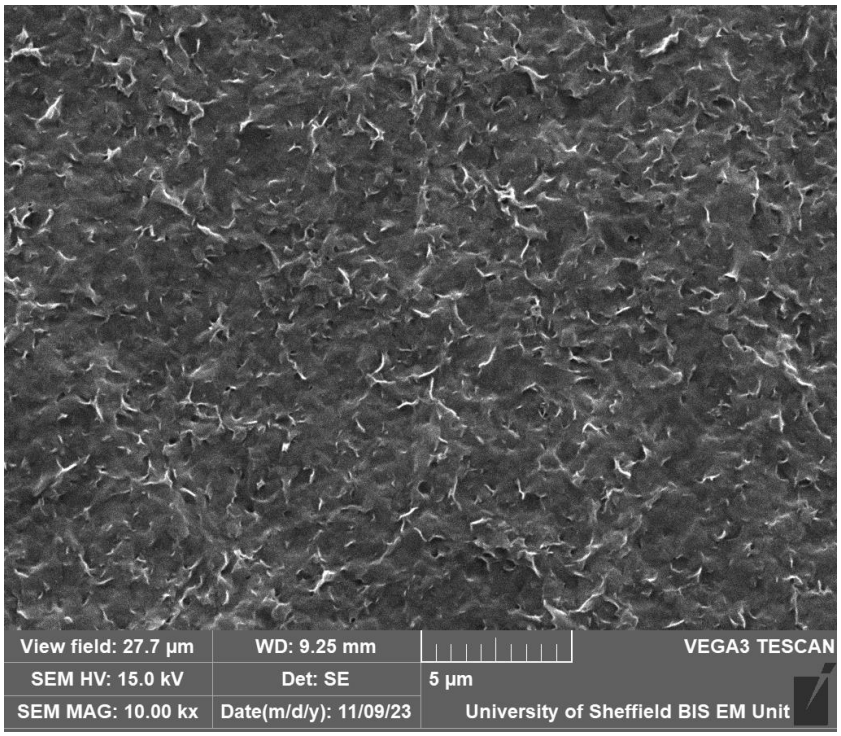


**Figure S2.** SEM image of Zr-BTB-$NH_2$ MONs.

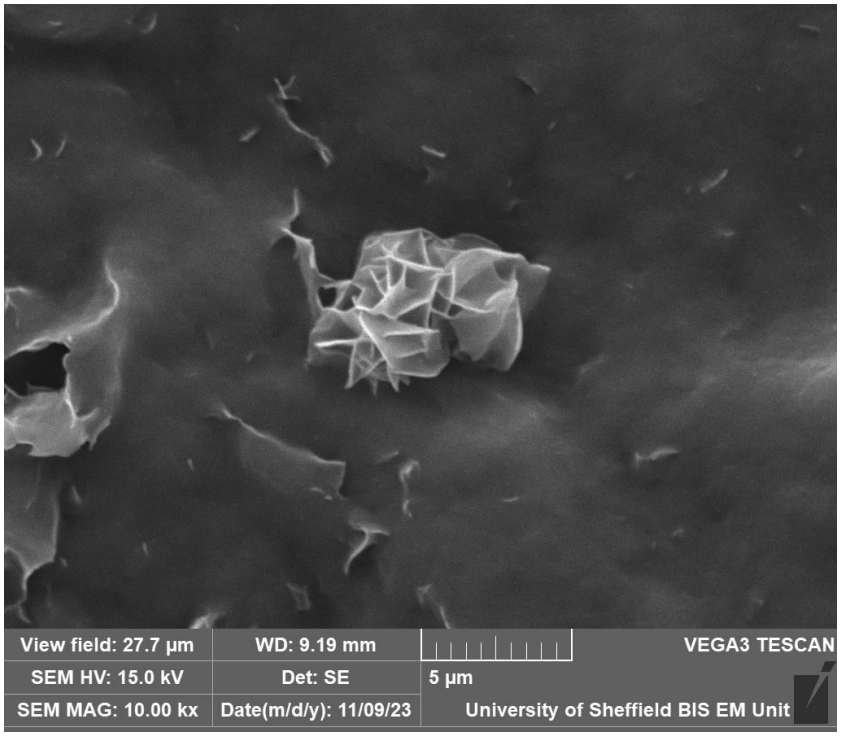


**Figure S3.** SEM image of Zr-TATB MONs.

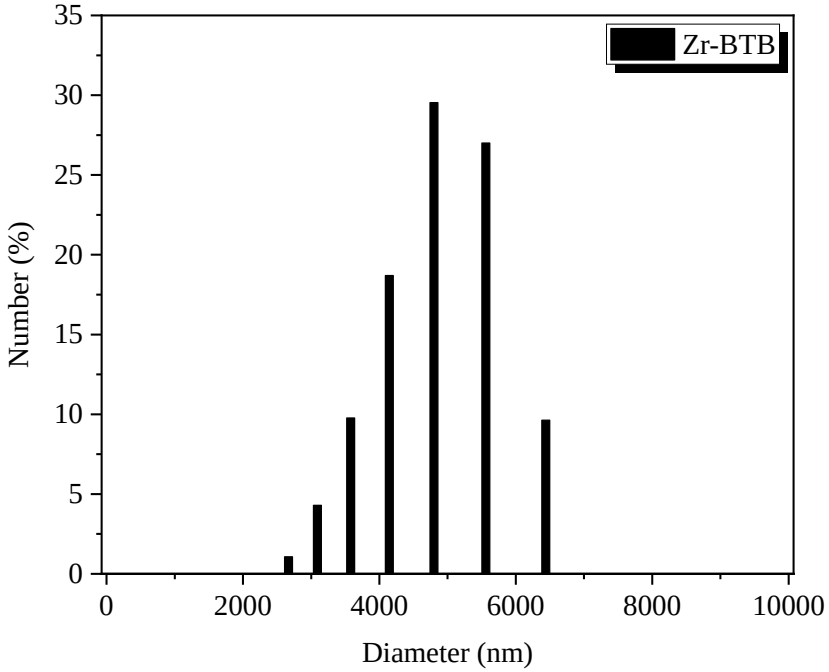


**Figure S4.** DLS graph showing particle size distribution of Zr-BTB MONs.

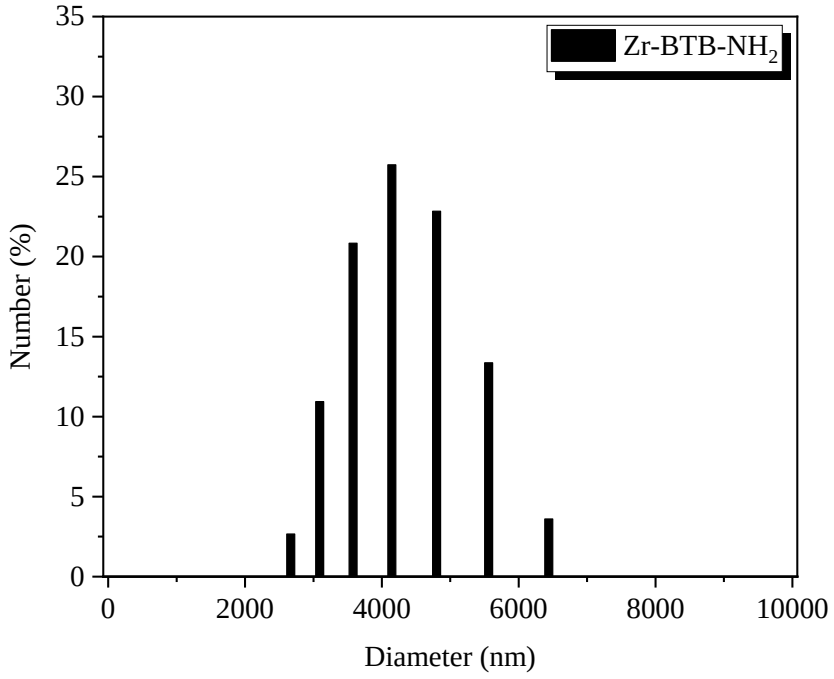


**Figure S5.** DLS graph showing particle size distribution of Zr-BTB-$NH_2$ MONs.

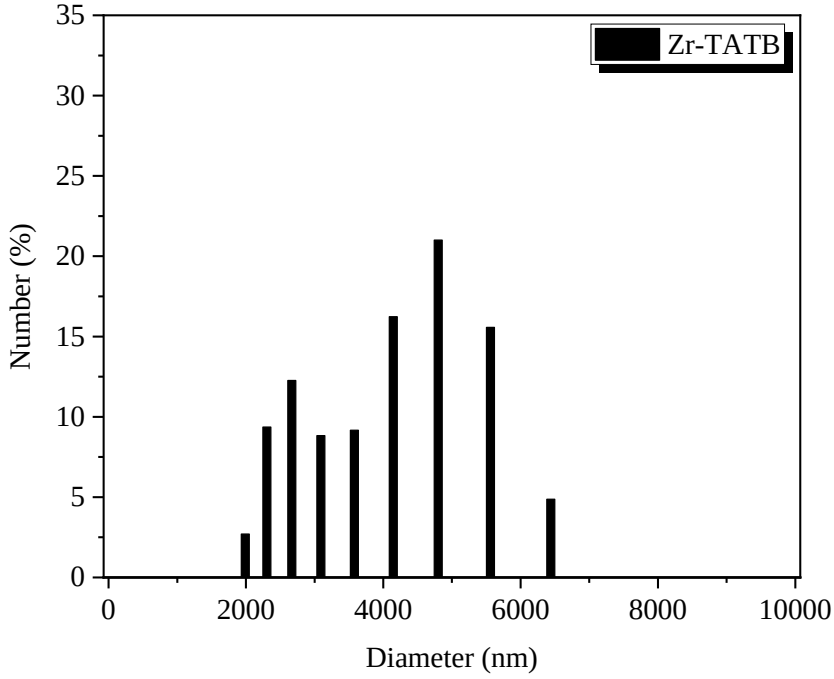


**Figure S6.** DLS graph showing particle size distribution of Zr-TATB MONs.

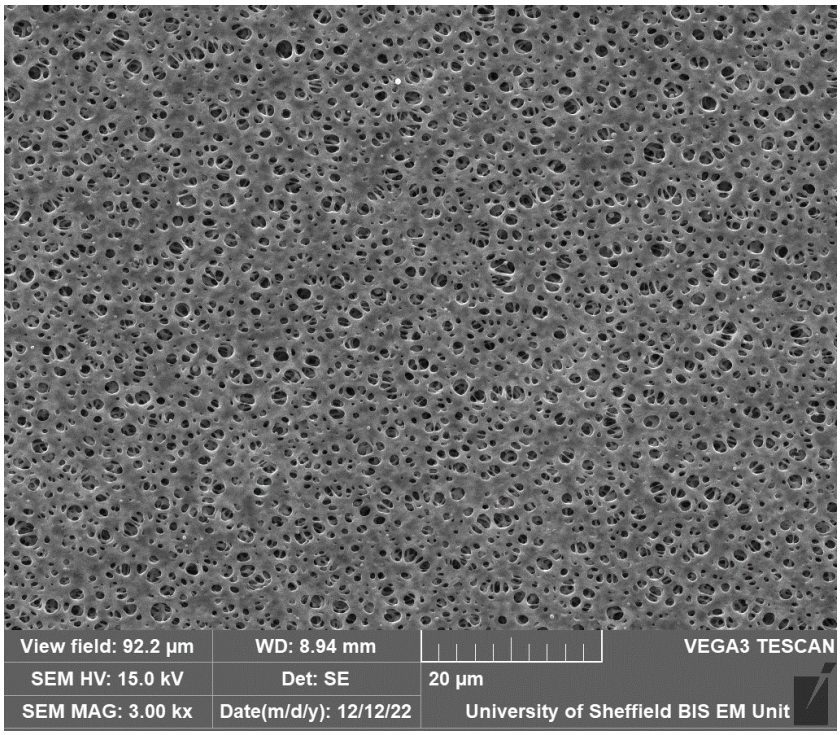


**Figure S7.** SEM image of PES support.

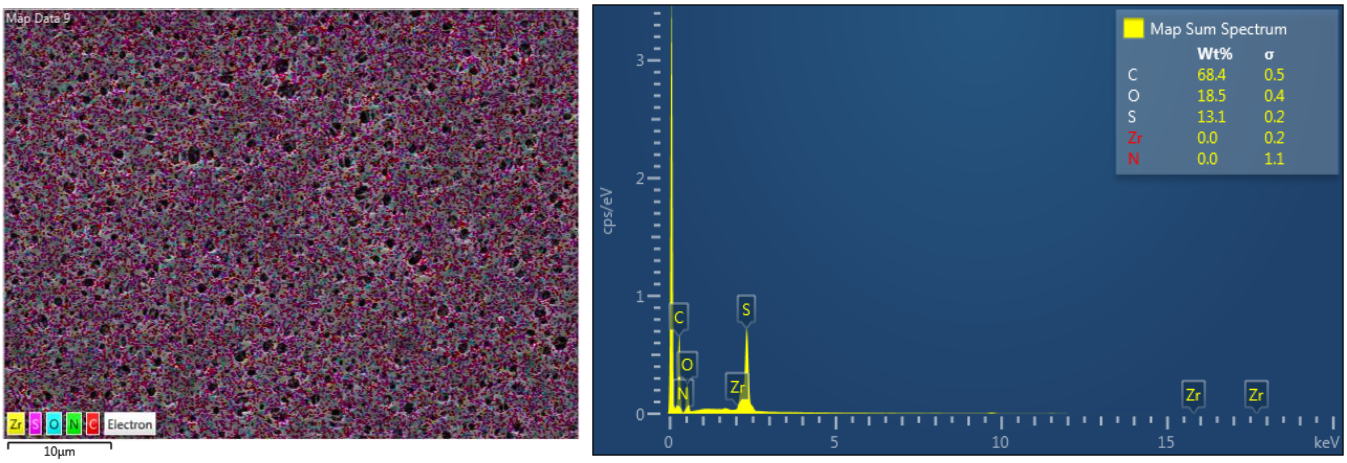


**Figure S8.** EDS element layered image of PES support and corresponding EDS spectrum.

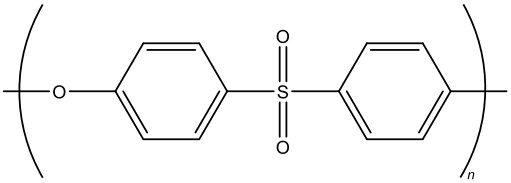


**Figure S9.** Chemical structure of polyethersulfone (PES).

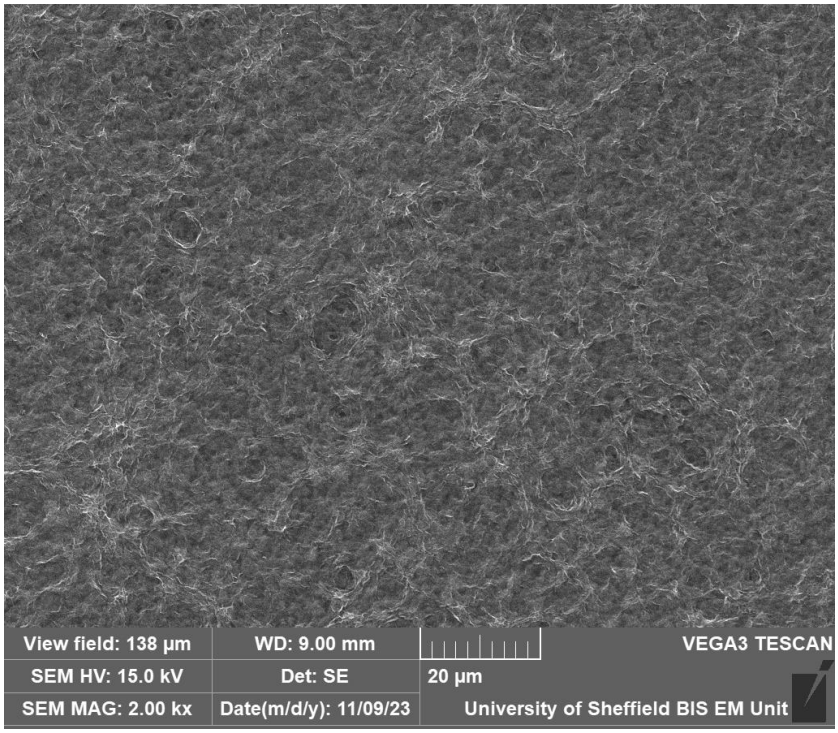


**Figure S10.** SEM image of Zr-BTB/PES membrane.

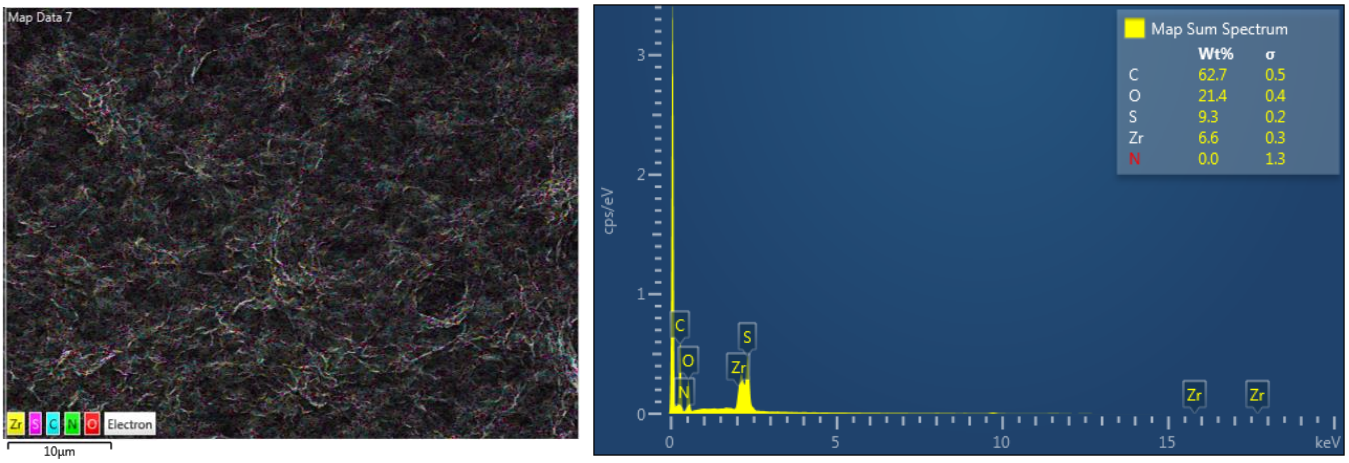


**Figure S11.** EDS element layered image of Zr-BTB/PES membrane and corresponding EDS spectrum.

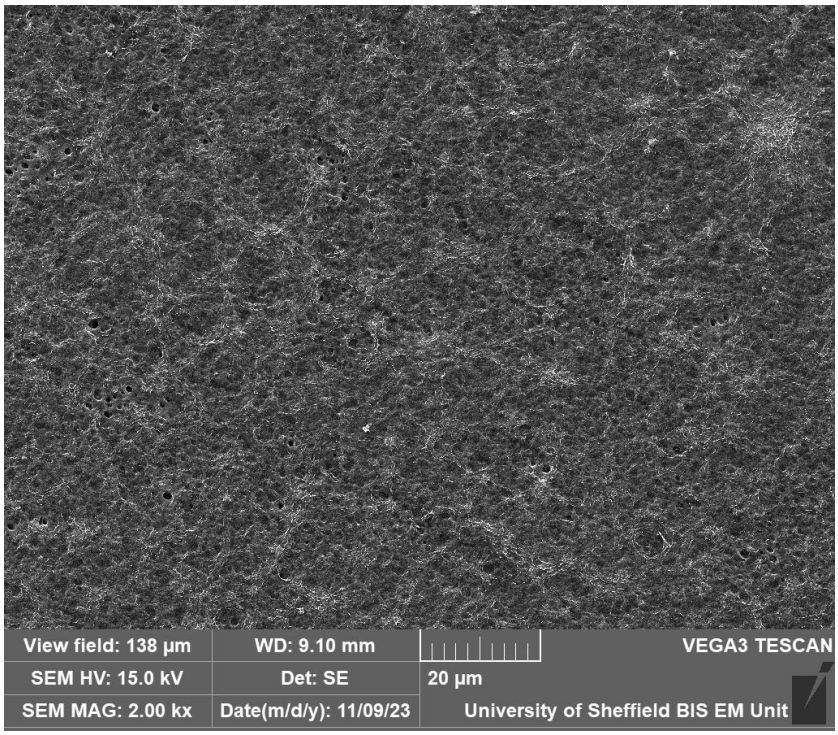


**Figure S12.** SEM image of Zr-BTB-$NH_2$/PES membrane.

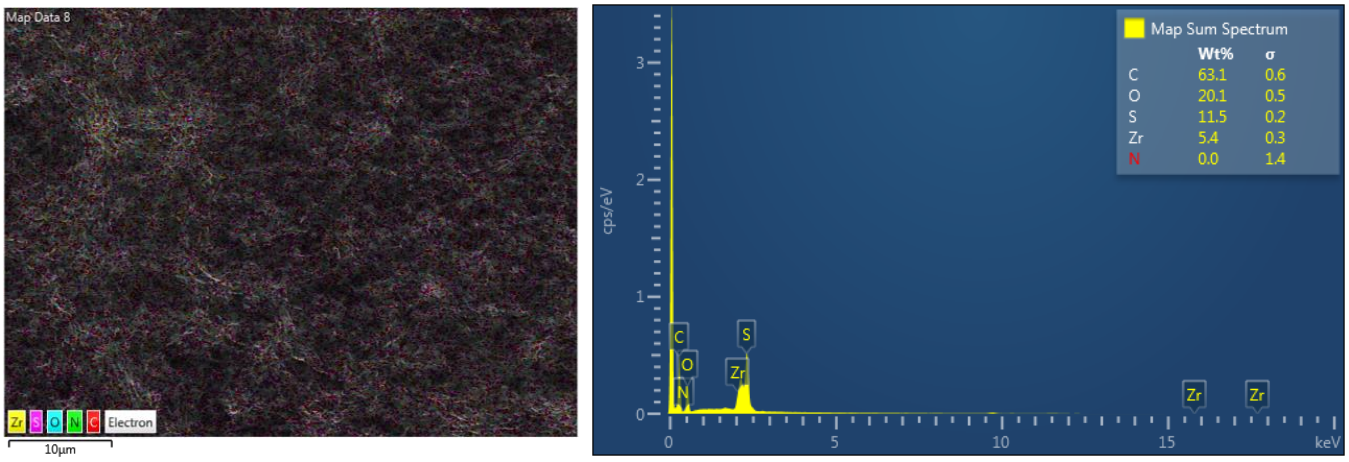


**Figure S13.** EDS element layered image of Zr-BTB-$NH_2$/PES membrane and corresponding EDS spectrum.

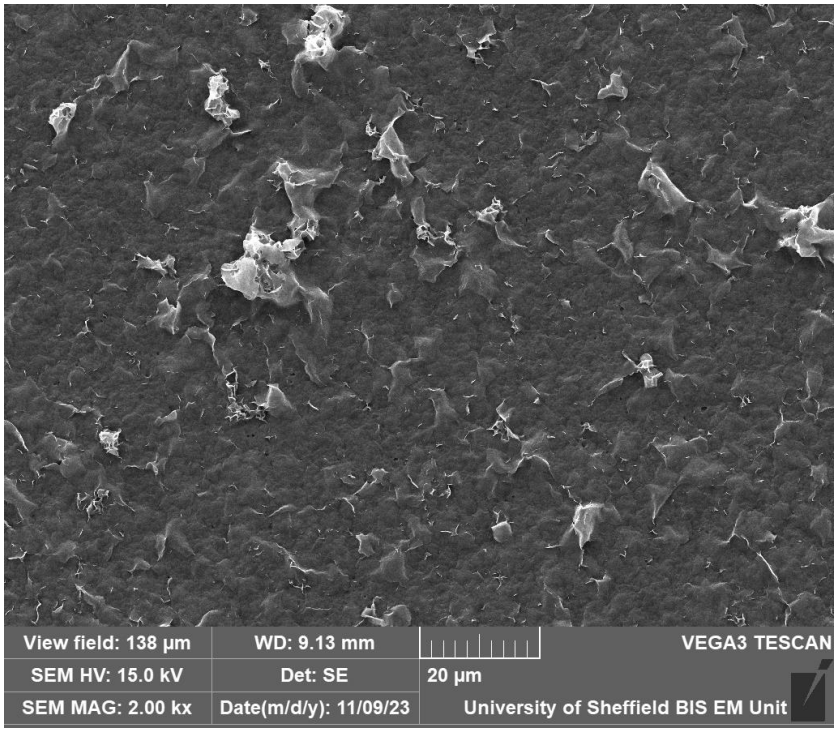


**Figure S14.** SEM image of Zr-TATB/PES membrane.

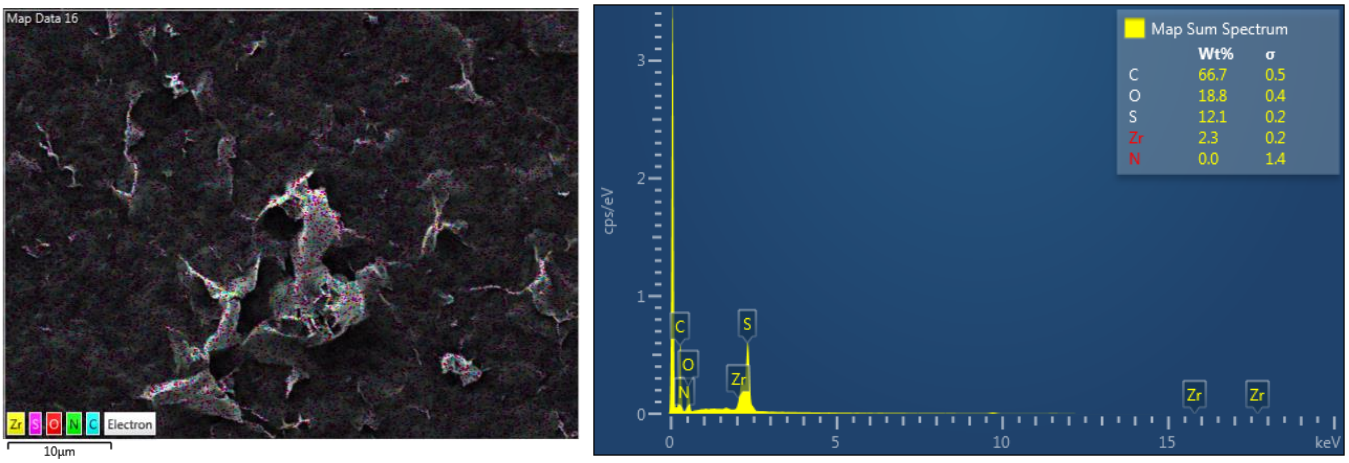


**Figure S15.** EDS element layered image of Zr-TATB/PES membrane and corresponding EDS spectrum.

## S3. Water Purification Experiments

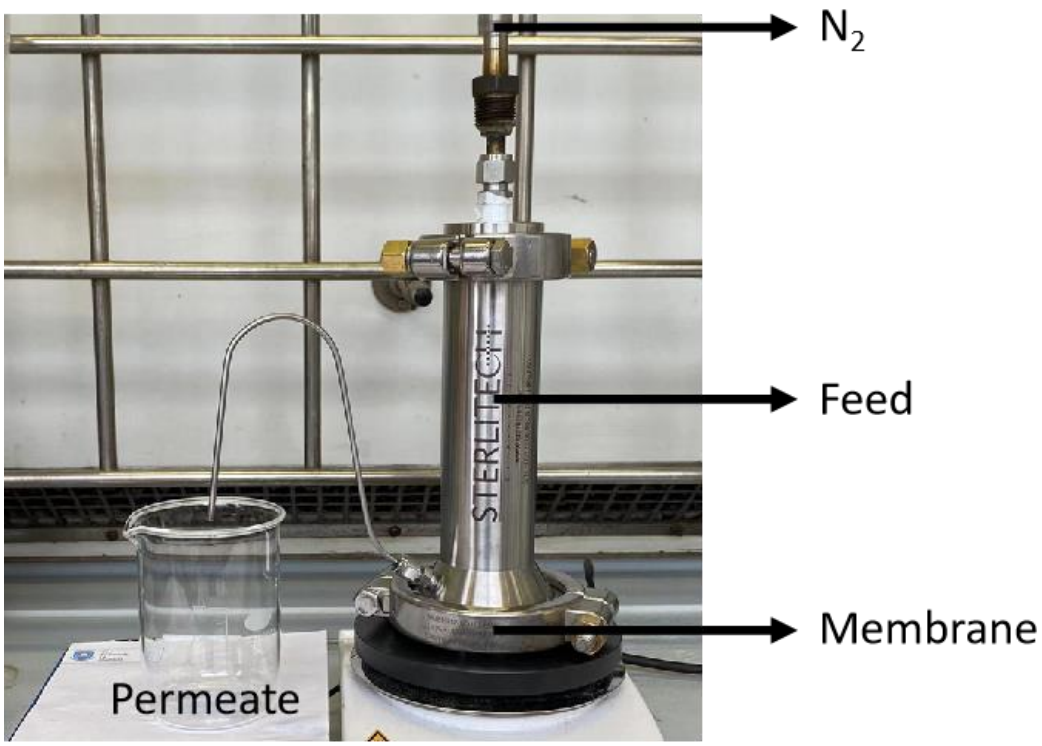


**Figure S16.** The Sterlitech HP4750 stirred cell for water purification experiments.

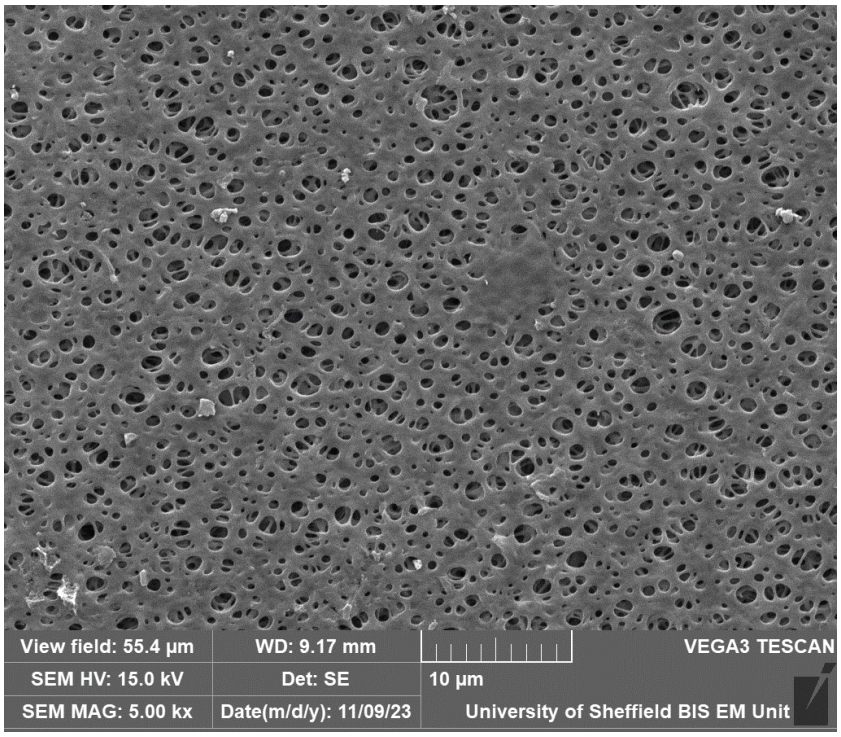


**Figure S17.** SEM image of PES support after BBG separation experiment.

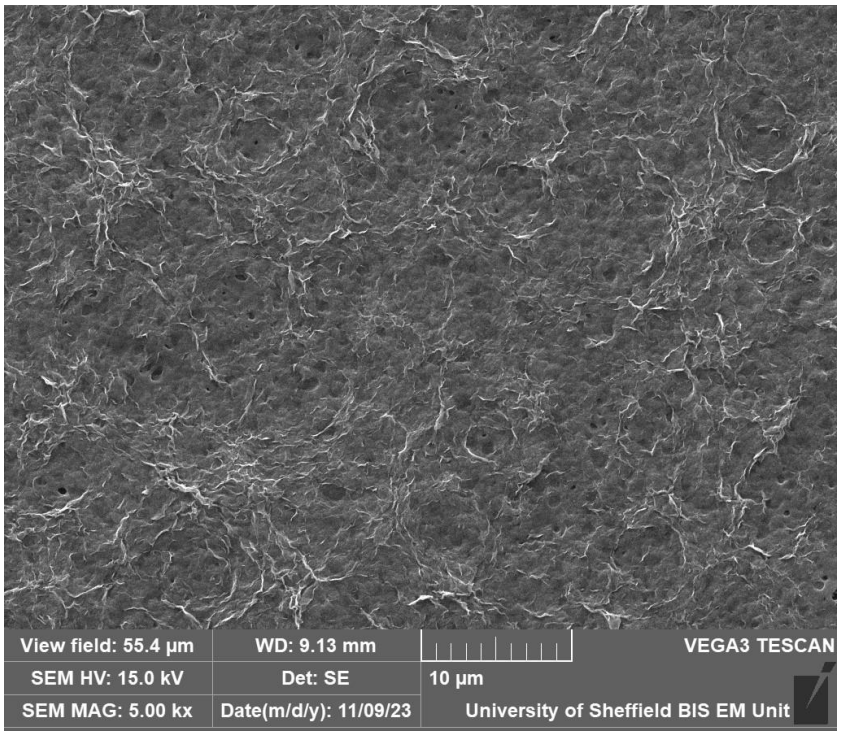


**Figure S18.** SEM image of Zr-BTB/PES membrane after BBG experiment.

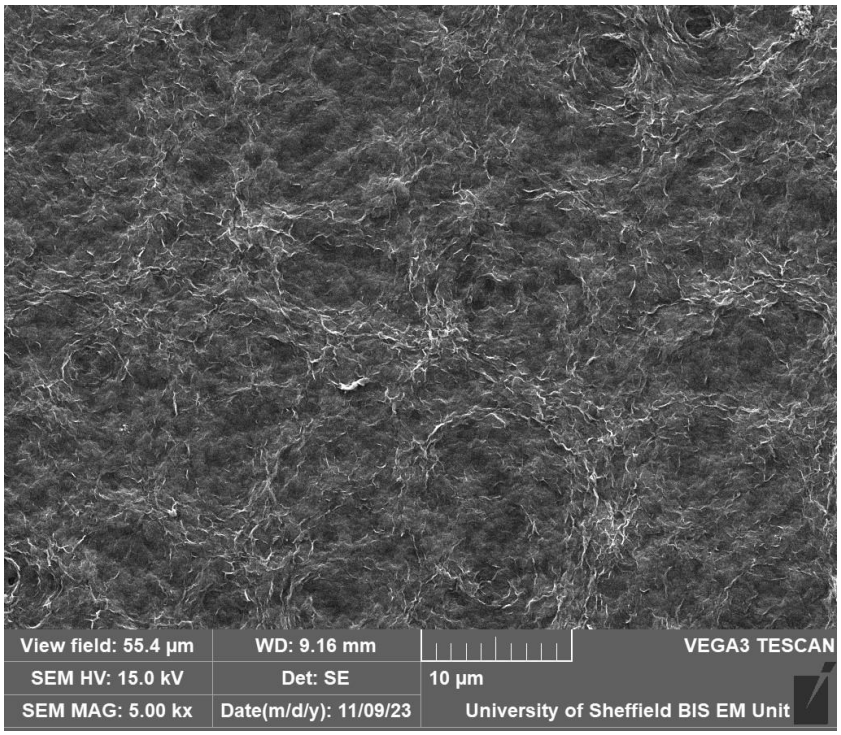


**Figure S19.** SEM image of Zr-BTB-$NH_2$/PES membrane after BBG experiment.

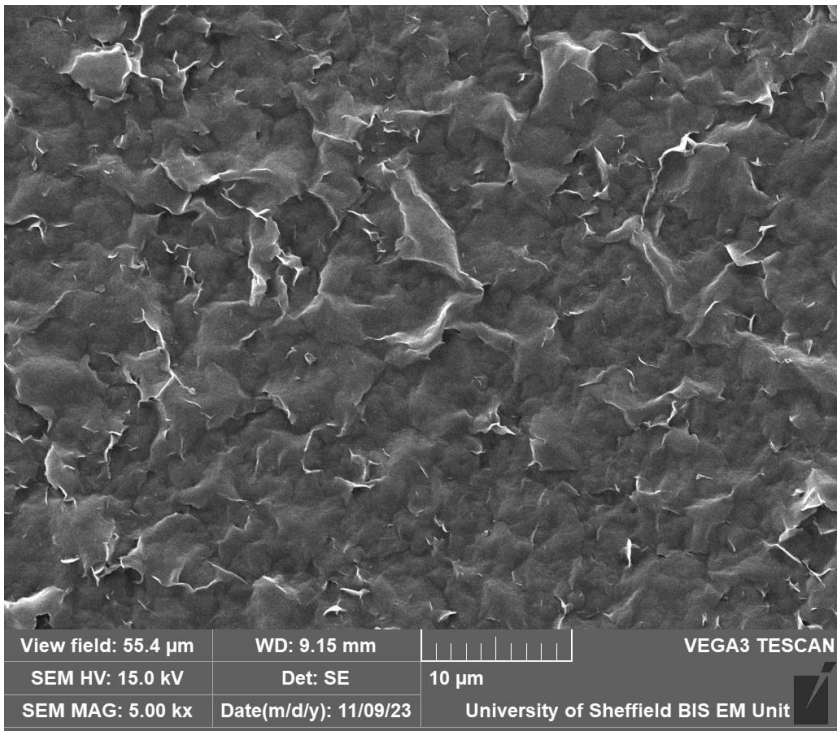


**Figure S20.** SEM image of Zr-TATB/PES membrane after BBG experiment.

# Chapter 4

# Zirconium-Based Metal-Organic Nanosheets for Gas Separation Applications

## Chapter 4

Zirconium-based metal-organic nanosheets for gas separation applications

Unpublished paper (full article)

**Jiangtian Tan,** Elsa Lasseuguette, Qian Jia, Ram R. R. Prasad, Maria-Chiara Ferrari, Paul A. Wright, and Jonathan A. Foster

**Author Contributions**

| | |
|---|---|
| **Jiangtian Tan** | Performed syntheses and characterisations of MONs and membranes. Performed gas permeation experiments. Drafted manuscript and SI and created all figures. |
| Elsa Lasseuguette | Performed syntheses of composite membranes and SEM characterisations of all membranes. Assisted Jiangtian Tan with the gas permeation experiments. Assisted in editing of manuscript. |
| Qian Jia | Performed gas adsorption experiments and assisted Jiangtian Tan with the preparation of mixed matrix membranes. |
| Ram R. R. Prasad | Provided $H_3$BTB-$NH_2$ ligand for the synthesis of MONs. |
| Maria-Chiara Ferrari | Supervised Elsa Lasseuguette. |
| Paul A. Wright | Supervised Qian Jia. |
| Jonathan A. Foster | Supervised Jiangtian Tan and Ram R. R. Prasad. Assisted in editing of manuscript. |

ARTICLE

# Zirconium-based metal-organic nanosheets for gas separation applications

Received 00th January 20xx,
Accepted 00th January 20xx

DOI: 10.1039/x0xx00000x

Jiangtian Tan,[a] Elsa Lasseuguette,[b] Qian Jia,[c] Ram R. R. Prasad,[a] Maria-Chiara Ferrari,*[b] Paul A. Wright*[c] and Jonathan A. Foster*[a]

Metal-organic nanosheets (MONs) are an emerging class of porous two-dimensional materials that have shown great potential for use in membrane-based separation applications. We investigated MONs composed of $Zr_6$ clusters and two different organic ligands for $CO_2/N_2$ separation application, 1,3,5-benzenetribenzoate (BTB) and 2'-amino-5'-(4-carboxyphenyl)-[1,1':3',1''-terphenyl]-4,4''-dicarboxylate (BTB-$NH_2$). The Zr-BTB and Zr-BTB-$NH_2$ MONs were incorporated into Matrimid and PEBAX polymers to prepare mixed matrix membranes (MMMs). Addition of 5 wt% of Zr-BTB into Matrimid did not significantly change its $CO_2$ permeability but increased its $N_2$ permeability, and thus decreased the $CO_2/N_2$ selectivity of the membrane. The decrease in selectivity was attributed to the agglomeration of Zr-BTB fillers which resulted in defects in the Zr-BTB/Matrimid MMM. Incorporation of 5 wt% of Zr-BTB or Zr-BTB-$NH_2$ MONs into PEBAX resulted in membrane densification, decreasing the $CO_2$ permeability and the $CO_2/N_2$ selectivity of the membrane. In addition, ethanol suspensions of the two MONs were coated onto porous polyacrylonitrile (PAN) supports to prepare composite membranes. However, high gas permeability and no $CO_2/N_2$ selectivity was observed for the composite membranes similar to the PAN support, which was attributed to the relatively large pore size of the two MONs and defects in the composite membranes. The MMMs and composite membranes will be optimised to improve their gas separation performance.

## Introduction

Increasing $CO_2$ emissions due to anthropological activities pose a great threat to the global environment and human society. Carbon capture and storage (CCS) has been proposed to reduce global $CO_2$ emission.[1] Various technologies have been developed for CCS, such as absorption by chemical solvents,[2] adsorption by porous materials[3] and membrane separations.[4,5] Among them, separation with membranes has gained significant interest due to its advantages of low capital investment, small footprint and high energy efficiency.[6,7] However, the current membrane market is dominated by polymeric membranes, and most of them suffer from a trade-off problem between their gas permeability and selectivity, which is known as the Robeson upper bounds.[8,9]

Various approaches have been developed to enhance the gas separation performance of conventional polymeric membranes. Among them, addition of organic or inorganic fillers into the polymeric membranes to prepare mixed matrix membranes (MMMs) has gained great interest.[10] Metal-organic frameworks (MOFs) are porous materials composed of metal ions or metal clusters linked by organic ligands.[11] MOFs have high surface areas, well-defined pore sizes, and diverse and tunable structures and chemical properties, making them ideal fillers for the preparation of MMMs for gas separation applications.[12,13]

Metal-organic nanosheets (MONs) are two-dimensional analogues of MOFs,[14] which have been explored in various applications, including sensing,[15] catalysis[16] and drug delivery,[17] and they are particularly suited for separation applications due their porous nature and well-defined pore sizes.[6,18] Similar to MOFs, MONs have also been used as fillers to prepare MMMs for gas separation applications.[19-22] For example, Gascon and co-workers reported that the incorporation of CuBDC (BDC = 1,4-benzenedicarboxylate) MONs into Matrimid 5218 polyimide polymers increased the $CO_2/CH_4$ separation selectivity of the membrane compared to the pure Matrimid membrane.[19] Apart from Matrimid, CuBDC MONs have also been blended with other polymers to prepare MMMs for use in gas separation applications, such as 6FDA-DAM (6FDA = 4,4'- (hexafluoroisopropylidene)diphthalic anhydride, DAM = diaminomesitylene) and PIM-1 (PIM = polymer of intrinsic microporosity).[20] Apart from CuBDC, other MONs such as $NH_2$-MIL-53(Al)[21] (MIL = Materials Institute Lavoisier) and ZIF-L (ZIF = zeolitic imidazolate framework)[22] have also been used to prepare MMMs for gas separation applications.

MONs composed of $Zr_6$ clusters and tritopic carboxylate ligands have attracted considerable attention. Due to their high stability and ease of synthesis and functionalisation,[23-25] they have shown great potential for use in catalysis,[26] sensing,[27] water purification[28] and particularly gas separation applications. For example, Zhao *et al.* incorporated Zr-BTB MONs as fillers (BTB = 1,3,5-benzenetribenzoate) into PIM-1 polymers to fabricate MMMs.[29] Due to π-π interactions and hydrogen bonding interactions between the MON fillers and the PIM-1 polymers, enhanced membrane crystallinity was observed after the addition of Zr-BTB MONs,

[a] *Department of Chemistry, University of Sheffield, Sheffield, UK. E-mail: jona.foster@sheffield.ac.uk.*
[b] *School of Engineering, University of Edinburgh, Edinburgh, UK. E-mail: M.Ferrari@ed.ac.uk.*
[c] *EaStCHEM School of Chemistry, University of St Andrews, St Andrews, UK. E-mail: paw2@st-andrews.ac.uk.*

† Footnotes relating to the title and/or authors should appear here.
Electronic Supplementary Information (ESI) available: [details of any supplementary information available should be included here]. See DOI: 10.1039/x0xx00000x

improving the $CO_2/CH_4$ and $CO_2/N_2$ selectivity of the PIM-1 membrane. Similar to Zr-BTB, the addition of Zr-BTB-COOH MON fillers was also found to enhance the crystallinity of PIM-1 membranes, improving their gas separation performance.[30] Zr-BTB-$NH_2$ MONs composed of $Zr_6$ clusters and 2'-amino-5'-(4-carboxyphenyl)-[1,1':3',1''-terphenyl]-4,4''-dicarboxylate (BTB-$NH_2$) ligands, have also been blended with PIM-1 polymers to prepare MMMs, which exhibited superior $CO_2/N_2$ separation performances that surpassed the 2008 Robeson upper bound.[9,31]

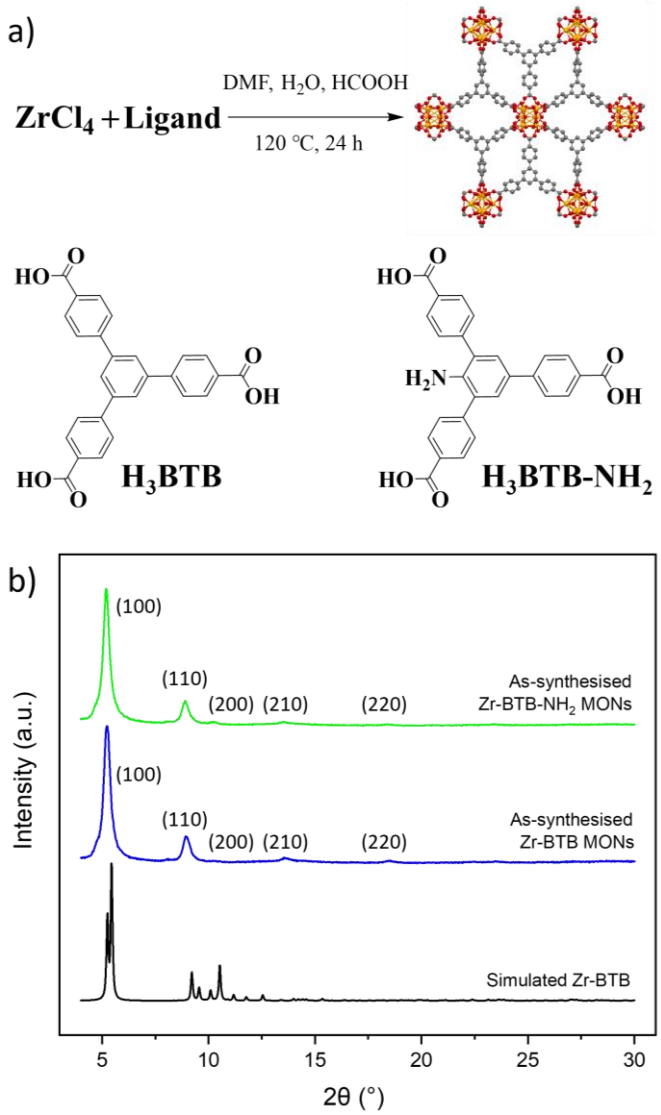


**Figure 1.** (a) Synthesis of Zr-BTB and Zr-BTB-$NH_2$ MONs. The crystal structure is downloaded from CCDC (deposition number: 1567188).[25] (b) PXRD patterns of the as-synthesised Zr-BTB and Zr-BTB-$NH_2$ MONs, comparing with the simulated pattern of Zr-BTB.

These examples showed the great potential of Zr-tricarboxylate based MONs for use in membrane-based gas separation applications. However, these MONs have only been incorporated as fillers into PIM-1 polymers to prepare MMMs,[29-31] and their interactions and compatibility with other polymers have not been investigated. Therefore, in this work, we incorporated Zr-BTB and Zr-BTB-$NH_2$ MONs into widely used Matrimid 5218[19,21] and PEBAX MH1657[32,33] polymers to prepare MMMs to investigate the effect of different filler-polymer interactions on the gas separation performance of the membranes. In addition, it was reported that the Zr-BTB MONs could be used to prepare composite membranes by a doctor blade casting method, and the membranes showed excellent dye separation and desalination performance.[28] In this work, we used a similar method and prepared composite membranes with Zr-BTB and Zr-BTB-$NH_2$ MONs and compared their $CO_2/N_2$ separation performance with the MMMs.

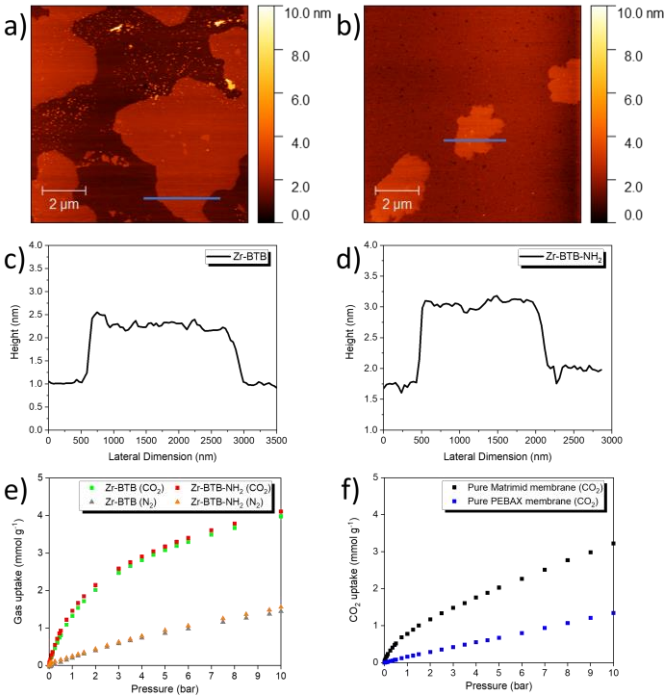


**Figure 2.** AFM images of (a) Zr-BTB MONs and (b) Zr-BTB-$NH_2$ MONs. (c,d) Height profiles measured along the blue lines on the AFM images (a) and (b), respectively. (e) $CO_2/N_2$ adsorption isotherms collected at 25 °C for as-synthesised Zr-BTB and Zr-BTB-$NH_2$ MONs. (f) $CO_2$ adsorption isotherms collected at 25 °C for pure Matrimid membrane and pure PEBAX membrane.

## Results and Discussion

**Preparation and characterisation of MONs.** The Zr-BTB and Zr-BTB-$NH_2$ MONs were prepared by adapting the solvothermal synthesis method reported by Zhao *et al*.[24] As shown in **Figure 1a**, zirconium(IV) chloride ($ZrCl_4$, 0.129 mmol) and $H_3BTB$ or $H_3BTB$-$NH_2$ (0.068 mmol) were dissolved in a mixture of *N,N*-dimethylformamide (DMF, 15 mL), formic acid (HCOOH, 2 mL) and deionised water ($H_2O$, 2 mL), which was incubated in a reaction oven at 120 °C for 24 h. The resulting suspensions of nanosheets were then centrifuged and washed three times with fresh DMF then ethanol to remove the unreacted metal salts and ligands. The washed MONs were stored in fresh ethanol as homogeneous suspensions until needed.

Ethanol suspensions of Zr-BTB and Zr-BTB-$NH_2$ MONs (1 mL) were dried using a hot plate at 80 °C to remove most of the solvent and then at 120 °C for complete drying. The resulting solids were characterised by powder X-ray diffraction (PXRD). The PXRD patterns of the as-synthesised Zr-BTB and Zr-BTB-$NH_2$ MONs were consistent with the ones reported in the literature,[24,31] indicating that phase pure materials were prepared (**Figure 1b**). Compared to the simulated pattern of 3D Zr-BTB,[25] the as-synthesised MONs showed

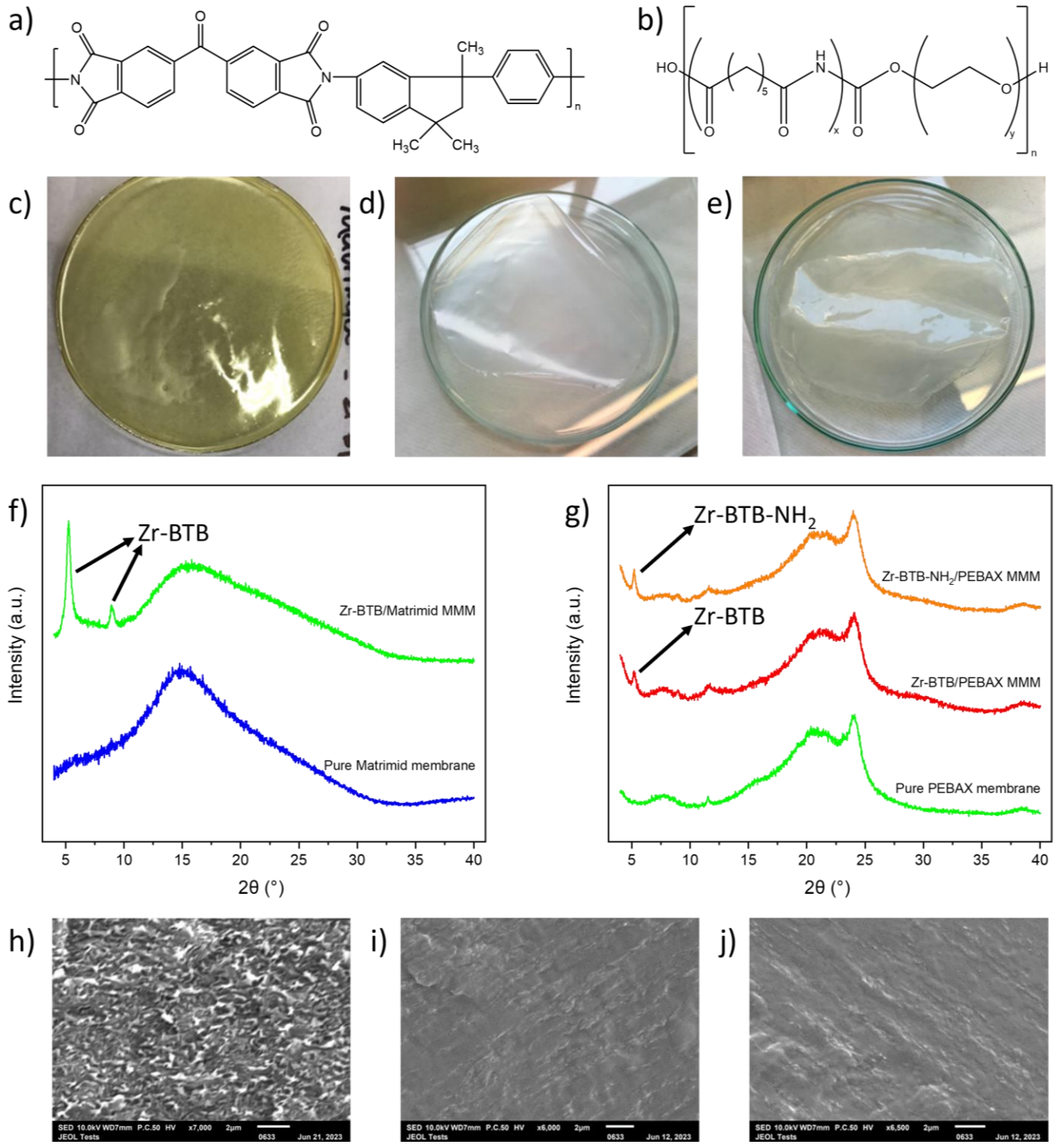


**Figure 3.** Chemical structures of (a) Matrimid 5218 and (b) PEBAX MH1657 (x = 40, y =60). Photos of (c) Zr-BTB/Matrimid MMM, (d) Zr-BTB/PEBAX MMM and (e) Zr-BTB-$NH_2$/PEBAX MMM. The content of MONs in all MMMs is 5 wt%. (f) PXRD patterns of pure Matrimid membrane and Zr-BTB/Matrimid MMM. (g) PXRD patterns of pure PEBAX membrane, Zr-BTB/PEBAX MMM and Zr-BTB-$NH_2$/PEBAX MMM. SEM cross-sectional images of (h) Zr-BTB/Matrimid MMM, (i) Zr-BTB/PEBAX MMM and (j) Zr-BTB-$NH_2$/PEBAX MMM.

only two peaks at 2θ = 5.1° and 8.9°, and the other peaks were not observed, which could be attributed to the extreme aspect ratios of the MONs resulting in line broadening and preferred orientation effects.[29] The hkls were assigned on the PXRD patterns of the as-synthesised MONs which matched with a 2D hexagonal lattice.

The Zr-BTB and Zr-BTB-$NH_2$ MONs were also characterised by atomic force microscopy (AFM) and the results showed that the two MONs have large lateral dimensions of a few micrometres (**Figure 2a-2d**). The thicknesses of Zr-BTB and Zr-BTB-$NH_2$ MONs are similar to each other and are about 1.5 nm. This thickness is comparable to the

van der Waals size of $Zr_6$ clusters (1.2 nm) in Zr-BTB reported by Lin *et al.*,[34] indicating the formation of monolayer nanosheets.

The $CO_2$ and $N_2$ uptakes of Zr-BTB and Zr-BTB-$NH_2$ MONs were measured using a Hiden Intelligent Gravimetric Analyser (IGA) at 25 ℃. The results showed that the $CO_2$ adsorption capacity of the two MONs were similar to each other, which was higher than their $N_2$ adsorption capacity under the same pressure (**Figure 2e**). The Zr-BTB and Zr-BTB-$NH_2$ MONs also exhibited higher $CO_2$ adsorption capacity compared to the pure Matrimid and the pure PEBAX membranes under the same pressure (**Figure 2f**). Therefore, incorporation of the two MONs as fillers into both Matrimid and PEBAX polymers would theoretically increase the $CO_2$ adsorption capacity of the membranes and potentially improve their gas separation performance.

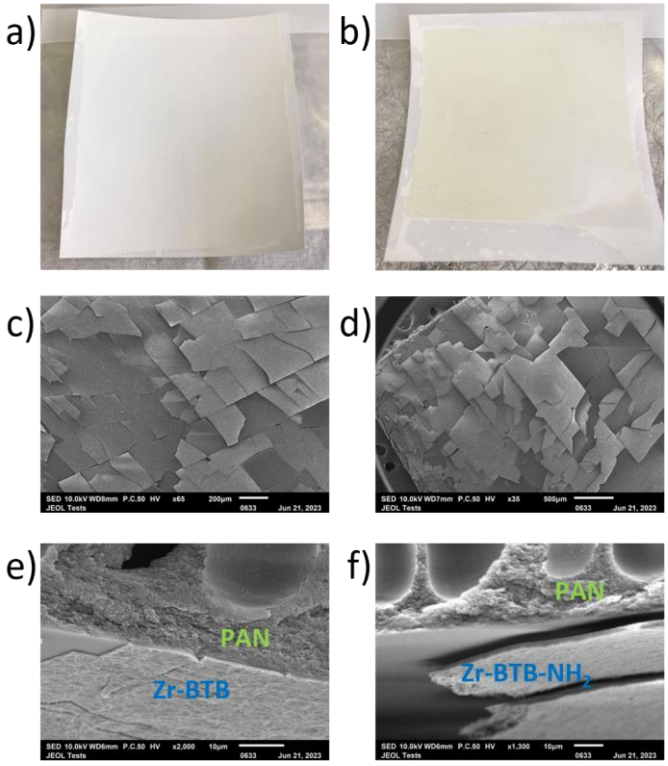


**Figure 4.** Photos of (a) Zr-BTB/PAN and (b) Zr-BTB-$NH_2$/PAN composite membranes. SEM images of (c,e) Zr-BTB/PAN composite membrane and (d,f) Zr-BTB-$NH_2$/PAN composite membrane.

**Mixed matrix membranes.** MMMs composed of 5 wt% of MON fillers (Zr-BTB and Zr-BTB-$NH_2$) and 95 wt% of polymers (Matrimid and PEBAX, **Figure 3a and 3b**) were prepared by a facile solution casting method. Briefly, mixed solutions containing the MONs and the polymers were poured into glass Petri dishes, and the membranes were peeled off from the Petri dishes following slow solvent evaporation at room temperature. The obtained membranes are denoted as Zr-BTB/Matrimid MMM, Zr-BTB/PEBAX MMM and Zr-BTB-$NH_2$/PEBAX MMM, respectively (**Figure 3c-3e**).

Agglomeration of Zr-BTB MONs was observed in the Zr-BTB/Matrimid MMM (**Figure 3c and Figure S6**), which could be attributed to the increased surface energy of the 2D MONs compared to the 3D MOFs that could easily result in their agglomeration,[29] and this phenomenon is also observed in other 2D material-based membranes reported in the literature.[35] Compared to Matrimid, the MONs were more uniformly distributed in the Zr-BTB/PEBAX MMM and Zr-BTB-$NH_2$/PEBAX MMM, and no filler agglomeration was observed (**Figure 3d and 3e**). This indicated that the compatibility between the PEBAX and the MONs is better than that of the Matrimid.

All membranes were characterised by PXRD. As shown in **Figure 3f and 3g**, the pure Matrimid membrane is amorphous, whereas the pure PEBAX membrane showed some crystalline peaks (2θ = 11.5° and 24.0°). The two characteristic peaks belonging to the Zr-BTB and Zr-BTB-$NH_2$ MONs (2θ = 5.1° and 8.9°) were observed in all MMMs, indicating that the crystallinity of MONs was maintained during membrane preparation (**Figure 3f and 3g**). The most prominent peak belonging to the nanosheets in the MMMs is at 2θ = 5.1°, which can be ascribed to the diffraction from the (0 0 1) crystal plane. This indicated that most of the nanosheets have the same orientation in the MMMs, and this particular orientation can maximise the separation efficiency of the nanosheets in the membranes, because it can expose the pores of MONs in the direction of the gas flux.[29] Zhao *et al.* previously used Zr-BTB MONs and PIM-1 to prepare MMMs and observed enhanced polymer matrix crystallinity after the addition of nanosheets (i.e., the intensity of the peak belonging to the PIM-1 polymer became stronger after adding Zr-BTB).[29] However, this phenomenon was not observed in either of our membranes, indicating that the interfacial interactions between the MONs and the PEBAX or Matrimid are not as strong as those of PIM-1.

**Table 1.** $CO_2/N_2$ permeability and selectivity of the pure Matrimid membrane, the pure PEBAX membrane and the MMMs.

| Membrane | P($CO_2$) (Barrer) | P($N_2$) (Barrer) | α |
|---|---|---|---|
| Pure Matrimid membrane | 11.12 | 0.35 | 32.23 |
| Zr-BTB/Matrimid MMM | 13.82 | 2.43 | 5.68 |
| Pure PEBAX membrane | 49.50 | 1.10 | 45.00 |
| Zr-BTB/PEBAX MMM | 15.04 | 0.60 | 25.07 |
| Zr-BTB-$NH_2$/PEBAX MMM | 24.80 | 1.16 | 21.40 |

The interfacial morphologies between the MON fillers and the polymers were characterised using scanning electron microscopy (SEM). Compared to the pure Matrimid membrane (**Figure S1**), the addition of Zr-BTB MONs increased the roughness of membrane cross-section (**Figure 3h and Figure S3)**. In the Zr-BTB/PEBAX MMM and the Zr-BTB-$NH_2$/PEBAX MMM, the MON fillers were found to be uniformly distributed in the membranes and no microscale filler-polymer phase segregation was observed (**Figure 3i,3j and Figure S4,S5**). Moreover, a comparison of the morphologies of the pure PEBAX membrane (**Figure S2**) and the MMMs indicated densification of the PEBAX membrane following addition of Zr-BTB and Zr-BTB-$NH_2$ MONs, which was attributed to the adhesion of polymer chains onto the surface of nanosheets.

**Composite membranes.** Composite membranes were prepared by coating ethanol suspensions of Zr-BTB and Zr-BTB-$NH_2$ MONs onto porous polyacrylonitrile (PAN) supports, and the membranes obtained following solvent evaporation at room temperature are denoted as Zr-BTB/PAN and Zr-BTB-$NH_2$/PAN (**Figure 4a and 4b**).

SEM characterisations of the composite membranes showed two types of defects in them: (1) cracks in the nanosheet layers (**Figure 4c and 4d**), and (2) poor adhesions between the nanosheets and the PAN supports (**Figure 4e and 4f**), which can result in low $CO_2/N_2$ selectivity of the membranes, because both $CO_2$ and $N_2$ can easily pass through these defects. Zr-BTB/PAN membranes were also prepared using a cold plate (**Figure S7**) to slow down the solvent evaporation rate, but these membrane defects still existed (**Figure S8a and S8b**).

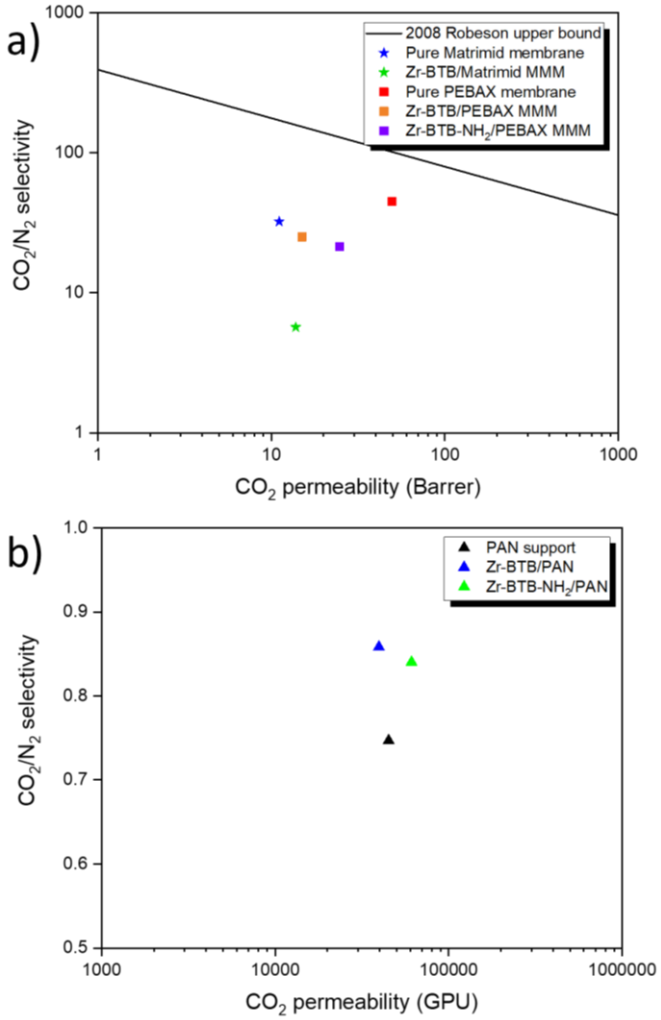


**Figure 5.** (a) $CO_2$ permeability and $CO_2/N_2$ selectivity of the pure Matrimid membrane, the pure PEBAX membrane and the MMMs, comparing with the 2008 Robeson upper bound.[9] (b) $CO_2$ permeability and $CO_2/N_2$ selectivity of the PAN support and the composite membranes.

**Gas separation experiments.** Single gas permeation experiments of all membranes were conducted using a custom-built constant volume-variable pressure apparatus (**Figure S9**)[33] to study their $CO_2/N_2$ permeability and selectivity. Details of the experiments and calculations can be found in the **Experimental** section and the results are summarised in **Table 1 and Table 2**.

In terms of the MMMs, the incorporation of Zr-BTB MONs into Matrimid did not significantly change the $CO_2$ permeability of the membrane, but increased its $N_2$ permeability from 0.35 to 2.43 Barrer, resulting in a decrease in the $CO_2/N_2$ selectivity of the membrane from 32.23 to 5.68 (**Figure 5a and Table 1**). This decrease in selectivity could be attributed to the filler agglomeration which resulted in defects in the Zr-BTB/Matrimid membrane. Whereas, the incorporation of Zr-BTB and Zr-BTB-$NH_2$ MONs into PEBAX decreased the $CO_2$ permeability of the membrane from 49.50 to 15.04 and 24.80 Barrer, respectively (**Figure 5a and Table S1**). This could be attributed to the densification of PEBAX membrane after the addition of MONs (**Figure 3i,3j and Figure S4,S5**), which is a known factor that can decrease the gas diffusivity and permeability of membranes.[36,37] Compared to the large decrease in $CO_2$ permeability of the PEBAX membrane, the change in its $N_2$ permeability after the additions of Zr-BTB and Zr-BTB-$NH_2$ MONs was not significant. Therefore, the $CO_2/N_2$ selectivity of PEBAX membrane decreased after the additions of the two MONs. The Robeson upper bound plots are commonly used for comparing the gas separation performance of different types of membranes, such as pure polymer membranes and MMMs.[8,9] As shown in **Figure 5a**, the gas separation performance the MMMs prepared in this work did not surpass the 2008 Robeson upper bound.[9]

**Table 2.** $CO_2/N_2$ permeability and selectivity of the PAN support and the composite membranes.

| Membrane | P($CO_2$) (GPU)* | P($N_2$) (GPU) | α |
|---|---|---|---|
| PAN support | 45092 | 60377 | 0.8 |
| Zr-BTB/PAN | 39591 | 46124 | 0.9 |
| Zr-BTB-$NH_2$/PAN | 61079 | 72688 | 0.8 |

*GPU is the abbreviation for gas permeation unit.

The $CO_2/N_2$ separation performances of the composite membranes were also investigated. As shown in **Figure 5b and Table 2**, the porous PAN support showed high baseline gas permeability and no $CO_2/N_2$ selectivity (0.75). Deposition of Zr-BTB and Zr-BTB-$NH_2$ MONs onto the PAN supports did not significantly improve their $CO_2/N_2$ selectivity, which could be attributed to the following reasons: (1) the two MONs have relatively large pore size (5.4 Å) compared to the sizes of $CO_2$ (3.3 Å) and $N_2$ (3.68 Å), making them difficult to separate the gases, and (2) there are defects in the membranes, including cracks in the MON layers (**Figure 4c and 4d**) and gaps between the MON layers and the PAN supports due to the poor adhesions between them (**Figure 4e and 4f**). These factors allowed both $CO_2$ and $N_2$ to pass easily through the membranes. Therefore, the $CO_2/N_2$ selectivity of the composite membranes was as low as the PAN support.

## Conclusions

Monolayer Zr-BTB and Zr-BTB-$NH_2$ MONs were investigated for membrane-based $CO_2/N_2$ separation application. In terms of the MMMs, the incorporation of 5 wt% of Zr-BTB MONs as fillers into Matrimid membrane did not significantly change the $CO_2$ permeability of the membrane, but increased its $N_2$ permeability, resulting in a decrease in the $CO_2/N_2$ selectivity of the membrane. The decrease in selectivity could be attributed to filler agglomeration which resulted in defects in the Zr-BTB/Matrimid MMM. The

incorporations of 5 wt% of Zr-BTB or Zr-BTB-$NH_2$ MONs as fillers into PEBAX membrane resulted in a drop in its $CO_2$ permeability due to membrane densification. Compared to the large decrease in $CO_2$ permeability of the membrane, the change in its $N_2$ permeability was not significant. Therefore, a decrease in the $CO_2/N_2$ selectivity of the PEBAX membrane was observed after the additions of Zr-BTB and Zr-BTB-$NH_2$ MONs. In terms of the composite membranes, no improvement in $CO_2/N_2$ selectivity was observed after depositions of the two MONs onto porous PAN supports. This could be attributed to the relatively large pore size of the two MONs and the defects in the composite membranes, which allowed both $CO_2$ and $N_2$ to easily pass through the membranes.

In the future, different filler loadings will be attempted to minimise the filler agglomeration and membrane densification problems of the MMMs to improve their gas separation performance. In terms of the composite membranes, post-synthetic functionalisation of the MONs to tune their pore size, and cross-linking of the MONs with polymer cross-linkers, or coating a polymer layer on top of the composite membranes to minimise their defects will be attempted to improve their gas separation performance.

## Experimental

**General considerations.** Chemicals and solvents were obtained from commercial suppliers and used without any purification, apart from the $H_3$BTB-$NH_2$ ligand which was provided by Ram R. R. Prasad. Details of all equipment used and material characterisations can be found in the Supplementary Information.

**Preparation of Zr-BTB and Zr-BTB-$NH_2$ MONs.** The two MONs were prepared by adapting the solvothermal synthesis method reported by Zhao *et al*.[24] $ZrCl_4$ (0.129 mmol) and $H_3$BTB or $H_3$BTB-$NH_2$ (0.068 mmol) were dissolved in a mixture of DMF (15 mL), $H_2O$ (2 mL), and HCOOH (2 mL) in a glass reaction vial. The vial was placed in a rection oven and heated at 120 °C for 24 h. The resulting suspensions of MON were then centrifuged and washed three times with fresh DMF then ethanol. The washed Zr-BTB and Zr-BTB-$NH_2$ MONs were stored in fresh ethanol as homogeneous suspensions until needed.

**Preparation of Zr-BTB/Matrimid MMM.** Matrimid 5218 (0.5 g) was dissolved in THF (5.5 g) in a round-bottom flask by magnetic stirring at room temperature. Ethanol suspension of Zr-BTB MONs were centrifuged and washed four times with THF. The washed MONs were suspended in fresh THF with a concentration of 4.9 mg $mL^{-1}$. The THF suspension of Zr-BTB MONs (5.37 mL) was then mixed with the Matrimid solution by magnetic stirring at 300 rpm for 3.5 hours. The resulting solution was then poured into a glass Petri dish. The Petri dish was covered with a lid and was placed under a top-drilled box. The Zr-BTB/Matrimid MMM was collected from the glass Petri dish following solvent evaporation at room temperature. The content of Zr-BTB MONs in the Zr-BTB/Matrimid MMM is 5 wt%.

As a reference, the pure Matrimid membrane was prepared by an identical method without the addition of MONs.

**Preparation of Zr-BTB/PEBAX and Zr-BTB-$NH_2$/PEBAX MMMs.** PEBAX MH1657 (0.5 g) was dissolved in a mixture of $H_2O$ (2.33 g) and EtOH (3.68 g) in a round-bottom flask by magnetic stirring at 80 °C. When the PEBAX solution was cooled to room temperature, ethanol suspension of Zr-BTB MONs (5.16 mL, 5.1 mg $mL^{-1}$) was added to the PEBAX solution and they were mixed by magnetic stirring at 300 rpm for 1.5 hours. The resulting solution was then poured into a glass Petri dish. The Petri dish was covered with a lid and was placed under a top-drilled box. The Zr-BTB/PEBAX MMM was collected from the Petri dish following solvent evaporation at room temperature. The Zr-BTB-$NH_2$/PEBAX MMM was prepared by an identical method. The content of Zr-BTB and Zr-BTB-$NH_2$ MONs in the MMMs is 5 wt%.

As a reference, the pure PEBAX membrane was prepared by an identical method without the addition of MONs.

**Preparation of Zr-BTB/PAN and Zr-BTB-$NH_2$/PAN composite membranes.** Ethanol suspensions of Zr-BTB and Zr-BTB-$NH_2$ MONs were poured onto PAN supports fixed on glass plates. A casting knife film applicator at a set height of 100 μm was then used to shape the suspensions of MONs into thin films. The wet Zr-BTB/PAN and Zr-BTB-$NH_2$/PAN membranes were placed under top-drilled boxes and were collected from the glass plates following solvent evaporation at room temperature.

**Gas separation experiments.** Single gas permeation experiments of all membranes were conducted using a custom-built constant volume-variable pressure apparatus (**Figure S9**)[33] using pure $N_2$ and $CO_2$ at 1.2 bar and room temperature.

The gas permeability of the membranes was obtained from the evolution of the pressure of the downstream side. The permeability coefficient, $\boldsymbol{P}$, was determined from the slope of the downstream pressure versus time curve under the steady-state condition and was calculated by **equation 1**.

$$\boldsymbol{P} = \frac{\boldsymbol{l}}{\boldsymbol{A}} \frac{\boldsymbol{V_{down}}}{\boldsymbol{P_{up} R T}} \left[ \left( \frac{\mathbf{d} \boldsymbol{P_{down}}}{\mathbf{d} \boldsymbol{t}} \right)_{\mathbf{ss}} \right] \quad \text{(equation 1)}$$

Where, $\boldsymbol{l}$ is the thickness of the membrane, $\boldsymbol{A}$ is the area of the membrane, $\boldsymbol{P_{up}}$ is the upstream pressure, $\boldsymbol{P_{down}}$ is the downstream pressure, $\boldsymbol{T}$ is the temperature recorded during each experiment, $\boldsymbol{R}$ is the gas constant, and $\boldsymbol{V_{down}}$ is the downstream volume ($\boldsymbol{V_{down}}$ = 23.8 $cm^3$/176 $cm^3$). $\boldsymbol{V_{down}}$ is chosen according to the permeability of the sample, the larger one (176 $cm^3$) is for the highly permeable PAN support and composite membranes, whereas the smaller one (23.8 $cm^3$) is for the less permeable pure Matrimid membrane, pure PEBAX membrane and MMMs.

The unit of the permeability coefficient, $\boldsymbol{P}$, for the pure Matrimid membrane, the pure PEBAX membrane and the MMMs is Barrer. 1 Barrer = $10^{-10}$ $cm^3$ $cm/cm^{-2}$ $s^{-1}$ $cmHg^{-1}$ at standard temperature and pressure (STP). The unit of $\boldsymbol{P}$ for the PAN support and the composite membranes is gas permeation unit (GPU), because the thicknesses of the PAN support and the composite membranes are not taken into account. 1 GPU = $10^{-6}$ $cm^3$ $cm^{-2}$ $s^{-1}$ $cmHg^{-1}$ at STP.

The $CO_2/N_2$ ideal selectivity, $\boldsymbol{\alpha}$, of the membranes is calculated by **equation 2**.

$$\boldsymbol{\alpha} = \frac{\boldsymbol{P(CO_2)}}{\boldsymbol{P(N_2)}} \quad \text{(equation 2)}$$

## Conflicts of interest

There are no conflicts to declare.

## Acknowledgements

Thanks to the Grantham Centre for Sustainable Futures for funding this project. The GO Fund (Grantham Opportunities Fund) enables Jiangtian Tan to visit Maria-Chiara Ferrari's group and Paul A. Wright's group to conduct essential experiments for this project. Thanks to CSC for funding Qian Jia and EPSRC for funding Elsa Lasseuguette and Ram R. R. Prasad.

## Notes and references

1. V. Scott, S. Gilfillan, N. Markusson, H. Chalmers and R. S. Haszeldine, *Nat. Clim. Change*, 2012, **3**, 105-111.
2. F. Vega, F. M. Baena-Moreno, L. M. Gallego Fernández, E. Portillo, B. Navarrete and Z. Zhang, *Appl. Energy*, 2020, **260**, 114313.
3. R. L. Siegelman, E. J. Kim and J. R. Long, *Nat. Mater.*, 2021, **20**, 1060–1072.
4. A. Katare, S. Kumar, S. Kundu, S. Sharma, L. M. Kundu and B. Mandal, *ACS Omega*, 2023, **8**, 17511-17522.
5. J. Míguez, J. Porteiro, R. Pérez-Orozco and M. Gómez, *Energies*, 2018, **11**, 3153.
6. Y. Peng and W. Yang, *Adv. Mater. Interfaces*, 2019, **7**, 1901514.
7. Y. Cheng, Y. Pu and D. Zhao, *Chem Asian J.*, 2020, **15**, 2241-2270.
8. L. M. Robeson, *J. Membr. Sci.*, 1991, **62**, 165−185.
9. L. M. Robeson, *J. Membr. Sci.*, 2008, **320**, 390-400.
10. M. Wang, Z. Wang, S. Zhao, J. Wang and S. Wang, *Chin. J. Chem. Eng.*, 2017, **25**, 1581-1597.
11. H. C. Zhou and S. Kitagawa, *Chem. Soc. Rev.*, 2014, **43**, 5415-5418.
12. M. Z. Ahmad, M. Navarro, M. Lhotka, B. Zornoza, C. Téllez, W. M. de Vos, N. E. Benes, N. M. Konnertz, T. Visser, R. Semino, G. Maurin, V. Fila and J. Coronas, *J. Membr. Sci.*, 2018, **558**, 64-77.
13. S. N. Wijenayake, N. P. Panapitiya, S. H. Versteeg, C. N. Nguyen, S. Goel, K. J. Balkus, I. H. Musselman and J. P. Ferraris, *Ind. Eng. Chem. Res.*, 2013, **52**, 6991-7001.
14. D. J. Ashworth and J. A. Foster, *J. Mater. Chem. A*, 2018, **6**, 16292-16307.
15. F. Moghzi, J. Soleimannejad, E. C. Sañudo and J. Janczak, *ACS Appl. Mater. Interfaces*, 2020, **12**, 44499-44507.
16. J. Nicks, J. Zhang and J. A. Foster, *Chem. Commun.*, 2019, **55**, 8788-8791.
17. Y. Song, J. Yang, L. Wang and Z. Xie, *ChemMedChem*, 2020, **15**, 416-419.
18. J. Nicks, K. Sasitharan, R. R. R. Prasad, D. J. Ashworth and J. A. Foster, *Adv. Funct. Mater.*, 2021, **31**, 2103723.
19. T. Rodenas, I. Luz, G. Prieto, B. Seoane, H. Miro, A. Corma, F. Kapteijn, I. X. F. X. Llabres and J. Gascon, *Nat. Mater.*, 2015, **14**, 48-55.
20. Y. Yang, K. Goh, R. Wang and T. H. Bae, *Chem. Commun.*, 2017, **53**, 4254-4257.
21. A. Pustovarenko, M. G. Goesten, S. Sachdeva, M. Shan, Z. Amghouz, Y. Belmabkhout, A. Dikhtiarenko, T. Rodenas, D. Keskin, I. K. Voets, B. M. Weckhuysen, M. Eddaoudi, L. de Smet, E. J. R. Sudholter, F. Kapteijn, B. Seoane and J. Gascon, *Adv. Mater.*, 2018, **30**, e1707234.
22. S. Kim, E. Shamsaei, X. Lin, Y. Hu, G. P. Simon, J. G. Seong, J. S. Kim, W. H. Lee, Y. M. Lee and H. Wang, *J. Membr. Sci.*, 2018, **549**, 260-266.
23. G.-Y. Qiao, S. Yuan, J. Pang, H. Rao, C. T. Lollar, D. Dang, J.-S. Qin, H.-C. Zhou and J. Yu, *Angew. Chem. Int. Ed.*, 2020, **59**, 18224–18228.
24. H. Yuan, G. Liu, Z. Qiao, N. Li, P. J. S. Buenconsejo, S. Xi, A. Karmakar, M. Li, H. Cai, S. J. Pennycook and D. Zhao, *Adv. Mater.*, 2021, **33**, e2101257.
25. Z. Hu, E. M. Mahdi, Y. Peng, Y. Qian, B. Zhang, N. Yan, D. Yuan, J.-C. Tan and D. Zhao, *J. Mater. Chem. A*, 2017, **5**, 8954-8963.
26. X. Feng, Y. Ren, H. Wang, W. Wu and H. Jiang, *Catal. Sci. Technol.*, 2023, **13**, 7036-7045.
27. D. Zhan, Z. Yu, A. Saeed, Q. Hu, N. Zhao, W. Xu, J. Wang, L. Kong and J. Liu, *J. Mater. Chem. C*, 2023, **11**, 10738-10747.
28. H. Yuan, K. Li, D. Shi, H. Yang, X. Yu, W. Fan, P. J. S. Buenconsejo and D. Zhao, *Adv. Mater.*, 2023, **35**, e2211859.
29. Y. Cheng, S. R. Tavares, C. M. Doherty, Y. Ying, E. Sarnello, G. Maurin, M. R. Hill, T. Li and D. Zhao, *ACS Appl. Mater. Interfaces*, 2018, **10**, 43095-43103.
30. D. Wang, Y. Ying, Y. Zheng, Y. Pu, Z. Yang and D. Zhao, *J. Membr. Sci. Lett.*, 2022, **2**, 100017.
31. Y. Pu, Z. Yang, V. Wee, Z. Wu, Z. Jiang and D. Zhao, *J. Membr. Sci.*, 2022, **641**, 119912.
32. E. Lasseuguette, L. Fielder-Dunton, Q. Jian and M.-C. Ferrari, *Membranes*, 2022, **12**, 584.
33. Q. Jia, E. Lasseuguette, M. M. Lozinska, M. C. Ferrari and P. A. Wright, *ACS Appl. Mater. Interfaces*, 2022, **14**, 46615-46626.
34. X. Feng, Y. Song and W. Lin, *J. Am. Chem. Soc.*, 2021, **143**, 8184-8192.
35. X. Zhu, C. Tian, C. L. Do-Thanh and S. Dai, *ChemSusChem*, 2017, **10**, 3304-3316.
36. S. Kalantari, M. Omidkhah, A. Ebadi Amooghin and T. Matsuura, *Appl. Mater. Today*, 2020, **18**, 100491.
37. A. Husna, I. Hossain, I. Jeong and T. H. Kim, *Polymers*, 2022, **14**, 655.

# Supplementary Information

## Zirconium-based metal-organic nanosheets for gas separation applications

Jiangtian Tan,[a] Elsa Lasseuguette,[b] Qian Jia,[c] Ram R. R. Prasad,[a] Maria-Chiara Ferrari,*[b] Paul A. Wright*[c] and Jonathan A. Foster*[a]

[a]*Department of Chemistry, University of Sheffield, Sheffield, UK.*

[b]*School of Engineering, University of Edinburgh, Edinburgh, UK.*

[c]*EaStCHEM School of Chemistry, University of St Andrews, St Andrews, UK.*

**Table of contents**

## S1. Equipment and Software

### S1.1. Atomic force microscopy

Atomic force microscopy (AFM) images were recorded using a Bruker Multimode 5 Atomic Force Microscope, operating in soft-tapping mode in air under standard ambient temperature and pressure, fitted with Bruker OTESPA-R3 silicon cantilevers. Samples were prepared by drop-casting 10 µL of diluted Zr-BTB and Zr-BTB-$NH_2$ metal-organic nanosheets (MONs) suspensions onto the centre of freshly cleaved mica sheets heated to 120 °C on a hot plate. These mica sheets were stuck to stainless steel, magnetic Agar scanning probe microscopy specimen discs. All AFM images reported in this work were processed using Gwyddion software.

### S1.2. Gas adsorption experiments

All samples were degassed under vacuum at 145 ℃ for 10 hours to remove the moisture prior to the gas adsorption experiments. The high-pressure gas adsorption experiments were conducted using a Hiden Intelligent Gravimetric Analyser (IGA) at 25 ℃, and the mass change was recorded in each adsorption/desorption step, and each step stopped when the uptake reached 98% of the asymptotic equilibrium value or after 90 mins, whichever was shorter.

### S1.3. Powder X-ray diffraction

Powder X-ray diffraction (PXRD) data of the MONs and the membranes were collected using a Bruker-AXS D8 diffractometer using Cu $K_\alpha$ (λ=1.5418 Å) radiation and a LynxEye position sensitive detector in Bragg Brentano parafocussing geometry using a flat silicon plate.

### S1.4. Scanning electron microscopy

Scanning electron microscopy (SEM) characterisations of the pure Matrimid, pure PEBAX, MMMs, and composite membranes were conducted using JSM-IT100 (JEOL, Japan). Before SEM characterisations, the membrane samples were fractured using liquid nitrogen and then sputtered with gold to form a conductive surface.

## S2. Membranes

### S2.1. Pure Matrimid and pure PEBAX membranes

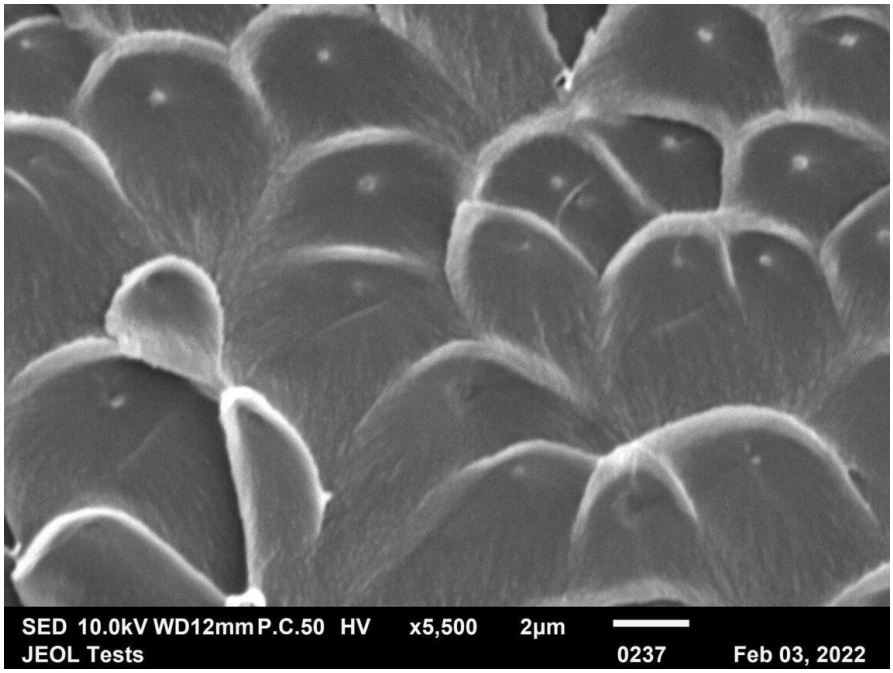


**Figure S1.** SEM cross-sectional image of pure Matrimid membrane.

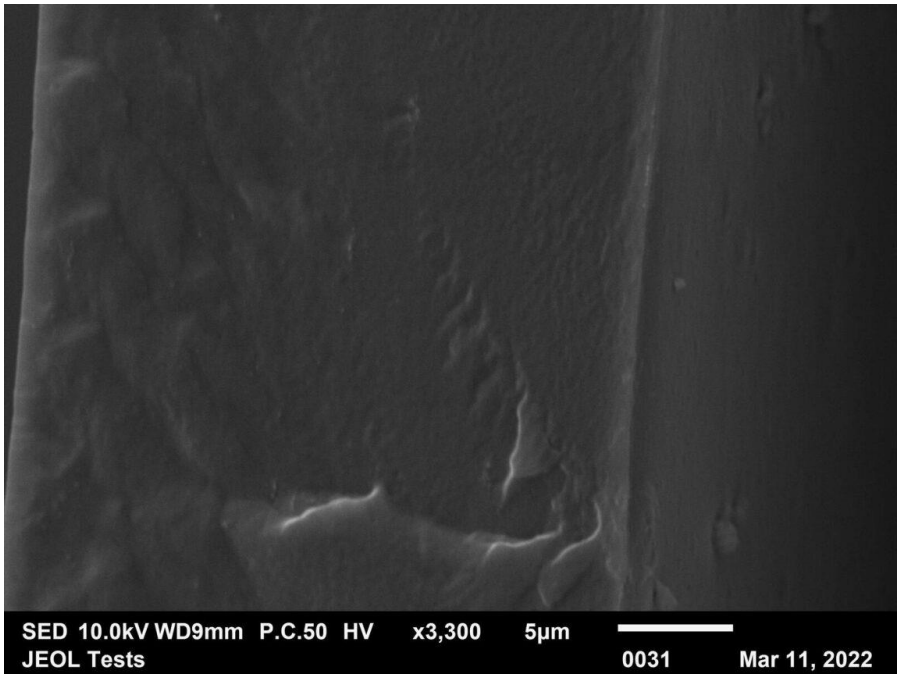


**Figure S2.** SEM cross-sectional image of pure PEBAX membrane.

**S2.2. Mixed matrix membranes (MMMs)**

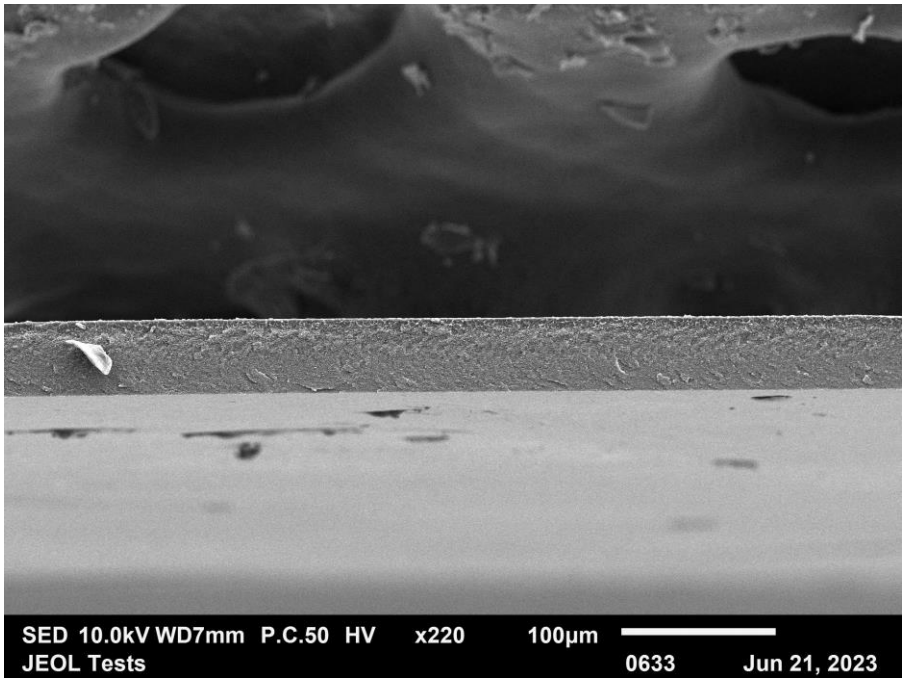


**Figure S3.** SEM cross-sectional image of Zr-BTB/Matrimid MMM.

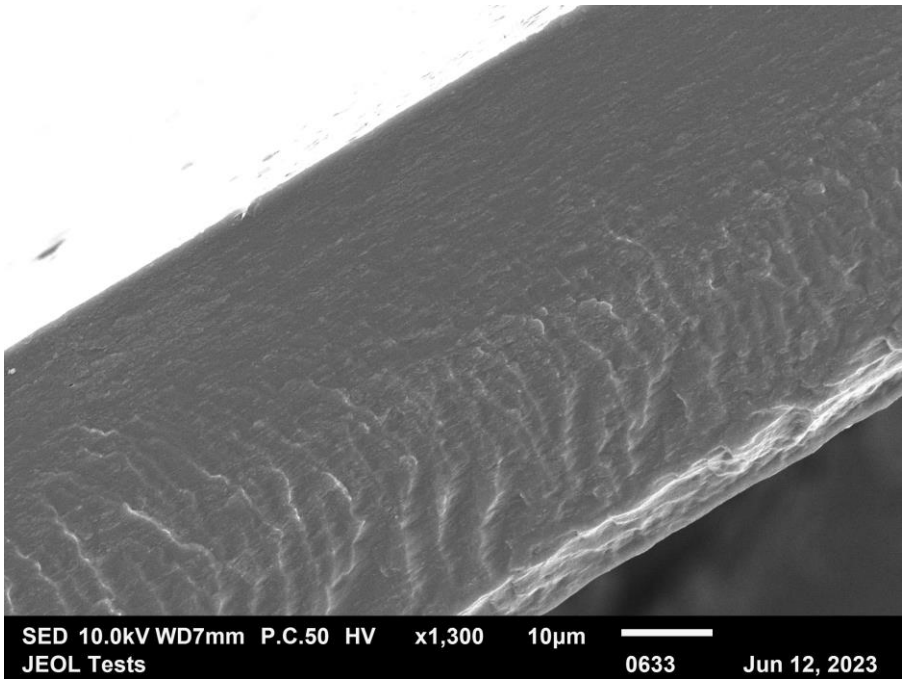


**Figure S4.** SEM cross-sectional image of Zr-BTB/PEBAX MMM.

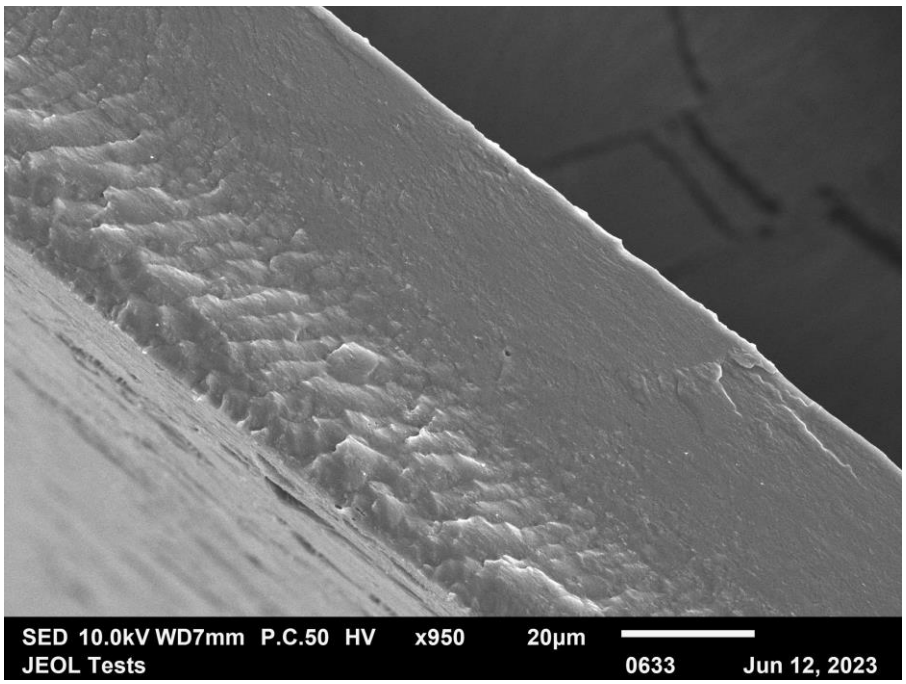


**Figure S5.** SEM cross-sectional image of Zr-BTB-$NH_2$/PEBAX MMM.

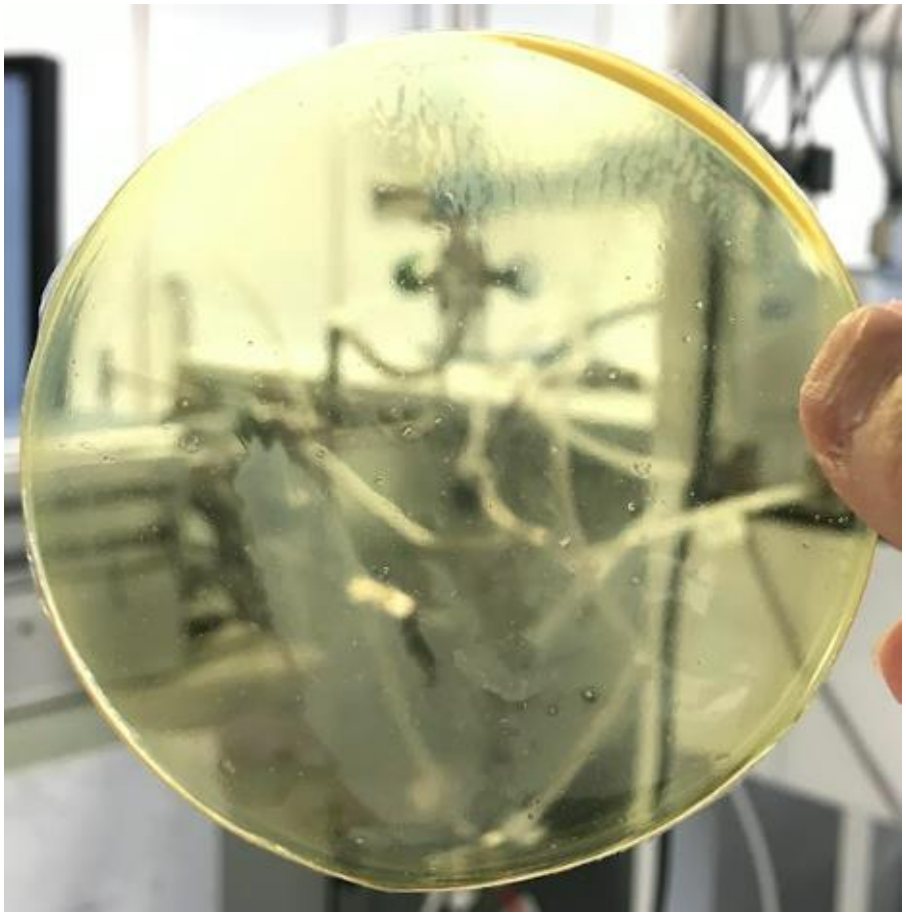

**Figure S6.** Photo of Zr-BTB/Matrimid MMM showing agglomeration of Zr-BTB MONs.

**S2.3. Zr-BTB/PAN composite membrane**

To study the effect of solvent evaporation rate on membrane preparation, the Zr-BTB/PAN composite membrane was also prepared using a cold plate (**Figure S6**). Ethanol suspension of Zr-BTB MONs was poured onto a polyacrylonitrile (PAN) support fixed on the cold plate. A casting knife film applicator at a set height of 100 µm was then used to shape the MON suspension into a thin film. The Zr-BTB/PAN composite membrane was collected from the cold plate following slow solvent evaporation. The temperature of the cold plate was maintained at 13 ℃ using a water-cooling system.

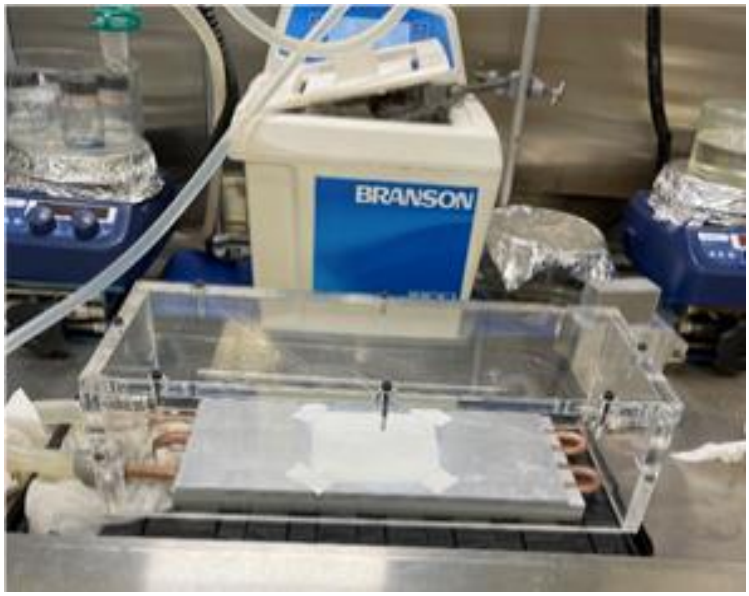


**Figure S7.** Cold plate used to prepare Zr-BTB/PAN composite membrane.

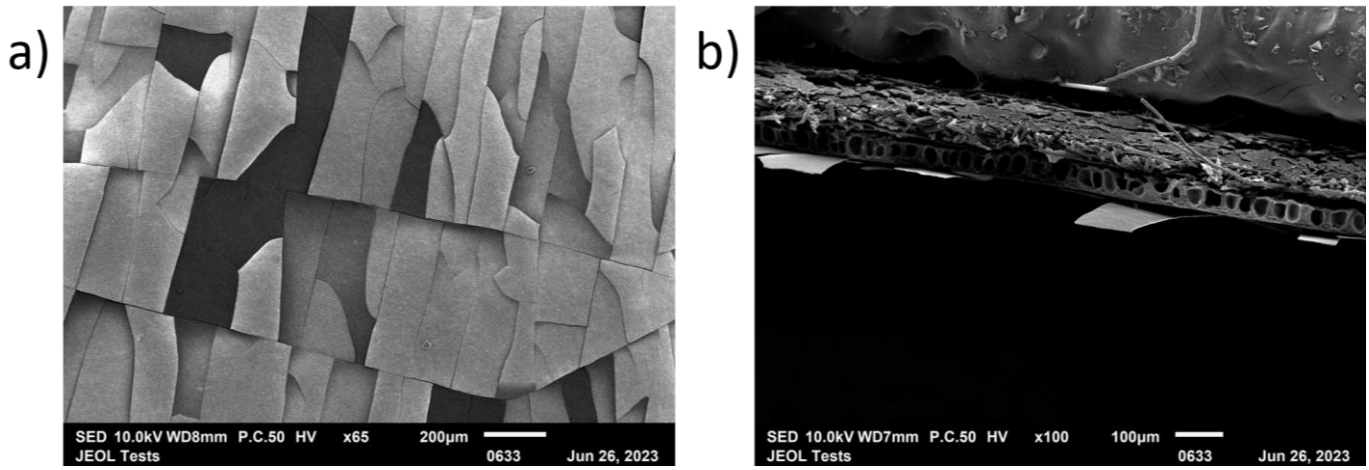


**Figure S8.** (a,b) SEM images of Zr-BTB/PAN composite membrane prepared using the cold plate.

**S2.4. Gas permeation experiments**

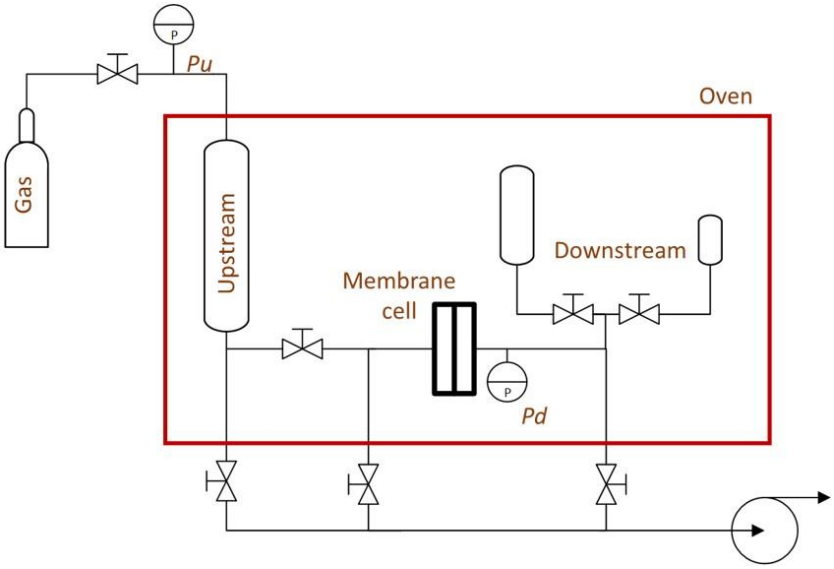


**Figure S9.** Schematic illustration of the constant volume-variable pressure apparatus used to study the $CO_2/N_2$ separation performance of the membranes.[1]

## S3. References

1. Q. Jia, E. Lasseuguette, M. M. Lozinska, M. C. Ferrari and P. A. Wright, *ACS Appl. Mater. Interfaces*, 2022, **14**, 46615-46626.

# Chapter 5

# Conclusions and Outlook

## 5.1 Conclusions

Metal-organic nanosheets (MONs) are an emerging class of two-dimensional materials for use in separation applications.[1, 2] Zirconium-based MONs, especially Zr-BTB, have well-defined pore size, tunable functionalities, good stability in water, good thermal and chemical stability and good solution processability,[3-5] making them promising candidates for use in the separation of dyes and salts in aqueous solutions[6] and gas separation applications.[7-10] Zhao and co-workers previously reported a facile and scalable bottom-up method for the preparation of Zr-BTB MONs,[5] in which $ZrCl_4$ + $H_3BTB$ were dissolved in a mixture of DMF, HCOOH and $H_2O$, and the nanosheets were prepared after incubating the mixed solution at 120°C for 24 h.

In this thesis, we confirmed that Zhao's method was reliable,[5] and the prepared monolayer Zr-BTB MONs had a thickness of approximately 1.5 nm and high aspect ratios, and they could form homogeneous suspensions in different solvents such as deionised water and ethanol.

In **Chapter 2**, the Zr-BTB MON suspensions were found to form gels after solvent evaporation or centrifugation. Rheological measurements of the gels showed their self-healing behaviour which could be attributed to the electrostatic interaction between the MONs forming a "house of cards" structure. Rapid and selective loading of the gels with different molecular cargoes was achieved by centrifugation of mixtures containing the Zr-BTB MON suspensions and the cargo solutions. In comparison with neutral cargo molecules such as trans-anethole (T-Ane) and carbamazepine (CBZ), significantly higher loadings were observed for charged cargo molecules such as methylene blue (MnB), methyl orange (MO) and brilliant blue G (BBG). These cargo molecules were also found to diffuse out of the gels at different rates, which could be attributed to the different pathways available to them depending on their size and charge. The neutral T-Ane molecules were found to diffuse more rapidly out of the gels than the neutral CBZ molecules. This was because the T-Ane molecules were small enough to pass through the pores of Zr-BTB MONs, whilst the larger CBZ molecules had to take more tortuous and longer pathways around the nanosheets when they were diffusing out of the gels. Due to electrostatic interaction, charged cargo molecules (MnB, MO and BBG) stuck to the surface of Zr-BTB MONs, resulting in their slower release rates compared to the neutral ones. The mechanism proposed here was similar to the molecular separation mechanism of MON-based membranes discussed in **Chapter 1** (**Figure 10b**),[1] in which molecules smaller than the pore size of MONs could rapidly permeate through the membranes along the short permeation pathways, whilst molecules larger than the pore size of MONs had to take more tortuous and longer permeation pathways, leading to their different permeation rates and the effective separation of

molecules based on their different sizes. Therefore, in **Chapter 3** and **Chapter 4**, the Zr-BTB MONs were processed into such membranes and their use in the separation of organic dyes and the separation of gases were investigated, respectively.

In **Chapter 3**, the Zr-BTB MON suspensions were spin-coated onto polyethersulfone (PES) supports to fabricate composite membranes for use in the separation of different organic dyes in aqueous solutions. The fabricated membranes exhibited a high permeability toward small negatively charged dyes such as MO and a high rejection rate of up to ~90% toward larger negatively charged dyes such as BBG. This could be attributed to the size exclusion effect of the nanosheet membranes, which selectively separated the large BBG dyes in aqueous solutions, whilst allowing the small MO dyes to rapidly pass through the membranes. In addition, deposition of the Zr-BTB MONs onto the PES supports increased the adsorption of positively charged MnB dyes on the membranes and finally improved their rejection rates toward MnB. Therefore, both size exclusion and adsorption played important roles in the effective separation of organic dyes in aqueous solutions.

In **Chapter 4**, the Zr-BTB MONs were incorporated as fillers into Matrimid and PEBAX polymers to fabricate mixed matrix membranes for use in the separation of $CO_2$ and $N_2$. It was found that the incorporation of 5 wt% of nanosheets into the Matrimid membrane did not significantly change its $CO_2$ permeability but increased its $N_2$ permeability, and thus decreased the $CO_2/N_2$ separation selectivity of the membrane. The decrease in selectivity could be attributed to the agglomeration of Zr-BTB MONs which resulted in defects in the mixed matrix membrane. Whereas, the incorporation of 5 wt% of Zr-BTB MONs into the PEBAX membrane resulted in membrane densification, decreasing the $CO_2$ permeability and the $CO_2/N_2$ separation selectivity of the membrane. The Zr-BTB MONs were also deposited onto polyacrylonitrile (PAN) supports to prepare composite membranes. However, due to the relatively large pore size of Zr-BTB MONs (5.4 Å) compared to the sizes of $CO_2$ (kinetic diameter = 3.3 Å) and $N_2$ (kinetic diameter = 3.68 Å) as well as defects in the nanosheet layer deposited on the PAN support, and poor adhesion between the nanosheets and the supports, the prepared composite membranes exhibited high gas permeability but almost no $CO_2/N_2$ separation selectivity.

Zr-BTB derivatives were also investigated in this thesis, including Zr-BTB-$NH_2$ and Zr-TATB. Atomic force microscopy characterisations of the two nanosheets showed that they had high aspect ratios and their thicknesses were between 1 and 1.5 nm which were similar to the thickness of Zr-BTB MONs. Powder X-ray diffraction characterisations of Zr-BTB-$NH_2$ and Zr-TATB MONs showed that their characteristic peaks were located at the same positions as Zr-BTB MONs, indicating that the three MONs had an

isoreticular structure, and thus they had the same pore size. This explained why the separation performances of the Zr-BTB-$NH_2$ and Zr-TATB membranes toward organic dyes (BBG, MO and MnB) and gases ($CO_2$ and $N_2$) were similar to the separation performances of the Zr-BTB membranes.

**5.2 Outlook**

Compared to Zr-BTB MONs, the use of Zr-BTB-$NH_2$ and Zr-TATB did not significantly improve the separation performances of the membranes toward small organic dyes and gas molecules. This could be attributed to the same pore size of the three nanosheets, which was too large to separate such small molecules. However, it is possible to functionalise the Zr-BTB-$NH_2$ MON to tune its pore size and surface properties to improve the separation performances of the membranes toward small molecules. Previous work of our group showed that the layered copper 2-aminobenzenedicarboxylate MOF, Cu(ABDC)(DMF), could be post-synthetically functionalised by treating the MOF suspension in chloroform with 1,3-propanesultone and stirring at 55 ℃, and the functionalised MOF was exfoliated into nanosheets for use in catalysis application.[11] This method could be used to functionalise the Zr-BTB-$NH_2$ MONs, and the sulfonate chains attached to the -$NH_2$ groups could potentially go into the pores of the MONs, decreasing their pore size, allowing them to separate small dyes and gas molecules. The addition of the sulfonate groups may also change the surface charge of the MONs and the fabricated membranes, increasing the adsorption of charged dyes on the membranes, thus increasing their rejection rates toward charged dyes. Another work of our group showed that the surface properties of MONs could be tuned by post-exfoliation functionalisation using click chemistry to add a wide range of different functional groups.[12] This method could be used to functionalise the Zr-BTB-$NH_2$ MONs, and the introduced functional groups might also decrease the pore size of the MONs, and thus improving the separation performances of the fabricated membranes toward small molecules. It would also be interesting to compare the water purification performances of the membranes fabricated with the Zr-BTB-$NH_2$ MONs bearing different functional groups, because their surface properties (hydrophilicity/hydrophobicity) might be different. In addition, Zhao and co-workers previously fabricated composite membranes by depositing Zr-BTB MONs onto polyacrylonitrile (PAN)-400 supports using a doctor blade casting method and the membranes they fabricated showed excellent desalination performance (rejection rate >98% for $Mg^{2+}$ and $Al^{3+}$).[6] Therefore, in the future, it is worth attempting Zhao's method to fabricate membranes with Zr-BTB, Zr-BTB-$NH_2$, Zr-TATB and the functionalised MONs to investigate their use in desalination applications.

In summary, through functionalisation of zirconium-based MONs to systematically tune their pore size and surface properties and attempting the other advanced membrane preparation methods reported in the broad literature, we anticipate progress in the use of two-dimensional zirconium-based metal-organic nanosheets in the separation of nanometer-sized and subnanometer-sized chemical species, such as dyes, gas molecules and salts.

Further work includes: 1. preparing gels with other MONs and solvents to study the generalisability of the centrifugation method, 2. exploring the use of MON gels in drug release applications with model drugs including ibuprofen and doxorubicin, 3. optimising the water purification membranes by post-synthetic functionalisation of the MONs to tune their pore sizes and surface properties, 4. exploring the use of membranes in desalination and direct lithium extraction applications, and 5. optimising the MMMs by changing filler loadings and optimising the composite membranes by polymer cross-linking or polymer coating to improve their gas separation performances.

**5.3 References**


1. Y. Peng and W. Yang, *Adv. Mater. Interfaces*, 2019, **7**, 1901514.
2. J. Nicks, K. Sasitharan, R. R. R. Prasad, D. J. Ashworth and J. A. Foster, *Adv. Funct. Mater.*, 2021, **31**, 2103723.
3. Z. Hu, E. M. Mahdi, Y. Peng, Y. Qian, B. Zhang, N. Yan, D. Yuan, J.-C. Tan and D. Zhao, *J. Mater. Chem. A*, 2017, **5**, 8954-8963.
4. G. Y. Qiao, S. Yuan, J. Pang, H. Rao, C. T. Lollar, D. Dang, J. S. Qin, H. C. Zhou and J. Yu, *Angew. Chem.*, 2020, **59**, 18224-18228.
5. H. Yuan, G. Liu, Z. Qiao, N. Li, P. J. S. Buenconsejo, S. Xi, A. Karmakar, M. Li, H. Cai, S. J. Pennycook and D. Zhao, *Adv. Mater.*, 2021, **33**, e2101257.
6. H. Yuan, K. Li, D. Shi, H. Yang, X. Yu, W. Fan, P. J. S. Buenconsejo and D. Zhao, *Adv. Mater.*, 2023, **35**, e2211859.
7. Y. Li, T. Wang and D. Liu, *Chem Asian J.*, 2021, **16**, 3413-3418.
8. Y. Cheng, S. R. Tavares, C. M. Doherty, Y. Ying, E. Sarnello, G. Maurin, M. R. Hill, T. Li and D. Zhao, *ACS Appl. Mater. Interfaces*, 2018, **10**, 43095-43103.
9. Y. Pu, Z. Yang, V. Wee, Z. Wu, Z. Jiang and D. Zhao, *J. Membr. Sci.*, 2022, **641**, 119912.
10. D. Wang, Y. Ying, Y. Zheng, Y. Pu, Z. Yang and D. Zhao, *J. Membr. Sci. Lett.*, 2022, **2**, 100017.
11. J. Nicks, J. Zhang and J. A. Foster, *Chem. Commun.*, 2019, **55**, 8788-8791.
12. J. Nicks and J. A. Foster, *Nanoscale*, 2022, **14**, 6220-6227.